JOURNAL OF APPLIED ENGINEERING SCIENCES
ISSN: 2247-3769 / e-ISSN: 2284-7197
sciendo
VOL. 14(27), ISSUE 1/2024
ART.NO. 398 pp. 81-88

NUMERICAL SIMULATION OF IMPROVING THE EFFICIENTY OF PHOTOVOLTAIC THERMAL PANELS

C.-G. Popovici [a], G. Filipescu[a] , N.-C. Chereches [a]*, S.-V. Hudișteanu [a], E.-F.Țurcanu [a], Ana Diana Ancas [a] , Marina Verdeș [a], P. V. Roșu[a]

[a] Technical University "Ghe. Asachi" of Iasi, Faculty of Civil Engineering and Building Servicies, Department Building Sevicies, D. Mangeron 67 str.,700050, Romania; E-mails: catalin-george.popovici@academic.tuiasi.ro, george.filipescu@student.tuiasi.ro, *nelu.chereches@academic.tuiasi.ro, valeriu-sebastian.hudisteanu@academic.tuiasi.ro, florin-emilian.turcanu@academic.tuiasi.ro, ana-diana.ancas@academic.tuiasi.ro, marina.verdes@academic.tuiasi.ro, rosupetru@yahoo.com

Received: 22.01.2024 / Accepted: 14.02.2024 / Revised: 26.02.2024 / Available online: 31.05.2024

DOI: 10.2478/jaes-2024-0010

KEY WORDS: green energy, photovoltaic thermal panels, numerical simulation, Ansys Software.

ABSTRACT:

The need to optimize the operation of photovoltaic modules inevitably arises with the development of green energy production technology. In order to achieve a good technological yield, durability and efficiency in production, continuous studies and innovations are required. This study focuses on simulating the operation of water-cooled and uncooled PV modules in order to understand the temperature-dependent PV operation. This cooling module consists, in the first phase, of a copper coil through which water circulates, and in the second phase, of a coolant distributor/collector system. The module is attached to the lower surface of the photovoltaic panel, respectively to the teller foil layer. For this simulation we used the Ansys software package (Discovery, Fluent and Space Claim).

1.INTRODUCTION

One of the most widespread renewable energy technologies is the use of photovoltaic (PV) systems, which convert solar radiation into usable electrical energy (Hu J. et. al. 2016; Yau YH et. al. 2016, Markvart T. 2020). This renewable energy production technology is pollution-free during operation, mitigates global warming issues, reduces operational costs, and requires minimal maintenance compared to other renewable energy technologies (Wang Y. et.al. 2006; Bhubaneswari P. et. al.2011).

In the world, there are significant concerns about a potential energy crisis, and the majority of countries still rely on conventional sources of energy production (Pomares-Hernandez C et.al.2021; Kannan N. et.all. 2016) The situation, exacerbated by the world's population growth and industrial progress, has led to an increased demand for energy, causing significant environmental problems due to the intensive exploitation of fossil fuels. In this context, interest in renewable energy sources such as solar or wind energy has grown (Pomares-Hernandez C. et.al.2021; Rauf A. et al. 2018; Robles A. Et.al. 2018).

The development of the present cooling module was conceived for its application on any type of rigid photovoltaic panel. The study includes simulations, taking into account the dimensional characteristics of the most commonly used photovoltaic modules available on the market. Such a method is designed to reduce both the time and cost of maintaining photovoltaic systems, as the cooling prolongs the system's lifespan. This aspect of durability has a positive impact on the environment by reducing costs and production, thereby lowering pollution, optimizing operational efficiency, and reducing harmful emissions into the atmosphere. Moreover, the obtained thermal energy from this cooling process can be stored for future use in domestic or industrial settings, further reducing the direct consumption of electricity required for thermal energy.

Despite the numerous advantages of PV technology, this conversion system faces climate-related challenges, such as hail, dust, and surface operating temperature, which can negatively affect the system's efficiency (DaSilva RM et al. 2010). External climatic parameters, such as wind velocity, ambient temperature, relative humidity, accumulated dust, and solar radiation, are the most common natural factors that influence the surface temperature of a photovoltaic module (Elbreki A.M. et. al.2016). Generally, for every 1°C increase in the temperature on the PV module's surface, there is a 0.5% reduction in efficiency (Kumar K. Et.al. 2007, Chandrasekar, M et al. 2015). As a result of the temperature rise, not all the absorbed solar energy by the photovoltaic cells is converted into electrical energy. To comply with the law of energy conservation, the remaining solar energy is transformed into heat (Tahar M. et. al. 2022). The consequences of this heat loss lead to an overall reduction in conversion efficiency. To make this renewable energy production technology the best solution, it is necessary to improve the efficiency of solar energy conversion systems (Reddy, S.R. et al. 2015). To turn it into a

* Corresponding author: Nelu-Cristian Chereches, e-mail: nelu.chereches@academic.tuiasi.ro

viable solution, different means of addressing this temperature issue must be found, resulting in an overall increase in conversion efficiency (Wang Y. et.al. 2006; Bhubaneswari P. et. al.2011).

2. CASE OF STUDY

The present study aims to calculate the temperature distribution on the surface of a photovoltaic panel under fixed ambient temperature and solar radiation conditions. The solar radiation has been chosen to be 1000W/m2K. Two types of active cooling methods were used: one with a serpentine cooling system and the other with a distributor/collector cooling system. Additionally, the simulation also includes the baseline scenario without any cooling. The inlet temperature of the cooling agent is set to be 20°C, and the thermal agent's circulation velocity. The system was simulated at 0.1; 0.3; 0.5; 0.7; and 0.9 m/s for each of the two cooling systems, as well as for the non-cooling scenario. This resulted in 11 simulations that were compared to understand which type of active cooling is more suitable under these conditions compared to the system without cooling. The data extracted from these simulations were provided a clearer understanding of this phenomenon. The PV surface has a size of 2m² and was subjected to uniform solar radiation over its entire surface.

The simulation results highlights the temperature distribution on the PV surface, the temperatures obtained at the PV surface, and the water temperatures at the outlet of the cooling circuit (for cases with cooling).

For this simulation and numerical analysis study, a standard photovoltaic panel with dimensions of 2000/1000mm was used, composed of the following layers:

- Cover and protective layer made of glass
- EVA layer 1 (ethylene-vinyl acetate)
- PV cells
- EVA layer 2
- Tedlar film (polyvinyl fluoride (PVF) film)

The materials used are the most commonly used in the photovoltaic panel industry, and their physical parameters such as thermal conductivity, density, thickness, and specific heat have been respected.

In constructing the photovoltaic panel, the weighted average of the physical parameters for each layer based on its thickness was considered. This resulted in a unique, compact, and homogeneous layer referred to as the 'PV layer', with specific characteristics (Table 1), which were introduced as calculation parameters for the simulation.

Layer material	Thickness (m)	Thermal Conductivity (W/m°C)	Specific Heat (J/kg°C)	Density (kg/mc)
PV	0,0045	14,44	885,73	2447,11

Table 1. Properties and Dimensions of the Material in the PV Layer Composition

The photovoltaic panel was constructed taking into account real specifications using the Ansys 2023 R1 and R2 student version software package. The limitation in this version was in the Meshing phase, where the calculation nodes and points cannot exceed 500,000 nodes. Generally, this is not a problem; the simulation can proceed smoothly with a level of calculation detail accepted in the research field. The geometry was created using the SpaceClaim program, which is integrated into the same Ansys package.

Fig. 1 and Fig. 2 represent a cross-sectional view of the photovoltaic panel created using the SpaceClaim software.

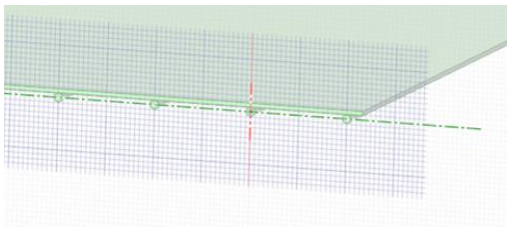


Figure 1. PV Cross-Section, 3D Top View

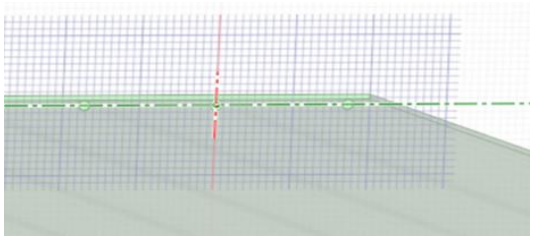


Figure 2. PV Cross-Section, 3D Bottom View

Fig.3 and Fig.4 represent the view in X-Z axis view of the PV with Serpentine Cooling respectively the PV with Distributor/Collector Cooling.

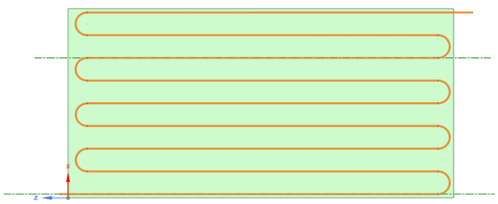


Figure 3. Lower X-Z Axis View of PV with Serpentine Cooling

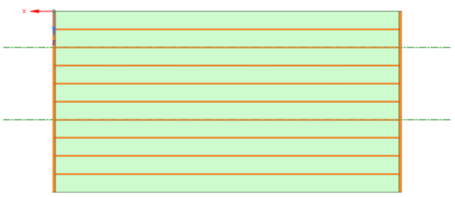


Figure 4. Lower X-Z Axis View of PV with Distributor/Collector Cooling

In Fig. 5-7 is presented the model of the frame used in the PV geometry; it was created using the Ansys Discovery program, version 2023 R1.

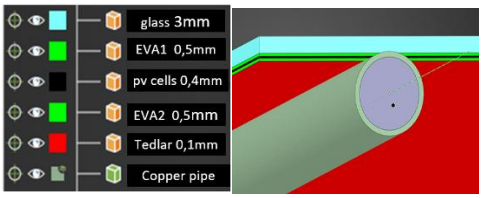


Figure 5. View of the Component Layers of PV

The system involves facilitating heat exchange between the photovoltaic panel and water through an installation composed of Copper pipes with diameters of Dn10mm (for the serpentine cooling system) and Dn16mm (the collector and distributor are constructed using Dn16mm pipes, while the circuits are built with Dn10mm pipes), directly attached to the Tedlar film exposed at the bottom of the PV panel.

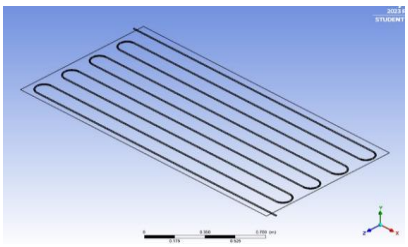


Figure 6. View of the Component Layers of PV

The serpentine cooling system consists of a sequence of 9 copper pipes with a diameter of Dn10mm, Fig. 8. The distance between the pipes is 101mm, and they are consecutively connected to each other through bends with a radius of 55mm. The total length of the serpentine is 18m.

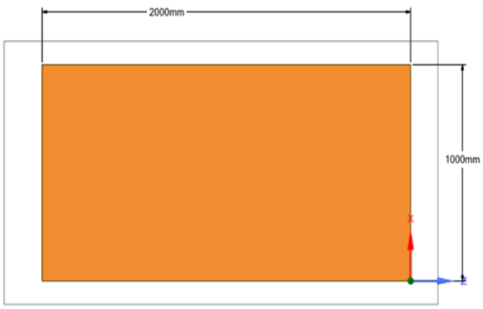


Figure 7. PV Dimensions

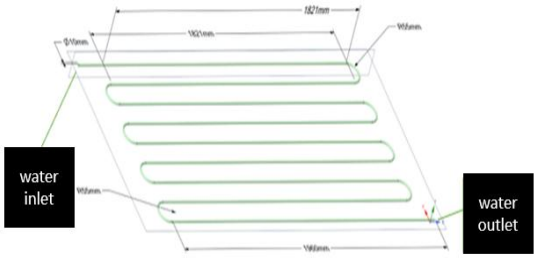


Figure 8. Dimensions of the Serpentine Cooling System

The dimensions of the distributor/collector cooling system are present in Fig. 9, and the distance between the secondary pipes, namely 101mm, is maintained.

The distance between the main pipes (distributor and collector) is 2018mm. This geometry is the only possible configuration to maintain the same physical attachment characteristics to the Tedlar film. Under these conditions, the volume of water in the secondary pipes is preserved and precisely corresponds to the same equivalent volume as in the serpentine pipes.

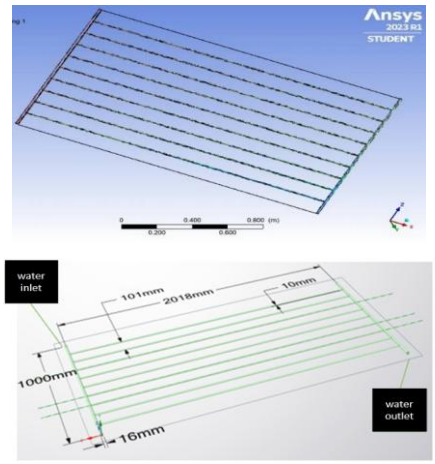


Figure 9. Geometry and Dimensions of the Distributor/Collector Cooling System

3. NUMERICAL SIMULATION

The numerical simulation was performed using the Ansys Workbench 2023-R1 program, student version. The geometry was created with the same CAD program, specifically the three-dimensional (3D) subdivision in SpaceClaim, followed by the Meshing phase, settings, solution, and results carried out with Ansys Fluent, a computational fluid dynamics (CFD) tool capable of physical modeling and simulation.
In this project, the numerical simulation for the operation of the same photovoltaic panel includes 3 cases:

- 3.1 Simulation of PV operation without cooling (G1)
- 3.2 Simulation of PV operation with serpentine cooling system (G2)
- 3.3 Simulation of PV operation with distributor/ collector cooling system (G3)

3.1. Simulation of PV operation without cooling

The numerical simulation for the case of the photovoltaic panel without cooling was possible with the following input parameters:

- Solar power: 1000W/m²
- Air density: constant
- Heat transfer air-PV: through conduction
- PV thermal resistance: negligible the calculation processes were set to 1000 iterations.

PV Characteristics:

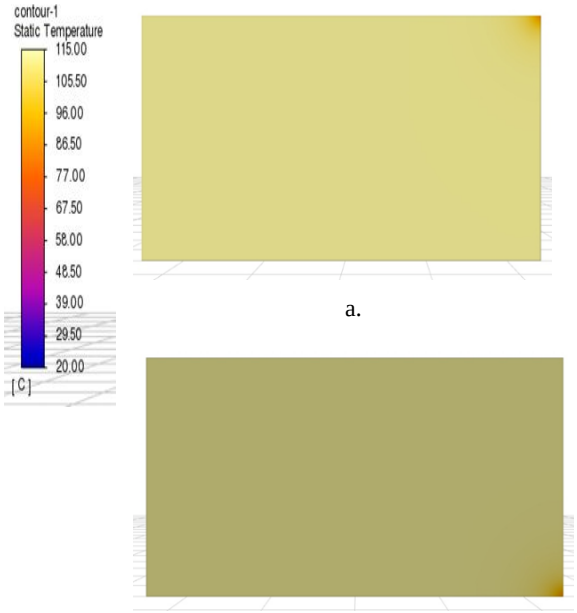
- Material: Mixed (glass, eva1, PV cells, eva2, tedlar)
- Mixed PV layer thickness: 0.0045 m
- Mixed material density: 2447.11 kg/m³
- Specific heat: 885.73 J/kg°C
- Thermal conductivity: 14.44 W/m°C.

The results obtained from the numerical simulation for the photovoltaic panel without cooling are presented in Table 2.

Photovoltaic panel 2000/1000 mm without cooling system					
V_{H2O} (m/s)	T_{H2Oint} (°C)	T_{H2Oout} (°C)	T_{minPV} (°C)	T_{maxPV} (°C)	T_{medPV} (°C)
NO	NO	NO	64,5	112,3	88,4

Table 2. Data from Numerical Simulation of PV Without Cooling

In Fig. 10, the temperature contour on the surface of the photovoltaic panel can be observed for the color spectrum set within the range of 20...110°C. The maximum temperature of the PV panel is at 112.3°C. The average temperature is 88.4°C. The minimum temperature is 64.5°C.



a.

b.

Figure 10. a. Front; b.Bottom View of PV in the Numerical Simulation Without Cooling

3.2. Simulation of PV operation with serpentine cooling

The numerical simulation for the case of the photovoltaic panel with serpentine cooling system was possible with the following input parameters:

- Solar power: 1000W/m²
- Air density: constant
- Heat transfer air-PV: through conduction
- Heat transfer PV-water: through convection and conduction
- PV thermal resistance: negligible
- Water inlet temperature: 20°C
- Water circulation velocity: 0.1...0.9 m/s

The results obtained from the numerical simulation for the PV operation with the serpentine cooling system are presented in Table 3.

Photovoltaic panel 2000/1000 mm with serpentine cooling system					
V_{H2O} (m/s)	T_{H2Oint} (°C)	T_{H2Oout} (°C)	T_{minPV} (°C)	T_{maxPV} (°C)	T_{medPV} (°C)
0,1	20	90,5	55,9	105,3	78,8
0,3	20	44,2	37,5	54,1	44,9
0,5	20	34,8	32,7	42,7	37,1
0,7	20	30,6	30,5	37,5	33,5
0,9	20	28,33	29,1	34,6	31,5

Table 3. Data from Numerical Simulation of PV with Serpentine Cooling

In Fig. 11, the temperature contour on the surface of the photovoltaic panel can be observed for the color spectrum set within the range of 20...110°C. The water circulation velocity ranges from 0.1 to 0.9 m/s.

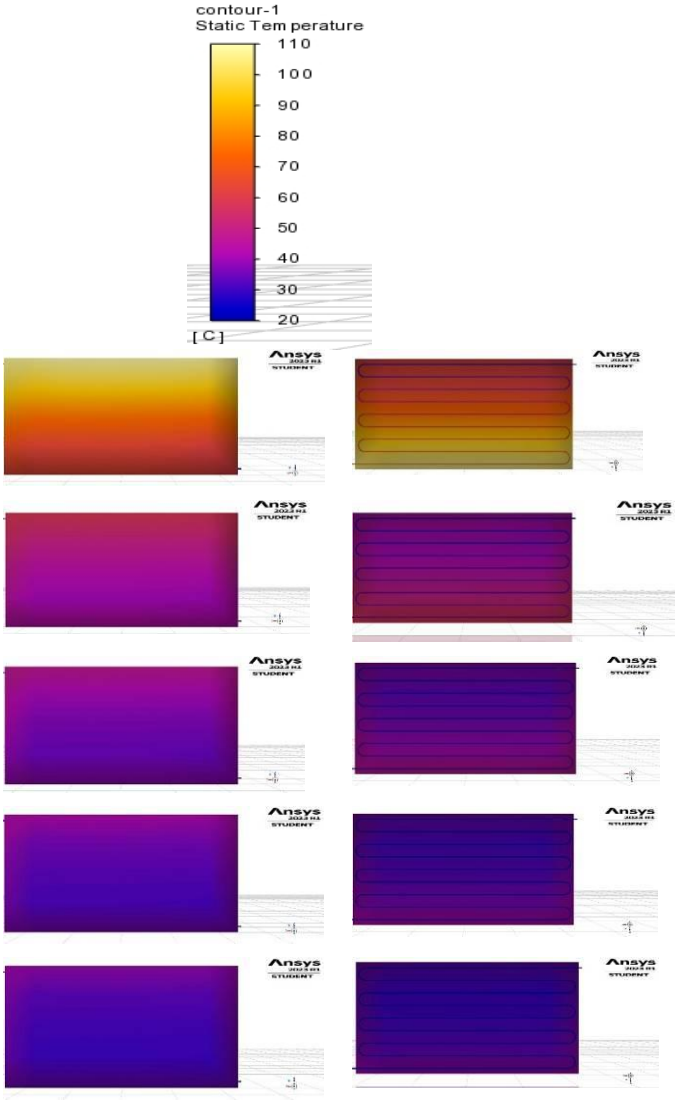


Figure 11. PV with Serpentine Cooling, with the Cooling Agent Circulation at 0.1...0.9 m/s

3.3. Simulation of PV operation with distributor/collector cooling

The numerical simulation for the case of the photovoltaic panel with distributor/collector cooling system was possible with the following input parameters:

- Solar power: 1000W/m²
- Air density: constant
- Heat transfer air-PV: through conduction

- Heat transfer PV-water: through convection and conduction
- PV thermal resistance: negligible
- Water inlet temperature: 20°C
- Water circulation velocity: 0.1...0.9 m/s

The results obtained from the numerical simulation for the PV operation with the distributor/collector cooling system are presented in Table 4.

Photovoltaic panel 2000/1000 mm with distributor/collector cooling system					
V_{H2O} (m/s)	T_{H2Oint} (°C)	T_{H2Oout} (°C)	T_{minPV} (°C)	T_{maxPV} (°C)	T_{medPV} (°C)
0,1	20	79,8	45,8	84,2	64,9
0,3	20	47,5	37,8	57,0	45,8
0,5	20	38,3	33,7	49,2	39,9
0,7	20	34,5	31,2	45,2	36,6
0,9	20	32,5	29,8	42,5	34,5

Table 4. Data from Numerical Simulation of PV with Distributor/Collector Cooling

In Fig, 12, the temperature contour on the surface of the photovoltaic panel can be observed for the color spectrum set within the range of 20...110°C. The water circulation velocity ranges from 0.1 to 0.9 m/s.

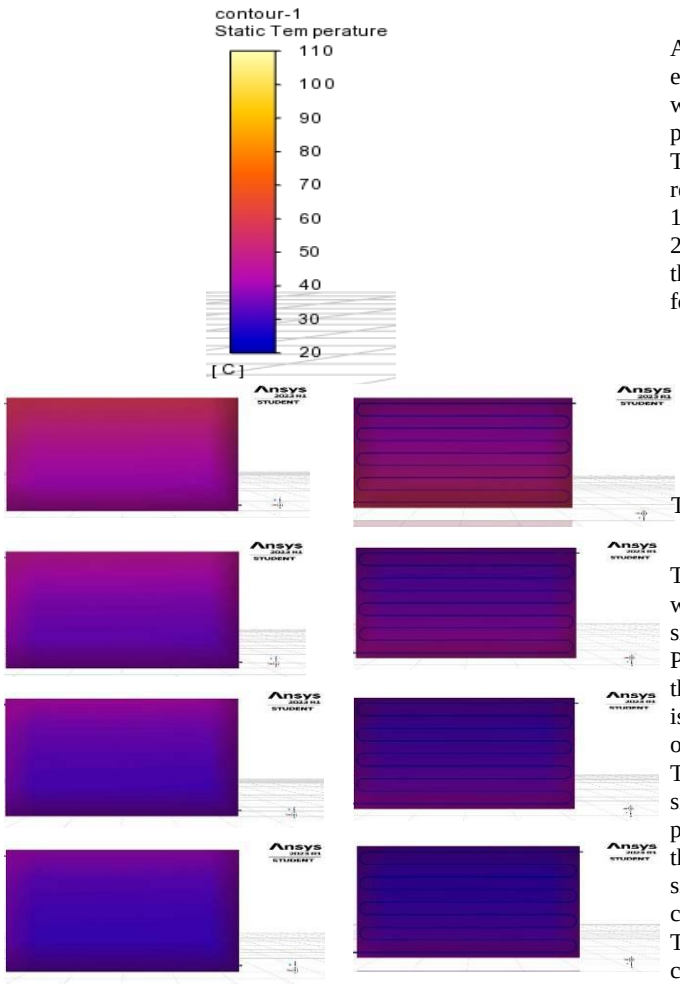


Figure 12. PV with Distributor/Collector Cooling, with the Cooling Agent Circulation at 0.1...0.9 m/s

4. COMPARATIVE STUDY

A total of 11 simulations were conducted. The thermal potential available on the surface of the photovoltaic panels was extracted, including:

- PV without cooling
- PV with serpentine cooling
- PV with distributor/collector cooling

In the following chart (Fig. 13), the temperature dynamics for the PV system without cooling can be observed.

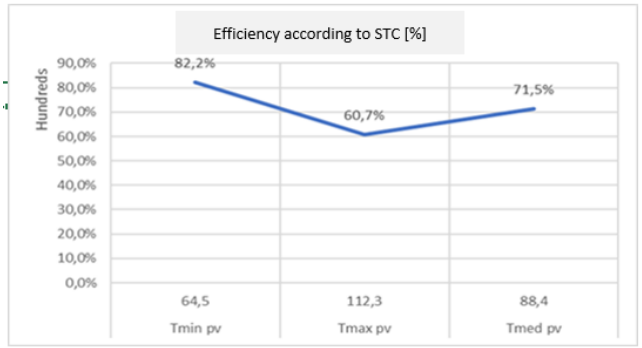


Figure 13. Distribution of PV temperatures for the System Without Cooling

According to the study it is mentioned that for an average external temperature of 25°C and solar radiation of 1000W/m², with uniform and direct exposure of the PV panel to the sun, the photovoltaic cells offer maximum electrical power production. This test is referred to as Standard Test Condition (STC). As a result of this conducted study, it was observed that for every 1°C increase in the photovoltaic panel's temperature above 25°C, there is a reduction in efficiency by 0.45%. Based on these findings and considering the STC test, we can extract the following calculation from Table 5.

		Efficienty according to STC (%)
$Tmin_{PV}$	64,5	82,225
$Tmax_{PV}$	112,3	60,715
$Tmed_{PV}$	88,4	71,47

Table 5. PV Efficiency according to STC - PV Without Cooling

The temperatures obtained during the operation of the PV without cooling reach excessively high levels, leading to a significant decrease in its performance. As seen in Fig. 13, the PV efficiency for the resulting average temperature reaches a threshold of 71%. A reduction to two-thirds of the PV capacity is considerable. It is well-known that the operating temperature of photovoltaic panels is crucial in electricity production. Therefore, at such temperatures obtained in this initial simulation, the capacity to produce electricity by the photovoltaic panel decreases dramatically. Taking into account the maximum temperature obtained from the numerical simulation, the efficiency reduction approaches half. The capacity to produce energy by PV is reduced by up to 60%. This parameter should be considered more, especially concerning the maximum temperature, to verify the functioning under the most adverse conditions.

In the domain of PV operation with serpentine cooling, as shown in Fig. 14, the graph of temperatures obtained from the numerical simulation is presented. Similarly, I consider the obtained maximum temperatures as preliminary data to ensure the logical operation of PV under the most adverse exterior climatic conditions. At the beginning of each serpentine cooling cycle, for each of the five allowed circulation velocities considered, a maximum temperature is observed. In the velocity domain from 0.1 m/s to 0.5 m/s, the maximum temperature obtained does not match the STC efficiency calculation. In this case, the resulting temperatures are too high. In the rest of the approached velocity domain, given the forced circulation of the cooling agent and better distribution on the PV surface, the operating temperatures are lower and even optimal in terms of efficiency.

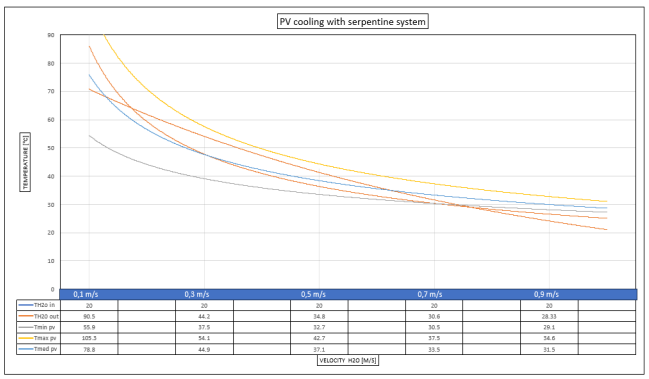


Figure 14. Distribution of PV Temperatures for the Serpentine Cooling System

Table 6, according to the STC test, we extract the following calculation for the efficiency of the PV system with serpentine cooling.

Velocity of cooling agent (m/s)	0,1	0,3	0,5	0,7	0,9
$Tmin_{PV}$(°C)	55,9	37,5	32,7	30,5	29,1
STC(%)	86,095	94,375	96,535	97,525	98,155
$Tmed_{PV}$(°C)	78,8	44,9	37,1	33,5	31,5
STC(%)	75,79	45,79	94,555	96,175	97,075
$Tmax_{PV}$(°C)	105,3	105,3	42,7	37,5	34,6
STC(%)	63,865	63,865	92,035	94,375	95,68

Table 6. Calculation of PV efficiency with Serpentine Cooling according to STC

Fig. 15 illustrates the efficiency of the photovoltaic panel with serpentine cooling, depending on the temperature extracted from the numerical simulation for the five cases of coolant circulation velocity. It is evident that for all temperatures, minimum, average, and maximum, the PV efficiency increases with decreasing temperatures. As expected, the maximum efficiency of PV is achieved at the minimum temperatures obtained on its surface, reaching 98.1%. However, the maximum temperature reached, 105°C, is not favorable in terms of efficiency, and it rapidly decreases the system's reliability over time.

Regarding the PV cooling system with distributor/collector, Fig. 16 displays the graph of temperatures obtained from the numerical simulation. The maximum temperatures obtained serve as preliminary data to ensure the logical operation of PV under the most extreme external climate conditions. At the beginning of each cooling cycle with the distributor/collector, for each of the five allowable circulation velocitys considered, a maximum temperature is observed. In the range of velocitys from 0.1 m/s to 0.3 m/s, the maximum temperature obtained does not match the STC efficiency calculation, indicating that the resulting temperatures are too high. However, in the rest of the velocity range considered, due to the forced circulation of the cooling agent and a uniform and constant distribution over the entire PV surface, the operating temperatures are lower.

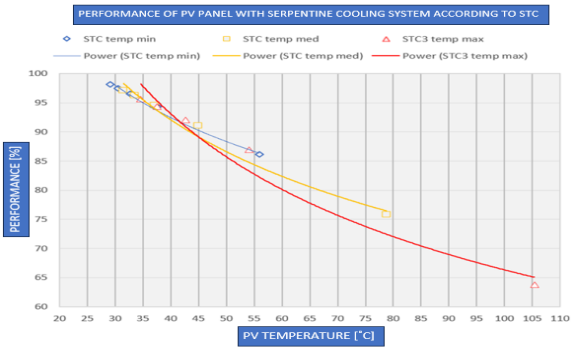


Figure 15. Efficiency of the PV with serpentine cooling according to STC at the obtained temperatures

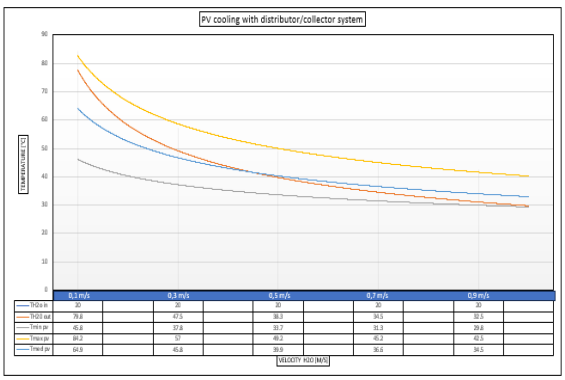


Figure 16. Distribution of temperatures for the PV system with distributor/collector cooling

In Table 7, according to the STC test, we extracted the following calculation for the efficiency of the PV system with distributor/collector cooling.

Velocity of cooling agent (m/s)	$Tmin_{PV}$ (°C)	STC1(%)	$Tmed_{PV}$ (°C)	STC2(%)	$Tmax_{PV}$ (°C)	STC3(%)
0,1	45,8	90,64	64,9	82,045	84,2	73,36
0,3	37,8	94,24	45,8	90,64	57,0	85,6
0,5	33,7	96,085	39,9	93,295	49,2	89,11

0,7	31,3	97,175	36,6	94,78	45,2	90,91
0,9	29,8	97,84	34,5	95,725	42,5	92,125

Table 7. PV Efficiency Calculation with Distributor/Collector according to STC

In the graph (Fig. 17), we can observe the efficiency of the photovoltaic panel with distributor/collector cooling, based on temperature, extracted from the numerical simulation for the five cases of cooling agent circulation velocitys. It is evident for all temperatures, minimum, average, and maximum, that the PV efficiency increases with decreasing temperatures. As expected, the maximum PV efficiency is achieved at the lowest temperatures obtained on its surface, reaching 97.8%. The maximum temperature obtained does not exceed 85°C.

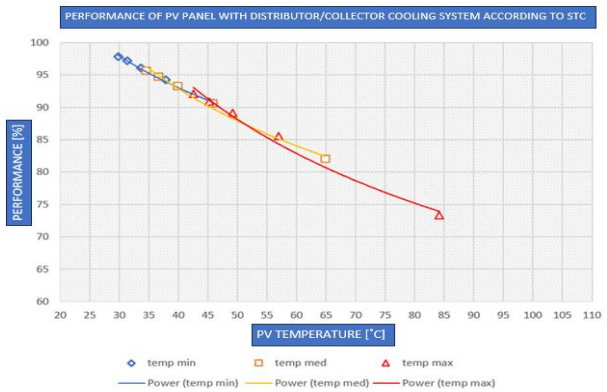


Figure 17. PV Efficiency with Distributor/Collector Cooling - Temperature Dependency

4. CONCLUSIONS

1. In the domain of minimum temperature, in the case of operation without a cooling system, the minimum operating temperature of the PV is high, reaching 64.5°C, considering its distribution over a very small surface. The most favorable minimum PV temperature is obtained with the distributor cooling system at a velocity <0.5 m/s. This results in a better distribution of the cooling agent over the PV surface, leading to improved operating efficiency. Additionally, the cooling water in this case has a higher temperature, making it suitable for thermal energy storage in a secondary system. On the other hand, the cooling system with a serpentine is more effective for velocitys >0.5 m/s. However, the water distribution in this case is not as uniform, resulting in some areas of the PV being better cooled than others. This thermal non-uniformity can have a negative impact on the system's durability, reliability, and energy production, as unevenly functioning photovoltaic cells may experience premature aging.

2. In the domain of average temperature, in the case of operation without a cooling system, the average operating temperature of the PV is 88.4°C. With cooling systems, we observe that the serpentine cooling system achieves lower temperatures at velocitys >0.5 m/s compared to the distributor cooling system. At velocity <0.5 m/s, the distributor cooling system manages to exchange heat more efficiently, resulting in lower temperatures and higher efficiency for the entire PV system.

3. In the domain of maximum working temperature of the system, in the case of simulations without cooling, the minimum temperature obtained on the PV surface remains relatively high at 112°C. It was illustrated the temperature evolution for all three cases analyzed for each of the cooling agent circulation velocitys (excluding PV without cooling). This high temperature can significantly affect the system's efficiency, leading to a considerable decrease in productivity. However, for systems with cooling, the situation improves. Lower temperatures are achieved, and the distributor cooling system works better at velocitys <0.3 m/s. This is due to the uniform distribution of the cooling agent, and the circulation velocity is well suited for this case. At velocitys >0.3 m/s, the continuity is maintained, and the distribution is equally good, resulting in acceptable temperatures and increased efficiency. In the case of serpentine cooling, the disadvantage lies in the non-uniform temperature distribution on the PV surface, but we observe areas with better cooling at velocitys >0.3 m/s. This is due to the fact that a higher cooling agent circulation velocity facilitates more favorable heat exchange at the beginning of the cooling circuit. Thus, a significant temperature discrepancy is observed between two halves of the PV, with one being better cooled than the other. This is undesirable as the system is not thermally balanced, and PV materials and cells may experience unequal transformations over the entire surface, leading to decreased efficiency and reliability over time. The cooling agent's outlet temperature is crucial as it results from a heat exchange process with the PV surface. A higher cooling agent temperature leads to better heat exchange and, consequently, better cooling.

4. In Fig. 18, there is presented the graph of cooling agent operating temperatures for all three simulation cases, i.e., no cooling system and systems with cooling. Lower PV operating temperatures and better system functionality and reliability are achieved. Cooling agent temperature is studied for cases G2 and G3, where the cooling system is involved. At velocitys <0.3 m/s, an advantage of the serpentine system is observed, thanks to its slow, one-directional flow of the cooling agent. At velocitys >0.3 m/s, the distributor/collector cooling system compensates effectively because the cooling agent is distributed through multiple paths, resulting in simultaneous heat exchange. As expected, a better heat exchange benefits the photovoltaic system's operation, durability, and reliability.

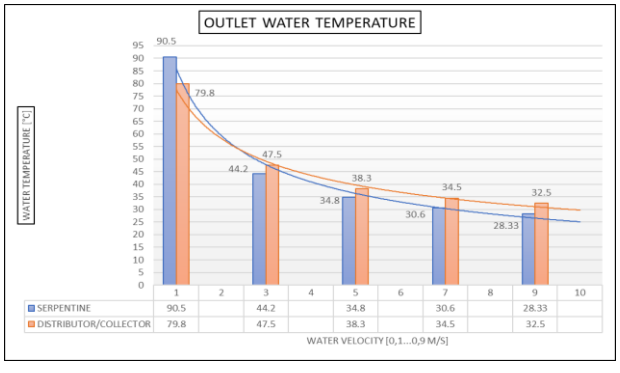


Figure 18. Cooling agent outlet temperature graph

As already evident, in this simulation, we numerically identified this thermal potential. The benefits of improved heat exchange are reflected in the efficient operation, durability, and reliability of the photovoltaic system, as well as the available thermal potential. Thermal energy storage is possible, and there are numerous approaches in this regard. The advantage lies in reducing the environmental impact in the field of electricity and thermal energy production through this hybrid electro-thermal system, optimizing electricity and thermal consumption, reducing fossil fuel consumption, minimizing the environmental impact, reducing assembly and maintenance periods for photovoltaic-thermal (hybrid) systems, and ultimately reducing costs.

References

Hu J, Chen W, Yang D, Zhao B, Song H, Ge B, *Energy Performance of ETFE cushion roof integrated photovoltaic/thermasystem on hot and cold days*, 2016, Appl Energy,173:40–51.

Yau YH, Lim KS. *Energy analysis of green office buildings in the tropics-Photovoltaic system*. Energy Build 2016; 126:177–93

Markvart, T. Solar Electricity, 2nd ed.; John Wiley & Sons: Chichester, UK, 2000.

Wang Y, Zhou S, Hou H, *Cost and CO2 reductions of solar photovoltaic power generation in China: perspectives for 2020*, 2006, Renew Sustain Energy Rev 20 14;39:370–80. Reserve de indiu conform USGS Mineral Commodity Summaries.

Bhubaneswari P, Iniyan S, Goic R, *A review of solar photovoltaic technologies*, 2011, Renew Sustain Energy Rev 15:1625–36.

Da Silva RM, Fernandes JLM, *Hybrid photovoltaic/thermal (PV/T) solar systems simulation with Simulink/Matlab*, 2010, Sol Energy 2010;84:1985–96.

Elbreki AM, Alghoul MA, Al-Shamani AN, Ammar AA, Yegani B, Alsanossi , Aboghrara M, Rusaln MH, Sopian K, *The role of climatic-design-operational parameters on combined PV/T collector performance: a critical review*, 2016,Renew Sustain Energy Rev ,57:602–47.

Kumar K, Sharma SD, Jain L, *Standalone Photovoltaic (PV) module outdoor testing facility for UAE Climate*, 2007, Submitted to CSEM-UAE Innovation Centre LLC.

Chandrasekar, M.; Rajkumar, S.; Valavan, D. *A review on the thermal regulation techniques for non integrated flat PV modules mounted on building top*. Energy and Buildings 2015, 86, 692-697.

Pomares-Hernández, C.; Zuluaga-García, E.A.; Escorcia Salas, G.E.; Robles-Algarín, C.; Sierra Ortega, *J. Computational Modeling of Passive and Active Cooling Methods to Improve PV Panels Efficiency*, 2021, Appl. Sci. , 11, 11370.

Kannan, N., Vakeesan, D, *Solar energy for future world—A review*, 2016, Renew. Sustain. Energy Rev. 62, 1092–1105. [CrossRef].

Rauf A, Liu X, Amin W, Ozturk I, Rehman O.U, Sarwar S, *Energy and ecological sustainability: Challenges and panoramas in belt and road initiative countries*, 2018, Sustainability, 10, 2743. [CrossRef].

Robles Algari, C., Rodríguez Álvarez, O, *An overview of the renewable energy in the World, Latin America and Colombia*, 2018, Espacios, 39, 1–16.

Tahar, M., Rosli, N., *Simulation Study of Cooling System for Photovoltaic Panel Using Ansys M.S.M*, 2022, Journal of Modern Manufacturing Systems and Technology (JMMST) vol. 6, issue 2, 26 – 33.

Reddy, S.R.; Ebadian, M.A.; Lin, C.X. A review of PV-T systems: Thermal management and efficiency with single phase cooling. International Journal of Heat and Mass Transfer 2015, 91, 861-871.

applied sciences

IMPACT FACTOR 2.9

CITESCORE 6.1

Article

Effect of Wind Direction and Velocity on PV Panels Cooling with Perforated Heat Sinks

Sebastian Valeriu Hudișteanu, Florin Emilian Țurcanu, Nelu-Cristian Cherecheș, Cătălin-George Popovici, Marina Verdeș, Diana-Ana Ancaș and Iuliana Hudișteanu

Special Issue

Urban Sustainability and Resilience of the Built Environments

Edited by

Dr. Ilinca Nastase and Dr. Florin Ioan Bode

MDPI

https://doi.org/10.3390/app12199665

applied sciences

MDPI

Article

Effect of Wind Direction and Velocity on PV Panels Cooling with Perforated Heat Sinks

Sebastian Valeriu Hudișteanu *, Florin Emilian Țurcanu *, Nelu-Cristian Cherecheș *, Cătălin-George Popovici, Marina Verdeș, Diana-Ana Ancaș and Iuliana Hudișteanu

Department of Building Services, Faculty of Civil Engineering and Building Services, Gheorghe Asachi Technical University of Iasi, 700050 Iași, Romania

* Correspondence: sebastian.hudisteanu@tuiasi.ro (S.V.H.); emilian-florin.turcanu@tuiasi.ro (F.E.Ț.); chereches@tuiasi.ro (N.-C.C.)

Abstract: The numerical modeling of the effect of wind direction and velocity over the air cooling of PV panels with heat sinks is realized. During the study, a random PV panel with typical characteristics was analyzed for three different wind directions—towards its back, towards its front and from the side. The analysis was realized on a fixed PV panel, oriented to the south, with an inclination of 45 degrees from the horizontal position. The accuracy of the numerical simulation was achieved by comparison with the experimental studies presented in the literature and by comparing the NOCT conditions. The numerical study is focused on different types of heat sinks attached to a typical PV panel. The fins were distributed both horizontally and vertically. A challenging task consisted in simulation of the real wind conditions around the PV panel by taking into account the entire air domain. The simulations were realized for air velocity v_{air} from 1 m/s to 5 m/s, solar radiation of G = 1000 W/m^2 and ambient temperature t_{air} = 35 °C. The output parameters analyzed were the average temperature of PV panels and their power production. Although the lowest temperatures were achieved for the back wind, the cooling effect was more intense for the side wind. The other direction studied also determined the cooling of PV panels. The passive cooling solutions analyzed introduced a rise of maximum power production between 1.85% and 7.71% above the base case, depending on the wind direction and velocity.

Keywords: CFD analysis; wind direction; PV temperature; air cooling; perforated heat sinks; NOCT validation

check for updates

Citation: Hudișteanu, S.V.; Țurcanu, F.E.; Cherecheș, N.-C.; Popovici, C.-G.; Verdeș, M.; Ancaș, D.-A.; Hudișteanu, I. Effect of Wind Direction and Velocity on PV Panels Cooling with Perforated Heat Sinks. *Appl. Sci.* **2022**, *12*, 9665. https://doi.org/10.3390/app12199665

Academic Editor: Luisa F. Cabeza

Received: 2 September 2022
Accepted: 21 September 2022
Published: 26 September 2022

Publisher's Note: MDPI stays neutral with regard to jurisdictional claims in published maps and institutional affiliations.

Copyright: © 2022 by the authors. Licensee MDPI, Basel, Switzerland. This article is an open access article distributed under the terms and conditions of the Creative Commons Attribution (CC BY) license (https://creativecommons.org/licenses/by/4.0/).

1. Introduction

The current global political, economic and energy context is characterized by high demand and consumption of population, instability, uncertainty and rampant inflation, right in the area of resources and energy [1]. Even without taking into account the current context, there is the well-known concept of Overshoot Day which is "celebrated" each year. In essence, this day represents the moment when humanity had already used up all of the renewable resources of the current year and unfortunately it takes place earlier and earlier each year. For the current year, this day was on 28 July 2022, meaning that from 29 July onwards, we started consuming additional resources compared to how much the planet could regenerate [2].

In this context, the use of solar-related energy could reduce the vulnerability of the European Community and eliminate the dependence of third-party oil or gas producers. Solar energy and its conversion into electricity by using photovoltaic (PV) panels became a major attraction in order to reduce the dependence on fossil fuels. After commissioning, there is obtained a clean and sustainable form of energy [2,3]. The photovoltaic systems could represent a stable and competitive area [4], taking into account both the recent actions in Europe [5] and the general tendency on the energy market that have quickly affected the stability of the world countries.

The advantages of photovoltaic technology are well documented in literature [6], but the control of the PV panels temperature is also an important challenge that could assure the enhancement of their efficiency [7].

The irreversible effect of heat generation in PV panels cannot be avoided, taking into account that the PV panel is constantly exposed to high levels of solar energy. Taking into account the efficiency of recently photovoltaic panels (of 20–25%), it can be stated that the vast majority of the remaining solar energy absorbed is converted into heat. This phenomenon, corroborated with the temperature-dependent variation of the efficiency of PV panels [7], determines a continuous concern on reducing the operating temperature. The data from literature present a decrease of the PV efficiency with the temperature between −0.30 and −0.50%/°C [8,9]. It must be specified that, in contrast to STC (Standard Test Conditions), in normal operation the photovoltaic panels can reach temperatures of 70 °C or higher [8,10,11], at 1000 W/m^2, leading to a significant decrease in their efficiency.

It is well known that, when it is possible, it is recommended to use cooling solutions for improving PV panels' efficiency and develop PVT panels (photovoltaic–thermal) as a consequence [12–15]. There are considerable research studies in the literature regarding the cooling solutions for improving the efficiency of photovoltaic panels by reducing their operating temperature [6,9,10,13–15].

The air-cooling effect using heat sinks is tested for different areas: residential sector, urban and power plants [16,17].

The aim of this study was to analyze the effect of wind direction and velocity over different types of heat sinks attached to PV panels in comparison to the base case (without a cooling solution). The main target of the work was to quantify the cooling effect of various heat sinks in variable wind conditions. The presence of heat sinks is influencing the performance of PV panels, but the wind directions could also be an important factor in this regard. In contrast to the majority of similar studies in the literature, in this paper, the numerical modeling was conducted in more realistic wind conditions and inclination of the PV panel [18]. Taking into account the research from the literature, which concluded that the results for different temperature and radiation threshold are varying linearly for values of 20–35 °C and 600–1000 W/m^2, during this study, the most unfavorable conditions in terms of PV panel heating were detailed: solar radiation G = 1000 W/m^2 and ambient temperature t_{air} = 35 °C [6].

2. Related Research

There are numerous related research studies in the literature, both experimental and numerical, regarding the inverse dependence of the temperature of monocrystalline and polycrystalline PV panels with their efficiency, and consequently the necessity of cooling solutions for removing this shortcoming [6,8,9,11,19,20].

Related research works on PV panels' cooling by using air are presented in the literature, and a large number of technologies and solutions to improve their efficiency are presented [9,21–26]. Recent experimental and numerical studies regarding the passive air cooling of PV panels by using heat sinks [8,27,28] tend to confirm noticeable and promising results [6,8,22,23]. The two main materials used for manufacturing the heat sinks are aluminum and copper [23]. The cooling effect is analyzed through experimental tests under different conditions and the conclusion is that copper has superior results [23]. Also, numerical and experimental analysis showed that the presence of perforations on the fins of the heat sinks can improve the efficiency of the PV panels by reducing their operating temperature [6,23]. The predicted temperature drop, due to the use of these solutions, can reach values between 7 °C and 10 °C [23].

Numerical simulations regarding the wind direction towards the back, front and side of heat sinks attached to PV panels showed a potential of operating temperature reduction towards 10 °C below the basic case temperature (when no cooling is applied) [8,11,15,29,30]. The improvement of the PV panels' performance was determining a rise of normalized power production up to 0.90 of the standard test conditions one [31]. As an average, the

normalized power generation of photovoltaic panels can reach about 0.70–0.83 compared to the STC rating [18].

3. Materials and Methods

3.1. Problem Description

The study was focused on determining the effect of wind direction and velocity over the resulting operating temperatures of PV panels both in cooling and non-cooling conditions (base case). Taking into account the variety of PV panels on the market, a typical one is analyzed (with a power production of 320 W_p and a surface of 1.6 m^2). The PV panel is a monocrystalline Si-based one—AE320HM6-60—Table 1 [32], inclined at 45° from the horizontal position, in constant solar radiation G = 1000 W/m^2, constant ambient temperature of t_{air} = 35 °C and variable wind direction (from the back, front and side of the PV panel) and velocity (from 1 m/s to 5 m/s). This configuration is also used for validation of the model in NOCT (Nominal Operating Cell Temperature) conditions [31].

Table 1. The electrical and dimensional characteristics of the photovoltaic panel studied.

AE Solar AE320HM6-60 PV Panel [32]	
Maximum power P_{mp}	320 W_p
Voltage at maximum power V_{mp}	33.40 V
Current at maximum power I_{mp}	9.59 A
Open-circuit voltage V_{oc}	40.90 V
Short-circuit current I_{sc}	10.15 A
Efficiency η_{STC}	19.30%
Temperature factor of efficiency β	−0.37%/°C
Nominal operating cell temperature t_{NOCT}	47 °C
Dimensions of PV panel (length L × width l × height h)	1665 mm × 996 mm × 35 mm

During the study, there were different stages of analysis of the heat sinks attached to the PV panel. The study was initiated with the validation of the model for the base case (no cooling system attached to the photovoltaic panel). After that, a total of six configurations of heat sinks were attached to the PV panel and studied. The various heat sinks were obtained by changing the configuration of their fins. Therefore, for each type of fins (horizontal and vertical), there were the following cases: non-perforated fins vs. fins with perforations of 30 mm and 60 mm diameter (Φ).

The proposed heat sinks are placed in the backside of the PV panel. The contact region is represented by a copper sheet (plate). Perforated or non-perforated copper fins are connected to this plate in order to improve the heat transfer by amplifying the turbulence from the PV panel to the surrounding air (see Figure 1). Therefore, the perforations assure a quantitative and qualitative effect against the heating of the PV panel and could improve the photovoltaic efficiency.

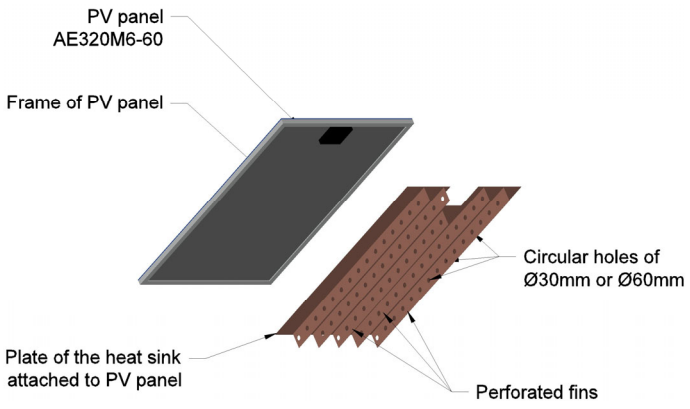


Figure 1. The PV panel—heat sink ensemble—Case of vertical fins with perforations.

The literature analysis showed that the circular holes made in the fins of the heat sinks have the potential to produce promising results for cooling the PV panels [6,8,22,23,29]. In this case, the resulting temperatures are lower by 2–3 °C than those obtained by using other shapes for perforations [18]. In the literature are presented various types of fins (continuous, discontinuous or staggered) [33]. During this study, continuous fins of 100 mm height were analyzed.

Two main configurations of the heat sinks studied were:

Model 1—**horizontal** fins (3 models: non-perforated, perforated with Φ = 30 mm holes and Φ = 60 mm holes);

Model 2—**vertical** fins (3 models: non-perforated, perforated with Φ = 30 mm holes and Φ = 60 mm holes).

3.2. Numerical Modeling

The ANSYS Fluent platform was used for numerical modeling in steady-state conditions. The geometric model and the mesh were created by using ANSYS Fluent-Meshing and ANSYS SpaceClaim.

Given the particularities of the flow (that is not aligned with the mesh), the simulations were realized in the SIMPLE method. The second-order accuracy was used for solving the governing equations of the phenomena involved [8,34].

The solar radiation was modeled by the aid of the native module of Fluent—Solar Ray Tracing. The conversion of solar radiation into heat is synthesized as an absorption coefficient of the PV panel of α = 0.7 [6,8].

The energy balance between the PV panel–heat sink ensemble and the surroundings were modeled by including both the convection and radiation effects [28]. The turbulence model used for the flowing air was the k–ε realizable model [34].

The geometry of the model was created using SpaceClaim. For all studied cases, after preliminary analysis, the distance between fins was imposed to s = 150 mm. The fins are orthogonal to the heat sink sheet, as shown in Figure 1. The circular perforations had 30 mm or 60 mm in diameter and they are located at 100 mm one to another according to previous research works [6,23]. In this way, a better air circulation is achieved near the heat sink and the cooling effect is enhanced.

It is well known that the accuracy and correctness of the mesh lead to precise CFD (Computational Fluid Dynamics) [34]; therefore, in order to solve the highly orthogonal mesh that could result from a conventional mesh. The polyhedral mesh for surfaces and poly-hex mesh for volumes determined an increase of the simulation time, maintaining the same precision of the results. In order to achieve an appropriate mesh, different refinements are necessary [34]. For the present numerical modeling, the PV panel, heat sink and air volume had a mesh quality as presented in Table 2.

Table 2. The mesh quality of the simulation domain.

Mesh Quality	
Aspect ratio	5.0–60
Skewness	0.4–0.7
Orthogonal quality	0.1–0.3

In order to optimize the number of the cells of the mesh and the simulation time, a mesh independence study was realized. The preliminary simulations showed that 3×10^6 cells for the base case and 5.5×10^6 cells for cases with heat sinks determined accurate results compared to a higher number of elements (see Figure 2).

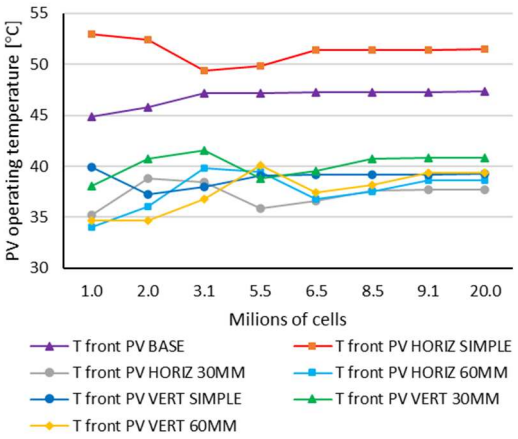


Figure 2. Mesh independence study for the numerical simulation.

3.3. Sensitivity Analysis of Grid Spacing

The spatial discretization error analysis was also performed. The Grid Convergence Index (*GCI*) method was used, according to [35,36]. The *GCI* represents a very accurate method used to evaluate how far the numerical computed values are compared to the asymptotic one [36]. The analysis was implemented on both base and heat sink cases. The following equations present the calculations used and the detailed values obtained. Three grid refinement levels were considered and the following *GCI* values were calculated:

$$GCI_{1-2} = \frac{F_s|\varepsilon_{1-2}|}{\left(r_{1-2}^{p} - 1\right)} \tag{1}$$

and

$$GCI_{2-3} = \frac{F_s|\varepsilon_{2-3}|}{\left(r_{2-3}^{p} - 1\right)} \tag{2}$$

where:

GCI_{1-2}—Grid Convergence Index for fine and medium grids;
GCI_{2-3}—Grid Convergence Index for coarse and medium grids;
F_s—Factor of safety (F_s = 1.25 in the present study);
ε—Relative error:

$$\varepsilon_{n-n+1} = \frac{f_{n+1} - f_n}{f_n} \tag{3}$$

p—Order of convergence:

$$p = \frac{ln\frac{f_{n+2}-f_{n+1}}{f_{n+1}-f_n}}{\ln\, r} \tag{4}$$

f—Significant parameter chosen for the comparison (f_1—the temperature calculated with the finest grid, f_2—with the medium grid, f_3—with coarsest one);
r—Constant refinement ratio (r = 2 in the present study):

$$r_{n-n+1} = \frac{h_{n+1}}{h_n} \tag{5}$$

h—Grid spacing, with:

$$h_1(= 1\text{ mm}) < h_2(= 2\text{ mm}) < h_3(= 3\text{ mm}) \tag{6}$$

For the present study, the f parameter consists in the average operating temperature of the PV panel, t_{PV}.

In order to achieve precise results from numerical simulations by using the lowest number of cells, the following auditing ratio should be as close as possible to 1:

$$\frac{GCI_{2-3}}{r^p GCI_{1-2}} \to 1 \tag{7}$$

In the case of using the finest grid, the predicted value at $h = 0$ is:

$$f = f_1 + \frac{f_1 - f_2}{r_{1-2}^p - 1} \tag{8}$$

For the specific values of the base case analysis ($r = 2, f_1 = 47.28, f_2 = 47.40, f_3 = 47.38$, $F_s = 1.25$), the following values were obtained: the order of convergence $p = 1.68$ and the predicted value $f = 47.31$. Also, $\varepsilon_{1-2} = 0.053\%$ and $\varepsilon_{2-3} = 0.169\%$, while the $GCI_{1-2} = 0.030\%$ and $GCI_{2-3} = 0.096\%$. The calculated auditing ratio is:

$$\frac{GCI_{2-3}}{r^p GCI_{1-2}} = 0.9977 \tag{9}$$

For the specific values of the heat sink case analysis ($r = 2$, $f_1 = 39.39$, $f_2 = 39.44$, $f_3 = 39.49$, $F_s = 1.25$), the following values were obtained: The order of convergence $p = 0.17$ and the predicted value $f = 39.80$. Also, $\varepsilon_{1-2} = 0.116\%$ and $\varepsilon_{2-3} = 0.130\%$, while the $GCI_{1-2} = 1.139\%$ and $GCI_{2-3} = 1.281\%$. The calculated auditing ratio is:

$$\frac{GCI_{2-3}}{r^p GCI_{1-2}} = 0.9975 \tag{10}$$

Therefore, the main verification of the grid quality confirms that the results are in the asymptotic range of convergence and the numerical model was further conducted by using the lowest cell number (coarse grid).

A large number of research studies from the literature are analyzing the photovoltaic panels either in the horizontal [19] or vertical [8,23] position. In addition, the surrounding air is most often simulated as a channel behind the photovoltaic panel [18]. Moreover, studies on cooling inclined photovoltaic panels are present in the literature, but in reduced number [6,11,27].

During this study, the numerical simulations were done considering the air circulation in the vicinity of an inclined PV panel cooled with heat sinks. It was possible due to the high accuracy mesh, which assured a realistic simulation of the airflow and heat transfer from the PV panel to the heat sink and to the surrounding air. In the present study, in order to simplify the numerical model, the influence of the relative humidity of the air was neglected. However, according to literature, the variation of the relative humidity could affect the final results by 4–5% [37]. The thermophysical properties of the materials defined for the simulations are presented in Table 3. The geometry and set-up of the simulation are shown in Figure 3.

Table 3. Thermophysical properties of the materials defined.

Material	g [mm]	λ [W/m·K]	ρ [kg/m^3]	c_p [J/kg·K]
Glass	3.00	1.00	2300	0.50
PV cells	0.35	168	2330	0.757
EVA	0.50	0.35	960	2.09
Tedlar	0.20	0.20	1500	1.20
Copper	1.00	386	8960	0.376
Air	-	0.025	1.20	1.005

where:

g—thickness of the layers composing the PV panel [m];

λ—thermal conductivity of the layers composing the PV panel [W/m·K];
ρ—density of the layers composing the PV panel [kg/m^3];
c_p—specific heat of the layers composing the PV panel [J/kg·K].

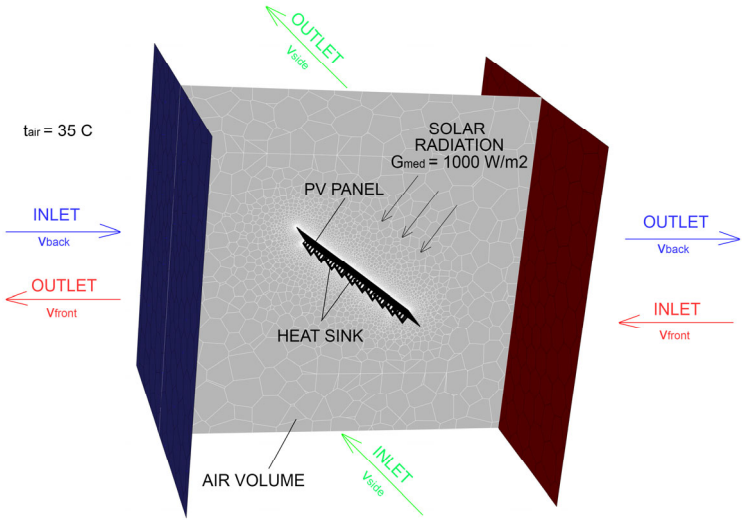


Figure 3. The geometry and set-up of the numerical simulation domain.

The steady-state conditions were assumed for the numerical modeling. During the simulations, the following inputs were established:

- **constant**: ambient temperature, t_{air} = 35 °C—worst scenario in terms of heating [6];
- **constant**: solar radiation, G_{med} = 1000 W/m^2—worst scenario in terms of heating [6];
- **variable**: velocity of the air, v_{air} = 1–5 m/s;
- **variable**: wind direction: towards the back, front and side of the PV panel;

The main results obtained from the simulations were:

- operating temperature of the photovoltaic panel;
- normalized power production.

In terms of wind direction, the simulations were made in 3 Scenarios—for each case, different faces of the volume represent the inlet and outlet of the flow—Figure 3. The blue arrows are used for the back wind. The red arrows are used for the front wind. The green arrows are used for the side wind.

The inlet face of the domain varies as the position but has the same boundary conditions for each case: constant air temperature of 35 °C, velocity vector normal to the inlet surface and variable wind velocity: from 1 m/s to 5 m/s. The boundary conditions regarding the flow were the turbulent intensity of 5% and turbulent viscosity ratio of 10.

3.4. Studied Cases

A total of seven cases were studied. The first one is the base case (Case 0), while the other six consist of the heat sinks analyzed:

0. Base case - no cooling;
1. Horiz Simple - heat sink and non-perforated horizontal fins;
2. Horiz 30 mm - heat sink and perforated Φ = 30 mm horizontal fins;
3. Horiz 60 mm - heat sink and perforated Φ = 60 mm horizontal fins;
4. Vert Simple - heat sink and non-perforated vertical fins;
5. Vert 30 mm - heat sink and perforated Φ = 30 mm vertical fins;
6. Vert 60 mm - heat sink and perforated Φ = 60 mm vertical fins.

The analysis was realized on a fixed PV panel, oriented to the south, with an inclination of 45° from the horizontal position, and wind direction was varied towards the back, front and side of it, as shown in Figure 4.

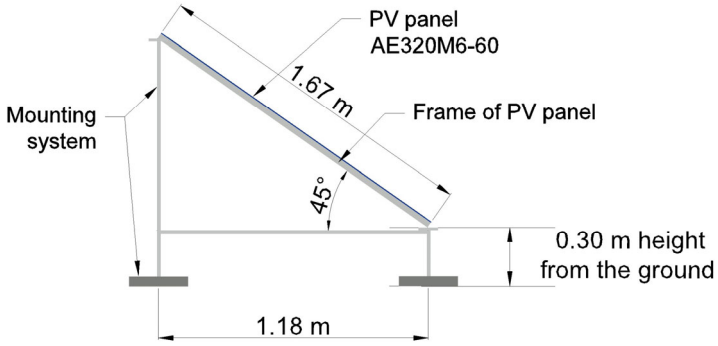
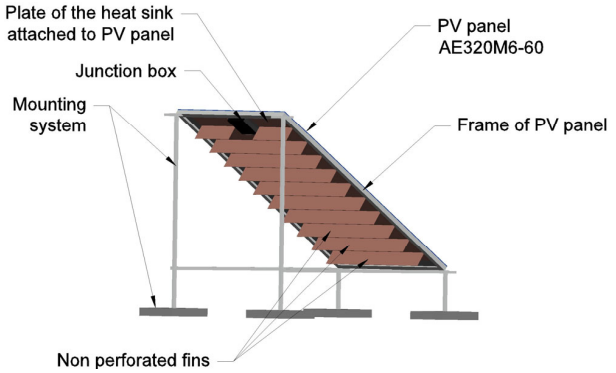
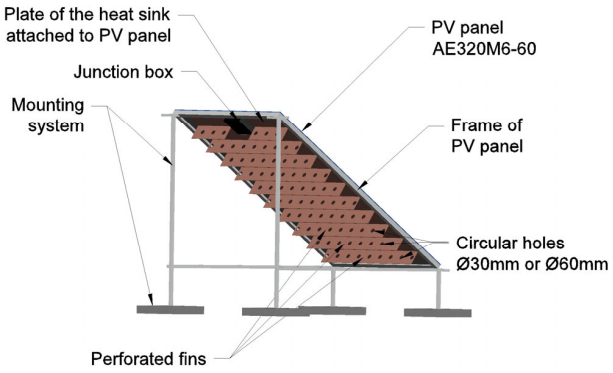
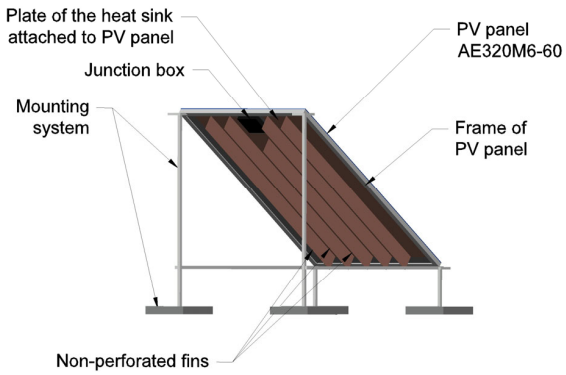
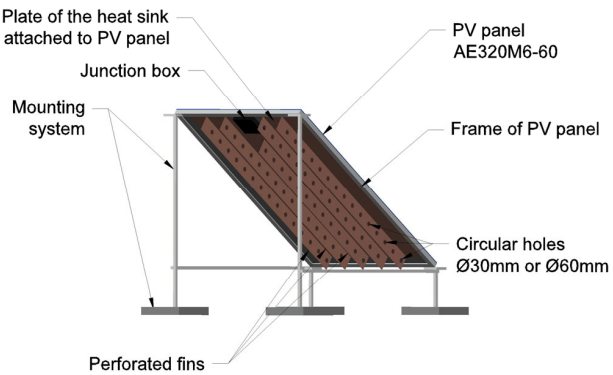


Figure 4. Side view of the set-up of the fixed PV panel, inclined at 45°.

The designed heat sinks consisted of a rectangular metal (copper) sheet with horizontal or vertical equidistant fins (Table 4). The main geometric characteristics of the heat sinks are: h_{fins} = 100 mm (height of all fins implemented), L_{fins} = 1520 mm (length of vertical fins) and L_{fins} = 860 mm (length of vertical fins)—Table 4.

Table 4. The perspective view of the heat sinks attached to the PV panel.

Case	3D Perspective View	
1–3		
4–6		

The fins, made of copper, are studied for both perforated and non-perforated cases. The base sheet of the heat sink is in direct contact with the backside of the PV panel. The diameter of the circular perforations of the fins were of 30 mm or 60 mm (Table 4). The holes were placed at an equal distance of d = 100 mm from one to another. In order to assure good air circulation, there was imposed an offset of 50 mm between two successive fins.

The main cases of cooling solutions analyzed are presented in Table 4. Cases 1–3 represent the horizontal (transversal) ones with no perforations or with perforations of 30

mm and 60 mm. Cases 4–6 are the vertical (longitudinal) ones, both with and without perforations.

4. Numerical Model Validation

4.1. Base Case Validation—Without Heat Sink

The base case was validated in two steps. The first one consisted in analyzing the behavior of the numerical model in NOCT conditions compared to the expected results according to the producer datasheet and literature. The NOCT conditions suppose a PV panel inclined at 45°, direct solar radiation on front of the PV panel of 800 W/m^2, air temperature of 20 °C and the wind velocity of 1 m/s towards the backside of the PV panel [31]. According to the producer of the PV panel [32], in these conditions, the average temperature of the PV panel t_{NOCT} should be 47 °C. Taking into account that the good matching of the PV temperature from simulation was 47.16 °C, the model was considered appropriate and the next steps of validation were covered.

A common Equation (1) from literature [31,38] extrapolates the NOCT results and makes the connection between the PV panel temperature (t_{PV}) and outside conditions (air temperature t_{air} and solar radiation G) for each PV panel, characterized by its own t_{NOCT}. By comparing the numerical results with those obtained with Equation (11), the following tendency of the PV panel temperature was observed (Figure 5).

$$t_{PV} = t_{air} + \frac{t_{NOCT} - 20}{800} \cdot G \tag{11}$$

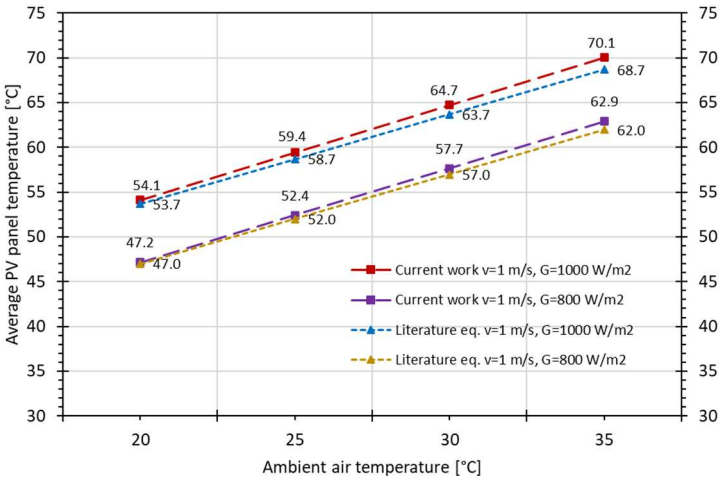


Figure 5. Validation of the numerical model using NOCT conditions and Equation (1).

The differences between the numerical model and Equation (1) were between 0.28 and 1.98%, which represents a very good correlation between them.

Also, experimental studies from literature [11,39] were compared with the present numerical simulation on the base case for different input variables. For the PV panel inclined to 45°, wind velocity of v = 1.5 m/s and solar radiation of G = 837 W/m^2, the difference between the present study (53.68 °C) and the experimental data (51.6 °C) [11] was 3.87%.

Additional results of simulation and experimental studies [23,39] are compared in Figure 6, and a good correlation can be found.

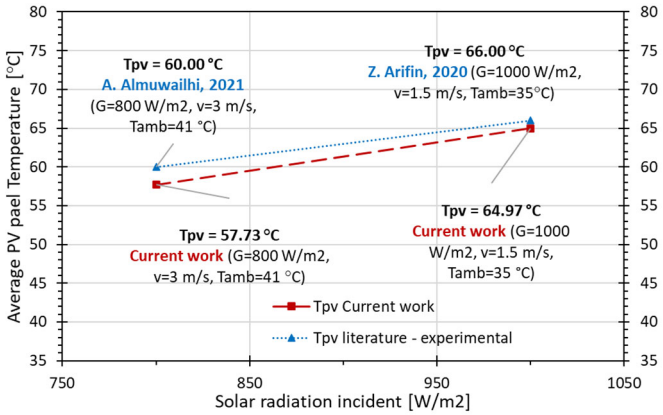


Figure 6. Validation of the numerical simulation—base case—PV panel without heat sink.

4.2. PV Panel and Heat Sink Validation

The heat sinks attached to a PV panel were also analyzed for validation. The comparison between experimental data [34] and the present model is presented in Figure 7.

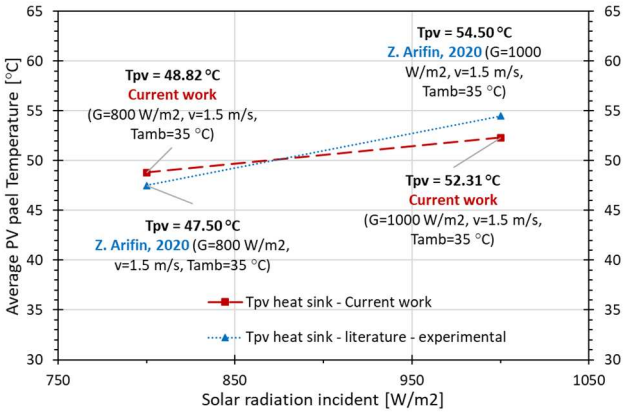


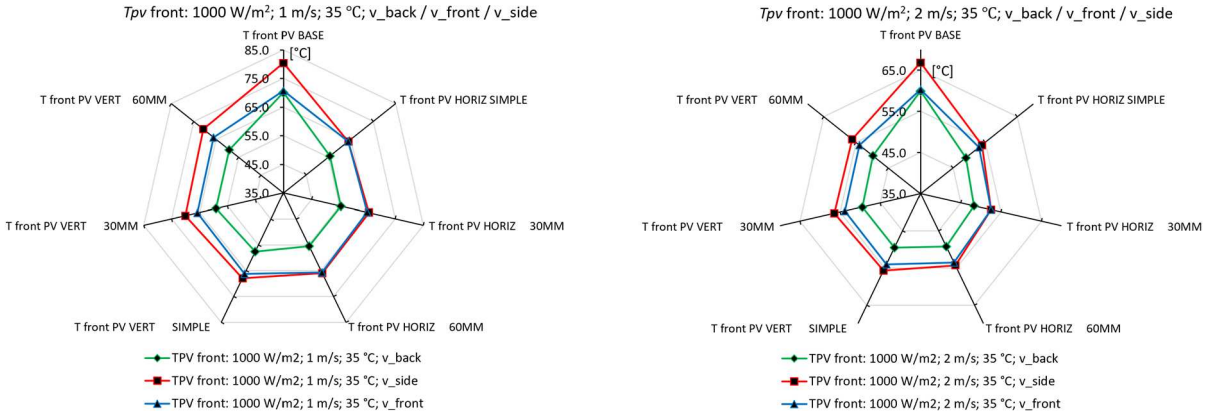
Figure 7. Validation of the numerical simulation—PV panel with heat sink.

In order to improve the accuracy, the model validation was realized also for various values of solar radiation and air temperature. The differences between the present numerical model and experiments from literature were from −5.18% to +4.03%. The narrow range of variation is considered acceptable [30], supporting the validity of the study. Therefore, the numerical modelling was considered to have little risk of error and the study was continued.

5. Results and Discussion

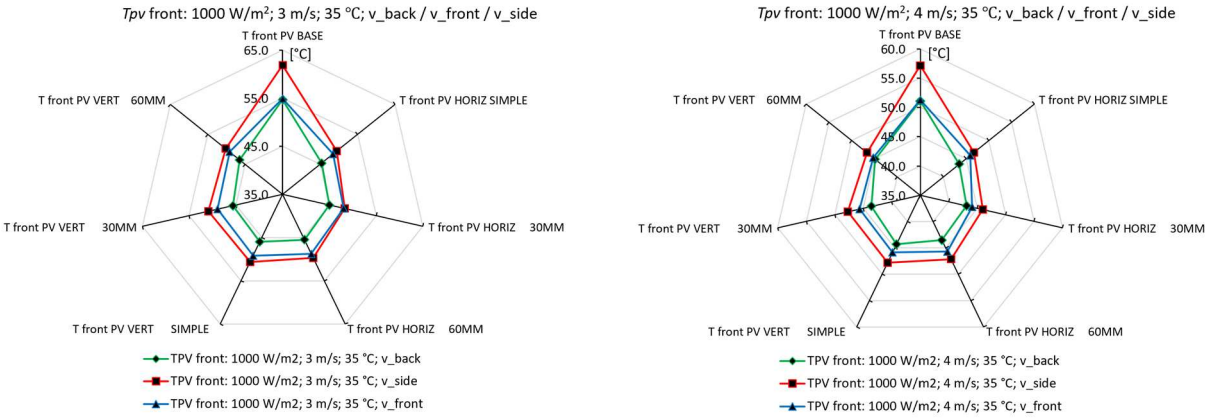
The present simulations have a higher level of accuracy compared to the majority of literature, because the air circulation around the PV panel–heat sink ensemble causes a change in temperatures distribution and non-homogeneous heat transfer. While the majority of existent studies are realized by using a constant convective heat transfer coefficient (h_c) in order to replace the air circulation around an object [18], in the present paper, the airflow near the photovoltaic panel and heat sink ensemble is also considered. This approach produces more realistic results and could represent a good starting point for future research in the literature, representing the connection between air velocity, direction and the power production obtained for these conditions.

The PV panel operating temperature and normalized power production were obtained. In Figures 8–10, there are presented qualitative and quantitative results regarding the average temperatures of the photovoltaic panels obtained for each model of the heat sink and various wind velocities and directions. These results are obtained by varying the set-up: t_{air} = 35 °C, v_{air} = 1–5 m/s and G = 1000 W/m^2 and three wind directions (Table 5).



(**a**) (**b**)

Figure 8. Variation of average operating temperature for (**a**) v_{air} = 1 m/s; (**b**) v_{air} = 2 m/s.



(**a**) (**b**)

Figure 9. Variation of average operating temperature for (**a**) v_{air} = 3 m/s; (**b**) v_{air} = 4 m/s.

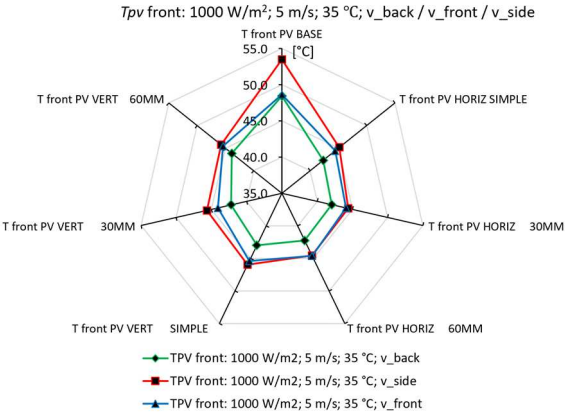


Figure 10. Variation of average operating temperature for v_{air} = 5 m/s.

Table 5. Operating temperature of PV panel for studied cases.

Case	v_{air}	Back Wind		Front Wind		Side Wind	
		Drop of t_{PV} Compared to Base Case, for t_{air} = 35 °C					
		°C	%	°C	%	°C	%
0. Base Case	1 m/s	70.1 °C	-	70.7 °C	-	80.4 °C	-
1. Horiz Simple		−14.46 °C	−20.6%	−6.88 °C	−9.7%	−16.56 °C	−20.6%
2. Horiz 30 mm		−14.61 °C	−20.9%	−5.85 °C	−8.3%	−14.89 °C	−18.5%
3. Horiz 60 mm		−14.54 °C	−20.8%	−5.03 °C	−7.1%	−14.46 °C	−18%
4. Vert Simple		−12.4 °C	−17.7%	−4.42 °C	−6.2%	−12.54 °C	−15.6%
5. Vert 30 mm		−10.93 °C	−15.6%	−4.85 °C	−6.9%	−10.27 °C	−12.8%
6. Vert 60 mm		−10.87 °C	−15.5%	−4.53 °C	−6.4%	−9.73 °C	−12.1%
0. Base Case	2 m/s	59.9 °C	-	60.2 °C	-	66.8 °C	-
1. Horiz Simple		−10.88 °C	−18.2%	−7.14 °C	−11.9%	−12.86 °C	−19.3%
2. Horiz 30 mm		−11.7 °C	−19.5%	−7.71 °C	−12.8%	−14.28 °C	−21.4%
3. Horiz 60 mm		−10.68 °C	−17.8%	−6.65 °C	−11%	−12.53 °C	−18.8%
4. Vert Simple		−10.38 °C	−17.3%	−6.17 °C	−10.2%	−11.15 °C	−16.7%
5. Vert 30 mm		−10.42 °C	−17.4%	−6.42 °C	−10.7%	−10.33 °C	−15.5%
6. Vert 60 mm		−10.13 °C	−16.9%	−6.27 °C	−10.4%	−10.67 °C	−16%
0. Base Case	3 m/s	54.7 °C	-	54.9 °C	-	61.9 °C	-
1. Horiz Simple		−9.33 °C	−17.1%	−6.45 °C	−11.8%	−12.46 °C	−20.1%
2. Horiz 30 mm		−9.7 °C	−17.7%	−6.85 °C	−12.5%	−13.59 °C	−22%
3. Horiz 60 mm		−9.2 °C	−16.8%	−6.13 °C	−11.2%	−12.14 °C	−19.6%
4. Vert Simple		−8.69 °C	−15.9%	−5.64 °C	−10.3%	−11.25 °C	−18.2%
5. Vert 30 mm		−9.04 °C	−16.5%	−5.94 °C	−10.8%	−10.99 °C	−17.8%
6. Vert 60 mm		−8.21 °C	−15%	−5.75 °C	−10.5%	−11.64 °C	−18.8%
0. Base Case	4 m/s	51.1 °C	-	51.3 °C	-	57.2 °C	-
1. Horiz Simple		−7.57 °C	−14.8%	−5.36 °C	−10.5%	−10.43 °C	−18.2%
2. Horiz 30 mm		−7.94 °C	−15.5%	−7.21 °C	−14.1%	−11.21 °C	−19.6%
3. Horiz 60 mm		−7.58 °C	−14.8%	−5.59 °C	−10.9%	−10.03 °C	−17.5%
4. Vert Simple		−6.8 °C	−13.3%	−5.41 °C	−10.6%	−9.4 °C	−16.4%
5. Vert 30 mm		−7.56 °C	−14.8%	−5.62 °C	−11%	−9.49 °C	−16.6%
6. Vert 60 mm		−6.24 °C	−12.2%	−5.98 °C	−11.7%	−10.52 °C	−18.4%
0. Base Case	5 m/s	48.5 °C	-	48.6 °C	-	53.5 °C	-
1. Horiz Simple		−6.15 °C	−12.7%	−4.23 °C	−8.7%	−8.36 °C	−15.6%
2. Horiz 30 mm		−6.41 °C	−13.2%	−4.57 °C	−9.4%	−9.12 °C	−17%
3. Horiz 60 mm		−6.21 °C	−12.8%	−4.03 °C	−8.3%	−9 °C	−16.8%
4. Vert Simple		−5.47 °C	−11.3%	−3.21 °C	−6.6%	−7.57 °C	−14.1%
5. Vert 30 mm		−6.26 °C	−12.9%	−4.57 °C	−9.4%	−7.87 °C	−14.7%
6. Vert 60 mm		−4.61 °C	−9.5%	−3.21 °C	−6.6%	−7.78 °C	−14.5%

These values could represent a good marker in order to choose, when possible, the right positioning of the PV panels related to the dominant wind in a certain geographical area. The best temperatures of the heat sinks were obtained when the wind was towards the heat sink—in the backside of the PV panel—determining a decrease of the average

operating temperature of approximately 15 °C. On the other hand, the best cooling effect was registered for the side wind, due to the higher temperatures resulted in the base case—when no cooling is applied. Although the lowest temperatures were achieved for the back wind, the cooling effect was more intense for the side wind. If, in the case of wind velocity, the effect of cooling evolves almost linearly from 1 m/s to 5 m/s, in terms of the wind direction, there is a slightly different behavior. Therefore, there are present some recirculation areas that modify the distribution of velocities and temperatures on the PV panel–heat sink ensemble. The worst wind direction, from this point of view, is the side one, causing a non-uniform temperature distribution, which is influencing the entire PV panel efficiency.

The quantitative results for v_{air} = 1 m/s, air temperature t_{air} = 35 °C and solar radiation G = 1000 W/m^2 for each case are presented in the following graphs: Figures 8–10. In these figures, the values displayed on the plots (35, 45, 55, 65, 75 and 85) represent the scale for the average operating temperatures of the PV panel measured in °C. The tendency registered for 1 m/s is also manifesting for higher velocities: 2–5 m/s, with the highest temperatures recorded for the base case (T front PV BASE) and the lowest ones for the horizontal heat sink with 30 mm perforations (T front PV HORIZ 30MM).

A remarkable result is found for the convective heat transfer coefficients. Therefore, the global air circulation determined by the presence of the heat sinks with horizontal fins is also improving the heat transfer coefficients h_c on the front of the PV. In this case, the h_c in front of the PV panel have closer values to the ones recorded on the back. This phenomenon is less intense for the vertical fins. The wind direction seems to change the best configuration (Case 2—horizontal 30 mm) only for particular cases. The temperature reduction determined for this case is presented in Table 5.

A general tendency of the data obtained showed that the horizontal (transversal fins) are superior to those vertical (longitudinal) for each wind direction and velocity, while the best wind direction for improving the cooling of the PV panel–heat sink ensemble is towards the back of the PV panel. Also, if analyzed separately, the smaller holes (Φ = 30 mm) determine better results for horizontal fins, while the larger ones (Φ = 60 mm) are suitable for the vertical ones.

The cooling effect over the global energy production is quantified as efficiency improvement, taking into account the data available from the producer data sheet—a linear reduction of the efficiency by −0.37%/°C [32]. Therefore, for these disadvantageous external conditions (t_{air} = 35 °C, G = 1000 W/m^2), the normalized power generation was calculated—as the ratio of the maximum theoretical power P_{STC} obtained in Standard Test Conditions.

The results regarding the power production are normalized and presented as a fraction of maximum theoretic power (320 Wp in STC conditions). Therefore, each degree of temperature above the standard test conditions temperature t_{STC} = 25 °C determines lower efficiencies compared to the STC one (η_{STC} = 19.30%) [32].

The visual effect over the improvement of the PV panel power generation determined by the heat sinks is presented in Figures 11–13. These figures present the normalized power productions as a ratio of the power produced in STC (considering the STC power as equal to 1). Each figure shows the amount of power produced in each case (from Case 0 to Case 6) for different wind directions (Figure 11—back wind, Figure 12—front wind and Figure 13—side wind. These charts present the results obtained for each case for the air velocity of 1 m/s. This trend is maintained for higher velocities, Table 6, but the effect compared to the base case is attenuated.



Figure 11. Normalized power production for **back wind**, v_{back} = 1 m/s, t_{air} = 35, G = 1000 W/m^2.

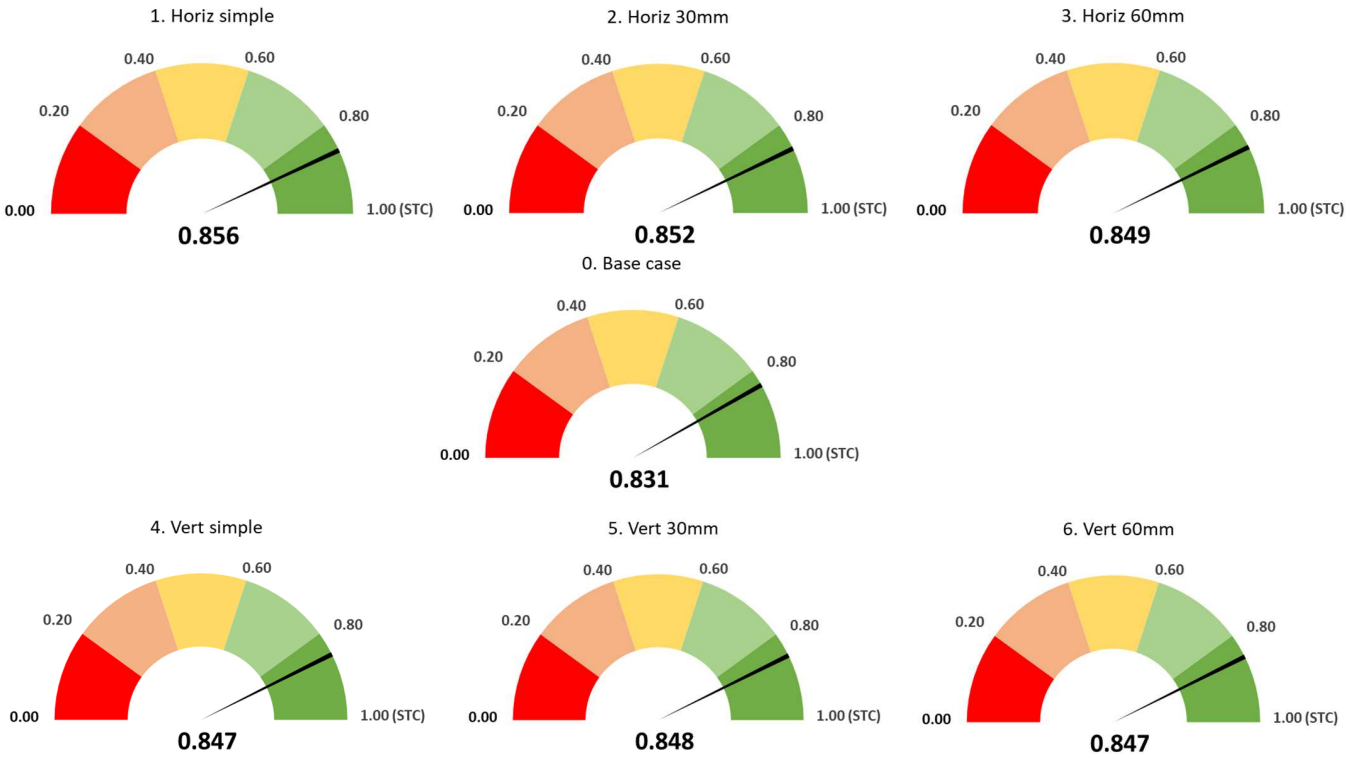


Figure 12. Normalized power production for **front wind**, v_{front} = 1 m/s, t_{air} = 35, G = 1000 W/m^2.

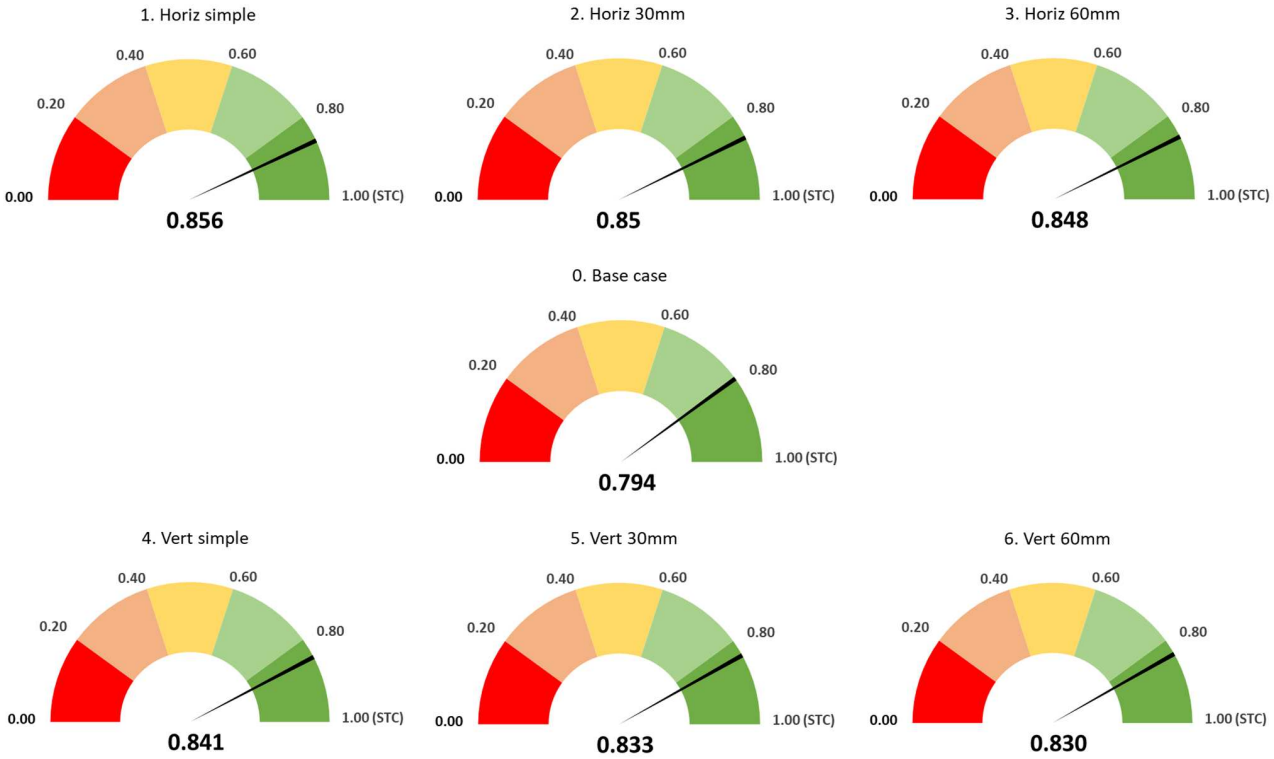


Figure 13. Normalized power production for **side wind**, v_{side} = 1 m/s, t_{air} = 35, G = 1000 W/m^2.

Table 6. Normalized power production of the PV panel for each model analyzed.

Case	v_{air}	Back Wind	Front Wind	Side Wind
		Normalized Power, for t_{air} = 35 °C		
		P_{STC} = 1.00 (320 Wp)		
0. Base Case	1 m/s	0.8333	0.8310	0.7949
1. Horiz Simple		0.8868	0.8564	0.8562
2. Horiz 30 mm		0.8874	0.8526	0.8500
3. Horiz 60 mm		0.8871	0.8496	0.8485
4. Vert Simple		0.8792	0.8473	0.8413
5. Vert 30 mm		0.8737	0.8489	0.8330
6. Vert 60 mm		0.8735	0.8478	0.8309
0. Base Case	2 m/s	0.8709	0.8697	0.8453
1. Horiz Simple		0.9111	0.8961	0.8929
2. Horiz 30 mm		0.9142	0.8982	0.8981
3. Horiz 60 mm		0.9104	0.8943	0.8917
4. Vert Simple		0.9093	0.8925	0.8865
5. Vert 30 mm		0.9094	0.8934	0.8835
6. Vert 60 mm		0.9083	0.8929	0.8848

Table 6. *Cont.*

Case	v_{air}	Back Wind	Front Wind	Side Wind
		Normalized Power, for t_{air} = 35 °C		
		P_{STC} = 1.00 (320 Wp)		
0. Base Case	3 m/s	0.8901	0.8894	0.8636
1. Horiz Simple		0.9246	0.9133	0.9097
2. Horiz 30 mm		0.9260	0.9148	0.9139
3. Horiz 60 mm		0.9241	0.9121	0.9086
4. Vert Simple		0.9223	0.9103	0.9053
5. Vert 30 mm		0.9236	0.9114	0.9043
6. Vert 60 mm		0.9205	0.9107	0.9067
0. Base Case	4 m/s	0.9035	0.9028	0.8809
1. Horiz Simple		0.9315	0.9226	0.9195
2. Horiz 30 mm		0.9329	0.9294	0.9224
3. Horiz 60 mm		0.9315	0.9234	0.9181
4. Vert Simple		0.9286	0.9228	0.9157
5. Vert 30 mm		0.9314	0.9236	0.9160
6. Vert 60 mm		0.9266	0.9249	0.9199
0. Base Case	5 m/s	0.9132	0.9125	0.8944
1. Horiz Simple		0.9359	0.9282	0.9254
2. Horiz 30 mm		0.9369	0.9294	0.9282
3. Horiz 60 mm		0.9361	0.9275	0.9277
4. Vert Simple		0.9334	0.9244	0.9225
5. Vert 30 mm		0.9363	0.9294	0.9236
6. Vert 60 mm		0.9302	0.9244	0.9232

Even if the highest energy production is obtained in the case of the wind direction behind the panel, for the horizontal heat sink with perforated fins, it should be specified that the most important impact in terms of cooling compared to the base case is recorded when the wind blows from the side.

It can be remarked that, for the simulated external conditions, t_{air} = 35 °C, G = 1000 W/m^2 and low air velocity v_{air} = 1 m/s, the normalized power production for the base case is between 0.79 and 0.83. Meanwhile, in the best cooling conditions for each wind directions, it could reach values from 0.85 to 0.88 (Case 3—horizontal 30 mm). The improvement in power generation is between 3.06% and 7.71% compared to the base case (when no cooling is applied).

It should be highlighted that the best configuration of heat sink is the low velocity conditions for various conditions of wind velocity and direction. Therefore, Case 3—Horizontal 30 mm determines the most important effect of cooling of the PV panel. The improvement of power production is important both for low velocities (1–2 m/s) and higher ones (3–5 m/s), but the effect is lower for higher velocities (1.85–5.82%), due to the suitable cooling of the PV panel in the base case.

In terms of wind direction, the lowest cooling effect is registered for the front wind. For these cases, the presence of the heat sink does not have a significant effect, determining a raise of power production between 1.85% and 3.06% compared to the base case.

6. Conclusions

The goal of this study was to deploy a numerical analysis regarding the air cooling of photovoltaic panels by using heat sinks with perforated and non-perforated fins. A random PV panel with typical characteristics was analyzed for different wind directions—towards its back, front and from the side. The PV panel is mounted in fixed position, facing south, inclined at 45 degrees from the horizontal. The input constants were the solar radiation G = 1000 W/m^2 and ambient temperature t_{air} = 35 °C, while the parameters varied during the study were the wind direction (towards its back, front and from the side of PV panel) and velocity v_{air} = 1–5 m/s.

The base case of the numerical model was calibrated according to the NOCT conditions, while the accuracy of the numerical simulation was achieved by comparison with the experimental studies from literature. The numerical study is focused on six types of heat sink with perforated and non-perforated fins attached to a typical PV panel. The fins were distributed both horizontally and vertically. A challenging task consisted in simulation of the real wind conditions around the PV panel by taking into account the entire air domain. The main results obtained were the average temperature of PV panels and the respective efficiency.

The passive cooling solutions analyzed introduced a rise of maximum power production between 1.85% (wind towards the front—worse case) and 7.71% (wind towards the side—best case) above the basic set-up, depending on the wind direction and velocity. The maximum power increase for each wind direction was of 7.71% for the side wind, 6.49% for the backside wind and 3.06% for the front wind. The effect is more intense for lower velocities. This phenomenon is achieved because of the lower convection near the PV panel in the base case, compared to usage of the heat.

Author Contributions: Conceptualization, S.V.H., F.E.Ț. and N.-C.C.; methodology, S.V.H., F.E.Ț. and N.-C.C.; software, S.V.H. and F.E.Ț.; validation, S.V.H., F.E.Ț., N.-C.C. and I.H.; formal analysis, S.V.H., D.-A.A. and I.H.; investigation, S.V.H., F.E.Ț., N.-C.C., C.-G.P., M.V., D.-A.A. and I.H.; resources, S.V.H., F.E.Ț. and C.-G.P.; data curation, S.V.H., F.E.Ț. and I.H.; writing—original draft preparation, S.V.H., F.E.Ț., N.-C.C., C.-G.P., M.V., D.-A.A. and I.H.; writing—review and editing, S.V.H., F.E.Ț., N.-C.C., C.-G.P., M.V. and I.H.; visualization, S.V.H., D.-A.A. and I.H.; supervision, S.V.H. and M.V.; project administration, S.V.H.; funding acquisition, S.V.H. All authors have read and agreed to the published version of the manuscript.

Funding: This work was supported by a grant of the Romanian Ministry of Education and Research, CCCDI-UEFISCDI, project number PN-III-P2-2.1-PED-2019-1294, within PNCDI III.

Institutional Review Board Statement: Not applicable.

Informed Consent Statement: Not applicable.

Data Availability Statement: Not applicable.

Acknowledgments: We would like to acknowledge the invaluable support provided by the FCI-TUIASI infrastructure in writing this article.

Conflicts of Interest: The authors declare no conflict of interest.

References

1. Available online: https://ec.europa.eu/eurostat/statistics-explained/index.php?title=Electricity_price_statistics (accessed on 15 August 2022).
2. Available online: https://www.overshootday.org (accessed on 15 August 2022).
3. AlAmri, F.; AlZohbi, G.; AlZahrani, M.; Aboulebdah, M. Analytical Modeling and Optimization of a Heat Sink Design for Passive Cooling of Solar PV Panel. *Sustainability* **2021**, *13*, 3490. [CrossRef]
4. Available online: https://www.euronews.com/2021/10/28/why-europe-s-energy-prices-are-soaring-and-could-get-much-worse (accessed on 15 August 2022).
5. Available online: https://www.nature.com/articles/d41586-022-00969-9 (accessed on 15 August 2022).
6. Hudișteanu, S.V.; Țurcanu, F.E.; Chereches, N.C.; Popovici, C.G.; Verdeș, M.; Hudisteanu, I. Enhancement of PV Panel Power Production by Passive Cooling Using Heat Sinks with Perforated Fins. *Appl. Sci.* **2021**, *11*, 11323. [CrossRef]

7. Hudișteanu, S.V.; Popovici, C.G. Numerical analysis of the efficiency and energy production of the building integrated photovoltaics for various configurations. In Proceedings of the CLIMA 2019 Congress, E3S Web of Conferences, Bucharest, Romania, 26–29 May 2019; Volume 111, p. 03044.
8. Popovici, C.G.; Hudisteanu, S.V.; Mateescu, T.D.; Chereches, N.C. Efficiency improvement of photovoltaic panels by using air cooled heat sinks. *Energy Procedia* **2016**, *85*, 425–432. [CrossRef]
9. Hernandez-Perez, J.G.; Carrillo, J.G.; Bassam, A.; Flota-Banuelos, M.; Patino-Lopez, L.D. A new passive PV heatsink design to reduce efficiency losses: A computational and experimental evaluation. *Renew. Energy* **2020**, *147*, 1209–1220. [CrossRef]
10. Gomaa, M.R.; Hammad, W.; Al-Dhaifallah, M.; Rezk, H. Performance enhancement of grid-tied PV system through proposed design cooling techniques: An experimental study and comparative analysis. *Sol. Energy* **2020**, *211*, 1110–1127. [CrossRef]
11. Colarossi, D.; Principi, P. Indoor and Outdoor Performance of an Enhanced Photovoltaic Panel through Graphene/Fins/Phase Change Materials. *Appl. Sci.* **2021**, *11*, 8807. [CrossRef]
12. Hudișteanu, S.V.; Chereches, N.C.; Popovici, C.G.; Verdeș, M.; Ciocan, V. Effect of cooling on power generated by photovoltaic panels. In *IOP Conference Series: Materials Science and Engineering, Proceedings of the Computational Civil Engineering (CCE 2021), Iasi, Romania, 27–29 May 2021*; IOP Publishing: Bristol, UK; Volume 1141, p. 012008.
13. Branoaea, M.; Burlacu, A.; Verdeș, M.; Ciocan, V.; Costel Balan, M.; Ștefan Vizitiu, R. Hybrid photovoltaic-thermic system with enhanced cell energy efficiency. In Proceedings of the CLIMA 2022 The 14th REHVA HVAC World Congress, Rotterdam, The Netherlands, 22–25 May 2022. [CrossRef]
14. Albatayneh, A.; Jaradat, M.; Al-Omary, M.; Zaquot, M. Evaluation of Coupling PV and Air Conditioning vs. Solar Cooling Systems—Case Study from Jordan. *Appl. Sci.* **2021**, *11*, 511. [CrossRef]
15. Hudișteanu, S.V.; Popovici, C.G. Experimental investigation of the wind direction influence on the cooling of photovoltaic panels integrated in double skin façades. In Proceedings of the CLIMA 2019 Congress, E3S Web of Conferences, Bucharest, Romania, 26–29 May 2019; Volume 111, p. 03045.
16. Hammami, M.; Torretti, S.; Grimaccia, F.; Grandi, G. Thermal and Performance Analysis of a Photovoltaic Module with an Integrated Energy Storage System. *Appl. Sci.* **2017**, *7*, 1107. [CrossRef]
17. Hudisteanu, S.V.; Mateescu, T.D.; Popovici, C.G.; Chereches, C.N. *The Influence of the Building Integrated Photovoltaic Panels Positions on the Conversion Efficiency*; Buletinul Institutului Politehnic din lasi: Sectia Constructii, Arhitectura, 2016.
18. Pérez Escobar, B.L.; Pérez Hernández, G.; Ocampo Ramírez, A.; Rojas Blanco, L.; Díaz Flores, L.L.; Vidal Asencio, I.; Hernández Perez, J.G.; Ramírez Morales, E. Analysis of Thermomechanical Stresses of a Photovoltaic Panel Using a Passive System of Cooling. *Appl. Sci.* **2021**, *11*, 9806. [CrossRef]
19. Arifin, Z.; Tjahjana, D.; Hadi, S.; Rachmanto, R.A.; Setyohandoko, G.; Sutanto, B. Numerical and Experimental Investigation of Air Cooling for Photovoltaic Panels Using Aluminum Heat Sinks. *Int. J. Photoenergy* **2020**, *2020*, 1574274. [CrossRef]
20. Bevilacqua, P.; Bruno, R.; Rollo, A.; Ferraro, V. A novel thermal model for PV panels with back surface spray cooling. *Energy* **2022**, *255*, 124401. [CrossRef]
21. Kuznetsov, P.; Yuferev, L.; Voronin, D.; Panchenko, V.A.; Jasiński, M.; Najafi, A.; Leonowicz, Z.; Bolshev, V.; Martirano, L. Methods Improving Energy Efficiency of Photovoltaic Systems Operating under Partial Shading. *Appl. Sci.* **2021**, *11*, 10696. [CrossRef]
22. Hudișteanu, S.V.; Mateescu, T.D.; Chereches, N.C.; Popovici, C.G. Numerical study of air cooling photovoltaic panels using heat sinks. *Rom. J. Civ. Eng.* **2015**, *6*, 11–20.
23. Arifin, Z.; Suyitno, S.; Tjahjana, D.; Juwana, W.E.; Putra, M.R.A.; Prabowo, A.R. The Effect of Heat Sink Properties on Solar Cell Cooling Systems. *Appl. Sci.* **2020**, *10*, 7919. [CrossRef]
24. Duan, J. A novel heat sink for cooling concentrator photovoltaic system using PCM-porous system. *Appl. Therm. Eng.* **2021**, *186*, 116522. [CrossRef]
25. Bayrak, F.; Oztop, H.F.; Selimefendigil, F. Effects of different fin parameters on temperature and efficiency for cooling of photovoltaic panels under natural convection. *Sol. Energy* **2019**, *188*, 484–494. [CrossRef]
26. Johnston, E.; Szabo, P.S.B.; Bennett, N.S. Cooling silicon photovoltaic cells using finned heat sinks and the effect of inclination angle. *Therm. Sci. Eng. Prog.* **2021**, *23*, 100902. [CrossRef]
27. Amr, A.A.R.; Hassan, A.A.M.; Abdel-Salam, M.; El-Sayed, A.M. Enhancement of photovoltaic system performance via passive cooling: Theory versus experiment. *Renew. Energy* **2019**, *140*, 88–103. [CrossRef]
28. El Fouas, C.; Chereches, N.C.; Hudișteanu, S.V.; Hajji, B.; Țurcanu, E.F.; Chereches, M.L. Numerical and Parametric Analysis for Enhancing Performances of Water Photovoltaic/Thermal System. *Appl. Sci.* **2022**, *12*, 646. [CrossRef]
29. Vittorini, D.; Cipollone, R. Fin-cooled photovoltaic module modeling—Performances mapping and electric efficiency assessment under real operating conditions. *Energy* **2019**, *167*, 159–167. [CrossRef]
30. Mattar, S.J.; Kavian Nezhad, M.R.; Versteege, M.; Lange, C.F.; Fleck, B.A. Validation Process for Rooftop Wind Regime CFD Model in Complex Urban Environment Using an Experimental Measurement Campaign. *Energies* **2021**, *14*, 2497. [CrossRef]
31. Photovoltaic (PV) module performance testing and energy rating—Part 1: Irradiance and temperature performance measurements and power rating. In *International Standard*; IEC 61853-1; International Electrotechnical Commission: Geneva, Switzerland, 2011.
32. Available online: https://ae-solar.com/wp-content/uploads/2018/10/AE_Eclipse-Ultra-Black_HM6-60_310W-320W.pdf (accessed on 15 August 2022).
33. Nizetic, S.; Papadopoulos, A.M.; Giama, E. Comprehensive analysis and general economic-environmental evaluation of cooling techniques for photovoltaic panels, Part I: Passive cooling techniques. *Energy Convers. Manag.* **2017**, *149*, 334–354. [CrossRef]

34. Ansys Fluent Documentation, 2021-R2. Available online: https://www.ansys.com/products/fluids/ansys-fluent (accessed on 15 August 2022).
35. Malvoni, M.; Baglivo, C.; Congedo, P.M.; Laforgia, D. CFD modeling to evaluate the thermal performances of window frames in accordance with the ISO 10077. *Energy* **2016**, *111*, 430–438. [CrossRef]
36. Congedo, P.M.; Lorusso, C.; De Giorgi, M.G.; Laforgia, D. Computational Fluid Dynamic Modeling of Horizontal Air-Ground Heat Exchangers (HAGHE) for HVAC Systems. *Energies* **2014**, *7*, 8465–8482. [CrossRef]
37. Szodrai, F. Heat Sink Shape and Topology Optimization with Pareto-Vector Length Optimization for Air Cooling. *Energies* **2020**, *13*, 1661. [CrossRef]
38. Nguyen, D.P.N.; Neyts, K.; Lauwaert, J. Proposed Models to Improve Predicting the Operating Temperature of Different Photovoltaic Module Technologies under Various Climatic Conditions. *Appl. Sci.* **2021**, *11*, 7064. [CrossRef]
39. Almuwailhi, A.; Zeitoun, O. Investigating the cooling of solar photovoltaic modules under the conditions of Riyadh. *J. King Saud Univ.-Eng. Sci.* **2021**, *186*, 116522. [CrossRef]

applied sciences

IMPACT FACTOR 2.9

CITESCORE 6.1

Article

Numerical and Parametric Analysis for Enhancing Performances of Water Photovoltaic/Thermal System

Chaimae El Fouas, Nelu Cristian Cherecheș, Sebastian Valeriu Hudișteanu, Bekkay Hajji, Emilian Florin Țurcanu and Monica Lilioara Cherecheș

Special Issue

Urban Sustainability and Resilience of the Built Environments

Edited by

Dr. Ilinca Nastase and Dr. Florin Ioan Bode

MDPI

https://doi.org/10.3390/app12020646

applied sciences

MDPI

Article

Numerical and Parametric Analysis for Enhancing Performances of Water Photovoltaic/Thermal System

Chaimae El Fouas [1], Nelu Cristian Chereches [2,*], Sebastian Valeriu Hudisteanu [2,*], Bekkay Hajji [1], Emilian Florin Țurcanu [2,*] and Monica Lilioara Chereches [3]

[1] Laboratory of Renewable Energy, Embedded System and Information Processing, National School of Applied Sciences, Mohammed First University, Oujda 60000, Morocco; c.elfouas@ump.ac.ma (C.E.F.); hajji.bekkay@gmail.com (B.H.)
[2] Department of Building Services, "Gheorghe Asachi" Technical University of Iași, 700050 Iași, Romania
[3] National Institute for Research and Development in Construction, Urban Planning and Sustainable Spatial Development, NR&DI URBAN-INCERC Iasi Branch, 700048 Iasi, Romania; monicachereches@gmail.com
* Correspondence: chereches@tuiasi.ro (N.C.C.); sebastian.hudisteanu@tuiasi.ro (S.V.H.); emilian-florin.turcanu@tuiasi.ro (E.F.Ț.)

Abstract: Photovoltaic/thermal (PV/T) systems are innovative cogeneration systems that ensure the cooling of photovoltaic (PV) backside and simultaneous production of electricity and heat. However, an effective cooling of the PV back is still a challenge that affects electrical and thermal performance of the PV/T system. In the present work, a PV/T numerical model is developed to simulate the heat flux based on energy balance implemented in MATLAB software. The numerical model is validated through the comparison of the three-layer PV model with the NOCT model and tested under the operation conditions of continental temperate climate. Moreover, the effect of velocity and water film thickness as important flow parameters on heat exchange and PV/T production is numerically investigated. Results revealed that the PV model is in good agreement with the NOCT one. An efficient heat transfer is obtained while increasing the velocity and water film thickness with optimal values of 0.035 m/s and 7 mm, respectively, at an inlet temperature of 20 °C. The PV/T system ensures a maximum thermal power of 1334.5 W and electrical power of 316.56 W (258.8 W for the PV). Finally, the comparison between the PV and PV/T system under real weather conditions showed the advantage of using the PV/T.

Keywords: photovoltaic thermal system; water cooling; solar energy; numerical model; electrical efficiency; thermal efficiency

check for updates

Citation: El Fouas, C.; Chereches, N.C.; Hudișteanu, S.V.; Hajji, B.; Țurcanu, E.F.; Chereches, M.L. Numerical and Parametric Analysis for Enhancing Performances of Water Photovoltaic/Thermal System. *Appl. Sci.* **2022**, *12*, 646. https://doi.org/10.3390/app12020646

Academic Editors: Ilinca Nastase and Florin Ioan Bode

Received: 16 November 2021
Accepted: 4 January 2022
Published: 10 January 2022

Publisher's Note: MDPI stays neutral with regard to jurisdictional claims in published maps and institutional affiliations.

Copyright: © 2022 by the authors. Licensee MDPI, Basel, Switzerland. This article is an open access article distributed under the terms and conditions of the Creative Commons Attribution (CC BY) license (https://creativecommons.org/licenses/by/4.0/).

1. Introduction

Increasing energy demand for industrial and domestic purposes has led to greater interest in renewable energy as a substitute for fossil fuels. Sun radiation is the primary source of all types of renewable energy sources. Photovoltaic (PV) technology is one of the common methods of direct converting the solar radiation into electricity [1]. Instead, the performance of PV panels falls by 0.5% for every degree rise in temperature, depending on the type of solar cells used [2]. Since the PV temperatures can reach as high as 80 °C in the summer, it is necessary to find efficient cooling methods to achieve higher heat dissipation rates from PV modules and increase his electrical efficiency and longevity.

An efficient version of the PV module is the photovoltaic–thermal (PV/T) module which uses cooling systems to remove the excess thermal energy. The commercially available technologies are classified into passive and active cooling systems [3]. Active cooling systems use forced circulation of air [4–6], water [7–10], or nanofluids [11] while the passive ones use natural circulation of working fluids in which no external source of power is needed as well as heat pipes [12] or phase change materials (PCMs) to naturally

transport heat through a boiling–condensing process to the ambient air [13]. Some recent related review articles also provide updates on the important aspects of PV/T cooling systems [14–18].

Water cooling methods provide improved performance over air cooling methods due to the increase in heat-carrying capacity of water over air [19]. Nahar et al. [20] studied the performance of a PV/T module with parallel plate flow channel without absorber plate both numerically and experimentally at outdoor conditions. They observed that the overall efficiency increases numerically by 22.1% and experimentally by 20% with an increase in water inlet velocity from 0.0003 to 0.0007 m/s under an irradiation level of 1000 W/m^2 and inlet water temperature of 34 °C.

A novel compound system through connecting a PV/T system with a solar collector in series was proposed by Kazemian et al. [21]. The results showed that using the optimum condition given by Taguchi-based gray relational optimization, electrical, thermal and total power generation of the system increased by 23.86%, 35.78%, and 34.75%, respectively.

A hybrid photovoltaic/thermal (PV/T) collector with serpentine exchanger was studied by Boumaarafa et al. [22] showing that combining both types of heat and electrical offers a better thermal performance with an overall thermal efficiency around 79.43%.

Different parameters for enhancing heat transfer performance of photovoltaic thermal systems was investigated by Nahar et al. [23]. Results revealed that PV/T electrical and thermal efficiency increase with both Reynolds and Prandtl number and a maximum reduction in cell temperature of 10.2 °C was achieved for increasing channel depth from 10 to 20 mm.

Even with the large number of papers related to the PV/T system, there is little research work that treats enhancement of flow parameters, e.g., the inlet velocity and water film thickness simultaneously for an effective cooling of PV cells. This paper presents a transient numerical PV/T model based on an energy balance equation developed in MATLAB software and resolved by the Runge–Kutta numerical method. This model is built based on the three layers PV model validated with the NOCT model. Moreover, the energy balance equations for the cooling unit (absorber 1, fluid, absorber 2) are driven from a PV/T model validated experimentally in previous work [24]. Thus, based on the developed model, a parametric study was conducted to determine the optimal flow parameters.

2. Methodology

2.1. Numerical Model

A numerical model was developed to evaluate the thermal and electrical behavior of a PV/T system, operating in dynamic conditions. The parametric analysis was performed by varying some PV/T key flow parameters, such as the water velocity from 0.01 m/s to 0.035 m/s, water film thickness from 3 mm to 10 mm, and water inlet temperature from 20 °C to 30 °C.

The PV/T system investigated in this work consists mainly of four solid components and cooling liquid (water). According to the PV/T system design shown in cross section in Figure 1a, six sub-numerical models were established as follows:

- Sub-numerical model for the glass cover;
- Sub-numerical model for the PV module;
- Sub-numerical model for the Tedlar layer;
- Sub-numerical model for the upper aluminum layer;
- Sub-numerical model for the water film in channel;
- Sub-numerical model for the lower aluminum layer.

For the six PV/T system sub-models, a heat balance equation was done separately, based on the internal energy variation equation [25] and the heat transfer between layers as shown in Figure 1b. Moreover, the Runge–Kutta numerical method (RK4) was used for resolving the (ODE) governing equations in MATLAB Software. The main advantage of the developed numerical model is allowing the determination of the mean temperature of

each PV/T layer (glass cover, PV cells, Tedlar, absorbers, and fluid), based on the different heat exchanges between these ones.

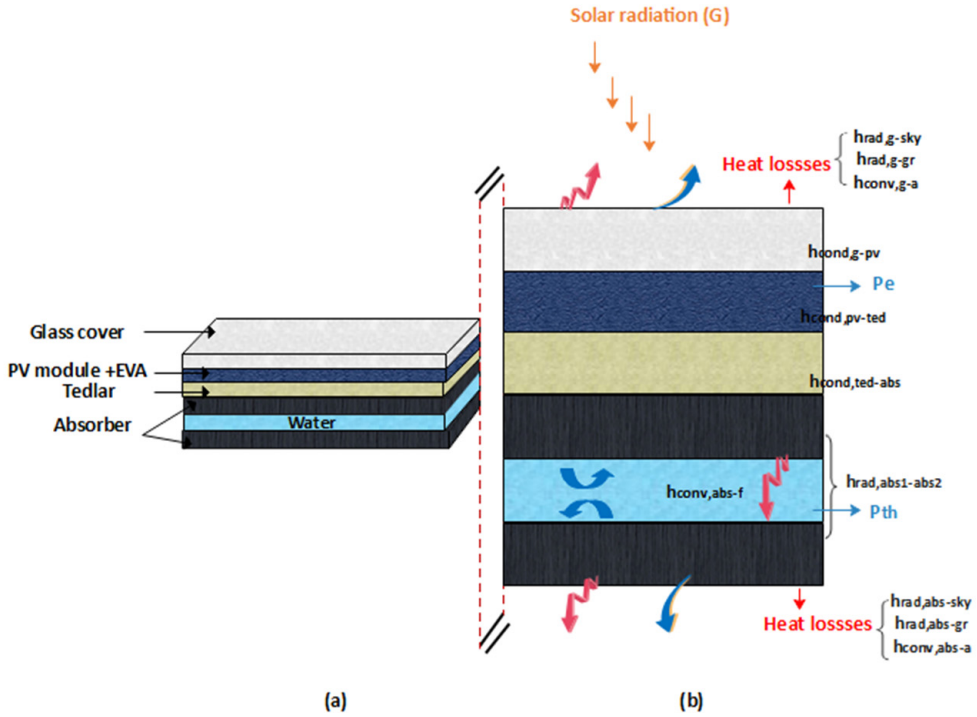


Figure 1. Components (**a**) and heat exchange mechanism in the PV/T system (**b**).

The main PV technical characteristics (applied to Standard Test Conditions of solar irradiance of 1000 W/m^2 and ambient temperature of 25 °C) and the selected PV/T system properties are reported in Tables 1 and 2. Moreover, the assumptions considered in developing the PV/T model due to its different components were [22,23,26]:

- A (1D) numerical model is built since the layers thickness are very thin relative to the other dimensions. As a result, heat losses are considered to be neglected at the PV/T sides and average uniform temperature is determined for each layer;
- The amount of absorbed solar irradiation that is not converted into electricity is transferred from the PV cells back to the rest of system;
- The material properties remain constant in the PV/T system, for a temperature limited range;
- The heat flux between PV cells and EVA is supposed to be negligible;
- A perfect contact between PV/T components is supposed;
- The effects of dust and partial shading were neglected.

Table 1. PV module technical characteristics applied to STC.

PV Type	Pmax (W)	Vmp (V)	Imp (A)	Voc (V)	Isc (A)	η_e (%)	NOCT (°C)
AE320HM-60 Mono-crystalline	320	33.40	9.59	40.90	10.15	19.30	45 ± 2

Table 2. PV/T investigated parameters.

Dimensions	1665 × 996 (mm × mm)			
Properties	**Glazing**	**PV Cells**	**Tedlar**	**Aluminum Absorber**
Density (kg/m^3)	2300	2330	1500	2700
Thermal conductivity (W/m·K)	1.0	168.0	0.2	160
Specific heat (kJ/kgK)	500	757	1200	900
Thickness (m)	0.003	0.00035	0.0015	0.003

2.2. Heat Balance Governing Equations

In the present work, a PV/T transient model was conducted based on a heat balance established for solid and fluid domains. In all solid components (glass, PV module, Tedlar, aluminum absorbers), the heat exchange process occurs by conduction mechanism, while in the flow duct, the thermal transfer to fluid (water) is through the convection mode. For each PV/T layer, the energy balance equation is a function of the layer internal energy variation taking into account some external parameters, e.g., the solar irradiance, ambient temperature, wind speed, and mass flow rate. Thus, the energy governing equations for solid and fluid layers were obtained considering the selected thermo-physical proprieties summarized in Table 2.

2.2.1. Solid Layers

The heat flux for the PV/T solid layers can be obtained using Equation (1). It is a function of the density ρ_S, specific heat capacity $c_{p,S}$ and the thickness δ_s of the selected layer as well the thermal heat exchange coefficient h_s:

$$\rho_S \, \delta_s c_{p,s} \, \frac{\mathrm{dT_s}}{\mathrm{dt}} = \Sigma \, h_s \, \Delta \mathrm{T_s} + \alpha \, E_{sun} - \vartheta E_e \tag{1}$$

where $\Delta \mathrm{T_s}$ is the temperature gradient and E_{sun} is the absorbed solar irradiance for each solid layer. In fact, a significant part of the incident solar irradiance is absorbed by the PV cells and converted to electrical energy E_e while the remainder is lost with environment. Thus, the absorption and electricity production terms for PV cell are $\alpha \neq 0$; $\vartheta = 1$ and for the other solid layers are $\alpha = 0$; $\vartheta = 0$.

The expression of heat exchange coefficient h_s is directly dependent on the heat transfer mechanisms between layers. In case of solid layers *i,j* where heat is transferred by conduction, h_s is given by:

$$h_s = hc_{i,j} = \frac{1}{\left(\frac{\delta_i}{\lambda_i} + \frac{\delta_j}{\lambda_j}\right) A_{i,j}} \tag{2}$$

where: λ_i and δ_i are the thermal conductivity and thickness of the layer *i*; λ_j and δ_j are the thermal conductivity and thickness of the layer *j* and $A_{i,j}$ is the exchange area between the layers *i,j*.

For the front of the PV/T system, three expressions of the heat exchange coefficient h_{s1}, h_{s2}, and h_{s3} are used, due to the heats transfer by radiation between the glass-sky, glass-ground and by convection between the glass-ambient:

$$h_{s1} = hr_{g,sky} = \sigma \varepsilon_g F_{g,sky} \, A\left(T_{sky} + T_g\right) \cdot \left(T_{sky}^2 + T_g^2\right) \tag{3}$$

$$h_{s2} = hr_{g,\mathrm{gr}} = \sigma \varepsilon_g F_{g,gr} \, A\left(T_{gr} + T_g\right) \cdot \left(T_{gr}^2 + T_g^2\right) \tag{4}$$

$$h_{s3} = hv_{g,a} = \left(hv_{forced}{}^3 + hv_{free}{}^3\right)^{1/3} \tag{5}$$

where ε_g, is the glass emissivity; $F_{g,sky}$ and $F_{g,gr}$ are the view factors [24].

The glass-ambient heat transfer coefficient h_{s3} is determined as the sum of the forced and natural convective heat transfer coefficients hv_{forced} and hv_{free}. If $Gr/Re^2 << 1$, the forced convection regime has been evaluated. Thus, the following correlation [27] based on the wind speed velocity w is used:

$$hv_{forced} = 2.8w + 3 \tag{6}$$

Otherwise, for $Gr/Re^2 >> 1$, the correlation of Bejan et al. [28] depending on the air thermal conductivity λa and Nusselt number Nu_{free} is adopted:

$$hv_{free} = \frac{Nu_{free}\ \lambda a}{L} \tag{7}$$

$$Nu_{free} = 0.14\left[(Gr\ Pr)^{\frac{1}{3}} - (Gr_{cr}\ Pr)^{\frac{1}{3}}\right] + 0.56(Gr_{cr} Pr \cos\theta) \tag{8}$$

At the back side of the PV/T system, the heat losses by radiation between the absorber-sky, absorber -ground, and by convection between the absorber–ambient were considered. Moreover, three heat exchange coefficients h_{s1}, h_{s2}, and h_{s3} can be expressed as follows:

$$h_{s1} = hr_{absl,sky} = \sigma\varepsilon_{absl}F_{sky,absl}\ A\left(T_{sky} + T_{absl}\right)\cdot\left(T_{sky}^2 + T_{absl}^2\right) \tag{9}$$

$$h_{s2} = hr_{absl,gr}\ \sigma\varepsilon_{absl}F_{absl,gr}\ \ A\left(T_{gr} + T_g\right)\cdot\left(T_{gr}^2 + T_g^2\right) \tag{10}$$

$$h_{s3} = hv_{a,absl} \tag{11}$$

where ε_{absl}, is heat transfer between the absorber and the ambient.

The heat exchange coefficient $h_{s3} = hv_{absl,a}$ could be calculated as function of the forced or the free convection regime using the following correlations considered in [29].

In case of forced convection:

$$hv_{absl,a} = 5.7\ w \tag{12}$$

While in free convection is determined by:

$$hv_{absl,a} = \frac{Nu_{free}\ \lambda a}{L} \tag{13}$$

$$Nu_{free} = \left\{0.825 + \frac{0.387Ra^{1/6}}{\left[1 + \left(\frac{0.492}{Pr}\right)^{9/16}\right]^{8/27}}\right\}^2 \tag{14}$$

For the duct formed by the two aluminum plates, the heat exchange coefficient h_s is due to the radiation mechanism as expressed in [30].

Table 3 shows the set of governing equations introduced in the numerical model for the solid PV/T layers.

Table 3. Governing equations for the PV/T solid layers.

Layers	Equations	
Glass	$\left(\rho_g \delta_g C_g\right) \frac{dT_g}{dt} = \alpha_g E_{sun} + hr_{g,sky}\left(T_{sky} - T_g\right) + hr_{g,gr}\left(T_{gr} - T_g\right) + hv_{g,a}\left(T_a - T_g\right) + hc_{PV,g} PF\left(T_{PV} - T_g\right) + hc_{Ted,g}(1 - PF)\left(T_{Ted} - T_g\right)$	(15)
PV cells	$PF(\rho_{PV}\delta_{PV}C_{PV})\frac{dT_{PV}}{dt} = \left[\left(\tau_g \alpha_{PV} - \eta_e\right) E_{sun} + hc_{PV,g}\left(T_g - T_{PV}\right) + hc_{Ted,PV}\left(T_{Ted} - T_{PV}\right)\right] PF$	(16)
Tedlar	$(\rho_{Ted}\delta_{Ted}C_{Ted})\frac{dT_{Ted}}{dt} = (1 - PF)\tau_g \alpha_{Ted} + (1 - PF) hc_{Ted,g}\left(T_g - T_{Ted}\right) + PF \cdot hc_{Ted,PV}\left(T_{PV} - T_{Ted}\right) + hc_{abs1,Ted}\left(T_{abs1} - T_{Ted}\right)$	(17)
Absorber 1	$(\rho_{abs}\ \delta_{abs}\ C_{abs})\frac{dT_{abs1}}{dt} = hc_{abs1,Ted}\left(T_{Ted} - T_{absh}\right) + hr_{abs1,abs2}\left(T_{absl} - T_{absh}\right) + hc_{f,abs1}\left(T_f - T_{absh}\right)$	(18)
Absorber 2	$(\rho_{abs}\delta_{abs}C_{abs})\frac{dT_{abs2}}{dt} = hc_{abs2,f}\left(T_f - T_{abs2}\right) + hr_{abs1,abs2}\left(T_{abs2} - T_{abs1}\right) + hr_{abs2,sky}\left(T_{sky} - T_{abs2}\right) + hr_{abs2,gr}\left(T_{gr} - T_{abs2}\right) + hv_{a,absl}\left(T_a - T_{abs2}\right)$	(19)

2.2.2. Fluid Layers

For the cooling fluid flows in the duct of the PV/T system, the energy balance equation is given as:

$$\left(\rho_f \delta_f\ C_f\right)\frac{dT_f}{dt} = hc_{f,abs1}\left(T_{abs1} - T_f\right) + hc_{abs2,f}\left(T_{abs2} - T_f\right) - \dot{m}C_f\ \left(T_{out} - T_{int}\right) \quad (20)$$

where $\dot{m}$, C_f, and T_{int} and T_{out} are respectively the fluid mass flow rate, the fluid specific heat capacity, and the temperature at the inlet and outlet of the PV/T system.

The heat transfer coefficients $hc_{f,abs1}$ and $hc_{f,abs2}$ characterize the convection between the two absorbers and fluid and can be evaluated as a function of the fluid thermal conductivity λ_f, duct hydraulique diameter D_h, and Nusselt number Nu_f:

$$hc_{f,abs1} = hc_{f,abs2} = \frac{Nu_f\ \lambda_f}{D_h} \quad (21)$$

The Nusselt number for water cooling flow between absorber plates is deduced from the correlations of Kudish et al. [31]:

$$Nu_f = 1.86\left[R_e\ P_r\left(\frac{D_h}{L}\right)\right]^{\frac{1}{3}}\left(\frac{\mu_f}{\mu_f\prime}\right)^{0.14}, \text{ case of laminar flow} \quad (22)$$

$$Nu_f = 0.023\ [\ {R_e}^{0.8}{P_r}^{0.33}], \qquad \text{case of turbulent flow} \quad (23)$$

where R_e , P_r, and μ_f are respectively the Reynolds number, Prandlt number, and fluid dynamic viscosity; $\mu_f' = \mu_f(T_p)$ [32].

By rearranging the governing Equations (15)–(20), a set of energy differential equations was built. Thereafter, a MATLAB solution program was developed where the Runge–Kutta (RK4) numerical method was used to solve the energy balance system. Finally, the basic simulation allowed to determine the temperature profile as well as the thermal, electrical, and global performances. The calculation steps in MATLAB software are summarized in flow chart form as shown in Figure 2.

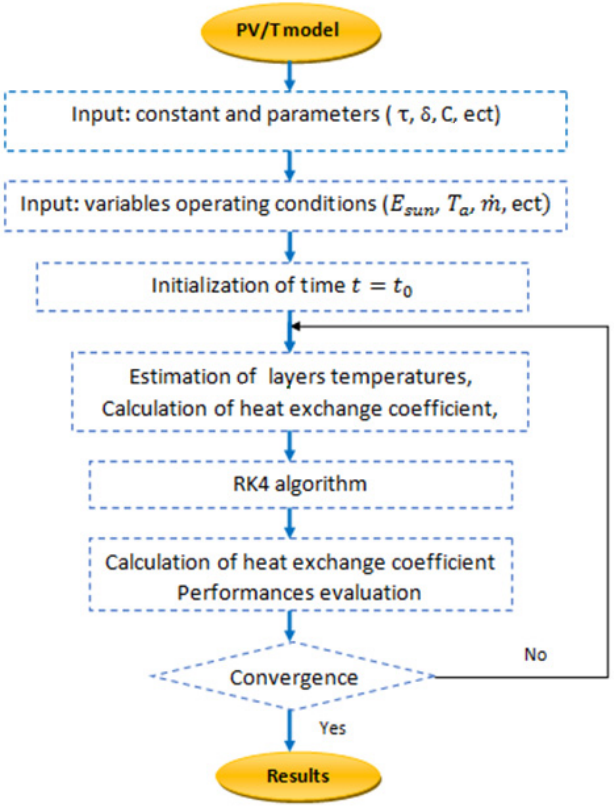


Figure 2. Flow chart of the PV/T numerical modeling.

2.3. Energy Analysis Method

In order to analyze the developed numerical model for the PV/T system, a performance evaluation is required. Therefore, the solar irradiance as an energy source was supposed uniform and perpendicular on the PV/T surface. Absorber solar irradiance by the PV cells layer was given as function of the glass layer transmittance τ_g, the cell absorptivity α_{PV}, and the incident solar irradiance E_{sun} by [33]:

$$E'_{sun} = \tau_g \alpha_{PV} \ E_{sun} \tag{24}$$

The electrical production from the PV cells is determined by Equation (24):

$$E_e = A_{pv}\, \eta_e E'_{sun} \tag{25}$$

For evaluation of the electrical performance, the following expression was used [30]:

$$\eta_e = \eta_{ref}[1 - \beta(T_{PV} - T_{STc})] \tag{26}$$

where η_{ref} is the reference efficiency; β is the temperature coefficient; T_{PV} is the PV cells temperature; and T_{STc} is PV cells temperature at STC conditions equal to 25 °C. According to the AE320HM-60 PV commercial unit with characteristic reported in Table 1, the η_{ref} is about 19.30% and β is equal to 0.0045 C^{-1} [34].

The thermal production of PV/T system is a function of fluid mass flow rate $\dot{m}$, fluid specific heat capacity C_f , and the temperature difference of the fluid at the inlet and outelt of the PV/T system [35]:

$$E_{th} = \dot{m} C_f \ (T_{out} - T_{int}) \tag{27}$$

For assessment of thermal efficiency, the fraction of the thermal production on the absorbed solar irradiance was conducted according to Equation (28):

$$\eta_{th} = \frac{E_{th}}{E'_{sun}} \tag{28}$$

Combining both electrical and thermal efficiencies, the PV/T global performance was obtained by:

$$\eta_g = \eta_e + \eta_{th} \tag{29}$$

3. Results and Discussion

In this section, the set of obtained results is presented and discussed. To test the accuracy of the developed PV/T model allowing the prediction of both thermal and electrical behavior of the system, a model validation is processed. Based on the same thermal model, a comprehensive analysis is further performed to assess the effect of some PV/T key parameters on its outputs. Finally, the PV/T optimized model is tested under the real weather data of Iasi, Romania and performance comparison with conventional PV panel is conducted.

3.1. Model Validation

The validation process included the model of the PV unit, mainly formed by the glass, PV cells, and Tedlar (Equations (15)–(17)). This model was tested under different operating conditions, e.g., solar irradiance and outdoor temperature. Furthermore, the results were compared with the data for Nominal Operating Cell Temperature conditions (NOCT: E_{sun} = 800 W/m^2, T_a = 20 °C and w = 1 m/s). In Figure 3, the PV cells temperature is evaluated for different solar irradiances of 600 W/m^2, 800 W/m^2, and 1000 W/m^2 with an ambient temperature of 20 °C, 25 °C, and 35 °C, respectively. From this figure, the effect of environmental conditions on a PV temperature is clearly shown (a minimum PV temperature was noted at about 39 °C when solar radiation and ambient temperature were lower, about 600 W/m^2 and 20 °C). It can be also observed that the difference between PV temperature values and NOCT is quite negligible. According to the commercial PV datasheet characteristic summarized in Table 1, the NOCT value was 45 ± 2 °C, while for the three layers model, the PV temperature was 43.96 °C, which proves the effectiveness of PV developed model. For the rest of the PV/T system (absorber 1, fluid and absorber 2), the developed Equations (18)–(20) were written based on the PV/T model validated experimentally in [24].

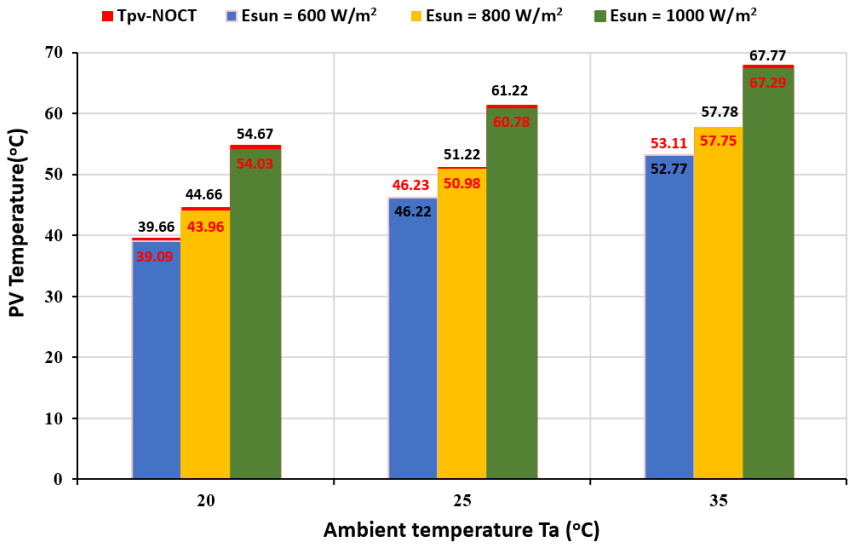


Figure 3. Comparison of the developed PV model and NOCT model.

3.2. Parametric Analysis

3.2.1. Effect of Water Velocity

Based on the developed numerical model, the effect of water velocity on the PV/T performance was analyzed. The environmental conditions involved in this analysis were a solar irradiance of 1000 W/m^2, an outdoor temperature of 35 °C, and a wind speed of 1 m/s. The fluid velocity as a flow control parameter had a significant effect on the cooling of the PV unit. Hence, Figure 4 investigates the PV temperature evolution as function of water inlet temperature for different water velocities of 0.010 m/s, 0.015 m/s, 0.02 m/s, 0.025 m/s, 0.030 m/s, and 0.035 m/s. As result, it is depicted that by increasing water velocity from 0.010 m/s to 0.035 m/s, a drop in the PV temperature was observed in the four cases, where the water film thickness was 3 mm, 5 mm, 7 mm, and 10 mm. In addition, a minimum value of PV operating temperature about 27.7 °C was observed for an inlet water temperature of 20 °C, water thickness of 7 mm, and highest velocity of 0.035 m/s. This underlines the effective cooling of the PV cells, where a significant heat is extracted from the PV back side while increasing the water velocity.

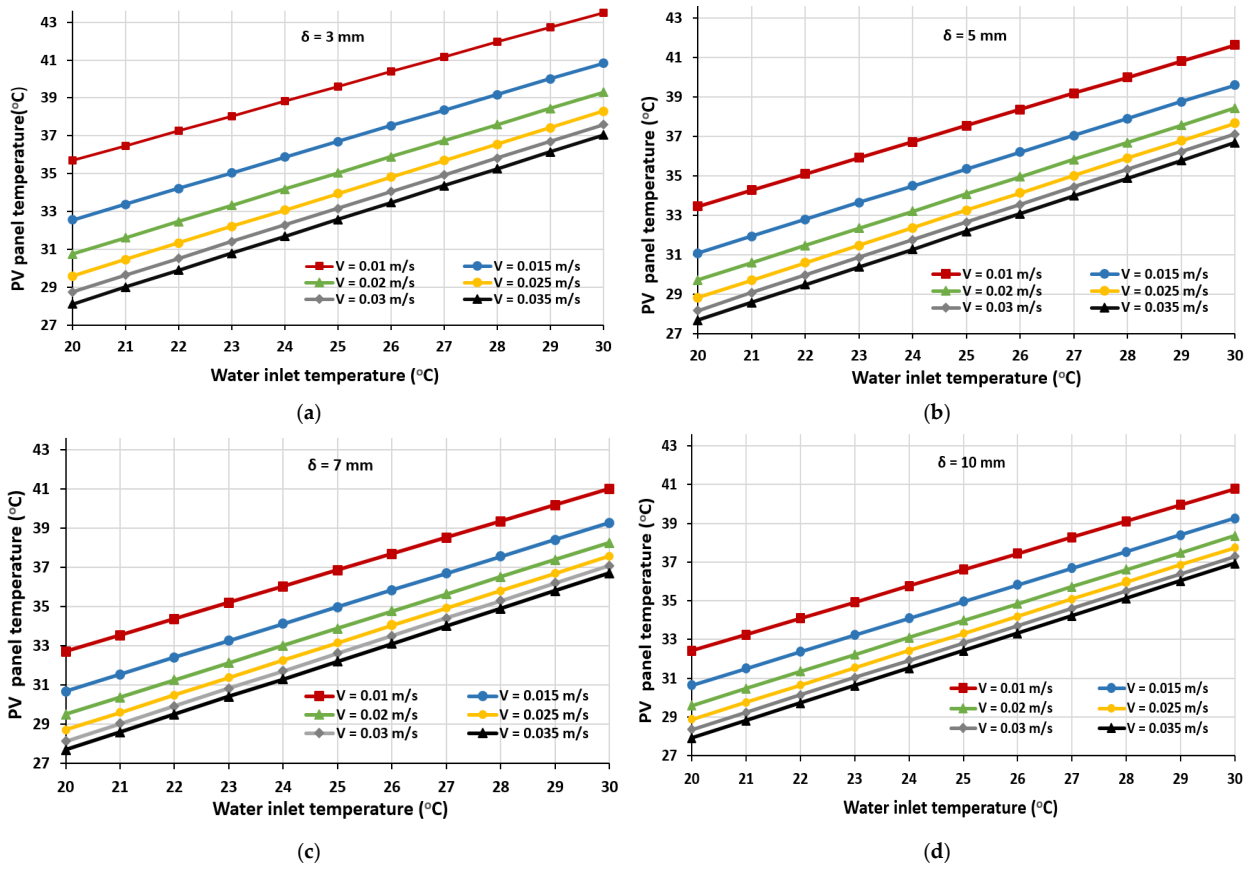


Figure 4. Effect of water velocity on the cooling of the PV cells for different thicknesses: (**a**) δ = 3 mm, (**b**) δ = 5 mm, (**c**) δ = 7 mm, (**d**) δ = 10 mm.

3.2.2. Effect of Water Film Thickness

Among the other geometry parameters for flow, the water film thickness presented an important effect on the optimized cooling of the PV cells and the PV/T electrical and thermal performances. Hence, four water thicknesses of 3 mm, 5 mm, 7 mm, and 10 mm were selected to investigate its impact on the cooling of the PV cells with water velocity and inlet temperature ranging from 0.010 to 0.035 m/s and 20 to 30 °C, respectively. The study was carried out under the same weather conditions mentioned above (solar irradiance of 1000 W/m^2, outdoor temperature of 35 °C, and wind speed of 1 m/s).

As illustrated in Figure 5, as the water film thickness increased (3 mm, 5 mm, 7 mm) for the different water velocity cases, the PV temperature decreased. This is due to the important heat removed from the PV panel, while by further increasing the water film thickness from 10 mm the PV temperature start increasing (inflexion point). As a result, a minimum value of PV temperature was noted to be 27.7 °C for an optimal water film thickness of 7 mm (water inlet temperature and velocity of 20 °C and 0.035 m/s, respectively).

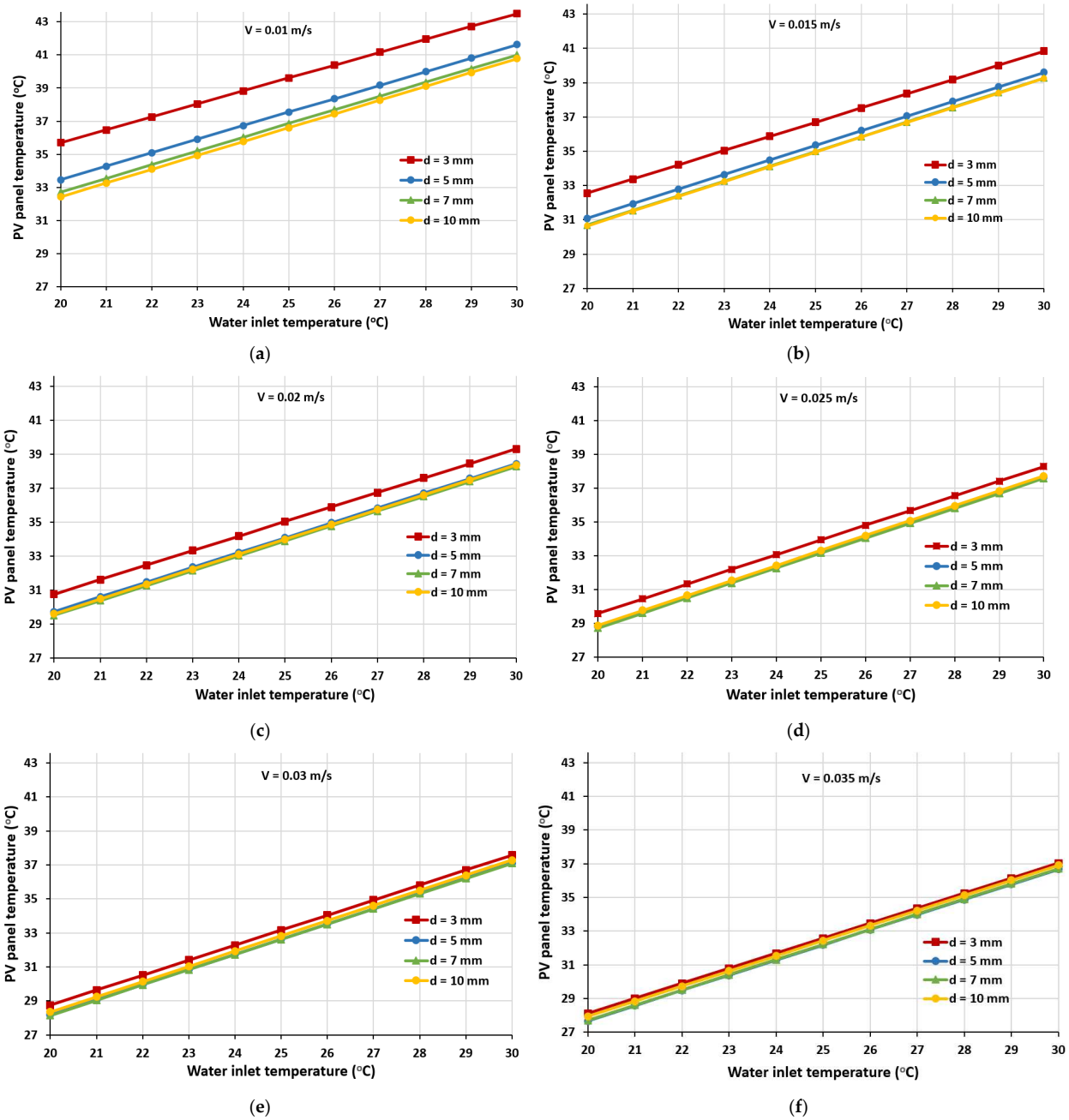


Figure 5. Effect of water thickness on the cooling of the PV cells for different velocities: (**a**) V = 0.01 m/s, (**b**) V = 0.015 m/s, (**c**) V = 0.02 m/s, (**d**) V = 0.025 m/s, (**e**) V = 0.03 m/s, (**f**) V = 0.035 m/s.

In Figure 6, the effect of the water film thickness on the fluid heat transfer coefficient and thermal power is illustrated for variable water velocity and inlet temperature. From this figure, it can be seen that with the increase in water thickness, the heat exchange coefficient dropped which decreases the fluid outlet temperature. However, the ther-

mal power increased and reached a maximum value of 1334.5 W at water thickness of 7 mm (water velocity of 0.035 m/s, inlet temperature of 20 °C, and outer temperature of 21.31 °C), Table 4.

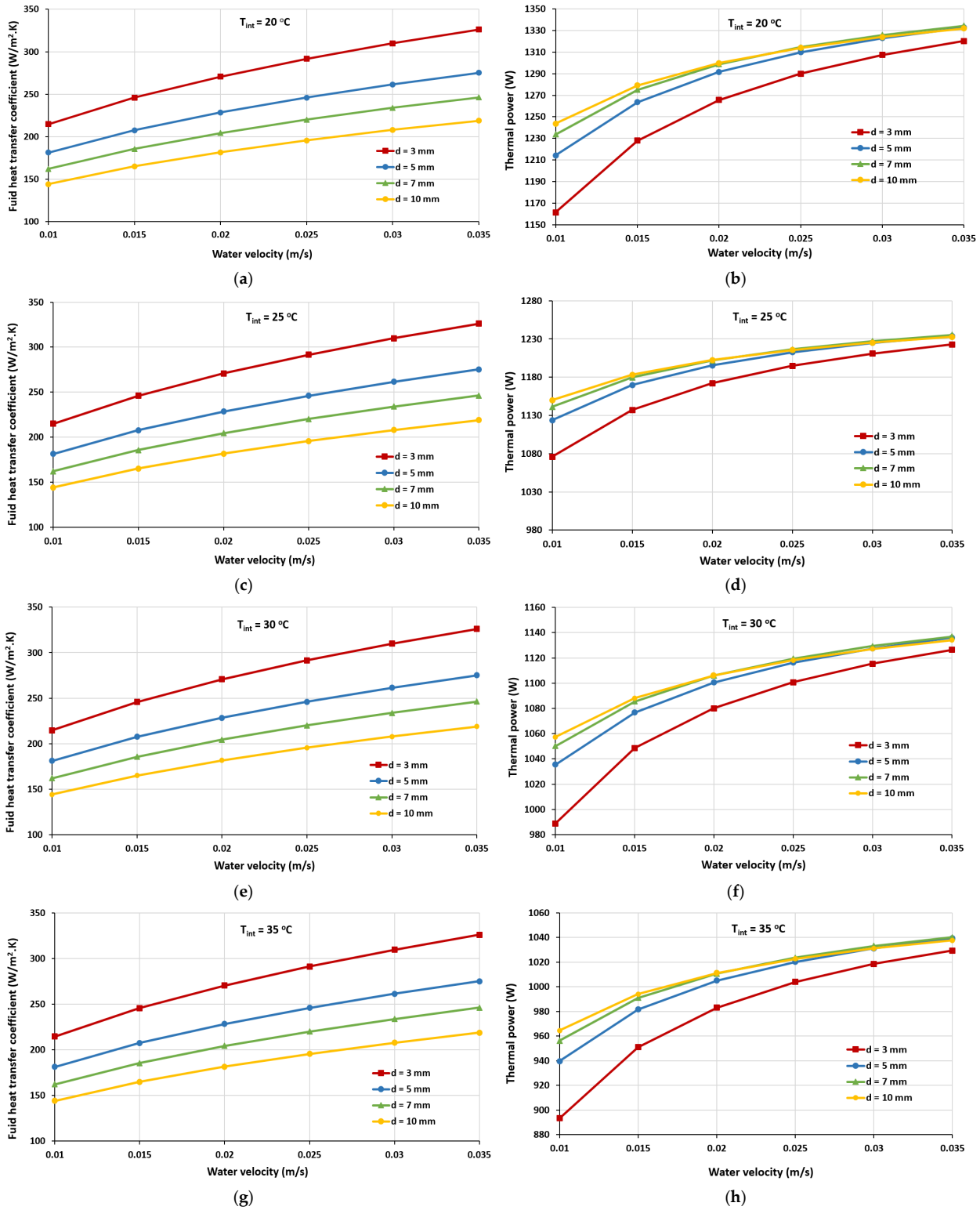


Figure 6. Effect of water thickness on fluid transfer coefficient and thermal power for different inlet temperatures: (**a**,**b**) T_{int} = 20 °C; (**c**,**d**) T_{int} = 25 °C; (**e**,**f**) T_{int} = 30 °C; (**g**,**h**) T_{int} = 35 °C.

Table 4. Comparison of PV and PV/T performances at E_{sun} = 1000 W/m^2, T_a = 35 °C, and T_{int} = 20 °C.

	T_{PV} (°C)	T_{out}(°C)	E_e (W)	E_{th} (W)	η_e (%)	η_{th} (%)
PV	67.7	-	258.8	-	15.60	-
PV/T	27.7	21.31	316.56	1334.5	19.07	80.3

According to Equation (27), the thermal power was not only depending on difference between the inlet and the outlet temperature, but also a function of the water mass flow rate. At a fixed value of water inlet temperature and velocity, the thermal power is related to the water mass flow rate and the outlet temperature. In this study, the water film thickness increase clearly affected the cooling of the PV unit and the heat gain. Noting that, further increase of water thickness will also affect the cost and the PV/T system heavy weight. Consequently, the PV/T system with a coupled optimum water velocity and thickness of 0.035 m/s and 7 mm provided the best cooling effect and highest electrical and thermal performances (Table 4).

The PV and PV/T performances were also depicted and compared under real weathers conditions of Iasi, Romania. A daily simulation was conducted for a typical day of summer (28 July 2016), with weather data involving solar irradiance E_{sun} and ambient temperature T_a reported by the PVGIS data [36] as shown in Figure 7. During this day, a maximum solar irradiance about 1022 W/m^2 and ambient temperature of 27.6 °C were noted at 13:00. The simulation was done supposing the inlet water temperature for PV cooling equal to the ambient one with a maximum temperature of 27.6 °C. The optimum case of PV/T system was chosen in terms of water velocity of 0.035 m/s and water film thickness of 7 mm.

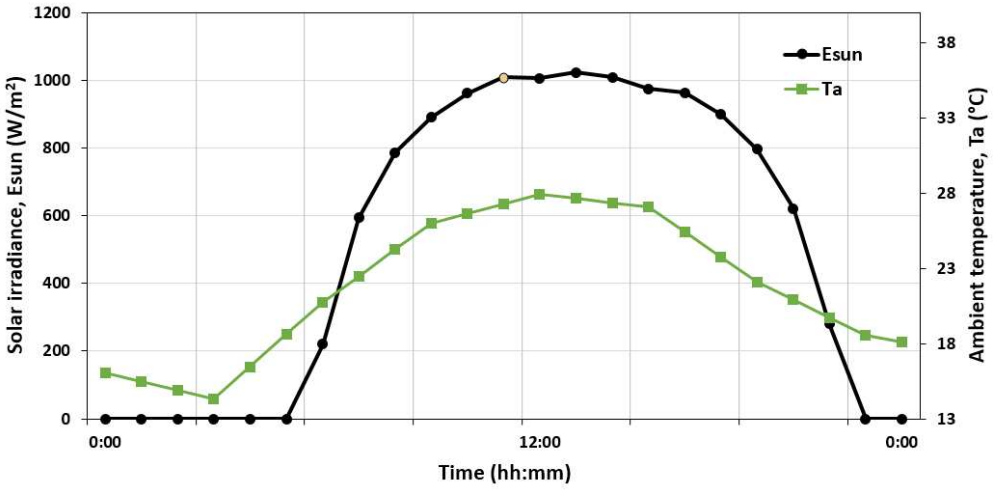


Figure 7. Variation of solar irradiance and ambient temperature (28 July 2016).

Given these weather conditions, the evolution of PV and PV/T temperatures (PV/T at T_{int} = T_a) is illustrated in Figure 8. It can be clearly observed that both temperatures presented the same trend during this day. Moreover, the PV/T system provided a lower PV cell temperature of 33.8 °C at 13:00, due to the cooling effect compared with the conventional PV unit (61 °C). According to the negative dependence between electrical production and operating temperature of the PV cells, an effective cooling enhances electrical power. As shown in Figures 9 and 10, the PV/T system provide a better electrical power and efficiency of about 313 W and 18.54% at 13:00, compared with the conventional PV panel.

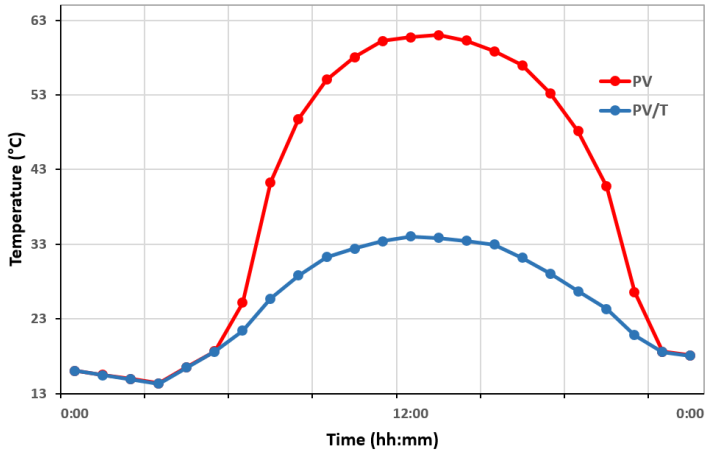


Figure 8. Comparison of PV and PV/T temperatures.

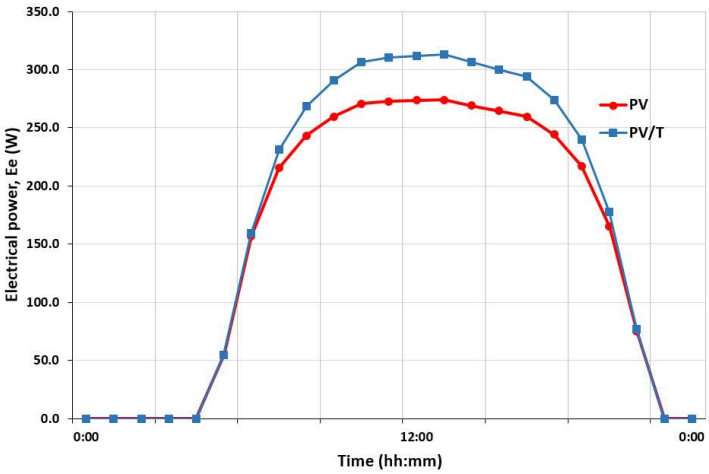


Figure 9. Comparison of PV and PV/T electrical power.

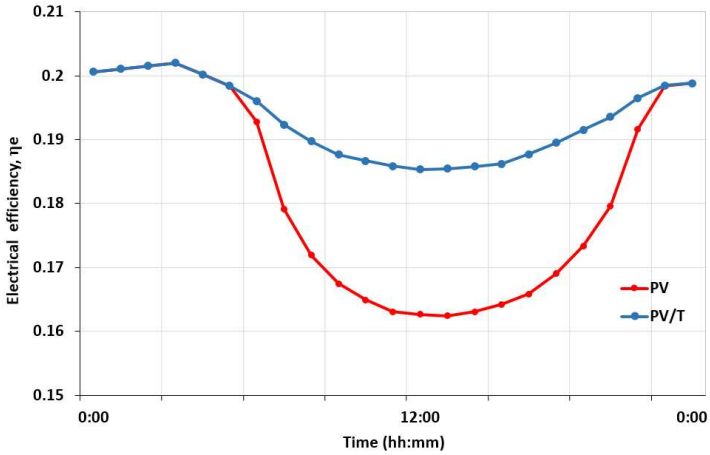


Figure 10. Comparison of PV and PV/T electrical efficiency.

4. Conclusions

This work proposes an improved dynamic numerical model for PV/T system based on the heat balance equations established for each layer and solved in MATLAB software. The main obtained outputs of the PV/T model are respectively the temperatures and the electrical and thermal power used for evaluating the advantages of using the PV/T system instead of PV conventional one.

This developed model was built regarding the other models presented in literature [37] and validated through comparison of the three layer PV model with the NOCT model and using the equations of the cooling unit, derived from a previous PV/T model validated experimentally in [24]. Consequently, results revealed good agreement. Thus, the model is considered a useful tool for other research works aiming to investigate the PV/T system and analyze its energy yield.

Thereafter, the PV/T model was used to investigate the effect of the water velocity and thickness on the cooling of the PV cells. Next, the improved PV/T model with optimum parameters values was applied in case operating conditions of Iasi, Romania, where the input variables, e.g., solar irradiance and ambient temperature, were given by PVGIS data [36]. Important conclusions of this work can be drawn as below:

- The effectiveness of the developed PV/T model based on the three layer PV model tested at different of solar irradiance and ambient temperature was proven.
- Inlet water temperature had a significant effect on the cooling of the PV panel. A lower PV temperature was noted when the inlet temperature was about 20 °C.
- As the water velocity ranged from 0.010 to 0.035 m/s, the cooling process improved. A lower PV temperature was obtained for water velocity of 0.035 m/s.
- The temperature of the PV panel decreased while increasing the water film thickness from 3 mm to 7 mm and started increasing by 10 mm.
- Optimal cooling of the PV cells (27.7 °C) was ensured, adopting optimum values of water velocity and thickness of 0.035 m/s and 7 mm, respectively, at inlet temperature of 20 °C.
- The improved PV/T model showed a better electrical performance (316.56 W) compared with the conventional PV panel (258.8 W). Furthermore, an important gain of 1334.5 W of thermal production was obtained.

Therefore, the PV/T system designing based on the optimum functional parameters can be an efficient way to produce electrical and thermal energy simultaneously where the electrical and thermal efficiency can reach 19.07% and 80.3%, respectively. Moreover, similar results found in literature [20,21] show economic advantages for implementing such systems in the same climate conditions, where the investment return can be up to 4.25 years with a 75% subsidy in the initial investment and six PV/T modules installed [38].

Future works foresee experimental programs for developing the PV/T model using a real experimental PV/T prototype that is installed on the roof of the Building Services Department, "Gheorghe Asachi" Technical University of Iași, Romania, in order to consider more climatic parameters, such as the wind speed and direction, which also affect the electrical and the thermal energy outputs of the PV/T system.

Author Contributions: Conceptualization, C.E.F., S.V.H., N.C.C. and B.H.; methodology, C.E.F. and B.H.; software, C.E.F.; validation, C.E.F., S.V.H. and E.F.Ț.; formal analysis, C.E.F., S.V.H. and M.L.C.; investigation, C.E.F., N.C.C., S.V.H., B.H., E.F.Ț. and M.L.C.; resources, N.C.C. and M.L.C.; data curation, C.E.F., N.C.C. and B.H.; writing—original draft preparation, C.E.F. and S.V.H.; writing—review and editing, C.E.F. and N.C.C.; supervision, N.C.C. and B.H.; project administration, N.C.C.; funding acquisition, N.C.C. All authors have read and agreed to the published version of the manuscript.

Funding: This paper was financed by the program Internal Grants—Publications granted by the "Gheorghe Asachi" Technical University of Iasi, Romania, project number GI/P35_Publications/2021.

Institutional Review Board Statement: Not applicable.

Informed Consent Statement: Not applicable.

Data Availability Statement: Data are contained within the article.

Acknowledgments: We would like to acknowledge the invaluable support provided by the FCI-TUIASI infrastructure in writing this article. The authors also acknowledge AUF for the support received through the postdoc scholarship for Chaimae El Fouas.

Conflicts of Interest: The authors declare no conflict of interest.

Nomenclature

A	Area (m^2)
C	Specific heat capacity (kJ/kg°C)
Ee	Electrical power (W)
Eth	Thermal power (W)
$F_{j,k}$	View factor between layer i and j
E_{sun}	Solar irradiance (W/m^2)
Gr	Grashof number
$hc_{,i,j}$	Conductive heat exchange coefficient between components i and j (W/m^2K)
$hr_{,j,k}$	Radiative heat exchange coefficient between components i and j (W/m^2K)
$hv_{,i,j}$	Convective heat transfer coefficient between components i and j (W/m^2K)
Isc	Short circuit current (A)
I_{mp}	Maximum current (A)
L	Length (m)
$NOCT$	Nominal operating cell temperature
Nu	Nusselt number
Pr	Prandlt number
P_{max}	Maximum power (W)
PF	Packing factor
Ra	Rayleigh number
Re	Reynolds number
STC	Standard test conditions
t	Time step (s)
T_i	Temperature of layer i (°C)
T_a	Ambient temperature (°C)
V	Water velocity (m/s)
V_{OC}	Open circuit voltage(V)
V_{mp}	Maximum voltage (V)
w	Wind speed (m/s)
Greek symbols	
α	Absorptivity
β	Reference temperature coefficient for efficiency
η_e	Electrical efficiency (%)
η_{th}	Thermal efficiency (%)
λ	Thermal conductivity (W/m K)
ρ	Material density (kg/m^3)
σ	Stefan–Boltzmann constant
Scripts	
Abs	Absorber
f	Fluid
g	Glass
gr	Ground
PV	Photovoltaic
PV/T	Photovoltaic/thermal
Ted	Tedlar

References

1. Markvart, T. *Solar Electricity*, 2nd ed.; John Wiley & Sons: Chichester, UK, 2000.
2. Chandrasekar, M.; Rajkumar, S.; Valavan, D. A review on the thermal regulation techniques for non integrated flat PV modules mounted on building top. *Energy Build.* **2015**, *86*, 692–697. [CrossRef]
3. Makki, A.; Omer, S.; Sabir, H. Advancements in hybrid photovoltaic systems for enhanced solar cells performance. *Renew. Sustain. Energy Rev.* **2015**, *41*, 658–684. [CrossRef]
4. Elminshawy, N.A.S.; Mohamed, A.M.I.; Morad, K.; Elhenawy, Y.; Alrobaian, A.A. Performance of PV panel coupled with geothermal air cooling system subjected to hot climatic. *Appl. Therm. Eng.* **2019**, *148*, 1–9. [CrossRef]
5. Hudisteanu, S.V.; Turcanu, F.E.; Chereches, N.C.; Popovici, C.G.; Verdes, M.; Huditeanu, I. Enhancement of PV Panel Power Production by Passive Cooling Using Heat Sinks with Perforated Fins. *Appl. Sci.* **2021**, *11*, 11323. [CrossRef]

6. Hudisteanu, S.V.; Popovici, C.G.; Mateescu, T.D.; Chereches, N.C. Efficiency analysis of BIPV systems for different locations in Romania. In *Sustainable Solutions for Energy and Environment, Proceedings of the EENVIRO, Bucharest, Romania, 26–28 October 2016*; Elsevier: Amsterdam, The Netherlands, 2017; Volume 112, pp. 404–411.
7. Siecker, J.; Kusakana, K.; Numbi, B.P. Optimal switching control of PV/T systems with energy storage using forced water circulation: Case of South Africa. *J. Energy Storage* **2018**, *20*, 264–278. [CrossRef]
8. Nizetic, S.; Coko, D.; Yadav, A.; Grubisic-Cabo, F. Water spray cooling technique applied on a photovoltaic panel: The performance response. *Energy Convers. Manag.* **2016**, *108*, 287–296. [CrossRef]
9. Hudisteanu, V.S.; Chereches, N.C.; Verdes, M.; Ciocan, V.; Popovici, C.G.; Turcanu, F.E.; Balan, M.C. Analysis of an innovative water-cooling solution for photovoltaic-thermal systems IOP Conference Series: Earth and Environmental Science. *IOP Sci.* **2021**, *664*, 1–10. [CrossRef]
10. Hudișteanu, S.V.; Chereches, N.C.; Popovici, C.G.; Verdeș, M.; Ciocan, V.; Balan, M.C.; Țurcanu, F.E.; Scurtu, I.C. Effect of cooling on power generated by photovoltaic panels IOP Conference Series: Materials Science and Engineering. *IOP Sci.* **2021**, *1141*, 1–12. [CrossRef]
11. Rostami, Z.; Rahimi, M.; Azimi, N. Using high-frequency ultrasound waves and nanofluid for increasing the efficiency and cooling performance of a PV module. *Energy Convers. Manag.* **2018**, *160*, 141–149. [CrossRef]
12. Senthil, R.; Elavarasan, R.M.; Pugazhendhi, R.; Premkumar, M.; Vengadesan, E.; Navakrishnan, S.; Islam, M.R.; Natarajan, S.K. A holistic review on the integration of heat pipes in solar thermal and photovoltaic systems. *Sol. Energy* **2021**, *227*, 577–605. [CrossRef]
13. Chandel, S.S.; Agarwal, T. Review of cooling techniques using phase change materials for enhancing efficiency of photovoltaic power systems. *Renew. Sustain. Energy Rev.* **2017**, *73*, 1342–1351. [CrossRef]
14. Hamzat, A.K.; Sahin, A.Z.; Omisanya, M.I.; Alhems, L.M. Advances in PV and PVT cooling technologies: A review. *Sustain. Energy Technol. Assess.* **2021**, *47*, 1–31. [CrossRef]
15. Bhakre, S.S.; Sawarkar, P.D.; Kalamkar, V.R. Performance evaluation of PV panel surfaces exposed to hydraulic cooling-A review. *Sol. Energy* **2021**, *224*, 1193–1209. [CrossRef]
16. Maleki, A.; Haghighi, A.; Assad, M.E.; Mahariq, I.; Nazari, M.A. A review on the approaches employed for cooling PV cells. *Sol. Energy* **2020**, *209*, 170–185. [CrossRef]
17. Verma, S.; Mohapatra, S.; Chowdhury, S.; Dwivedi, G. Cooling techniques of the PV module: A review. *Mater. Today-Proc.* **2021**, *38*, 253–258. [CrossRef]
18. Reddy, S.R.; Ebadian, M.A.; Lin, C.X. A review of PV-T systems: Thermal management and efficiency with single phase cooling. *Int. J. Heat Mass Transf.* **2015**, *91*, 861–871. [CrossRef]
19. Gomaa, M.R.; Hammad, W.; Al-Dhaifallah, M.; Rezk, H. Performance enhancement of grid-tied PV system through proposed design cooling techniques: An experimental study and comparative analysis. *Sol. Energy* **2020**, *211*, 1110–1127. [CrossRef]
20. Nahar, A.; Hasanuzzaman, M.; Rahim, N.A. Numerical and experimental investigation on the performance of a photovoltaic thermal collector with parallel plate flow channel under different operating conditions in Malaysia. *Sol. Energy* **2017**, *144*, 517–528. [CrossRef]
21. Kazemian, A.; Parcheforosh, A.; Salari, A.; Ma, T. Optimization of a novel photovoltaic thermal module in series with a solar collector using Taguchi based grey relational analysis. *Sol. Energy* **2021**, *215*, 492–507. [CrossRef]
22. Boumaaraf, B.; Boumaaraf, H.; Slimani, M.E.A.; Tchoketch-Kebir, S.; Ait-cheikh, M.S.; Touafek, K. Performance evaluation of a locally modified PV module to a PV/T solar collector under climatic conditions of semi-arid region. *Math. Comput. Simul.* **2020**, *167*, 135–154. [CrossRef]
23. Nahar, A.; Hasanuzzaman, M.; Rahim, N.A.; Parvin, S. Numerical investigation on the effect of different parameters in enhancing heat transfer performance of photovoltaic thermal systems. *Renew. Energy* **2019**, *132*, 284–295. [CrossRef]
24. El Fouas, C.; Hajji, B.; Gagliano, A.; Tina, G.M.; Aneli, S. Numerical model and experimental validation of the electrical and thermal performances of photovoltaic/thermal plant. *Energy Convers. Manag.* **2020**, *220*. [CrossRef]
25. Barbu, M.; Siroux, M.; Darie, G. Numerical model and parametric analysis of a liquid based hybrid photovoltaic thermal (PVT) collector. *Energy Rep.* **2021**. [CrossRef]
26. Rejeb, O.; Dhaou, H.; Jemni, A. A numerical investigation of a photovoltaic thermal (PV/T) collector. *Renew. Energy* **2015**, *77*, 43–50. [CrossRef]
27. El Fouas, C.; El Manssouri, O.; Hajji, B.; Bouselham, L.; Marco Tina, G.; Gagliano, A. Modeling of Dust Deposition Impact on PV/T Hybrid Collector Performances. In Proceedings of the 7th International Renewable and Sustainable Energy Conference (IRSEC), Agadir, Morocco, 27–30 November 2019; pp. 1–6. [CrossRef]
28. Bejan, A.; Kraus, A.D. *Heat Transfer Handbook*; John Wiley & Sons: Hoboken, NJ, USA, 2003.
29. Incropera, F.P.; DeWitt, D.P. *Fundamentals of Heat and Mass Transfer*; John Wiley & Sons: Hoboken, NJ, USA, 2002.
30. El Hocine, H.B.; Touafek, K.; Kerrour, F.; Haloui, H.; Khelifa, A. Model Validation of an Empirical Photovoltaic Thermal (PV/T) Collector. *Energy Procedia* **2015**, *74*, 1090–1099. [CrossRef]
31. Kudish, A.I.; Evseev, E.G.; Walter, G.; Leukefeld, T. Simulation study of a solar collector with a selectively coated polymeric double walled absorber plate. *Energy Convers. Manag.* **2002**, *43*, 651–671. [CrossRef]
32. Rabl, A. *Active Solar Collectors and their Applications*; Oxford University Press: New York, NY, USA, 1985; p. 503.

33. Kazemian, A.; Salari, A.; Hakkaki-Fard, A.; Ma, T. Numerical investigation and parametric analysis of a photovoltaic thermal system integrated with phase change material. *Appl. Energy* **2019**, *238*, 734–746. [CrossRef]
34. Kazemian, A.; Salari, A.; Ma, T. A year-round study of a photovoltaic thermal system integrated with phase change material in Shanghai using transient model. *Energy Convers. Manag.* **2020**, *210*, 112657. [CrossRef]
35. Salari, A.; Taheri, A.; Farzanehnia, A.; Passandideh-fard, M.; Sardarabadi, M. An updated review of the performance of nanofluid-based photovoltaic thermal systems from energy, exergy, economic, and environmental (4E) approaches. *J. Clean. Prod.* **2021**, *282*, 124318. [CrossRef]
36. EU SCIENCE HUB. Available online: https://ec.europa.eu/jrc/en/pvgis (accessed on 15 November 2021).
37. El Fouas, C.; Hajji, M.; Bouselham, L.; Hajji, B.; El Mehdi, A.; Bouali, H. Analysis and Design of an Energy System Based on PV/T Water Collector for Building Application. In Proceedings of the 2017 International Renewable and Sustainable Energy Conference (IRSEC), Agadir, Morocco, 4–7 December 2017; pp. 1–5. [CrossRef]
38. Aguilar-Jimenez, J.A.; Hernandez-Callejo, L.; Alonso-Gomez, V.; Velazquez, N.; Lopez-Zavala, R.; Acuna, A.; Mariano-Hernandez, D. Techno-economic analysis of hybrid PV/T systems under different climate scenarios and energy tariffs. *Sol. Energy* **2020**, *212*, 191–202. [CrossRef]

applied sciences

IMPACT FACTOR 2.9

CITESCORE 6.1

Article

Experimental Study on Airflow and Temperature Predicting in a Double Skin Façade in Hot and Cold Seasons in Romania

Monica Lilioara Chereches, Nelu Cristian Chereches, Adrian Alexandru Ciobanu, Sebastian Valeriu Hudișteanu, Emilian Florin Țurcanu, Aurelia Bradu and Cătălin George Popovici

Special Issue

Urban Sustainability and Resilience of the Built Environments

Edited by

Dr. Ilinca Nastase and Dr. Florin Ioan Bode

MDPI

https://doi.org/10.3390/app112412139

applied sciences

MDPI

Article

Experimental Study on Airflow and Temperature Predicting in a Double Skin Façade in Hot and Cold Seasons in Romania

Monica Lilioara Chereches [1], Nelu Cristian Chereches [2,*], Adrian Alexandru Ciobanu [1], Sebastian Valeriu Hudisteanu [2,*], Emilian Florin Țurcanu [2,*], Aurelia Bradu [1] and Cătălin George Popovici [2]

[1] National Institute for Research and Development in Construction, Urban Planning and Sustainable Spatial Development, NIRD URBAN-INCERC Iasi Branch, 700048 Iasi, Romania; monicachereches@gmail.com (M.L.C.); ciobanuadrianalexandru@yahoo.com (A.A.C.); bradu_aurelia@yahoo.com (A.B.)

[2] Faculty of Civil Engineering and Building Services, "Gheorghe Asachi" Technical University of Iași, 700050 Iasi, Romania; catalin.popovici@tuiasi.ro

* Correspondence: chereches@tuiasi.ro (N.C.C.); sebastian.hudisteanu@tuiasi.ro (S.V.H.); emilian-florin.turcanu@tuiasi.ro (E.F.Ț.)

Abstract: In the context of energy conservation and sustainable development, building design should take into account the energy efficiency criteria by using renewable energy sources. Double-skin facades (DSF) represent innovative energy-efficient techniques that have gained increasing interest worldwide. The present study reports the results of an experimental campaign performed on a full-scale double-skin façade using the in-situ measurement methodology. The thermodynamic behavior of the façade is studied under real exterior climatic conditions in Romania in hot and cold seasons, and performance indicators in terms of pre-heating efficiency and dynamic insulation efficiency were determined. Three summer periods are analyzed corresponding to the outdoor air curtain scenario for three ventilation modes in naturally or mechanically ventilated single-story DSF. Results revealed that the third ventilation scenario, which combines horizontal and vertical openings, gives the best efficiency of 71.3% in the double skin façade functioning. During the cold season, the channel façade behaved like a thermal buffer between the building and the exterior air, ensuring the thermal energy for partial or integral heating of the building.

Keywords: double skin facade; thermal performance; in situ monitoring; natural and forced ventilation; experimental study

check for updates

Citation: Chereches, M.L.; Chereches, N.C.; Ciobanu, A.A.; Hudisteanu, S.V.; Țurcanu, E.F.; Bradu, A.; Popovici, C.G. Experimental Study on Airflow and Temperature Predicting in a Double Skin Façade in Hot and Cold Seasons in Romania. *Appl. Sci.* **2021**, *11*, 12139. https://doi.org/10.3390/app112412139

Academic Editors: Ilinca Nastase and Florin Ioan Bode

Received: 22 November 2021
Accepted: 16 December 2021
Published: 20 December 2021

Publisher's Note: MDPI stays neutral with regard to jurisdictional claims in published maps and institutional affiliations.

Copyright: © 2021 by the authors. Licensee MDPI, Basel, Switzerland. This article is an open access article distributed under the terms and conditions of the Creative Commons Attribution (CC BY) license (https://creativecommons.org/licenses/by/4.0/).

1. Introduction

With the worldwide need for sustainable development, double skin façades were developed like strategies and technologies for decreasing the operational consumption of energy during a building's life cycle. Double Skin Façades (DSF) are building envelopes composed of two layers of glass separated by a ventilated air channel that acts as a thermal agent to improve indoor thermal comfort.

Numerous experimental and numerical studies have been conducted mainly in countries where these façades have been widely applied. More publications are related to experimental studies carried out on test facilities, under real weather conditions. Corgnati et al. [1] present extensive experiments on an active transparent façade, mechanically ventilated, in Italy. Saelens et al. [2] present measurements carried out at the Vliet test building of the Laboratory of Building Physics in Leuven, Belgium. It was shown that the location of the inlet air, airflow rate, and airflow distribution are important parameters that affect the performance of a DSF. These types of measurements are also presented by Zanghirella [3]. Using TWINS, the test facility for experimental investigation, a methodology was proposed to assess the energy performance of active transparent façades. Also, using the Permasteelisa campus, equipped with full-scale test rooms, Fuliotto [4] con-

ducted experimental research on DSF, in terms of both energetic consumption and internal environmental conditions.

Many studies have been performed in situ, on real buildings, by monitoring parameters for long periods of time (minimum one year) [5], determining the behavior of the façade under the influence of different climatic conditions and occupant perception on overall comfort. In general, such studies are the only ones that can provide information on the global interaction of the façade with the occupied building. Given that in situ monitoring requires restricted areas for the tests and periodic inspections of devices, experimental models are tested in the laboratory or in situ by building rooms subject to outdoor climate conditions.

Experimental studies on ventilated façades and fully glazed double skin type were carried out in laboratory conditions [6–8]. In addition, Gavan et al. [9] performed an experimental study in laboratory conditions, on a full-scale facility of DSF equipped with Venetian blinds, to minimize the radiation transmitted during the hot season to avoid overheating.

Due to the transient and complex air flow in the façade channel, the influence on the indoor environment and energy consumption is challenging to evaluate. Therefore, Computational Fluid Dynamics (CFD) can play an essential role in assessing and improving the thermodynamic behavior of a double skin facade. Andjelković et al. [10] presented a mathematical model to study the energy performance of a ventilated façade. Ignjatović et al. [11] investigated the influence of glazing types and ventilation principles in double skin façades on delivered heating and cooling energy during the heating season. Matour et al. [12] studied by CFD techniques the effects of opening configurations on airflow behavior, showing that the ratio between the areas of the front and lateral openings is a critical factor for improving the ventilation in the cavity at the wind incident angle between 0° and 30°. Also, it was concluded that employing three front openings on the external skin of DSF can increase the system's effectiveness in a broader range of wind direction and cavity size. Recently, Tao et al. [13,14] studied the naturally ventilated double-skin façade (NVDSF) with adjustable louvers. Using CFD techniques, they established the impacts of solar angle and intensity on natural ventilation rates, concluded that louvers can enhance or weaken natural ventilation compared to those without louvers. In all studied cases, it was concluded that adding a DSF zone to the south wall of the building leads to the decrease of delivered heating energy.

Most studies have been conducted in the Mediterranean climate [15,16], temperate climate [17–20], and cold climate conditions [21,22], summarizing the effect of structural parameters of DSF on thermal performance. For some studies, it was established that corresponding results could provide some reference for the buildings in similar climate regions [22]. The research has been extended to wet conditions [23,24], arid tropical climate [25,26], and, more recently, to a combined hot and humid environment [27] or a combined hot and dry climate [28]. In the context of an arid climate, it is argued that the cavity depth should be between 600 and 1000 mm to allow these areas to solve specific problems related to the presence of sand. Regarding the possibility of applying these facades in buildings located in specific climatic conditions of countries like Turkey, a significant reduction in energy consumption for heating in the winter was obtained [29].

Năstase et al. [30] studied the difference between a single skin facade and a box double skin facade from a heat transfer point of view, showing an increase in envelope insulation with benefits during the cold season. The mathematical model proposed and the analyses of the heat transfer indicators were described by tabular values and by one year chart for the Brasov region, in Romania.

Kuznik et al. [31] presented numerical modeling of a double skin façade (DSF) combined with a full-scale DSF experimentally studied in summer configuration with different airflow rates through the air channels of the façade and for different angles of the solar shading devices.

A recent study [32] investigated the evolution of building energy retrofit via double-skin and responsive façades, to show the development and adaptability to the current NZEB requirements. Hou et al. [33] investigated how constructional features affect the behavior of double skin façades (DSFs). In a review containing nearly 70 scientific articles on mechanically and naturally ventilated DSFs tested in different countries and climates (but none from Romania), it was established that complex interactions between more than one parameter at a time are primarily unexplored.

There are studies regarding DSF channel ventilation mode (between the cavity and external glazing openings) using openings on the lateral side of the channel. To avoid the overheating of the channel, the horizontal ventilation was studied experimentally [34] and numerically [35] or a supplementary lateral opening was adopted on the external glazing of the DSF [36]. This one can be a solution applied to enhance the wind-induced cavity natural ventilation using pressure differential.

However, there are very few buildings in which double-skin façades have actually been fully realized in Romania and little experience of the system behavior in operation. Furthermore, the specific climatic conditions of continental temperate are characterized by warm summers and cold winters, and these conditions differ from climates where DSFs have been widely applied.

In this study, an experimental analysis of double skin ventilated façade was conducted in the specific climate conditions of Romania, in July and November, for different strategies of ventilation in order to determine the thermodynamic behavior and performance assessment in terms of pre-heating efficiency during the cold season and the dynamic insulation efficiency during the hot one. This study aims to reflect on strategies for DSF that are responsive to the particular climate type. Moreover, in the hot season of the temperate climate, the combination of the vertical openings on the top of the ventilated channel with the lateral ones on the exterior glazing of the DSF is proposed.

2. Experimental Description

The study was carried out for a single-story façade built on the southwest face of the INCERC Laboratory of Applied Research and Testing in Constructions, National Institute of Research and Development URBAN-INCERC Iasi, a city in the north-east of Romania (Figure 1). The test facility was designed for thermal and airflow investigations of the DSF performance, functioning under natural or mechanical conditions and using various ventilation principles (outdoor air curtain, indoor air curtain, air supply, air exhaust, buffer zone) [37].



(**a**) (**b**)

Figure 1. View of the double-skin façade: (**a**) from the outside of the building and (**b**) from the inside of the interior room.

The experimental double-skin facade measured 2.0 m width by 2.8 m high and included the double skin glass façade and an interior room (Figure 2). The inner skin of the façade was a 24 mm thick double-insulated glass and the outer one was a single 12 mm

thick clear glass pane. The central part of the inner skin was designed to be opened and to facilitate access to the channel for experimental testing, cleaning, and maintenance purposes. The external skin was composed of two fixed parts of simple glazing for reasons of mechanical resistance. The air cavity between the two glazing panes was 0.45 m wide. Two openings were included in the exterior glazing of DSF, one for the air inlet located at the bottom of the façade and one for the air outlet in the upper part. The openings for ventilation with 0.1 m high cover the whole width of the stand.

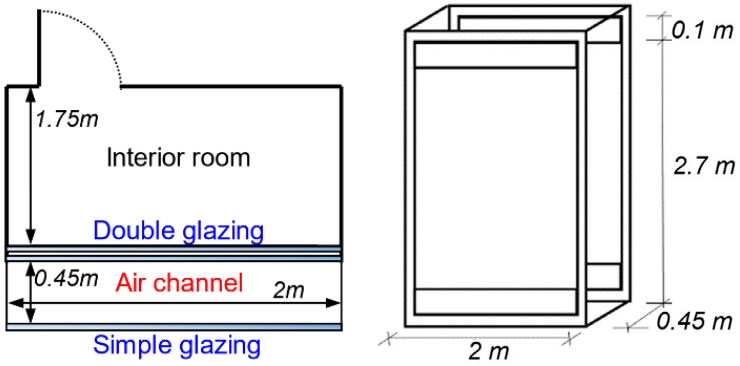


Figure 2. Schematic view of the double-skin façade: horizontal section (**a**) and perspective (**b**).

The interior room measures 2.0 m wide, 2.8 m high, and was 1.75 m in width and was very well insulated to reduce the influence of the indoor environment on the façade (Figure 2a). Using a cooling unit, the temperature of the test chamber was kept constant (27 ± 0.5 °C) starting on day 3 of each summer period (SET1-3). The interior chamber was left unconditioned for the first two days of these periods. For this experiment, no sun-shading device systems were used. The DSF materials and construction details and thermal and optical properties are presented in Table 1.

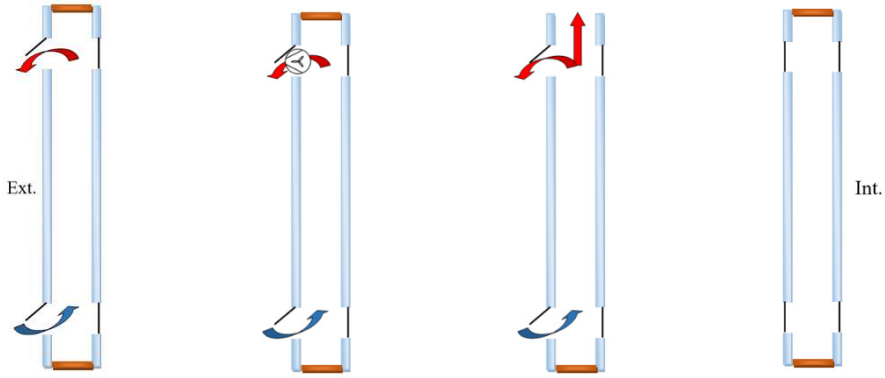
Table 1. Thermal and optical properties of DSF glass.

Component	Properties
Exterior glazing	single pane (8 mm), clear float glass, central glass U-value = 5.6 W/(m^2·K), transmission τ = 82%, absorption α = 11%, solar reflection ρ = 7%.
Exterior frame	aluminum frame with thermal barrier, U-value = 3.1 W/(m^2·K)
Interior glazing	double thermo-insulated pane glazing (4-16-4 mm), clear float glass, low-E coating, central glass U-value = 1.92 W/(m^2·K)
Interior frame	PVC frame with thermal barrier, U-value = 1.42 W/(m^2·K)

The experimental campaigns included four periods specific to the climate in Romania: three periods in the hot season of July corresponding to three modes of air curtain ventilation (ascendant air circulation between the exterior inlet and exterior outlet sections) and one period in the cold season of November for the buffer mode of DSF (closed air channel), Figure 3.

In the first period (SET 1: 7th–13th July), the exterior air inlet and the exterior air outlet were open, and natural ventilation occurred inside the channel.

In the second period (SET 2: 14th–20th July), due to the overheating problem that occurred inside of the DSF channel, the cavity was mechanically ventilated by adding three VORTICE fans in the upper opening of the exterior façade, each with a flow rate of 85 m^3/h (SET 2) and an electrical power of 15 W. The choice of the ventilation air rates was based on the criterion of minimum energy consumption of the fans. A higher air flow rate will cool the channel better but with more energy consumption, which will lower the benefits of the system.



SET 1	SET 2	SET 3	SET 4
07th–13th July	14th–20th July	21th–27th July	24th–30th November
Outdoor air curtain	Outdoor air curtain	Outdoor air curtain	Thermal Buffer
Natural ventilation	Forced ventilation	Natural ventilation	Closed channel

Figure 3. DSF ventilation modes according to the periods of experiments.

To improve the natural ventilation of the channel and eliminate energy consumption for ventilation, in the third period (SET 3: 21st–27th July), the evacuation of air occurs through the exterior air outlet and the upper part of the cavity over its entire section.

In the fourth period of the cold season (SET 4: 24th–30th November), in order to recover the heat loss from the building and to capitalize the solar thermal energy accumulated through the greenhouse effect during the day, the DSF channel was completely closed forming a buffer zone between the building and the exterior air.

2.1. Temperature Measurements

The DSF was equipped with 34 thermocouples type T (copper—constantan) connected to two dataloggers INFOSTAR ISU-L2-C24M with 24 inputs each (Figure 4c), which automatically collected data with a scan rate of 15 min. Thus, 10 thermocouples were used to measure air temperatures and 24 for glass surface temperatures (Figure 4a,b).



(**a**) (**b**) (**c**)

Figure 4. Type T thermocouples on DSF glass surfaces (**a**), thermo-hygrometer KIMO KTH 300 A KISTOCK (**b**), and Datalogger INFOSTAR ISU-L2-C24M (**c**).

The type-T thermocouples for air temperature measurements were placed in three horizontal sections, located at different heights above the floor level (0.5 m, 1.20 m, and 2.15 m, respectively) and 0.5 m from the lateral cavity closures, Figure 5. The air temperatures at the inlet and the outlet of the channel were measured at two points, each with thermocouples of the same type. In addition, the temperatures of the glass surfaces were measured on both sides, towards the air channel and the interior room.

Air temperature in the interior room was measured at 1.25 m from the interior glazing at a height of 1.20 m. To accurately measure the temperatures, the copper—constantan thermocouples were calibrated using the ice bath technique [20], Figure 6a,b.

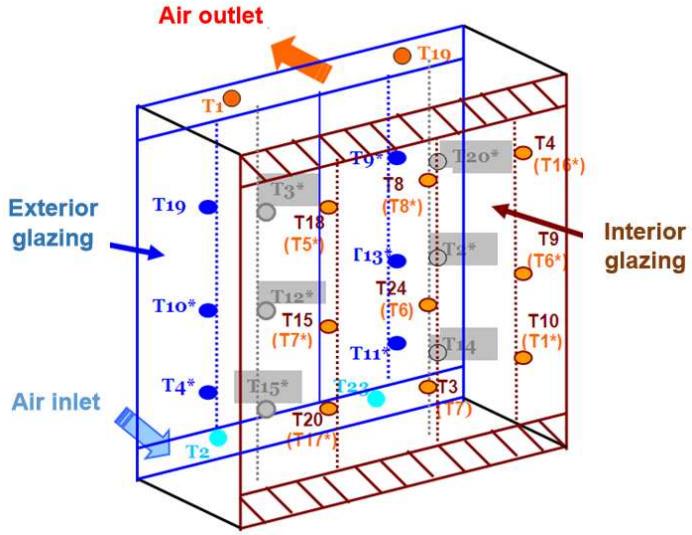
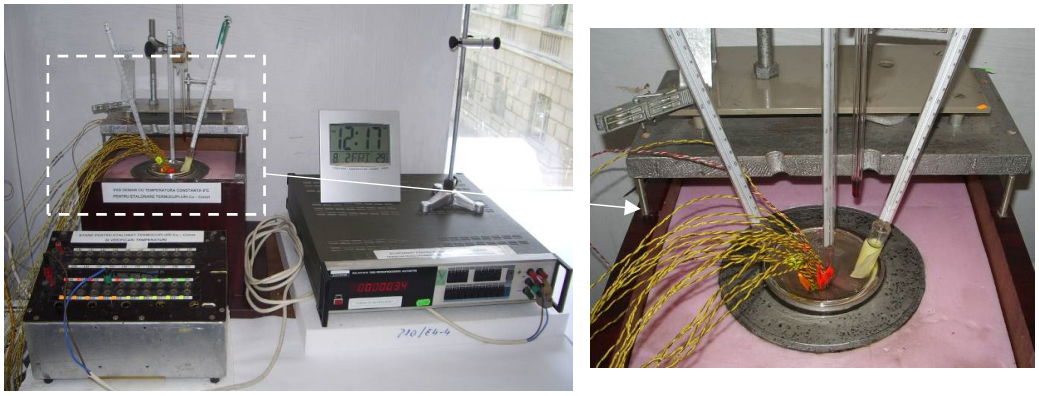


Figure 5. Locations of thermocouples for measuring air and surface temperatures. Air temperatures: T2*, T3*, T12*, T14*, T15*, T20*—inside the DSF channel (T_{cav}); T1, T19—to the exterior outlet from the channel (T_{out}); T2, T23—to the exterior inlet in the channel (T_e). Surface temperatures of the outer glass: T4*, T9*, T10*, T11*, T13*, T19—towards the air channel ($T_{s,e}$). Surfaces temperatures of the inner glass: T3, T4, T8, T9, T10, T15, T18, T20, T24—towards the interior chamber ($T_{s,i,i}$); T1*, T5*, T6, T6*, T7, T7*, T8*, T16*, T17*—towards the air channel ($T_{s,i,e}$).



(**a**) (**b**)

Figure 6. Thermocouple's calibration using an ice bath.

In order to monitor the humidity inside the DSF channel, a thermo-hygrometer KIMO KTH 300A KISTOCK with KILOG software was placed at a height of 1.20 m from the bottom of the channel, Figure 4b.

2.2. Air Velocity Measurements

The air velocities were measured for the three first modes of air curtain ventilation (SET 1–3), inside the DSF channel in three points: at the inlet, in the middle at 1.4 m height, and at the outlet using a multifunctional device KIMO AMI 300 with hot wire probe, Figure 7a–c.

2.3. Measurements of Climatic Parameters

To measure the outdoor temperature, together with the other outdoor climatic parameters (solar radiation, wind speed, and direction), the Meteorological Station Davis Instruments Vantage Pro2 with WeatherLink software was used, located on the building where the experimental facility was built, Figure 8a,b. Meteorological data were collected daily at an interval of 5 min. Still, there were also periods when the weather station did

not make any recordings due to technical problems (fluctuations in power supply, which caused the data console to shut down). The values recorded in the four periods in which the measurements were performed on the experimental stand are presented in Tables 2–5. All three summer periods have approximately the same daily maximum solar irradiation, and the prevailing wind direction is north.



(**a**) (**b**) (**c**)

Figure 7. Air velocity measurement at the inlet in the channel using the hot wire probe.



(**a**) (**b**)

Figure 8. Meteorological Station Davis Instruments Vantage Pro2.

Table 2. Climatic data recorded by the weather station—SET 1: 07th–13th July.

Day	Outside Temperature (°C)			Average Wind Speed (km/h)	Maximum Solar Radiation (W/m^2)	Dominant Wind Direction
	Mean	Low	High			
1	-	-	33.7	2.3	-	NNE
2	30.3	22.7	37.1	0.6	583	NNE
3	30.9	23.4	39.2	1.1	552	NE
4	27.7	22.2	33.9	1.9	544	N
5	26.0	20.4	31.8	1.9	372	N
6	24.4	20.1	34.6	1.3	618	N
7	24.8	17.9	31.8	1.9	569	N

Table 3. Climatic data recorded by the weather station—SET 2: 14th–20th July.

Day	Outside Temperature (°C)			Average Wind Speed (km/h)	Maximum Solar Radiation (W/m^2)	Dominant Wind Direction
	Mean	Low	High			
1	28.7	22.1	35.1	2.3	557	N
2	29.3	21.6	38.5	2.6	624	N
3	22.5	18.6	26.3	4.2	601	N
4	20.9	16.5	27.7	2.3	619	N
5	20.2	15.6	25.7	1.3	700	N
6	24.6	15.0	32.3	1.1	595	N
7	27.9	19.2	34.8	1.3	625	N

Table 4. Climatic data recorded by the weather station—SET 3: 21st–27th July.

Day	Outside Temperature (°C)			Average Wind Speed (km/h)	Maximum Solar Radiation (W/m^2)	Dominant Wind Direction
	Mean	Low	High			
1	27.2	20.2	36.8	2.1	534	N
2	21.1	16.8	27.0	4.2	633	N
3	22.8	17.4	29.1	6.0	629	N
4	25.3	18.6	31.2	4.0	547	N
5	28.2	20.0	35.4	3.2	546	N
6	29.6	20.9	36.4	1.6	552	N
7	28.4	20.3	35.8	1.4	580	N

Table 5. Climatic data recorded by the weather station—SET 4: 24th–30th November.

Day	Outside Temperature (°C)			Average Wind Speed (km/h)	Maximum Solar Radiation (W/m^2)	Dominant Wind Direction
	Mean	Low	High			
1	3.1	2.0	4.4	1.4	25	N
2	3.1	1.9	4.5	1.8	26	SSE
3	5.6	3.7	8.4	0.6	69	N
4	5.2	3.3	6.9	1.8	54	SSE
5	4.7	3.2	6.4	0.6	29	SE
6	6.7	2.4	14.1	3.1	144	N
7	12.2	8.2	16.2	1.0	107	N

3. Results and Discussions

3.1. Temperatures Prediction

Figures 9–12 present for the four periods of measurements and ventilation modes, the variations of the exterior air temperature, which also represents the air temperature at the entrance of the channel (T_e); the average temperature inside the DSF channel (T_{cav}); the temperature difference between the air inlet and outlet openings (DT); for the facade ventilated, respectively, the temperature difference between the air channel and the exterior for the closed façade (DT); the temperature in the interior room (T_i); and the solar radiation intensity (I_t). The air temperatures were calculated as the average of the values measured in different points inside the channel (T2*, T3*, T12*, T14*, T15*, T20*), inlet section (T2, T23), and outlet section (T1, T19), Figure 5.

The monitoring results show that for the first ventilation scenario (SET 1, Figure 9), the maximum air temperature (T_{cav}) inside the channel reaches 47.4 °C on the third day (13:00 p.m.) for an exterior temperature (T_e) of 37.6 °C and a solar radiation intensity (I_t) of 533 W/m^2, which is due to the greenhouse effect between the two layers of glass. The minimum value recorded inside the channel is 21.3 °C (6th day, 5:00 a.m.) when the exterior one is 20.3 °C. It can be observed that daily, the two temperatures are almost equal between 06:00 p.m. and 6:00 a.m. and a maximum difference of about 10–13 °C is recorded around noon (10:00 a.m.–02:00 p.m.), depending on the day, when the DSF channel becomes

overheating. This justifies the introduction of Venetian blinds inside the channel to reduce the heating of interior room from solar radiation [9]. The average value of the air inside the channel, T_{cav} for the entire period is 31.8 °C compared with the exterior one of 27.5 °C, for a wind speed of 1.6 km/h (N-NE direction). The average air relative humidity inside the channel has typical a value of 47%. The temperature inside the adjacent room of DSF (T_i) in the first two days without conditioning follows the variation of T_{cav} and T_e with an average value of 31.5 °C. Even if the exterior and the channel temperatures drop between 09:00 p.m. and 10:00 a.m., the air temperature of the interior room decreases very slowly at a minimum of 29.7 °C.

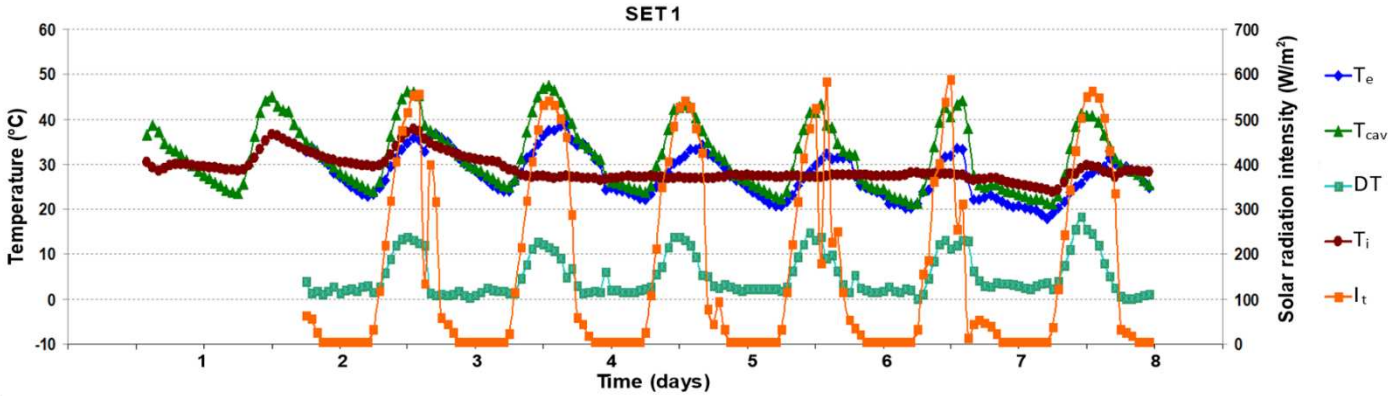


Figure 9. Evolution of air temperatures and solar radiation intensity in the first period (07th–13th July), outdoor air curtain, natural ventilation.

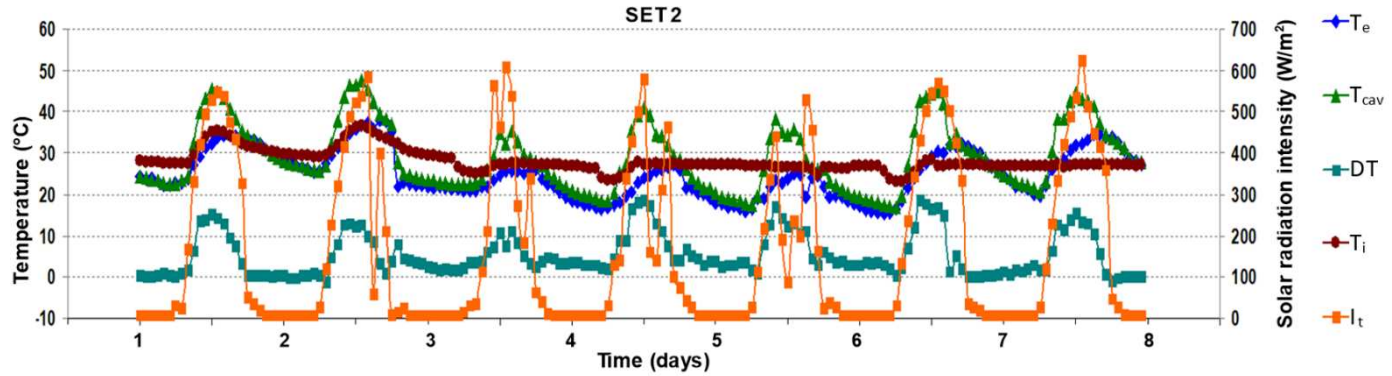


Figure 10. Evolution of air temperatures and solar radiation intensity in the second period (14th–20th July), outdoor air curtain, forced ventilation.

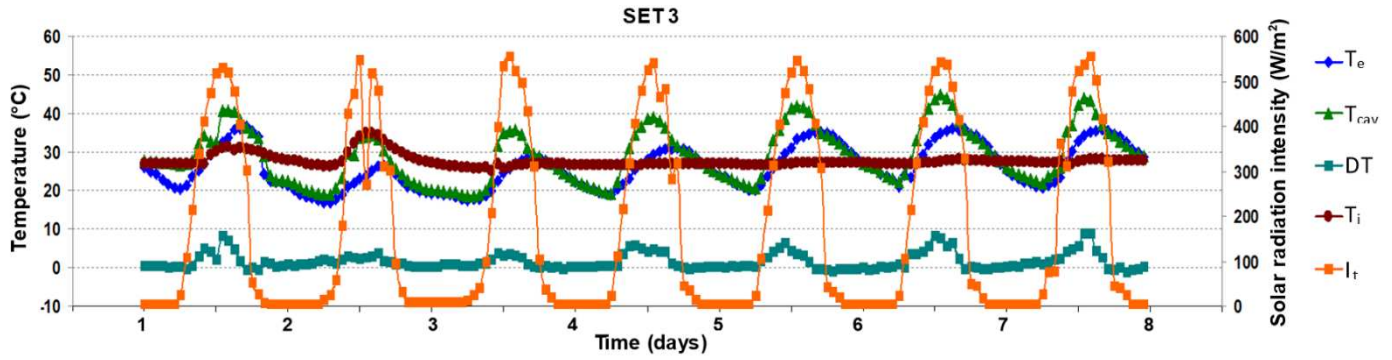


Figure 11. Evolution of air temperatures and solar radiation intensity in the third period (21th–27th July), outdoor air curtain, natural ventilation.

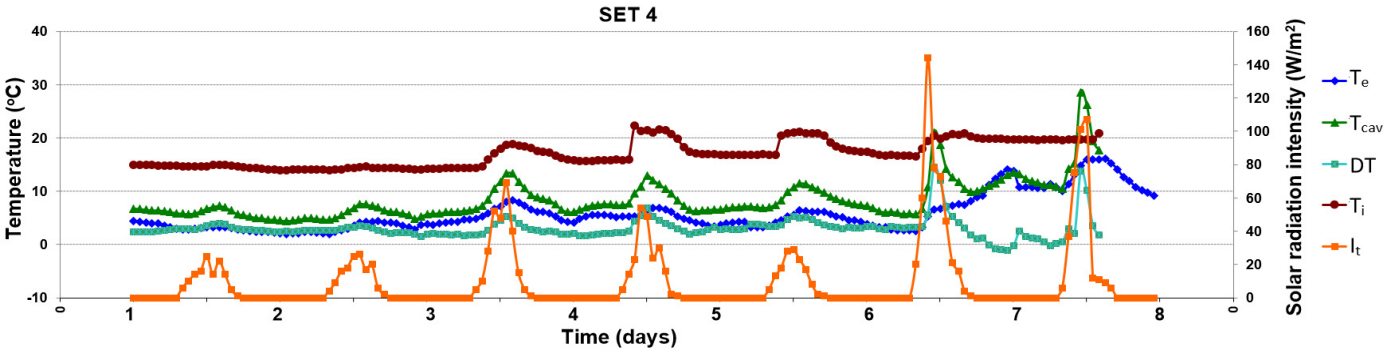


Figure 12. Evolution of air temperatures and solar radiation intensity in the fourth period (24th–30th November), thermal buffer, closed channel.

To facilitate the heat removal from the DSF channel, in the second period of measurements (SET 2, Figure 10) forced ventilation was chosen. The results show that the temperature variation inside the channel is closely related to the exterior ones with a maximum value of 47.7 °C on the second day (01:00 p.m.) for an exterior temperature (T_e) of 36.8 °C and a solar radiation intensity (I_t) of 540 W/m^2. This shows that forced ventilation does not have a significant impact on the temperature reduction inside the channel in the overheating period of 10:00 a.m.–02:00 p.m. when the average difference between the exterior ones remains around 12 °C. The minimum value recorded inside the channel was 16.8 °C (sixth day, 6.00 a.m.) when the exterior one has the same value. Compared to the SET1, the introduction of the three ventilators in the lateral outlet of the exterior glazing facilitate the channel temperatures to reach the exterior ones rapidly for a more extended period, between 04:00 p.m. and 08:00 a.m., and a drop of the solar intensity has a quick impact on them. The average air relative humidity inside the channel is recorded to be 48.3%, and the average value of the air temperature inside the channel, T_{cav} for the entire period is 29.0 °C for an exterior one of 24.9 °C and a wind speed of 2.2 km/h (N direction).

In the third ventilation scenario (SET 3, Figure 11) of summer conditions, two openings at the top of the channel were chosen (lateral and vertical) to naturally ventilate the DSF channel. In this case, the temperature difference between the channel and the ambient reaches small values of 7–10 °C between 10:00 a.m.–02:00 p.m. The maximum air temperature (T_{cav}) inside the channel reaches 44.8 °C on the sixth day (01:00 p.m.) for an exterior temperature (T_e) of 34.9 °C and a solar radiation intensity (I_t) of 545 W/m^2. The average value of the air inside the channel, T_{cav}, for the entire period is 29.08 °C compared with the exterior one of 26.07 °C with a difference of 3 °C, smaller than the first natural ventilation with one lateral opening, in the same weather conditions. The temperatures inside the channel and the exterior ones have almost the same value between 04:00 p.m. and 8:00 a.m. with an average difference of 1 °C, thus reducing the period of channel overheating. Compared to forced ventilation, the change in solar radiation intensity during the day has less impact on the temperatures of the DSF channel. The minimum value recorded inside the channel is 18.5 °C (3rd day) at 6:00 a.m. when the exterior one is 17.6 °C. The average air relative humidity inside the channel is comparable with the previous ones for the summer season of 47.8%. A time shift of approximately one hour exists between the highest solar radiation and the maximum temperature recorded in the channel [38].

Results for the first three ventilation scenarios during the summer season are synthesized in Table 6.

In the cold season in November (SET 4, Figure 12), the lateral and vertical openings are closed, and the channel façade behave like a thermal buffer. The aim was to recover the heat from inside the building and to valorize the greenhouse effect from solar radiation. Thus, it can be observed that the temperatures inside the DSF channel are more significant than the exterior ones with an average value of 2.2 °C for smaller solar radiation intensity of around 20 W/m^2 (8:00 a.m.–04:00 p.m.) in the first four days of the monitored period. On days 5 and 6, when the solar radiation intensity has maximum values around 12:00 a.m.

(144 W/m^2), the temperature inside the channel reaches 21.1 °C for an exterior one of 6.6 °C. Also, in this period of a day, the temperature inside the DSF adjacent chamber, where no conditioning system is functioning, reaches a comfort zone of 20 °C. During the night, T_{cav} records an average of 7 °C for an exterior one of 5 °C, and the temperature inside the interior room is around 16 °C. During the cold season, the time shift between the glass and cavity temperature is less than one hour, because of the small thermal mass available.

Table 6. Synthesized results of the ventilation scenarios during the summer season.

	SET 1 **07th–13th July**	**SET 2** **14th–20th July**	**SET 3** **21th–27th July**
$T_{cav\ max}$ (°C)	47.4 (3rd day, 01:00 p.m.)	47.7 (2nd day, 01:00 p.m.)	44.8 (6th day, 01:00 p.m.)
T_e (°C)	37.6 (3rd day, 01:00 p.m.)	36.8 (2nd day, 01:00 p.m.)	34.9 (6th day, 01:00 p.m.)
I_t (W/m^2)	533 (3rd day, 01:00 p.m.)	540 (2nd day, 01:00 p.m.)	545 (6th day, 01:00 p.m.)
$T_{cav\ min}$ (°C)	21.3 (6th day, 5:00 a.m.)	16.8 (6th day, 06:00 a.m.)	18.5 (3rd day, 06:00 a.m.)
$DT_{10:00a.m.–14:00p.m.}$ (°C)	10–13	11–12	7–10
$T_{cav\ average}$ (°C)	31.8	29.0	29.1
$T_{e\ average}$ (°C)	27.5	24.9	26.1
$v_{wind\ average}$ (km/h)	1.6 (N-NE)	2.2 (N)	3.2 (N-SSE)
$\%RH_{average}$	47%	48.3%	47.8%

In this particular case of no ventilation, the channel's humidity plays an essential role because of the condensation risk. Thus, the average recorded value of the relative air humidity recorded in the DSF channel was 80%, with a maximum of 94.9%, Figure 13. It can be seen that the humidity has more significant values during the night and morning when the temperatures are lowered, favoring the appearance of condensation on the DSF surfaces inside the channel, Figure 14.

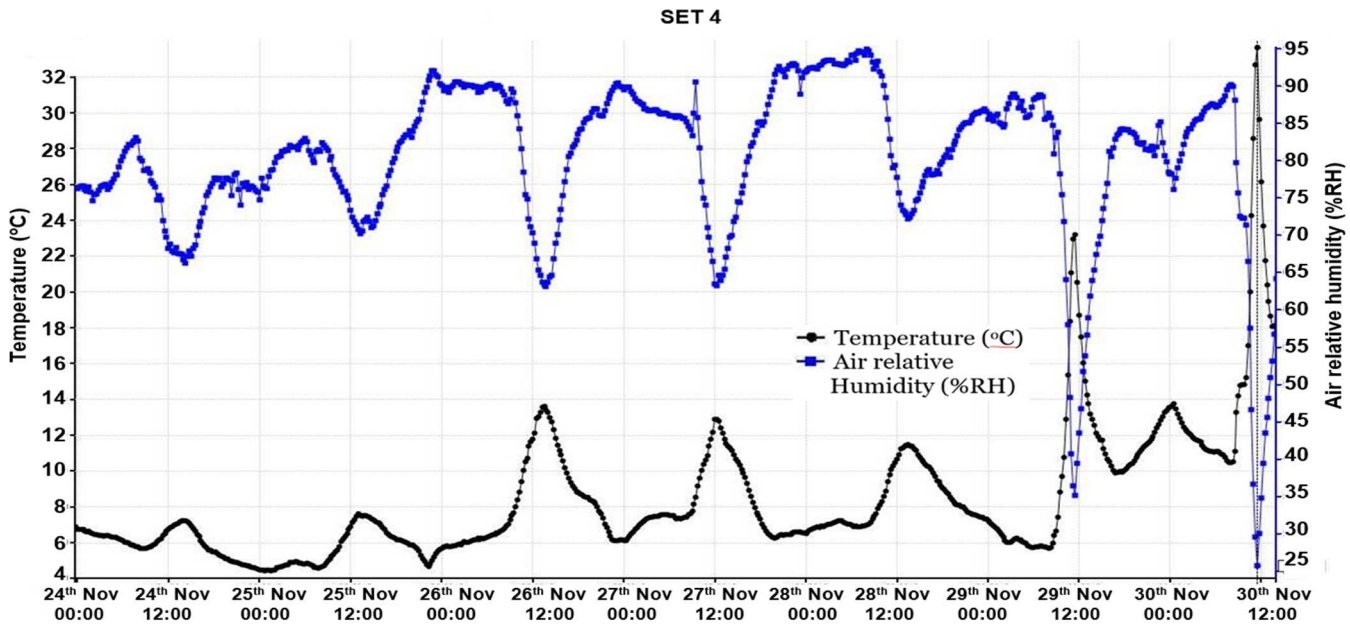


Figure 13. Evolution of air temperatures and relative humidity in the fourth period of cold season.

Figures 15–18 present for the four periods of measurements and ventilation modes, the variations of the exterior air temperature (T_e), the surface temperature of the outer glass ($T_{s,e}$), the average temperature inside the DSF channel (T_{cav}), the surface temperature of the inner glass towards the air channel ($T_{s,i,e}$) and towards the interior chamber ($T_{s,i,i}$), the temperature in the interior room (T_i), and the solar radiation intensity (I_t). The surface temperatures averaged over the height of the channel on the outer glass at six points (T4*,

T9*, T10*, T11*, T13*, T19), on the inner glass at nine points (T1*, T5*, T6, T6*, T7, T7*, T8*, T16*, T17*), and on the surface of the inner glass inside the chamber at nine points (T3, T4, T8, T9, T10, T15, T18, T20, T24), Figure 5.



(**a**) (**b**)

Figure 14. Condensation phenomena inside the DSF channel (**a**) exterior glazing—view from inside the channel, (**b**) interior glazing—view from inside the interior room.

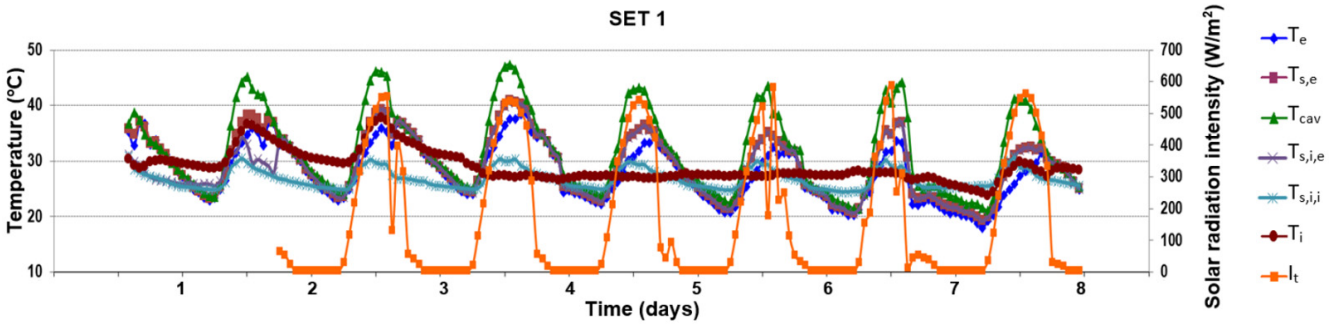


Figure 15. Evolution of surface temperatures and solar radiation intensity in the first period (07th–13th July), outdoor air curtain, natural ventilation.

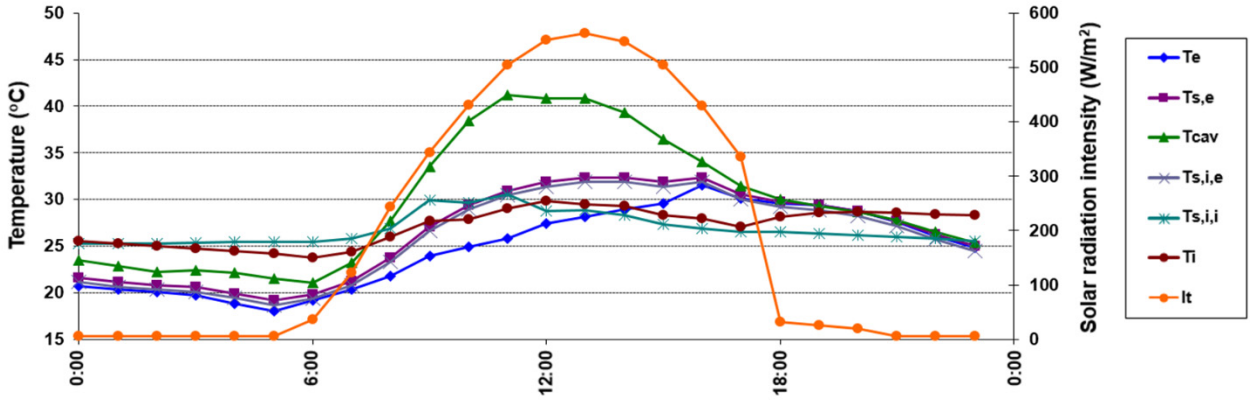


Figure 16. Temporal distribution of the surface temperatures during the first period for the seventh day (13th July).

The first scenario of natural ventilation with lateral openings (SET 1) is presented in Figure 15. During the day, the surface temperatures are highly correlated with solar radiation. The surface temperature of the DSF channel side of the exterior glazing ($T_{s,e}$) is lower than the air inside the channel (T_{cav}) and more significant than the exterior (T_e) one between 08:00 a.m. and 16:00 p.m. and almost the same during the night with an average difference of 1.2 °C. This tendency can also be observed in Figure 16, which presents the thermal distribution during the 7th day of the first scenario. Both interior surfaces $T_{s,e}$ and

$T_{s,i,e}$ have almost equal temperatures. The air inside the channel (T_{cav} = 41.2 °C) becomes warmer than the exterior glazing ($T_{s,e}$ = 30.9 °C) during the high values of solar radiation between 08:00 a.m. and 16:00 p.m. with a maximum difference of 10.3 °C in the seventh day (11:00 p.m.) for an exterior temperature (T_e) of 25.8 °C and a solar radiation intensity (I_t) of 504 W/m^2. An average value for the entire period of 29.3 °C is recorded for both glazing surfaces inside the channel ($T_{s,e}$ and $T_{s,i,e}$), situated between the air temperature inside the channel, T_{cav} of 31.4 °C and the exterior one of 28.0 °C. Because of the low interior double glazing U-factor, the interior surface temperature ($T_{s,i,i}$) is lower with 2 °C, tempering the indirect solar gains.

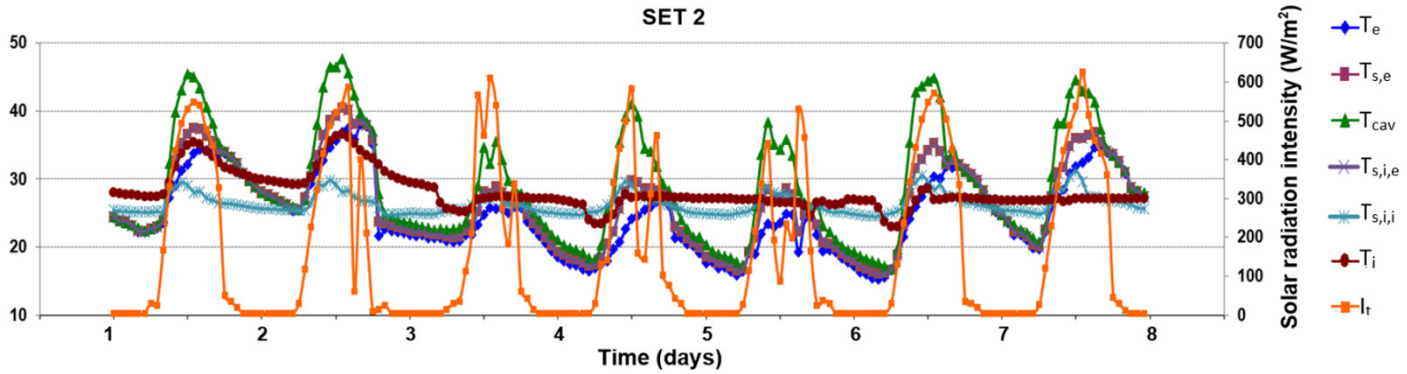


Figure 17. Evolution of surface temperatures and solar radiation intensity in the second period (14th–20th July), outdoor air curtain, forced ventilation.

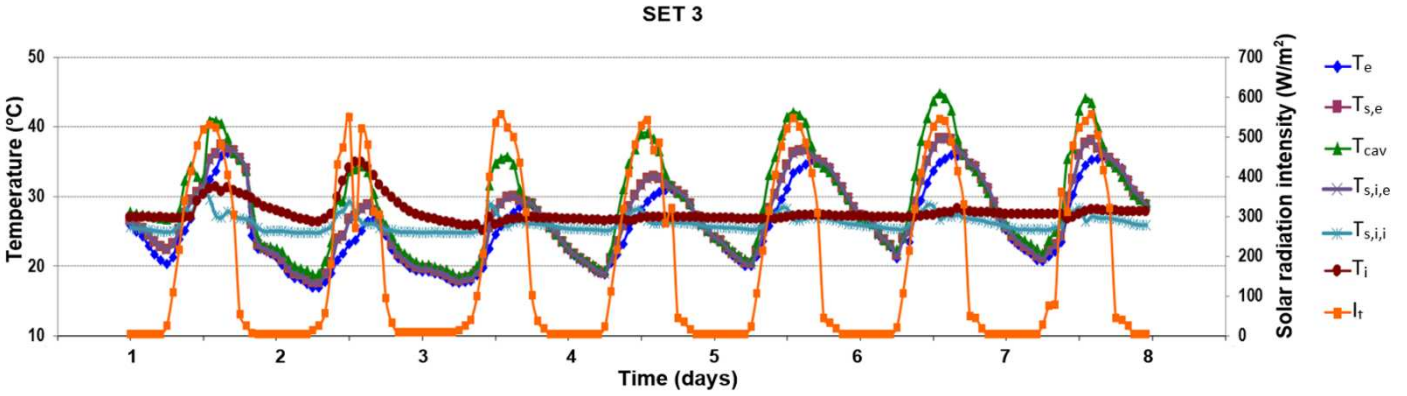


Figure 18. Evolution of surface temperatures and solar radiation intensity in the third period (21st–27th July), outdoor air curtain, natural ventilation.

During the second measurement period (SET 2, Figure 17), the forced ventilation does not change the variation tendency of surfaces temperatures inside DSF. The average difference between the surface temperatures and the air inside the channel is 2.8 °C higher for the last one, compared with the first scenario of 2.5 °C. This is because the temperature on the glass surface inside the room is lower than the room air and depends on direct solar radiation. The maximum recorded difference of 11.3 °C between the interior surfaces $T_{s,e}$ and $T_{s,i,e}$ inside the DSF channel and the air inside was recorded during the day at 11:00 a.m., when the air inside the DSF channel heats up due to the greenhouse effect. An average value for the entire period of 26.3 °C is recorded for $T_{s,e}$ and $T_{s,i,e}$, relative to the air channel, T_{cav} of 29.0 °C, and the exterior one of 24.9 °C.

In the third ventilation scenario (SET 3, Figure 18) of summer conditions, a maximum difference of 7.3 °C of the air channel is reached relative to the exterior glazing on the fourth day of measurements at 12:00 p.m., smaller than in the first two monitoring periods. The temperatures of the glass surfaces are higher relative to the ones of the exterior air

and lower than ones of the cavity air, during the direct solar radiation, between 07.00 a.m. and 04:00 p.m., when they become almost equal. In this period, an average of 27.1 °C is recorded for glass surfaces relative to the air temperature inside the channel of 29.1 °C and to the exterior one of 26.1 °C.

In the specific functioning of the fourth ventilation scenario (SET 4, Figure 19) during the cold season, the surface of the double glazing towards the channel $T_{s,i,e}$ is warmer than the exterior side of the channel ($T_{s,e}$), which is due to the heat loses from the interior room. The difference reached a maximum value of 13.7 °C ($T_{s,i,e}$ = 19.7 °C and $T_{s,e}$ = 6 °C) at 10:00 a.m. on the fifth day of the monitored period for an exterior air temperature T_e of 4.6 °C and the air channel T_{cav} of 8.3 °C.

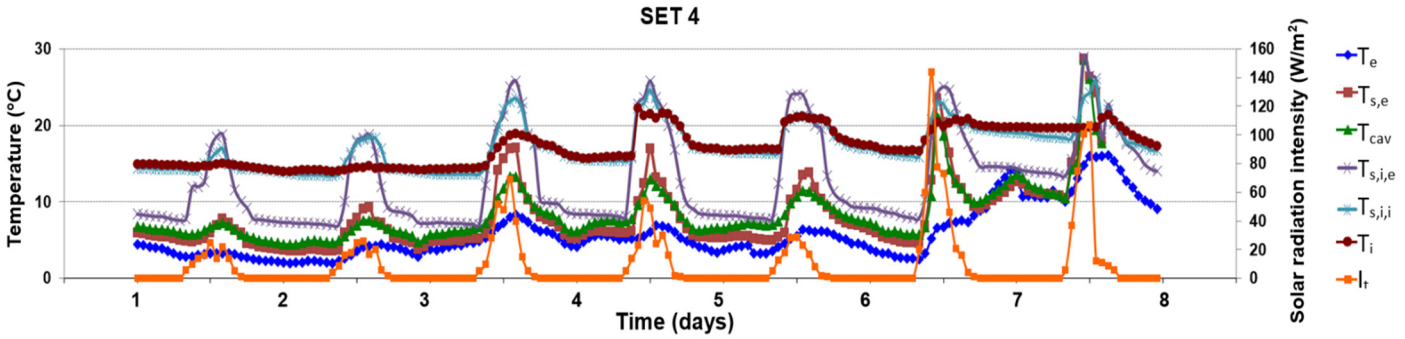


Figure 19. Evolution of surface temperatures and solar radiation intensity in the fourth period (24th–30th November), thermal buffer, closed channel.

For a smaller solar radiation intensity of around 20 W/m^2, between 8:00 a.m. and 04:00 p.m., the average difference of these two surfaces ($T_{s,i,e}$ and $T_{s,e}$) is 7.6 °C, higher near the interior room whose temperature is around 20 °C. During the night, this difference decreases by almost half at 2.8 °C in the conditions of the temperature inside the room of 16.3 °C. Between 10:00 a.m. and 02:00 p.m., due to the direct solar radiation on the exterior glazing, the surface temperature $T_{s,e}$ exceed the cavity one by almost 2 °C. The same for the glazing surface from the interior room, $T_{s,i,I}$, which is warmer than the air only during this period with a difference of 2.4 °C. Minimum values of temperatures are recorded during the night and in the morning on the exterior glazing inside the DSF channel (around 6 °C for an exterior of 5 °C), which favors the appearance of condensation, Figure 14.

3.2. Airflow Prediction

Velocity profiles are presented in Figure 20 for the first three scenarios of the outdoor air curtain in the summer season (SET 1–3: 7th–27th July). Each velocity profile is represented in correlation with other parameters that influence the operation of the facade, namely the wind speed, the exterior temperature, and the air temperature inside the DSF channel. The velocities were measured at three points at different heights in the channel: in the middle of the inlet section (h = 0.05 m), in the middle of the channel (h = 1.4 m), and in the middle of the outlet section (h = 2.75 m). The results in each measurement point and the correlation with the day and time are presented in Tables 7–9 for each period (SET 1–3).

Due to the more significant section of flow, in the middle of the DSF channel, the air velocities are lower relative to the inlet and the outlet of the façade, Figure 20. This is also caused by turbulences observed in the middle section with recirculation zones near the outside glazing of the DSF channel, Figure 21. Visualizations of the airflow pattern (Figure 21) were realized in forced convection using a laser plane (532 nm Green DPSS Laser 1000 mW) and a camera (Nikon D60 with 3.0 frames per second) inside the median section of the channel, where, at the left side is the interior double glazing and at the right side is the exterior single one. Thus, the obtained qualitative results in terms of airflow patterns highlight an ascendant flow near the interior double glazing of the DSF channel

and a descendant one near the exterior glazing, which validates the numerical results obtained in the previous works [37,39].

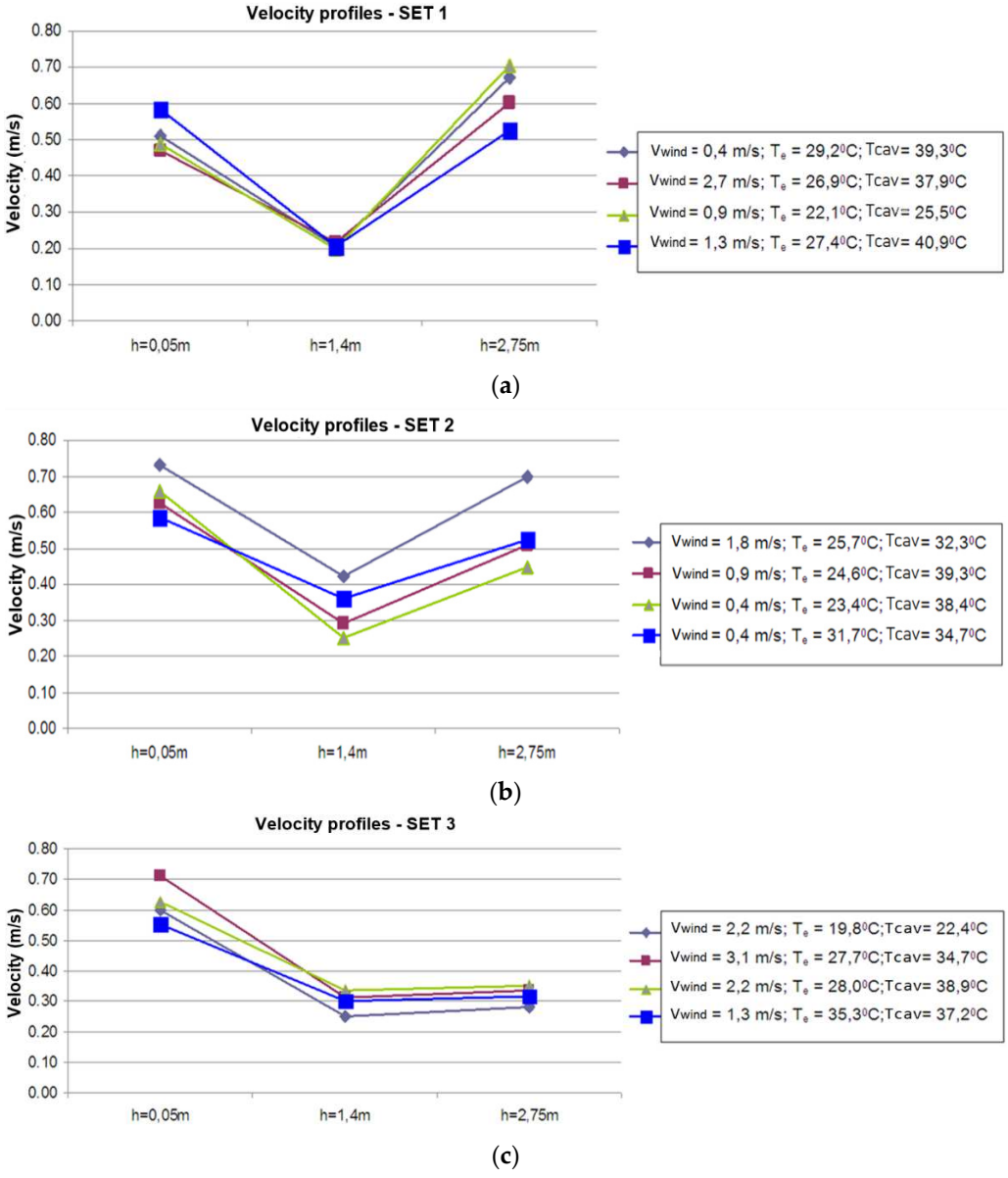


Figure 20. Air velocity profiles inside the DSF channel for ventilation modes of summer conditions: (**a**) SET 1-natural ventilation with lateral opening, (**b**) SET 2-forced ventilation with lateral opening, (**c**) SET 3-natural ventilation with vertical and lateral openings.

Due to the vertical and lateral openings, the velocities in the third scenario are lower relative to the first two ones, Figure 20. The forced ventilation mode determines the turbulent character of the flow in the middle of the channel with a variation of velocities between 0.25–0.42 m/s (Figure 20b). In the natural airflow ventilation scenarios (Figure 20a,c), the velocities inside the channel are almost constant for the lateral openings and a slight variation of 0.25–0.31 m/s for the lateral and vertical openings. This is because the air velocity at the inlet section depends on the wind speed and a higher temperature of the air inside the channel determines higher velocities in natural convection.

Table 7. Air velocities at different heights in the DSF channel for SET 1: 07th–13th July.

Day Hour	Measuring Point	Air Velocity, v (m/s)			v_{med} (m/s)	Q_v (m^3/h)	V_{wind} (m/s)	T_e (°C)	T_{cav} (°C)
12 July 10:00	Inlet	0.41	0.6	0.52	0.51	367	0.4	29.2	39.3
	h = 1.4 m	0.23	0.21	0.18	0.21	-			
	Outlet	0.62	0.68	0.72	0.67	482			
12 July 15:00	Inlet	0.36	0.51	0.54	0.47	338	2.7	26.9	37.9
	h = 1.4 m	0.23	0.22	0.2	0.22	-			
	Outlet	0.6	0.52	0.68	0.60	432			
12 July 17:00	Inlet	0.43	0.56	0.47	0.49	353	0.9	22.1	25.5
	h = 1.4 m	0.2	0.21	0.18	0.20	-			
	Outlet	0.74	0.65	0.72	0.70	504			
13 July 12:00	Inlet	0.59	0.52	0.64	0.58	418	1.3	27.4	40.9
	h = 1.4 m	0.23	0.21	0.18	0.21	-			
	Outlet	0.4	0.56	0.61	0.52	374			

Table 8. Air velocities at different heights in the DSF channel for SET 2: 14th–20th July.

Day Hour	Measuring Point	Air Velocity, v (m/s)			v_{med} (m/s)	Q_v (m^3/h)	V_{wind} (m/s)	T_e (°C)	T_{cav} (°C)
16 July 13:00	Inlet	0.68	0.79	0.72	0.73	526	1.8	25.7	32.3
	h = 1.4 m	0.39	0.42	0.46	0.42	-			
	Outlet	0.69	0.69	0.71	0.70	504			
17 July 13:00	Inlet	0.57	0.63	0.68	0.63	454	0.9	24.6	39.3
	h = 1.4 m	0.31	0.35	0.21	0.29	-			
	Outlet	0.42	0.58	0.53	0.51	367			
18 July 10:00	Inlet	0.66	0.64	0.68	0.66	475	0.4	23.4	38.4
	h = 1.4 m	0.23	0.25	0.27	0.25	-			
	Outlet	0.45	0.49	0.4	0.45	324			
19 July 16:00	Inlet	0.57	0.58	0.61	0.59	425	0.4	31.7	34.7
	h = 1.4 m	0.31	0.35	0.42	0.36	-			
	Outlet	0.52	0.49	0.56	0.52	374			

Table 9. Air velocities at different heights in the DSF channel for SET 3: 21th–27th July.

Day Hour	Measuring Point	Air Velocity, v (m/s)			v_{med} (m/s)	Q_v (m^3/h)	V_{wind} (m/s)	T_e (°C)	T_{cav} (°C)
23 July 10:00	Inlet	0.61	0.58	0.61	0.60	432	2.2	19.8	22.4
	h = 1.4 m	0.22	0.29	0.24	0.25	-			
	Outlet	0.26	0.28	0.31	0.28	2268			
23 July 15:00	Inlet	0.71	0.74	0.68	0.71	511	3.1	27.7	34.7
	h = 1.4 m	0.31	0.28	0.35	0.31	-			
	Outlet	0.37	0.36	0.28	0.34	1652			
24 July 12:00	Inlet	0.64	0.56	0.68	0.63	454	2.2	28	38.9
	h = 1.4 m	0.3	0.42	0.29	0.34	-			
	Outlet	0.4	0.32	0.34	0.35	2138			
25 July 16:00	Inlet	0.56	0.61	0.49	0.55	396	1.3	35.3	37.2
	h = 1.4 m	0.29	0.35	0.27	0.30	-			
	Outlet	0.31	0.35	0.29	0.32	1912			

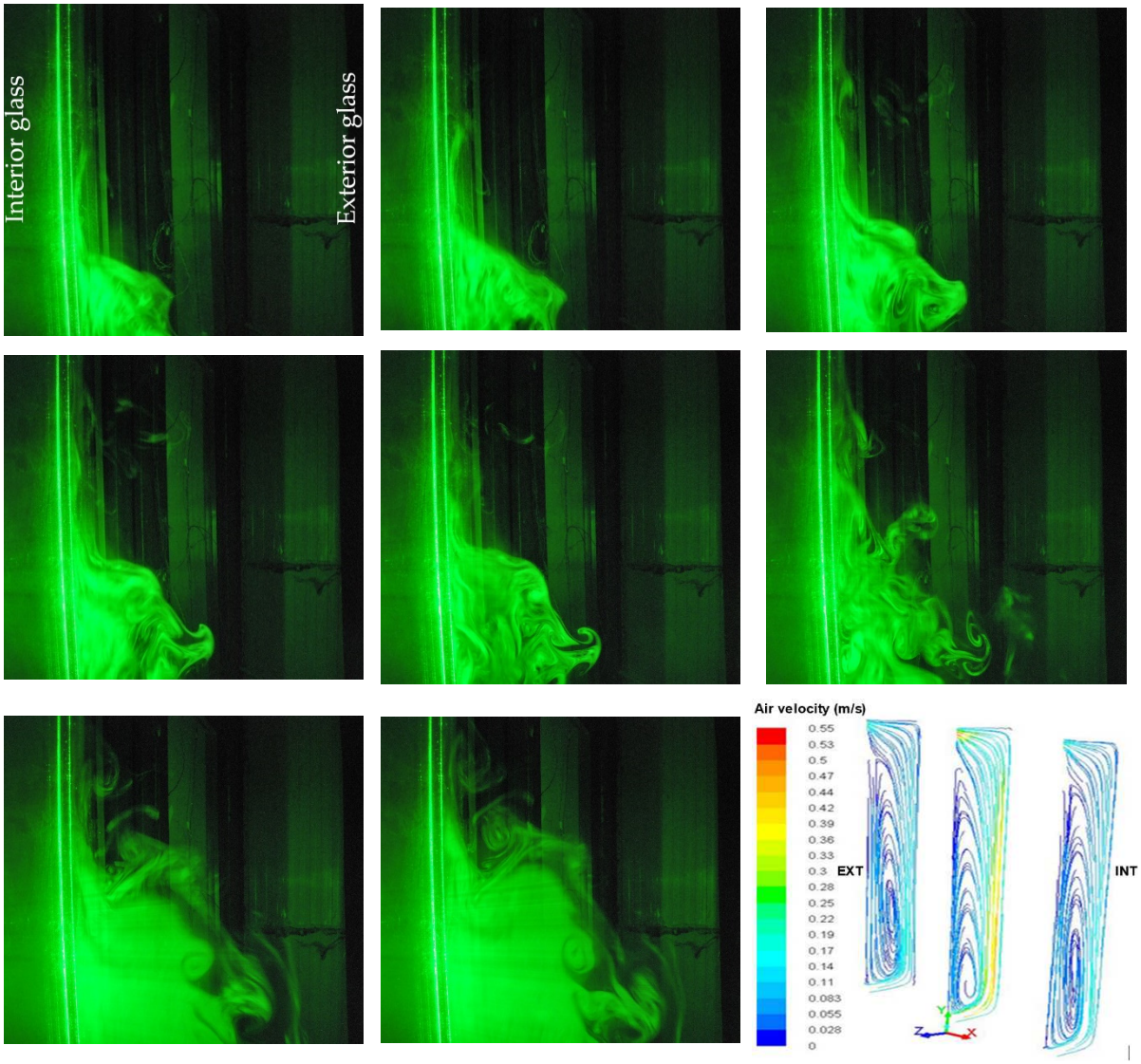


Figure 21. Visualization of airflow patterns in the median section of the double-skin façade channel compared to the numerical ones [37].

3.3. Energy Efficiency

Two different kinds of efficiency have been defined in order to assess the performance of the double-skin façade in terms of energy savings [1]:

- Pre-heating efficiency, η, and
- Dynamic insulation efficiency, ε.

The pre-heating efficiency, η, assesses the capacity of the façade to pre-heat the ventilation air flow rate during the cold season (heating periods) and is defined as:

$$\eta = \frac{T_{exh} - T_i}{T_i - T_e}. \quad (1)$$

where:

T_{exh}—temperature of the air exhaust (exiting from the façade), °C.
T_i—air temperature inside the room, °C.
T_e—exterior air temperature, °C.

The dynamic insulation efficiency, ε, is defined as the quota of the heat flux that enters through the outer surface of the façade in the hot season during the cooling period:

$$\varepsilon = \frac{\dot{Q}_r}{\dot{Q}_{inc}} \tag{2}$$

where $\dot{Q}_r$ is the heat flux removed by the air flowing through the façade, W, Equation (3):

$$\dot{Q}_r = \dot{m}_v \cdot c_p \cdot (T_{exh} - T_e) \tag{3}$$

where: $\dot{m}_v = v \cdot S \cdot \rho$ ventilation air mass flow rate inside the DSF channel (kg/s); c_p, ρ, specific heat of the air (1005 J/kg K) and the air density (1.165 kg/m^3).

The heat flux entering through the outside facing surface of the façade, $\dot{Q}_{inc}$ (W) is defined by Equation (4):

$$\dot{Q}_{inc} = \dot{Q}_S + \dot{Q}_i + \dot{Q}_r = I \cdot \tau_i \cdot A + U \cdot A \cdot (T_{exh} - T_i) + \dot{Q}_r \tag{4}$$

where: τ_i solar transmission coefficient through exterior and interior glazings (0.42); A area of the facade module (5.2 m^2); U overall heat transfer coefficient through the double glazing (1.92 W/m^{2}K, Table 1).

Finally, the equation of the dynamic insulation efficiency can be written as [1,40]:

$$\varepsilon = \frac{\dot{m}_v \cdot c_p \cdot (T_{exh} - T_e)}{I \cdot \tau_i \cdot A + U \cdot A \cdot (T_{exh} - T_i) + \dot{m}_v \cdot c_p \cdot (T_{exh} - T_e)} \tag{5}$$

Figure 22 presents the variation of the pre-heating efficiency, η, during the cold season (SET 4) when the channel is closed, and the double skin-façade behaves like a thermal buffer. The negative values of the pre-heating efficiency mean that the air temperature that exits from the ventilated facade, T_{exh}, is lower than the temperature of the indoor air, T_i, and there is no energy recovery. In this condition, the only benefit obtained from the ventilated façade is to increase the surface temperature of the inner glass pane inside the channel (Figure 19) and reduce the heat loss from the interior room. When $0 < \eta < 1$ during the last two days of higher solar radiation at noon (29th and 30th November, Figure 22), the air that exits from the façade is preheated at a temperature which is higher than the indoor one but the ventilation air still requires extra heating before being introduced into the room. A maximum value of 1.83 of the pre-heating efficiency is reached at 11:00 a.m. on the seventh day, for a maximum air temperature inside the DSF channel of 28.6 °C, which is higher than the interior one of 19.7 °C, solar radiation intensity of 101 W/m^2 and an ambient air temperature of 14.8 °C. At this moment, the façade heats the ventilation air to a higher temperature than the indoor temperature. Therefore, it allows the complete compensation of ventilation losses and the partial compensation of other thermal losses through the building elements.

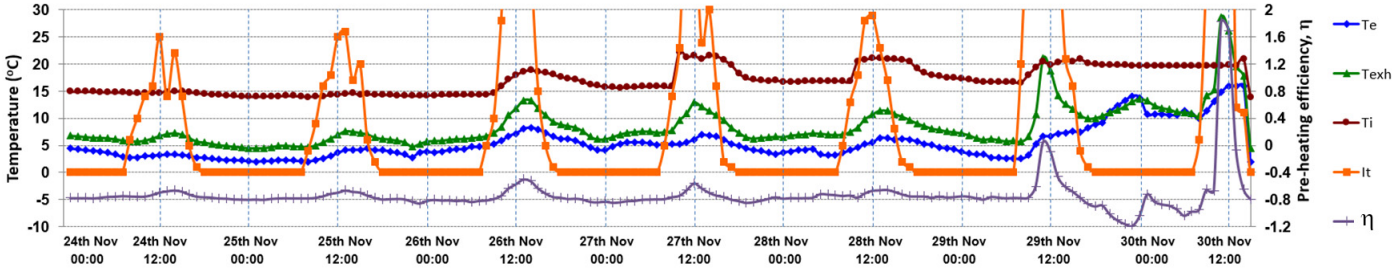


Figure 22. Pre-heating efficiency of DSF in the fourth period (24th–30th November) of cold season (thermal buffer, closed channel).

During the hot season, the dynamic insulation efficiency represents the quota of the heat flux removed by the air flowing inside the DSF channel compared to the total heat flux that enters through the outer glass pane. The results are presented in Tables 10–12 for the three ventilation modes (SET 1–3) when the velocities inside the channel were measured. The measurements of air velocities were performed at representative values of solar intensity and exterior and cavity temperatures.

Table 10. Dynamic insulation efficiency for the first ventilation mode (SET 1: 07th–13th July).

Day Hour	v_{med} (m/s)	T_e (°C)	T_{exh} (°C)	I_t (W/m^2)	$\dot{m}_v$ (kg/s)	Qr (W)	Qs (W)	Qi (W)	$Qinc$ (W)	ε (%)
12 July 10:00	0.46	29.2	39.3	402	0.11	1096	878	123	2097	**52.3**
12 July 15:00	0.43	26.9	37.9	14	0.10	1108	31	109	1247	**88.8**
12 July 17:00	0.46	22.1	25.5	54	0.11	369	118	−15	472	**78.2**
13 July 12:00	0.44	27.4	40.9	550	0.10	1380	1201	139	2720	**50.7**

Table 11. Dynamic insulation efficiency for the second ventilation mode (SET 2: 14th–20th July).

Day Hour	v_{med} (m/s)	T_e (°C)	T_{exh} (°C)	I_t (W/m^2)	$\dot{m}_v$ (kg/s)	Qr (W)	Qs (W)	Qi (W)	$Qinc$ (W)	ε (%)
16 July 13:00	0.62	25.7	32.3	610	0.14	953	1332	53	2338	**40.8**
17 July 13:00	0.48	24.6	39.3	160	0.11	1641	349	123	2113	**77.7**
18 July 10:00	0.45	23.4	38.4	442	0.11	1592	965	114	2671	**59.6**
19 July 16:00	0.49	31.7	34.7	425	0.11	344	928	77	1349	**25.5**

Table 12. Dynamic insulation efficiency for the third ventilation mode (SET 3: 24th–30th July).

Day Hour	v_{med} (m/s)	T_e (°C)	T_{exh} (°C)	I_t (W/m^2)	$\dot{m}_v$ (kg/s)	Qr (W)	Qs (W)	Qi (W)	$Qinc$ (W)	ε (%)
23 July 10:00	0.38	19.8	22.4	207	0.48	1261	452	−46	1667	**75.6**
23 July 15:00	0.45	27.7	34.7	499	0.58	4087	1090	77	5254	**77.8**
24 July 12:00	0.44	28.0	38.9	527	0.56	6177	1151	119	7447	**82.9**
25 July 16:00	0.39	35.3	37.2	408	0.50	954	891	102	1947	**49.0**

For lower values of solar radiation intensity and ambient air temperature and higher ones for the air flow rate inside the channel, the dynamic insulation efficiency has the highest importance. An average dynamic insulation efficiency of 71.3% was recorded for the natural ventilation with both openings on the lateral outer glass and the vertical one in the top of the channel (Table 12), relative to the first scenario with natural ventilation of 67.5% (Table 10) and the second one with forced ventilation of 50.9% (Table 11). Thus, in order to prevent the overheating of the façade during the hot season, combining vertical and horizontal openings in natural ventilation gives the best efficiency of the double-skin facade functioning.

4. Conclusions

In this work, the thermodynamic behavior of a double skin façade (DSF) and performance assessment in terms of pre-heating efficiency during the cold season and the dynamic insulation efficiency during the hot one is studied using an experimental measurement campaign in specific climate conditions of Romania. Experimental work was done on naturally and mechanically ventilated single-story DSF built on southwest façade of the INCERC Laboratory of Applied Research and Testing in Constructions in Iasi. During the hot season, three outdoor air curtain modes of ventilation were chosen: natural ventilation with lateral openings on the exterior glazing, forced ventilation with lateral openings, and natural ventilation combining lateral and vertical openings on the top of the channel. During the cold season, the lateral and vertical openings are closed, and the channel façade behaves like a thermal buffer between the building and the exterior air.

From the analysis of the measured data, the following considerations can be drawn.

During the cold season, the buffer façade offers the possibility to ensure the partial or integral heating of the interior room for a solar radiation intensity higher than 100 W/m^2, when the temperatures inside the channel exceed the value of 20 °C with a difference of 14 °C relative to the exterior ones. On the other hand, for smaller solar radiation intensity of 20 W/m^2, the difference drops to around 2 °C. In this condition, the negative values of the pre-heating efficiency showed that the only benefit obtained from the ventilated façade is to increase the surface temperature of the inner glass pane inside the channel and reduce the heat losses from the interior room. On the other hand, the condensation appearance on the interior DSF surfaces was observed when the humidity reached values above 80% between 06:00 p.m. and 10:00 a.m.

Results related to the summer period showed that the air and enclosing surfaces temperatures in the channel can reach values above 40 °C mainly between 10:00 a.m. and 02:00 p.m. due to the location and façade orientation, with a difference of about 12 °C relative to the exterior temperature, when the intensity of solar radiation reaches more than 500 W/m^2. Direct solar radiation intensity influences the increase of air temperature in the channel, even when the exterior temperature does not exceed 30 °C. In the evening and during the night, the two temperatures become almost equal with a difference of around 2 °C for one of the channels. The forced ventilation does not reduce the channel air and surface temperatures for the flow rates studied, but it can improve the cooling when no solar radiation is present. On the other hand, using a controlled mechanical ventilation system involves operating costs, energy consumption, and the need for an often complex system of technical management. The average air relative humidity in the channel was recorded around 48% and no risk of condensation phenomena was observed.

The supplementary opening at the top of the channel improves the natural ventilation and the temperature difference between the channel and the ambient drops by around 9 °C at the noon and 1 °C during the night. A time shift of approximately one hour exists between the highest solar radiation and the maximum temperature recorded in the channel. In summer, the risk of overheating the DSF channel is obvious. Still, it can be minimized by using natural ventilation with good-sized inlets and outlets, combining the vertical with horizontal ones.

The airflow analyses during the summer showed that its velocity at the inlet section depends on the wind speed and a higher temperature inside the channel determines higher velocities in natural convection. The forced ventilation mode determines the turbulent character of the flow in the middle of the channel with a variation of velocities between 0.25–0.42 m/s. This was confirmed by the visualizations of the airflow pattern inside the channel's median section, which highlighted an ascendant flow near the interior double glazing of the DSF channel and a descendant one near the exterior glazing.

The performance indicator specific for the hot season in terms of dynamic insulation efficiency recorded a value of 71.3% for natural ventilation with both openings on the lateral outer glass and the vertical one at the top of the channel. Thus, in order to prevent the overheating of the façade during the hot season, combining vertical and horizontal openings in natural ventilation give the best efficiency of the double-skin facade functioning.

Author Contributions: Conceptualization, M.L.C. and N.C.C.; methodology, M.L.C., N.C.C. and A.A.C.; validation, N.C.C. and M.L.C.; formal analysis, M.L.C., N.C.C., A.A.C. and S.V.H.; investigation, M.L.C., N.C.C., A.A.C., S.V.H., E.F.Ț., A.B. and C.G.P.; resources, M.L.C., N.C.C., A.A.C. and C.G.P.; data curation, N.C.C. and S.V.H.; writing—original draft preparation, N.C.C., M.L.C., A.B., S.V.H. and E.F.Ț.; writing—review and editing, N.C.C. and M.L.C.; visualization, N.C.C., S.V.H. and E.F.Ț.; supervision, M.L.C. and N.C.C.; project administration, N.C.C. and M.L.C.; funding acquisition, N.C.C. and M.L.C. All authors have read and agreed to the published version of the manuscript.

Funding: This paper was financed by the program Internal Grants—Publications granted by the "Gheorghe Asachi" Technical University of Iasi, Romania, project number GI/P35_Publications/2021.

Institutional Review Board Statement: Not applicable.

Informed Consent Statement: Not applicable.

Data Availability Statement: Data are contained within the article.

Acknowledgments: We would like to acknowledge the invaluable support provided by the NIRD URBAN-INCERC Iasi Branch and FCI-TUIASI infrastructure in writing this article.

Conflicts of Interest: The authors declare no conflict of interest.

References

1. Corgnati, S.P.; Perino, M.; Serra, V. Experimental assessment of the performance of an active transparent façade during actual operating conditions. *Sol. Energy* **2007**, *81*, 993–1013. [CrossRef]
2. Saelens, D.; Roels, S.; Hens, H. Strategies to improve the energy performance of multiple-skin facades. *Build. Environ.* **2008**, *43*, 638–650. [CrossRef]
3. Zanghirella, F. Numerical and Experimental Analysis of Active Transparent Façade. Ph.D. Thesis, Polytechnic University of Turin, Turin, Italy, 2008.
4. Fuliotto, R.; Cambuli, F.; Mandas, N.; Bacchin, N.; Manara, G.; Chen, Q. Experimental and numerical analysis of heat transfer and airflow on an interactive building facade. *Energy Build.* **2010**, *42*, 23–28. [CrossRef]
5. Hernandez, M. Experimental and Computational Evaluation of Thermal Performance and Overheating in Double Skin Facades. Ph.D. Thesis, University of Nottingham, Nottingham, UK, 2008.
6. Serra, V.; Zanghirella, F.; Perino, M. Experimental evaluation of a climate façade: Energy efficiency and thermal comfort performance. *Energy Build.* **2010**, *42*, 50–62. [CrossRef]
7. Perino, M. *State-of-the-Art Review: Vol. 2A. Responsive Building Elements: NNEX 44: Integrating Environmentally Responsive Elements in Buildings*; Aalborg University: Aalborg, Denmark, 2008.
8. Safer, N. Multi-Scale Modelling of Double Skin Façades Equipped with Solar Protections. Ph.D. Thesis, National Institute for Applied Sciences, Lyon, France, 2006.
9. Gavan, V.; Woloszyn, M.; Kuznik, F.; Roux, J.-J. Experimental study of a mechanically ventilated double-skin façade with venetian sun-shading device: A full-scale investigation in controlled environment. *Sol. Energy* **2010**, *84*, 183–195. [CrossRef]
10. Anđelković, A.; Cvjetkovic, T.; Djakovic, D.; Stojanovic, I. The development of simple calculation model for energy performance of double skin façades. *Therm. Sci.* **2012**, *16*, 251–267. [CrossRef]
11. Ignjatovic, M.; Blagojevic, B.; Stojanovic, B.; Stojiljković, M. Influence of glazing types and ventilation principles in double skin façades on delivered heating and cooling energy during heating season in an office building. *Therm. Sci.* **2012**, *16*, 461–469. [CrossRef]
12. Matour, S.; Garcia-Hansen, V.; Omrani, S.; Hassanli, S.; Drogemuller, R. Wind-driven ventilation of Double Skin Façades with vertical openings: Effects of opening configurations. *Build. Environ.* **2021**, *196*, 107804. [CrossRef]
13. Tao, Y.; Fang, X.; Chew, M.Y.L.; Zhang, L.; Tu, J.; Shi, L. Predicting airflow in naturally ventilated double-skin facades: Theoretical analysis and modelling. *Renew. Energy* **2021**, *179*, 1940–1954. [CrossRef]
14. Tao, Y.; Fang, X.; Setunge, S.; Tu, J.; Liu, J.; Shi, L. Naturally ventilated double-skin façade with adjustable louvers. *Sol. Energy* **2021**, *225*, 33–43. [CrossRef]
15. Torres, M.; Alavedra, P.; Guzman, A.; Cuerva, E.; Planas, C.; Clemente, R.; Escalona, V. Double Skin Facades—Cavity and exterior openings dimensions for saving energy on Mediterranean climate. *Build. Simul.* **2007**, *1–3*, 198–205.
16. Azarbayjani, M. Climatic based consideration of double skin facade system: Natural ventilation performance of a case study with double skin facade in mediterranean climate. In Proceedings of the Building Simulation 2013 13th International Conference of the International Building Performance Simulation Association, Chambery, France, 25–28 August 2013; pp. 512–519.
17. Hamza, N.; Cook, M.; Cropper, P. Comparative analysis of natural ventilation performance in non-unifrom double skin facades in temperate climates. In Proceedings of the 12th Conference of International Building Performance Simulation Association, Sydney, Australia, 14–16 November 2011; pp. 2401–2406.
18. Stec, W.; Van Paassen, A. Symbiosis of the double skin façade with the HVAC system. *Energy Build.* **2005**, *37*, 461–469. [CrossRef]
19. Pomponi, F.; Piroozfar, P.; Southall, R.; Ashton, P.; Farr, E.R. Energy performance of Double-Skin Façades in temperate climates: A systematic review and meta-analysis. *Renew. Sustain. Energy Rev.* **2016**, *54*, 1525–1536. [CrossRef]
20. Dama, A.; Angeli, D.; Larsen, O.K. Naturally ventilated double-skin façade in modeling and experiments. *Energy Build.* **2017**, *144*, 17–29. [CrossRef]
21. Aksamija, A. Context Based Design of Double Skin Facades: Climatic Considerations during the Design Process. *Perkins+Will Res. J.* **2009**, *1*, 54–69.
22. Jankovic, A.; Goia, F. Impact of double skin facade constructional features on heat transfer and fluid dynamic behaviour. *Build. Environ.* **2021**, *196*, 107796. [CrossRef]
23. Hien, W.N.; Liping, W.; Chandra, A.N.; Pandey, A.R.; Xiaolin, W. Effects of double glazed facade on energy consumption, thermal comfort and condensation for a typical office building in Singapore. *Energy Build.* **2005**, *37*, 563–572. [CrossRef]
24. Wong, P.; Prasad, D.; Behnia, M. A new type of double-skin façade configuration for the hot and humid climate. *Energy Build.* **2008**, *40*, 1941–1945. [CrossRef]
25. Hamza, N. Double versus single skin facades in hot arid areas. *Energy Build.* **2008**, *40*, 240–248. [CrossRef]

26. Qahtan, a.m. Thermal performance of a double-skin façade exposed to direct solar radiation in the tropical climate of Malaysia: A case study. *Case Stud. Therm. Eng.* **2019**, *14*, 100419. [CrossRef]
27. Aleksandrowicz, O.; Yezioro, A. Mechanically ventilated double-skin facade in a hot and humid climate: Summer monitoring in an office tower in Tel Aviv. *Arch. Sci. Rev.* **2018**, *61*, 171–188. [CrossRef]
28. Zomorodian, Z.S.; Tahsildoost, M. Energy and carbon analysis of double skin façades in the hot and dry climate. *J. Clean. Prod.* **2018**, *197*, 85–96. [CrossRef]
29. Yilmaz, Z.; Çetintaş, F.; Yılmaz, Z. Double skin façade's effects on heat losses of office buildings in Istanbul. *Energy Build.* **2005**, *37*, 691–697. [CrossRef]
30. Năstase, G.; Şerban, A.; Dragomir, G.; Bolocan, S.; Brezeanu, A.I. Box window double skin façade. Steady state heat transfer model proposal for energetic audits. *Energy Build.* **2016**, *112*, 12–20. [CrossRef]
31. Kuznik, F.; Catalina, T.; Gauzere, L.; Woloszyn, M.; Roux, J.-J. Numerical modelling of combined heat transfers in a double skin façade–Full-scale laboratory experiment validation. *Appl. Therm. Eng.* **2011**, *31*, 3043–3054. [CrossRef]
32. Ascione, F.; Bianco, N.; Iovane, T.; Mastellone, M.; Mauro, G.M. The evolution of building energy retrofit via double-skin and responsive façades: A review. *Sol. Energy* **2021**, *224*, 703–717. [CrossRef]
33. Hou, K.; Li, S.; Wang, H. Simulation and experimental verification of energy saving effect of passive preheating natural ventilation double skin façade. *Energy Explor. Exploit.* **2021**, *39*, 464–487. [CrossRef]
34. Larsen, S.F.; Rengifo, L.; Filippín, C. Double skin glazed façades in sunny Mediterranean climates. *Energy Build.* **2015**, *102*, 18–31. [CrossRef]
35. Guardo, A.; Coussirat, M.; Valero, C.; Egusquiza, E.; Alavedra, P. CFD assessment of the performance of lateral ventilation in Double Glazed Façades in Mediterranean climates. *Energy Build.* **2011**, *43*, 2539–2547. [CrossRef]
36. Hassanli, S.; Hu, G.; Kwok, K.; Fletcher, D.F. Utilizing cavity flow within double skin façade for wind energy harvesting in buildings. *J. Wind. Eng. Ind. Aerodyn.* **2017**, *167*, 114–127. [CrossRef]
37. Chereches, M. *The Thermo-Hygro-Energetic Behavior of the Ventilated Facades, Applicable to Public Buildings, in the Climatic Conditions in Romania. Prenormative Research*; Contract No. 493/2011; NIRD URBAN–INCERC: Iasi, Romania, 2011.
38. Saelens, D. Energy performance assessment of singlestorey multiple-skin facades. Ph.D Thesis, Katholieke Universiteit Leuven, Leuven, Belgium, 2002.
39. Hudişteanu, S.; Poenari, C.F.; Balint, B.I.; Cherecheş, M.; Cherecheş, N.C. Energy saving analysis inside a double skin façade. *Math. Model. Civ. Eng. J.* **2013**, *1*, 78–83.
40. Popovici, C.G.; Cirlan, V.V.; Mateescu, T.D.; Chereches, N.C.; Hudisteanu, S.V. Influence of various angles of the venetian blind on the efficiency of a double skin facade. *Energy Procedia* **2016**, *85*, 416–424. [CrossRef]

applied sciences

IMPACT FACTOR 2.9

CITESCORE 6.1

Article

Enhancement of PV Panel Power Production by Passive Cooling Using Heat Sinks with Perforated Fins

Sebastian Valeriu Hudișteanu, Florin Emilian Țurcanu, Nelu Cristian Cherecheș, Cătălin George Popovici, Marina Verdeș and Iuliana Huditeanu

Special Issue

Urban Sustainability and Resilience of the Built Environments

Edited by

Dr. Ilinca Nastase and Dr. Florin Ioan Bode

MDPI

https://doi.org/10.3390/app112311323

applied sciences

MDPI

Article

Enhancement of PV Panel Power Production by Passive Cooling Using Heat Sinks with Perforated Fins

Sebastian Valeriu Hudișteanu *, Florin Emilian Țurcanu *, Nelu Cristian Cherecheș *, Cătălin George Popovici, Marina Verdeș and Iuliana Huditeanu

Faculty of Civil Engineering and Building Services, Gheorghe Asachi Technical University of Iasi, 700050 Iași, Romania; catalin-george.popovici@academic.tuiasi.ro (C.G.P.); marina.verdes@academic.tuiasi.ro (M.V.); iuliana.hudisteanu@academic.tuiasi.ro (I.H.)

* Correspondence: sebastian.hudisteanu@tuiasi.ro (S.V.H.); emilian-florin.turcanu@tuiasi.ro (F.E.Ț.); chereches@tuiasi.ro (N.C.C.)

Abstract: This paper presents a numerical model regarding the passive cooling of PV panels through perforated and non-perforated heat sinks. A typical PV panel was studied in a fixed position, tilted at 45 degrees from the horizontal with the wind direction towards its backside. A challenging approach was used in order to calibrate the base case of the numerical model according to the NOCT conditions. Further validation of the accuracy of the numerical simulation consisted of a comparison between the results obtained for the base case, or heat sink, with horizontal non-perforated fins and the experiments presented in the literature. Six types of heat sink attached to the backside of the PV panel were numerically studied. The analyzed configurations focused on heat sinks with both perforated and non-perforated fins that were distributed horizontally and vertically. The CFD simulation was also conducted by modeling the air volume around the PV panel in real wind conditions. The main output parameters were the average temperature and the convective heat transfer coefficient on the front and back of the PV panel. The most important effect of cooling was achieved in low wind conditions and high levels of solar radiation. For v_{air} = 1 m/s, G = 1000 W/m^2 and ambient temperature t_{air} = 35 °C, the percentage of maximum power production achieved 83.33% for the base case, while in the best cooling scenario it reached 88.74%, assuring a rise in the power production of 6.49%.

Keywords: power enhancement; perforated heat sinks; passive cooling; operating PV temperature; NOCT validation; CFD analysis

check for updates

Citation: Hudișteanu, S.V.; Țurcanu, F.E.; Cherecheș, N.C.; Popovici, C.G.; Verdeș, M.; Huditeanu, I. Enhancement of PV Panel Power Production by Passive Cooling Using Heat Sinks with Perforated Fins. *Appl. Sci.* **2021**, *11*, 11323. https://doi.org/10.3390/app112311323

Academic Editors: Ilinca Nastase and Florin Ioan Bode

Received: 16 November 2021
Accepted: 24 November 2021
Published: 30 November 2021

Publisher's Note: MDPI stays neutral with regard to jurisdictional claims in published maps and institutional affiliations.

Copyright: © 2021 by the authors. Licensee MDPI, Basel, Switzerland. This article is an open access article distributed under the terms and conditions of the Creative Commons Attribution (CC BY) license (https://creativecommons.org/licenses/by/4.0/).

1. Introduction

The current global energy context is characterized by the energy consumption of humanity, which has reached impressive values in recent years. Thus, in the current year (2021) the well-known Overshoot Day was "celebrated" on 29 July. This meant that humanity had already used up all of the restorable resources of 2021. From 30 July we started consuming more resources than the planet could regenerate in a year [1]. Therefore, by the end of the year 2021, the energy consumption is projected to reach about 1.73× Earth's resource regeneration capacity. It is a global emergency and every small step in reducing this tendency to over consume energy will become decisive in this fight.

Solar energy is a clean and sustainable source of energy. It is involved directly or indirectly in the vast majority of other renewable energy sources, and it is also related to the conventional fuels—as most of them are the result of photosynthesis. The solar energy incident on the Earth could cover the annual energy demand for the entire world in only 1.5 h [2,3].

Regarding the conversion of solar radiation into electricity, this can be achieved by using photovoltaic (PV) cells or it can be generated through solar thermal technologies [1].

Photovoltaic conversion has important advantages: the energy source is renewable and free, and the processes of electricity production are environmentally friendly (in terms of CO_2 and NOx emissions, waste, noise etc.). The generation of electricity is achieved without the use of moving parts, so the cost of maintenance is reduced. Furthermore, the energy produced is consumed locally, which results in reduced power losses.

By implementing efficient PV systems, the safety of the users of the electricity supply is increased [4,5]. These systems also reduce the vulnerability of European space and could eliminate future energy crises or the lack of an energy supply. Considering the long service life and the low CO_2 emissions of PV systems, they represent a sustainable alternative to electricity production. In addition, the energy market in Europe, which lately has been affected by internal and external factors, could become more stable and competitive by increasing the power it produces and the number of users of photovoltaic systems [6].

The main environmental parameters, which are influencing the efficiency and the lifetime of PV panels are solar radiation, wind velocity and direction, dust, ambient temperature and their operating temperature. Most of these meteorological parameters are random and uncontrollable. From the point of view of the installation methods, the tilt angle, orientation and positioning are very difficult to manage in the case of typical PV systems [7,8]. However, the management of the operating temperature of PV cells has been demonstrated to be a good solution for enhancing their efficiency [9].

Almost 80% of the solar energy incident on the PV panel's surface is converted into heat, and it is well known that the performance of PV panels is temperature-dependent [9,10]. Skoplaki, E. et al. [10] analyzed different methods and relations for calculating the dependence between conversion efficiency and photovoltaic cell temperature; a linear dependence between efficiency and temperature has been proved. The decrease in the efficiency of the produced power related to the increase in the temperature has values between -0.46–$-0.50\%/^{\circ}C$ and -0.47–$-0.50\%/^{\circ}C$, respectively [11–13].

Taking into account that the power of a photovoltaic cell is influenced by the temperature and radiation levels, standard test condition (STC) parameters were defined: t_{PV} = 25 °C, G = 1000 W/m^2, AM1.5 [14]. In STCs the PV panels produce the watt peak power [Wp], but a real concern is that in regular operation, at 1000 W/m^2, the photovoltaic panels can reach extreme temperatures of 70–80 °C [11,15,16], leading to a significant decrease in the efficiency.

Complementary cooling solutions are recommended in order to achieve high productivity [17–21]. The literature presents a large number of papers on different solutions for improving the conversion efficiency by decreasing the temperature of the photovoltaic panels [13,15,20,22–27].

Concepts frequently used in analyzing PV systems are the NOCT (nominal operating cell temperature) conditions. In contrast to STCs, the NOCT conditions are closer to reality, taking into account the following operating conditions: tilt of PV panel = 45°; G = 800 W/m^2; t_{air} = 20 °C; v_{air} = 1 m/s towards the backside of PV panel [15]. According to these conditions, every producer must supply, via the data sheet, the average operating temperature of the PV panel—t_{NOCT}.

The aim of this study was to overcome technological and conceptual barriers that were currently attributed implicitly to photovoltaic systems by improving their efficiency during months with maximum energy production but lower efficiencies due to high operating temperatures. For example, in hot summer days it turned out that the most important cause of the production potential not being reached, when the intensity of solar radiation had the highest values of the year, was the uncontrolled increase in the operating temperatures of the photovoltaic panels.

The improvement in the efficiency of PV panels when air-cooled heat sinks were used, was reasonable for the residential sector, urban areas and power plants [28,29].

The novelty of the present study consisted of analyzing the impact of longitudinal and transversal heat sinks with perforated and non-perforated fins on the performance of PV panels. The impact was analyzed using more realistic wind conditions and tilt of the panel, compared to existing studies in the literature.

2. Related Research

Experimental tests and numerical analyses on monocrystalline or polycrystalline photovoltaic panels show that the decrease in efficiency, as the operating temperature increases, and the necessity of cooling solutions are current concerns in the literature [11–13,16,30,31].

Different technologies to improve the efficiency of photovoltaic panels by passive cooling, using air, are studied in the literature [8,13,32–39]. Detailed studies on air cooling of photovoltaic panels are carried out in the following works [11,40]. Air cooling with heat sinks and perforated fins is studied both numerically [11,32] and experimentally [34]. The characteristic values for multiple photovoltaic panels cooled with aluminum and copper heat sinks were compared through experimental tests under different conditions [34]. The results of the simulation and from the experiment showed that the heat sink with perforated fins can significantly reduce the temperature of the panel and increase its performance; there was an increase in the heat extracted from the photovoltaic cell and a decrease in its temperature, with values between 7 °C and 10 °C [34].

Also, numerical simulations on a particular case of backside ventilation [11,16,41] revealed that the temperature was reduced by 10 °C below the value obtained in the base case. This aspect was favorable for conversion efficiency, determining a generation of approximately 90% of the maximum power produced in STCs [14], while the average power production of PV panels was about 70–80% of P_{mp} in STCs [42].

3. Materials and Methods

3.1. Problem Description

The goal of this work was to develop a numerical model regarding the passive cooling of the PV panels, through perforated and non-perforated heat sinks, and determine the enhancement of operating temperatures compared to the base case (without cooling). A photovoltaic panel with an area of approximately S = 1.6 m^2 was studied in a fixed position and tilted at 45° from horizontal, as well as in variable solar radiation, wind velocity and ambient temperature. This setup, together with the wind direction towards the backside of the PV panel, was established according to NOCT conditions [14] in order to validate the model.

A common monocrystalline Si-based PV panel (AE Solar AE320HM6-60), with an advantageous position of the junction box, was analyzed with the following technical data (Table 1) [43].

Table 1. General characteristic for the considered PV panel.

AE Solar AE320HM6-60 PV Panel	
P_{mp}	320 Wp
V_{mp}	33.40 V
I_{mp}	9.59 A
V_{oc}	40.90 V
I_{sc}	10.15 A
η	19.30%
β	−0.37%/°C
t_{NOCT}	47 °C
Dimensions ($L \times l \times h$)	1665 mm × 996 mm × 35 mm

A step-by-step analysis of heat sink usage for cooling PV panels was conducted. After the initial validation of the base case—PV panel without heat sink—a total of six photovoltaic panels with attached heat sinks were analyzed. Two of them were non-perforated, while the other four had perforated fins.

The heat sink consisted of a metal plate with copper attached to the photovoltaic panel and perforated or non-perforated metal fins, Figure 1. The role of the designed holes on the fins was assumed to be both quantitative (by reducing the amount of material necessary for device construction) and qualitative (by amplifying the turbulence and heat transfer in the immediate vicinity of the PV panel).

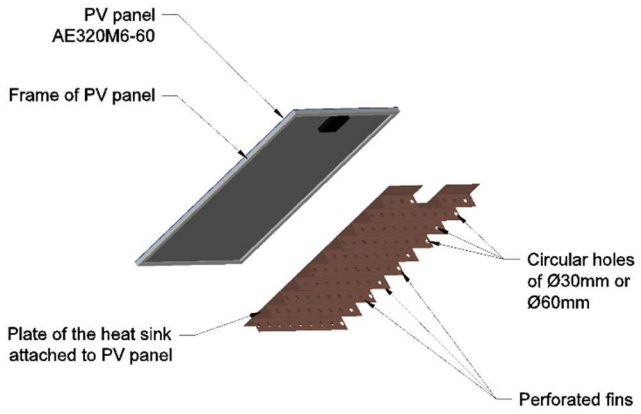


Figure 1. Overview of the components of the heat sink attached to the PV panel for cooling (case with perforated fins).

Due to preliminary analysis and the literature review [11,32,34,41], the 30 mm and 60 mm diameter circular perforations distributed on a single row turned out to be feasible. It emerged that other shapes, dimensions or multiple rows of perforations were heading towards lower performance of the heat sink (the operating temperatures were at least 2–3 °C higher). It must be specified that the literature comprises a diversity of heat sinks with different approaches of fins [42,44]. The present study is focused on using heat sinks with continuous fins.

Two types of heat sinks were analyzed:

Type 1—heat sinks with horizontal (transversal) fins of 100 mm height (with 3 subtypes: non-perforated, Φ = 30 mm perforations, Φ = 60 mm perforations);

Type 2—heat sinks with vertical (longitudinal) fins of 100 mm height (with 3 subtypes: non-perforated, Φ = 30 mm perforations, Φ = 60 mm perforations).

3.2. Numerical Simulation

The numerical simulation was performed using the ANSYS-Fluent 2021-R1 software. The geometry and discretization of the computing domain was performed within the platform using the Fluent-Meshing and SpaceClaim programs.

For simulation the control volume method, SIMPLE pressure–velocity coupling and second-order accuracy for equation solving were used, taking into account that the flow was not aligned with the mesh [45]. This method used a relationship between velocity and pressure corrections to enforce mass conservation and to obtain the pressure field. A fully implicit numerical scheme was employed, in which upwind differences were used for the convective terms and central differences for the diffusion terms [11]. The calculation was iterative, with a convergence criteria of 10^{-6} for the energy equation and 10^{-3} for the pressure, velocities, k, ε and continuity equations.

The simulation of solar radiation was realized using the Solar Ray Tracing model of the Fluent program. The absorption of solar radiation by the front of the PV panel was imposed as a global coefficient α = 0.7, taking into account all the layers of the PV panel [11,46].

The heat transfer balance was set in order to include the convection and radiation with the surroundings [46]. The numerical simulation was realized using the k–ε realizable model [45]. For all studied configurations, the distance between fins was set to 150 mm. The fins were perpendicular to the heat sink plate—Figure 1. For the case of perforated fins, they had circular holes of 30 mm or 60 mm diameter, which were placed at a distance of 100 mm to one to another [34]. Their role was to improve the air circulation near the heat sink and to extract more heat from the PV panel.

The accuracy and the solution time were both highly depend on the characteristic of the mesh. Computational fluid dynamics (CFDs) solvers depended on the highly orthogonal mesh that could be difficult to achieve on different types of geometries. For the present study, a polyhedral mesh was used for the surfaces and a poly-hex core for one of the volumes. The choice of these types of cells was made due to an increase in speed of simulation from 20 to 50% while maintaining the high level of accuracy. In addition, this approach in the simulation opened up the possibility of improving the solver speed and accuracy compared with the tetrahedral cells.

The mesh was realized with different refinements for the heat sink and air volume. The mesh quality achieved for the numerical analysis was as follows:

- Aspect ratio was in the range 5–60;
- Skewness was in the range 0.4–0.7;
- Orthogonal quality was in the range 0.1–0.3.

A mesh independence study was carried out, taking into account the large number of elements that resulted due to modeling the air volume that flowed over the PV panel and heat sinks. Figure 2 presents the mesh independence study, which was achieved for approximately 3 million cells in the base case and over 5.5 million cells for cases with heat sinks and perforated fins.

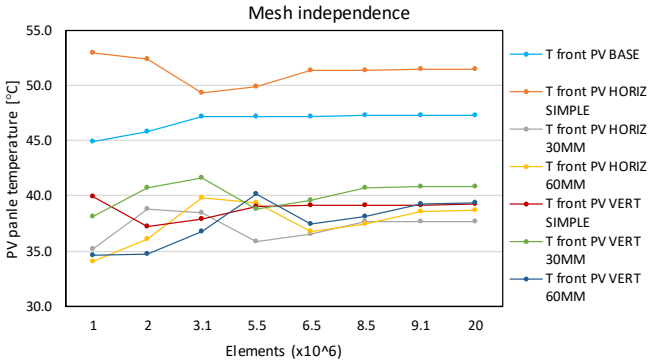


Figure 2. Mesh independence study for each model.

The numerical analysis was conducted on a workstation that had 48 cores, 256 GB of RAM and a graphical computing video card Nvidia Quadro P6000.

Typical approaches from the literature considered the position of the PV panel as either horizontal [31] or vertical [11,34], with a channel simulating the wind behind the PV panel. There were only a few studies on cooling tilted PV panels [16,40].

During this study the modelling was realized by taking into account the air circulation in the vicinity of a tilted PV panel cooled with heat sinks. In this way, by using an optimized resource consumer mesh, the airflow and the heat transfer were more realistic and easier to visualize and understand. The material properties used in the simulations are shown in Table 2, and the sketch of the model is presented in Figure 3.

Table 2. Material properties.

Material	g [mm]	λ [W/m·K]	ρ [kg/m^3]	c_p [J/kg·K]
Glass	3.00	1.00	2300	0.50
PV cells	0.35	168	2330	0.757
EVA	0.50	0.35	960	2.09
Tedlar	0.20	0.20	1500	1.20
Copper	1.00	386	8960	0.376
Air	-	0.025	1.20	1.005

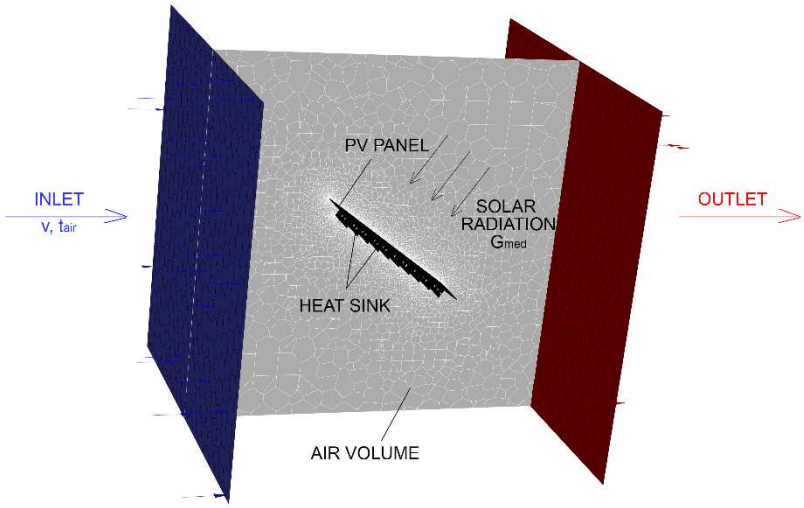


Figure 3. Main components of the numerical model.

During the study, the non-perforated heat sinks were compared with perforated heat sinks in order to determine the optimum configuration for implementation in NOCT conditions of wind.

Simulations were realized in steady state conditions with the following input parameters:

- ambient temperature, t_{air} = 20, 25, 30 and 35 °C;
- velocity of the air towards the back of the photovoltaic panel, v_{air} = 1–5 m/s;
- the normal component of solar radiation varied between 200–1000 W/m^2, assuming the typical conditions of operation for the PV panel.

It should be mentioned that heat sinks were studied on some of the worst scenarios of temperature operation for the base case. Therefore, some cases with low levels of solar radiation, low ambient temperatures or high wind velocities were excluded from the results presented during the paper.

The main outputs of the simulations were:

- average temperature of the PV panel;
- convective heat transfer coefficients, achieved for both the front and the back of the PV panel or heat sink.

Studied Cases

A total of six configurations of heat sinks were analyzed, plus the base case, these are shown in Table 3.

Table 3. Studied configurations.

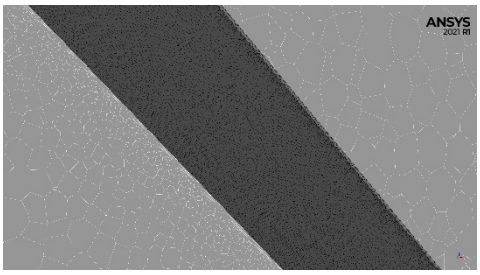
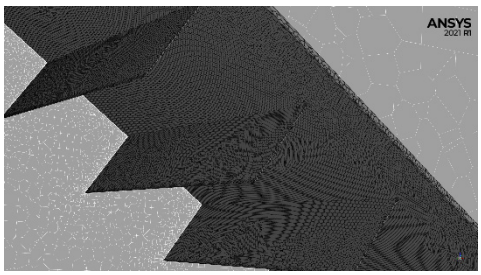
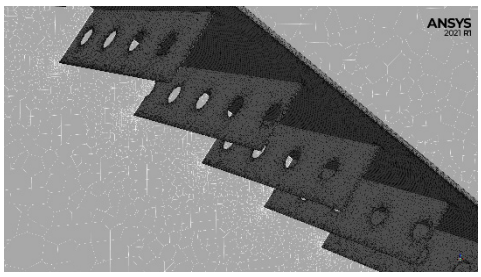
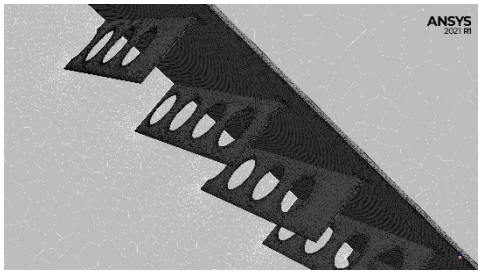
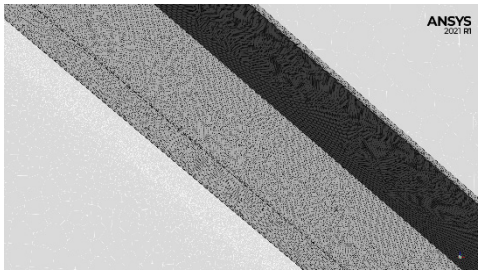
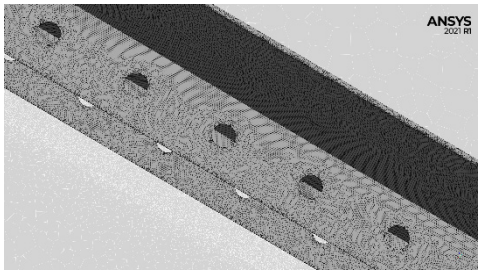
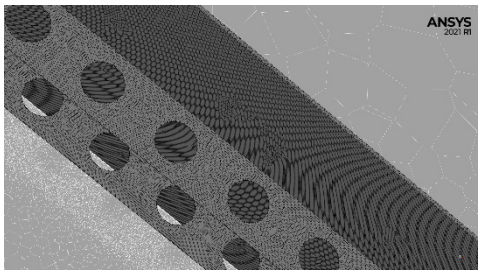
Case	Name	Mesh Detail	Description
0	Base		Pilot photovoltaic panel—normal installation—without cooling solution.
1	Horiz Simple		Air-cooled photovoltaic panel with heat sink and non-perforated horizontal (transversal) fins.
2	Horiz 30 mm		Air-cooled photovoltaic panel with heat sink and perforated horizontal (transversal) fins Φ = 30 mm.
3	Horiz 60 mm		Air-cooled photovoltaic panel with heat sink and perforated horizontal (transversal) fins Φ = 60 mm.
4	Vert Simple		Air-cooled photovoltaic panel with heat sink and non-perforated vertical (longitudinal) fins.

Table 3. *Cont.*

Case	Name	Mesh Detail	Description
5	Vert 30 mm		Air-cooled photovoltaic panel with heat sink and perforated vertical (longitudinal) fins Φ = 30 mm.
6	Vert 60 mm		Air-cooled photovoltaic panel with heat sink and perforated vertical (longitudinal) fins Φ = 60 mm.

The position of the PV panel and air circulation was set according to NOCT conditions: the PV panel was tilted at 45° and wind direction toward the backside of the PV panel (Figures 4 and 5).

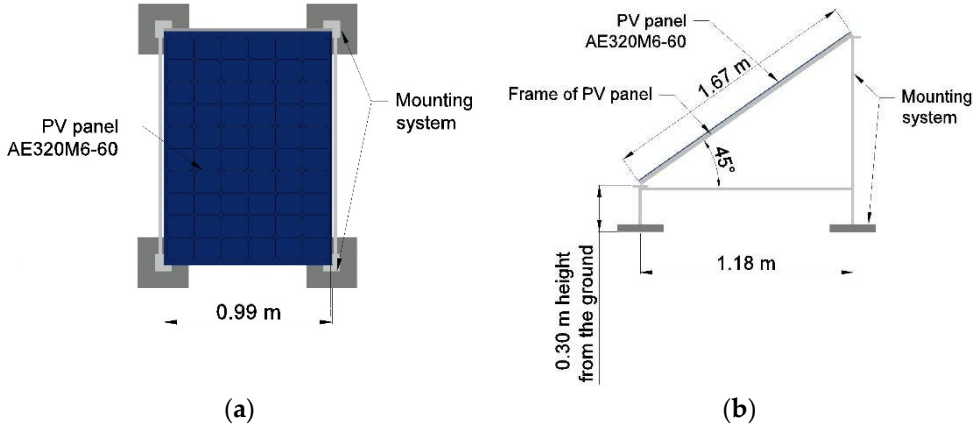


Figure 4. Position of the PV panel (fixed, tilted at 45°): (**a**) top view; (**b**) side view.

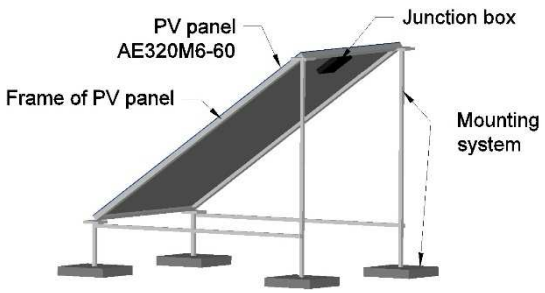
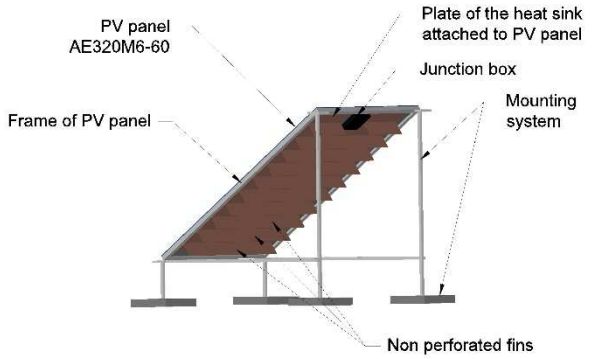
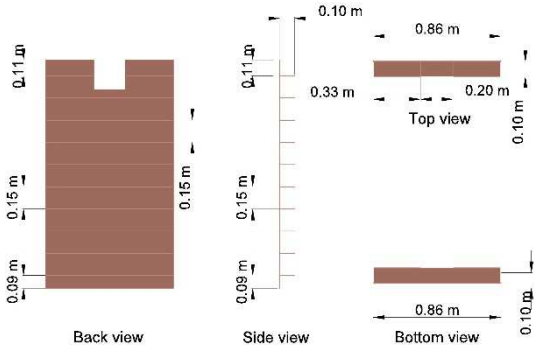
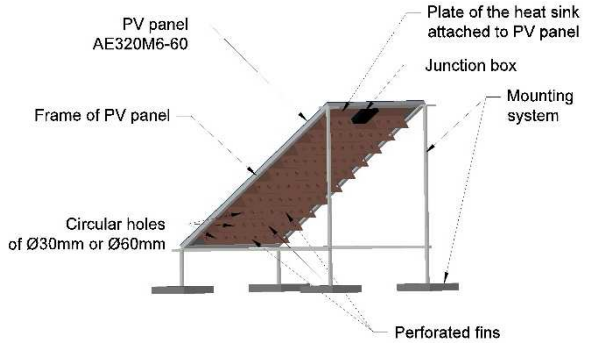
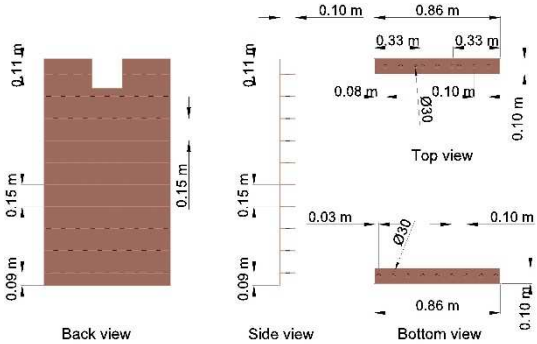
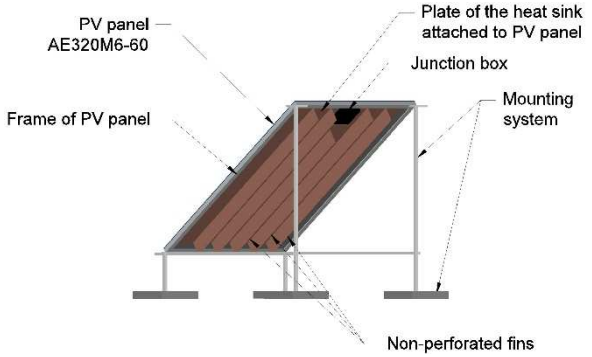
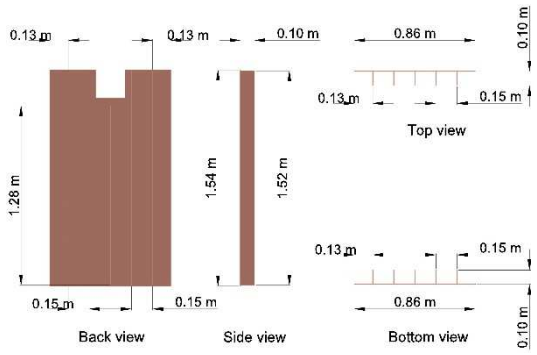
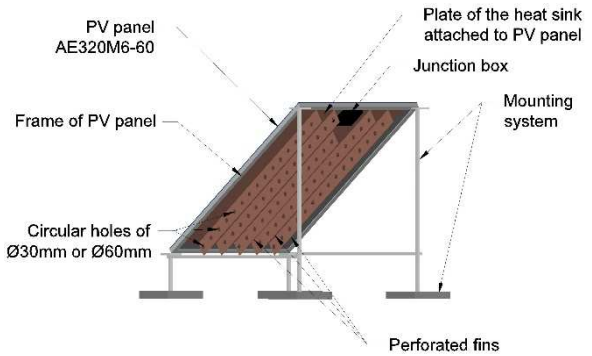
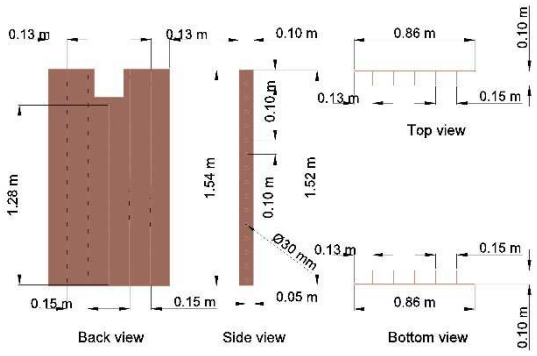


Figure 5. Base case—PV panel without cooling—3D perspective view.

Heat sinks consist of a metal plate and perforated or non-perforated longitudinal or transversal fins arranged at equal distances of 150 mm from each other (Table 4). Both the base plate and the fins were made of copper. The base plate was in direct contact with the

back of the photovoltaic panel. The fins had circular perforations with a diameter of 30 or 60 mm (Table 4).

Table 4. Components of the model and overall dimensions of the heat sinks.

Case	3D Perspective View	Overall Dimensions of the Heat Sink
1		
2, 3		
4		
5, 6		

During the study, the fins were arranged longitudinally (vertically—parallel to the length of the PV panel) or transversally (horizontally—parallel to the width of the PV panel). The distance between fins was s = 150 mm, while their height was h_{fins} = 100 mm.

The approximate length of the fins was L_{fins} = 1520 mm (for longitudinal ones) and L_{fins} = 860 mm (for transversal ones). The number of fins was 11 for the horizontal case and 5 for vertical case (Table 4).

The perforations had a circular shape and a diameter of Φ = 30 mm or Φ = 60 mm. The distance measured on the fins between the centers of the perforations was d = 100 mm. The perforations were staggered by 50 mm between two successive fins.

The back, side, top and bottom view of the heat sinks attached to the PV panel are presented in Table 4. In addition, the main components of the geometry conceptions of the photovoltaic panel, mounting system and heat sinks with perforated and non-perforated fins were easy to follow in 3D perspective views.

4. Validation of the Model

4.1. NOCT Calibration

The PV panel tilted at 45° was initially exposed to a direct solar radiation of 800 W/m^2, air temperature of 20 °C and wind velocity of 1 m/s from behind, similar to the NOCT conditions. According to the PV panel data sheet [43], in this scenario, the t_{NOCT} should be 45 ± 2 °C, while the operating temperature from simulation was 47.16 °C. Taking into account the good matching between results and expectation, further validation was conducted. Therefore, by comparing the results from modelling with those obtained by using the acknowledged Equation (1) [14,47], the following variation of the operating temperature was obtained (Figure 6).

$$t_{PV} = t_{air} + \frac{t_{NOCT} - 20}{800} \cdot G \quad (1)$$

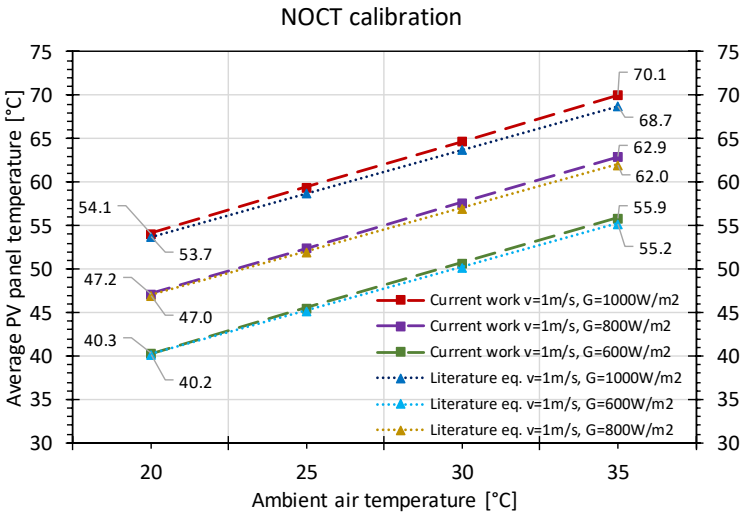


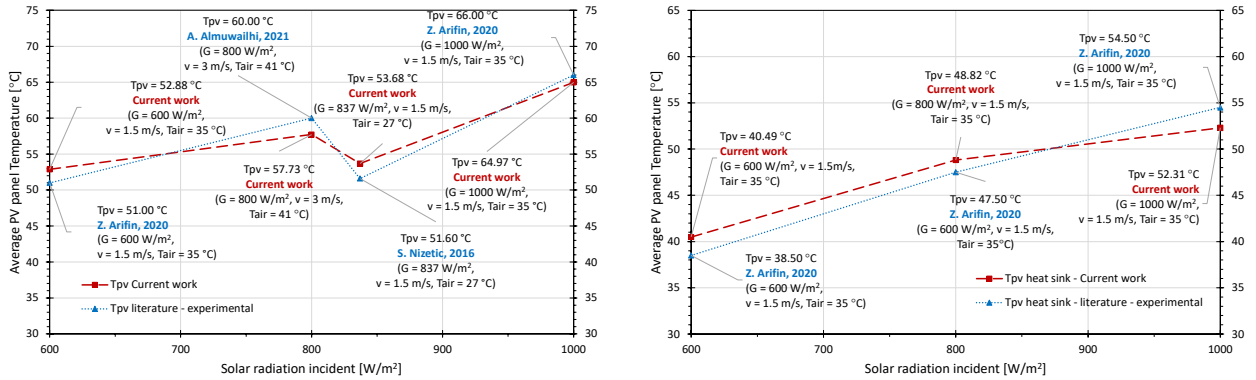
Figure 6. Calibration of the model according to NOCT conditions variation.

The results showed that the values computed using the current work differed from those of Equation (1) within the range of 0.28–1.98%.

4.2. Base Case Validation

Nizetic et al. [16] experimentally studied the thermal performance of PV panels on different inclination angles. In Case 1 of their study (45° tilt, v = 1.5 m/s, G = 837 W/m^2) the average temperature of the PV panel was 51.6 °C. For validation, the base case of the present work was set for the same parameters. The average temperature of the PV panel obtained in the current model was 53.68 °C, which represented a variation of 3.87%.

Also, experimental studies of Arifin et al. in 2020 [34], and Almuwailhi in 2021 [48], were examined and the correlations with the present work were presented together in Figure 7a.



(**a**) (**b**)

Figure 7. Validation of the model: (**a**) base case—without heat sink; (**b**) PV panel with heat sink.

4.3. Heat Sink Validation

An experimental study on heat sinks attached to a PV panel [34] were used in order to compare the results with the present model (Figure 7b).

A reasonable variation of the simulated PV panel average temperature compared to the literature for low and high ambient temperatures was recorded, in addition to different levels of radiation (Figure 7). The differences recorded were between −5.18% and +4.03%. According to the literature [49], this variation was acceptable so the study was considered consistent and the next step consisted of modelling the heat sinks with perforated fins (Cases 2–6) in the same conditions as those validated above.

5. Results and Discussion

Most simulations in the literature were realized by imposing a constant convective heat transfer coefficient (h_c), which determined a quasi-uniform temperature distribution [50]. In the present work, the simulation of the airflow near the PV panel determined a more realistic temperature distribution on its surface compared with the typical approaches [42], while the convective heat transfer coefficient was varying on the PV panel's surface.

The results of the simulations consisted of the photovoltaic panel temperature and convective heat transfer coefficient variation, depending on the type of the heat sink. The spectra of the operating temperatures of the PV panels and velocity path lines on the cross-sectional plane were obtained (Table 5). The following images present the qualitative visualization of the results for cases simulated in NOCT configuration: t_{air} = 20 °C, v_{air} = 1 m/s, G = 800 W/m^2 (Table 5).

Table 5. Temperature distribution on the PV panel and air velocity profile for the NOCT configuration.

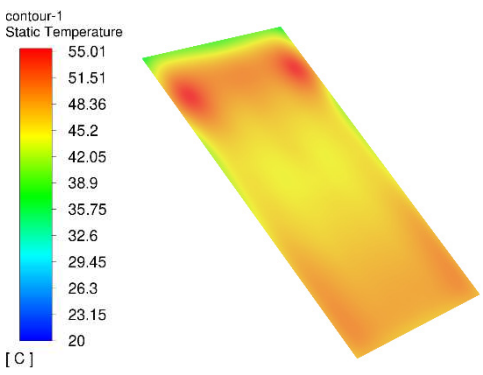
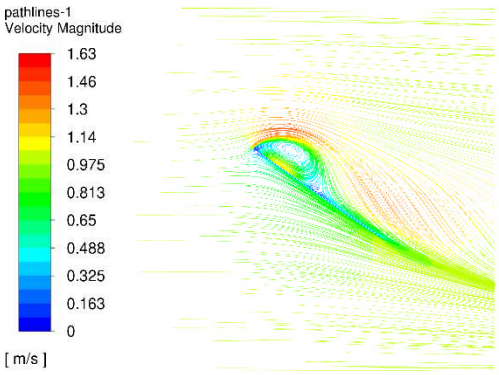
Front PV Temperature Distribution (t_{PV} [°C])	Wind Velocity Cross-Section Plane (v_{air} [m/s])
	
Base case: (a)	(b)

Table 5. *Cont.*

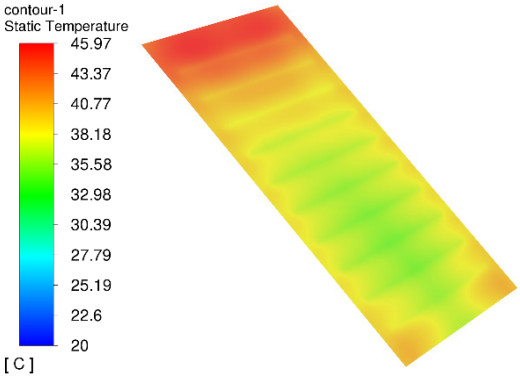
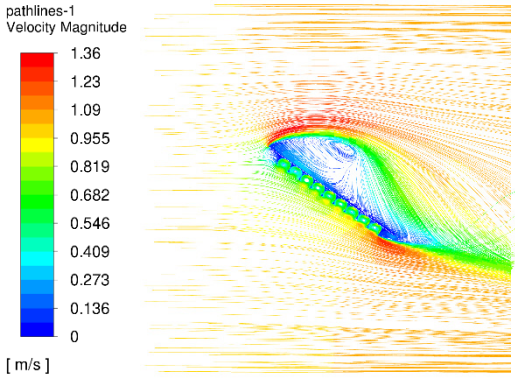
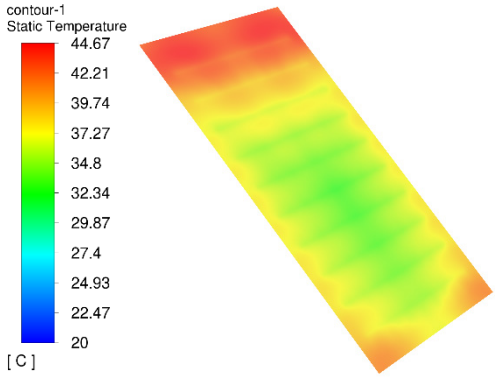
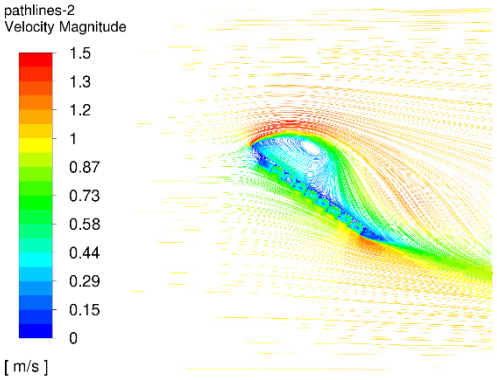
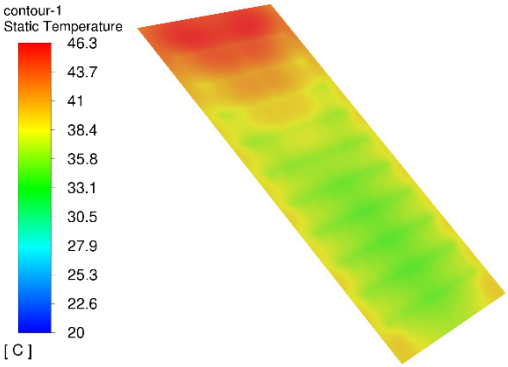
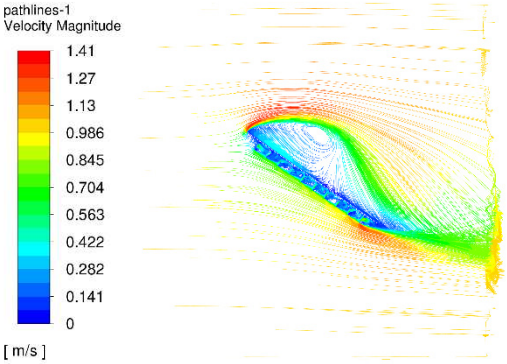
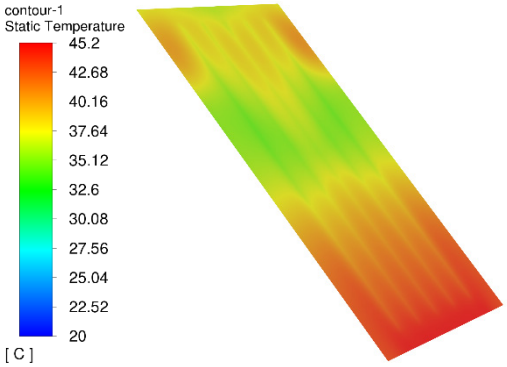
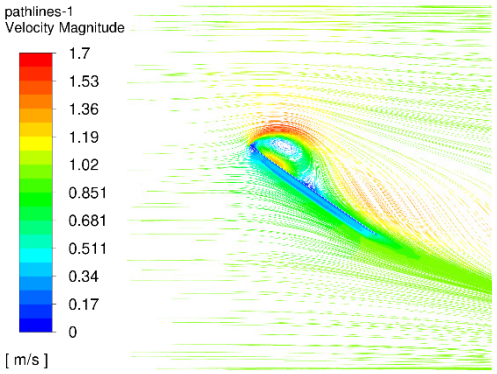
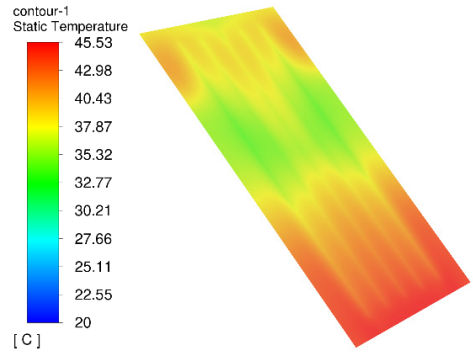
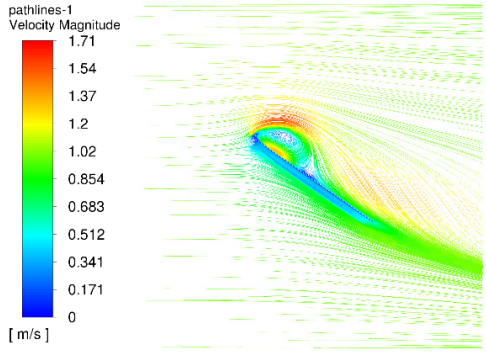
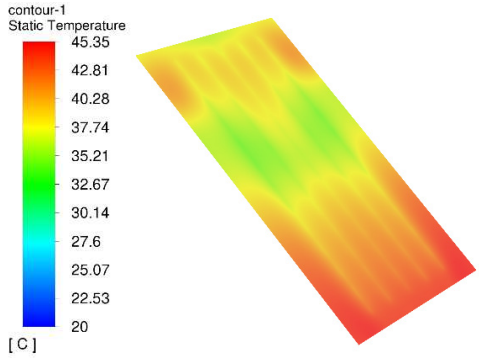
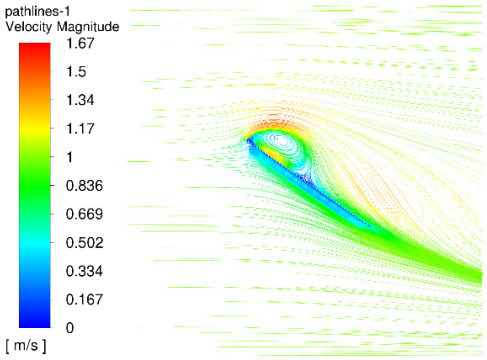
Front PV Temperature Distribution (t_{PV} [°C])	Wind Velocity Cross-Section Plane (v_{air} [m/s])
 Horizontal simple: (a)	 (b)
 Horizontal 30 mm: (a)	 (b)
 Horizontal 60 mm: (a)	 (b)
 Vertical simple: (a)	 (b)

Table 5. *Cont.*

Front PV Temperature Distribution (t_{PV} [°C])	Wind Velocity Cross-Section Plane (v_{air} [m/s])
 Vertical 30 mm: (a)	 (b)
 Vertical 60 mm: (a)	 (b)

The visual results clarify the temperature distribution achieved for each case analyzed, together with the air velocity field on the cross-sectional plane. The effect of the heat sinks was determining a decrease in maximum operating temperature of approximately 10 °C. In addition, from a qualitative point of view, for this particular wind direction (towards the backside of the PV panel), the air turbulence was increased compared to the base case, determining an improved heat transfer and a better cooling of the PV panel. In addition, each type of heat sink determined a slightly different distribution of wind velocities and recirculation areas. It can be remarked that the cooling effect was decreased in the zones with air recirculation in front of the PV panel compared to the rest of the area.

The results for v_{air} = 1 m/s, various inlet temperatures (t_{air} = 20–35 °C) and solar radiation (G = 600–1000 W/m^2) were merged in the following plots: Figures 8–10.

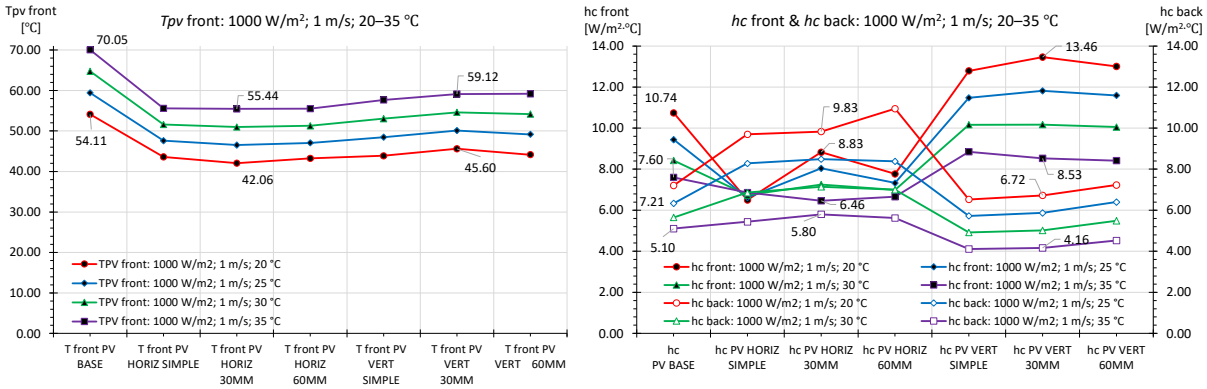


Figure 8. Variation of average operating temperature and convective heat transfer coefficient for studied cases. G = 1000 W/m^2, v_{air} = 1 m/s and t_{air} = 20–35 °C.

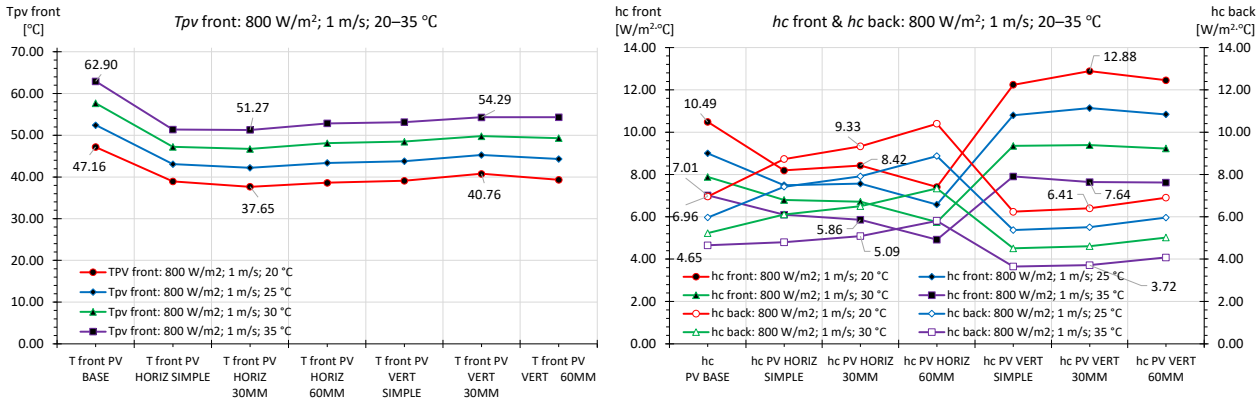


Figure 9. Variation of average operating temperature and convective heat transfer coefficient for studied cases (G = 800 W/m^2, v_{air} = 1 m/s and t_{air} = 20–35 °C).

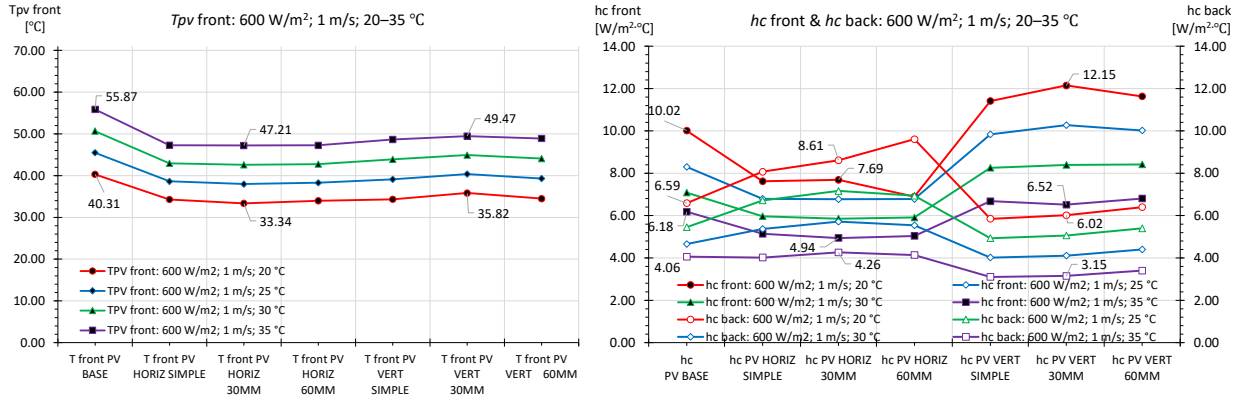


Figure 10. Variation of average operating temperature and convective heat transfer coefficient for studied cases (G = 600 W/m^2, v_{air} = 1 m/s and t_{air} = 20–35 °C).

An interesting aspect was recorded on convective heat transfer coefficients. Therefore, for horizontal heat sinks the h_c on the front of the PV panel were much closer to the h_c on the back, compared to vertical ones, where an important difference was recorded. The ambient temperature variation did not seem to change the best configuration (Case 2—horizontal 30 mm). This configuration determined a drop of temperature as presented in Table 6.

Table 6. Drop of the PV panel operating temperature for ambient air temperatures, t_{air} = 20–35 °C, wind velocity, v_{air} = 1–5 m/s and solar radiation, G = 600–1000 W/m^2.

Case	v_{air}	G = 600 W/m^2		G = 800 W/m^2		G = 1000 W/m^2	
		Drop of t_{PV} Compared to Base Case, for t_{air} = 20–35 °C					
		°C	%	°C	%	°C	%
0. BASE CASE	1 m/s	40.3–55.9	-	47.2–62.9	-	54.1–70.1	-
1. HORIZ SIMPLE		−6.02–−8.59	−14.9–−15.4	−8.22–−11.54	−17.4–−18.3	−10.52–−14.46	−19.4–−26.7
2. HORIZ 30MM		−6.97–−8.66	−17.3–−15.5	−9.51–−11.63	−20.2–−18.5	−12.05–−14.61	−22.3–−27
3. HORIZ 60MM		−6.35–−8.62	−15.8–−15.4	−8.55–−10.05	−18.1–−16	−10.88–−14.54	−20.1–−26.9
4. VERT SIMPLE		−5.98–−7.2	−14.8–−12.9	−8.07–−9.76	−17.1–−15.5	−10.25–−12.4	−18.9–−22.9
5. VERT 30MM		−4.49–−6.4	−11.1–−11.5	−6.4–−8.61	−13.6–−13.7	−8.51–−10.93	−15.7–−20.2
6. VERT 60MM		−5.82–−6.97	−14.4–−12.5	−7.84–−8.59	−16.6–−13.7	−9.97–−10.87	−18.4–−20.1

Table 6. *Cont.*

Case	v_{air}	G = 600 W/m^2		G = 800 W/m^2		G = 1000 W/m^2	
		Drop of t_{PV} Compared to Base Case, for t_{air} = 20–35 °C					
		°C	%	°C	%	°C	%
0. BASE CASE	2 m/s	34.5–49.9	-	39.4–54.9	-	44.3–59.9	-
1. HORIZ SIMPLE		−6.11–−6.18	−17.7–−12.4	−8.52–−8.6	−21.6–−15.7	−10.26–−10.88	−23.2–−18.2
2. HORIZ 30MM		−6.36–−6.79	−18.4–−13.6	−8.51–−9.32	−21.6–−17	−10.7–−11.7	−24.2–−19.5
3. HORIZ 60MM		−6–−6.37	−17.4–−12.8	−8.01–−8.73	−20.3–−15.9	−10.07–−10.68	−22.7–−17.8
4. VERT SIMPLE		−6.67–−6.17	−19.3–−12.4	−7.55–−8.26	−19.2–−15	−9.5–−10.38	−21.5–−17.3
5. VERT 30MM		−5.31–−6.21	−15.4–−12.4	−7.27–−8.3	−18.5–−15.1	−9.26–−10.42	−20.9–−17.4
6. VERT 60MM		−5.59–−4.48	−16.2–−9	−7.47–−8.14	−19–−14.8	−9.39–−10.13	−21.2–−16.9
0. BASE CASE	3 m/s	31.4–46.8	-	35.2–50.7	-	39.1–54.7	-
1. HORIZ SIMPLE		−4.88–−5.24	−15.5–−11.2	−6.72–−7.15	−19.1–−14.1	−8.53–−9.33	−21.8–−17.1
2. HORIZ 30MM		−5.3–−5.77	−16.9–−12.3	−7.17–−7.73	−20.3–−15.2	−9–−9.7	−23–−17.7
3. HORIZ 60MM		−5.11–−5.49	−16.3–−11.7	−6.85–−7.56	−19.4–−14.9	−8.62–−9.2	−22.1–−16.8
4. VERT SIMPLE		−4.59–−5.16	−14.6–−11	−6.33–−6.92	−18–−13.6	−7.96–−8.69	−20.4–−15.9
5. VERT 30MM		−5–−5.38	−15.9–−11.5	−6.7–−7.21	−19–−14.2	−8.41–−9.04	−21.5–−16.5
6. VERT 60MM		−4.53–−5.06	−14.4–−10.8	−6.08–−6.54	−17.2–−12.9	−7.64–−8.21	−19.5–−15
0. BASE CASE	4 m/s	29.2–44.6	-	32.4–47.8	-	35.5–51.1	-
1. HORIZ SIMPLE		−3.92–−4.07	−13.4–−9.1	−5.41–−5.68	−16.7–−11.9	−6.88–−7.57	−19.4–−14.8
2. HORIZ 30MM		−4.25–−4.75	−14.5–−10.6	−5.77–−5.87	−17.8–−12.3	−7.26–−7.94	−20.5–−15.5
3. HORIZ 60MM		−4.16–−4.53	−14.2–−10.2	−5.58–−5.76	−17.2–−12	−7.02–−7.58	−19.8–−14.8
4. VERT SIMPLE		−3.66–−4.05	−12.5–−9.1	−4.92–−5.41	−15.2–−11.3	−6.21–−6.8	−17.5–−13.3
5. VERT 30MM		−4.13–−4.49	−14.1–−10.1	−5.53–−6.02	−17.1–−12.6	−6.95–−7.56	−19.6–−14.8
6. VERT 60MM		−3.46–−3.72	−11.8–−8.3	−4.64–−4.98	−14.3–−10.4	−5.84–−6.24	−16.5–−12.2
0. BASE CASE	5 m/s	27.7–43.1	-	30.4–45.8	-	33–48.5	-
1. HORIZ SIMPLE		−3.15–−3.54	−11.4–−8.2	−4.38–−4.87	−14.4–−10.6	−5.56–−6.15	−16.9–−12.7
2. HORIZ 30MM		−3.64–−3.82	−13.1–−8.9	−4.87–−5.11	−16.1–−11.2	−6.1–−6.41	−18.5–−13.2
3. HORIZ 60MM		−3.41–−3.73	−12.3–−8.7	−4.57–−4.9	−15.1–−10.7	−5.76–−6.21	−17.5–−12.8
4. VERT SIMPLE		−2.95–−3.25	−10.6–−7.6	−3.95–−4.36	−13–−9.5	−4.98–−5.47	−15.1–−11.3
5. VERT 30MM		−3.42–−3.73	−12.3–−8.7	−4.59–−4.99	−15.1–−10.9	−5.75–−6.26	−17.4–−12.9
6. VERT 60MM		−2.62–−2.73	−9.4–−6.3	−3.52–−3.68	−11.6–−8	−4.42–−4.61	−13.4–−9.5

The results showed that for the studied wind conditions, the perforations did not improve the temperature of the PV panel when the fins were vertical. In addition, in the case of vertical fins, the larger perforations (Φ = 60 mm) were better, while for the horizontal fins the smaller ones (Φ = 30 mm) were better.

In terms of efficiency and power production, according to the assumption that the efficiency dropped linearly with the rise in temperature of −0.37%/°C [43], the following power production could be achieved—Table 7.

Table 7. Percentage of maximum power production achieved by the PV panel for each studied case.

Case	v_{air}	G = 600 W/m^2	G = 800 W/m^2	G = 1000 W/m^2
		of P_m at 25 °C, for t_{air} = 20–35 °C		
		%	%	%
0. BASE CASE	1 m/s	94.33–88.58	91.8–85.98	89.23–83.33
1. HORIZ SIMPLE		96.56–91.76	94.84–90.25	93.12–88.68
2. HORIZ 30MM		96.91–91.78	95.32–90.28	93.69–88.74
3. HORIZ 60MM		96.68–91.77	94.96–89.7	93.25–88.71
4. VERT SIMPLE		96.55–91.24	94.79–89.59	93.02–87.92
5. VERT 30MM		96–90.95	94.17–89.16	92.38–87.37
6. VERT 60MM		96.49–91.16	94.7–89.16	92.92–87.35
0. BASE CASE	2 m/s	96.48–90.79	94.68–88.95	92.87–87.09
1. HORIZ SIMPLE		98.74–93.08	97.84–92.13	96.67–91.11
2. HORIZ 30MM		98.83–93.3	97.83–92.39	96.83–91.42
3. HORIZ 60MM		98.7–93.15	97.65–92.18	96.6–91.04
4. VERT SIMPLE		98.95–93.07	97.47–92	96.39–90.93
5. VERT 30MM		98.44–93.09	97.37–92.02	96.3–90.94
6. VERT 60MM		98.55–92.45	97.45–91.96	96.35–90.83
0. BASE CASE	3 m/s	97.63–91.95	95.71–89.19	94.79–89.01
1. HORIZ SIMPLE		99.44–93.88	98.53–92.2	97.95–92.46
2. HORIZ 30MM		99.59–94.08	98.71–92.44	98.12–92.6
3. HORIZ 60MM		99.52–93.98	98.58–92.37	97.98–92.41
4. VERT SIMPLE		99.33–93.85	98.36–92.1	97.74–92.23
5. VERT 30MM		99.48–93.93	98.52–92.22	97.91–92.36
6. VERT 60MM		99.31–93.82	98.26–91.94	97.62–92.05
0. BASE CASE	4 m/s	98.43–92.74	96.54–89.26	96.12–90.35
1. HORIZ SIMPLE		99.88–94.25	99.09–91.94	98.67–93.15
2. HORIZ 30MM		100–94.5	99.25–92.02	98.81–93.29
3. HORIZ 60MM		99.97–94.42	99.16–91.97	98.72–93.15
4. VERT SIMPLE		99.79–94.24	98.85–91.81	98.42–92.86
5. VERT 30MM		99.96–94.41	99.14–92.09	98.69–93.14
6. VERT 60MM		99.71–94.12	98.72–91.61	98.28–92.66
0. BASE CASE	5 m/s	98.98–93.32	97.22–89.21	96.12–90.35
1. HORIZ SIMPLE		100.15–94.63	99.5–91.74	99.11–93.59
2. HORIZ 30MM		100.33–94.74	99.75–91.86	99.31–93.69
3. HORIZ 60MM		100.25–94.7	99.6–91.76	99.18–93.61
4. VERT SIMPLE		100.07–94.52	99.27–91.47	98.9–93.34
5. VERT 30MM		100.25–94.7	99.6–91.8	99.18–93.63
6. VERT 60MM		99.95–94.33	99.05–91.12	98.69–93.02

The power production was calculated as the percentage of maximum power possible, by assuming that at 25 °C the ratio achieved was 100% (320 Wp in STCs). From here on, we considered that the rise of temperature determined a drop in power production for each degree over t_{STC} = 25 °C, according to the PV panel's data sheet [43].

The most important effect of air cooling heat sinks was achieved in low wind conditions and high levels of solar radiation. It could be observed, Table 7, that for v_{air} = 1 m/s, G = 1000 W/m^2 and ambient temperature t_{air} = 35 °C, the percentage of maximum power production achieved was 83.33% for the base case, while the best cooling scenario (Case 3—horizontal 30 mm) could reach 88.74%. This meant a rise in power production of 6.49% compared to the base case.

For the position of the PV panel and wind direction studied in the paper, the best solution of heat sink for various conditions was the following: Case 3—Horizontal 30 mm. For this type of heat sink, the enhancement of power production was also reached for higher wind velocities (2–5 m/s), but with lower impact: from 3.60–4.97%, compared to the base case.

When lower ambient temperatures were involved, the effect of the heat sinks was decreased, this was due to inferior operating temperatures of the PV panel that were reached for base case. Therefore, the improvement of the power production reached values in the range 3.31–4.99%.

6. Conclusions

The goal of this manuscript was to develop and use a numerical model regarding the passive cooling of PV panels through perforated and non-perforated heat sinks. The PV panel was studied in a fixed position and tilted at 45 degrees from the horizontal, with the wind direction towards its backside. The input parameters, such as solar radiation, ambient temperature and wind velocity, were varied during the study. A challenging approach was used in order to calibrate the base case of the numerical model according to the NOCT parameters of the studied PV panel. A second validation of the accuracy of the numerical simulation consisted of comparison between the results obtained for the case of the heat sink with horizontal non-perforated fins and the experiments presented in the literature. Six types of heat sinks attached to the backside of the PV panel were numerically studied. The analyzed configurations focused on heat sinks with both perforated and non-perforated fins that were distributed horizontally and vertically. The CFD simulation was also conducted by modeling the air volume around the PV panel in real wind conditions. The main output parameters were the average temperature and the convective heat transfer coefficient on the front and back of the PV panel. In the best scenario, the perforated heat sink could assure a rise of the photovoltaic panel power production of 6.49%, compared to the base case.

Author Contributions: Conceptualization, S.V.H., F.E.Ț. and N.C.C.; methodology, S.V.H., F.E.Ț. and N.C.C.; software, S.V.H. and F.E.Ț.; validation, S.V.H., F.E.Ț., N.C.C. and I.H.; formal analysis, S.V.H. and I.H.; investigation, S.V.H., F.E.Ț., N.C.C., C.G.P., M.V. and I.H.; resources, S.V.H., F.E.Ț. and C.G.P.; data curation, S.V.H., F.E.Ț. and I.H.; writing—original draft preparation, S.V.H., F.E.Ț., N.C.C., C.G.P., M.V. and I.H.; writing—review and editing, S.V.H., F.E.Ț., N.C.C., C.G.P., M.V. and I.H.; visualization, S.V.H. and I.H.; supervision, S.V.H. and M.V.; project administration, S.V.H.; funding acquisition, S.V.H. All authors have read and agreed to the published version of the manuscript.

Funding: This work was supported by a grant of the Romanian Ministry of Education and Research, CCCDI-UEFISCDI, project number PN-III-P2-2.1-PED-2019-1294, within PNCDI III.

Institutional Review Board Statement: Not applicable.

Informed Consent Statement: Not applicable.

Data Availability Statement: Not applicable.

Acknowledgments: We would like to acknowledge the invaluable support provided by the FCI-TUIASI infrastructure in writing this article.

Conflicts of Interest: The authors declare no conflict of interest.

Nomenclature

STC	Standard test conditions
NOCT	Nominal operating cell temperature
AM	Air mass
t_{PV}	Cell temperature [°C]
G	Solar irradiance [W/m^2]
t_{air}	Ambient temperature [°C]
v_{air}	Wind speed towards backside of PV panel [m/s]
t_{NOCT}	Cell temperature in NOCT conditions [°C]
t_{STC}	Cell temperature in STC conditions [°C]
P_{mp}	Maximum power produced [Wp]
V_{mp}	Voltage at P_{mp} [V]
I_{mp}	Current at P_{mp} [A]
V_{oc}	Open circuit voltage [V]
I_{sc}	Short-circuit current [A]
η	PV panel efficiency [%]
β	P_{mp} temperature coefficient [%/°C]
L	Length of PV panel [m]
l	Width of PV panel [m]
h	Thickness of PV panel [m]
g	Thickness of the layers composing the PV panel [m]
λ	Thermal conductivity of the layers composing the PV panel [W/m·K]
ρ	Density of the layers composing the PV panel [kg/m^3]
c_p	Specific heat of the layers composing the PV panel [J/kg·K]
s	Distance between the fins of PV panel [m]
L_{fins}	Length of the fins [m]
h_{fins}	Height of the fins [m]
Φ	Diameter of the perforations of the fins [m]
d	Distance between the centers of the perforations [m]
$h_{c,front}$	Convective heat transfer coefficient on the front of PV panel [W/m^2·K]
$h_{c,back}$	Convective heat transfer coefficient on the back of PV panel [W/m^2·K]

References

1. 100 Days of Possibility. Available online: https://www.overshootday.org (accessed on 15 November 2021).
2. AlAmri, F.; AlZohbi, G.; AlZahrani, M.; Aboulebdah, M. Analytical Modeling and Optimization of a Heat Sink Design for Passive Cooling of Solar PV Panel. *Sustainability* **2021**, *13*, 3490. [CrossRef]
3. Taylor, M.; Ralon, P.; Ilas, A. The Power to Change: Solar and Wind Cost Reduction Potential to 2025. 2016. Available online: https://www.irena.org/publications/2016/Jun/The-Power-to-Change-Solar-and-Wind-Cost-Reduction-Potential-to-2025 (accessed on 15 November 2021).
4. Kuznetsov, P.; Yuferev, L.; Voronin, D.; Panchenko, V.A.; Jasiński, M.; Najafi, A.; Leonowicz, Z.; Bolshev, V.; Martirano, L. Methods Improving Energy Efficiency of Photovoltaic Systems Operating under Partial Shading. *Appl. Sci.* **2021**, *11*, 10696. [CrossRef]
5. Colarossi, D.; Principi, P. Indoor and Outdoor Performance of an Enhanced Photovoltaic Panel through Graphene/Fins/Phase Change Materials. *Appl. Sci.* **2021**, *11*, 8807. [CrossRef]
6. Why Europe's Energy Prices Are Soaring and Could Get Much Worse. Available online: https://www.euronews.com/2021/10/28/why-europe-s-energy-prices-are-soaring-and-could-get-much-worse (accessed on 15 November 2021).
7. Kamuyu, W.C.L.; Lim, J.R.; Won, C.S.; Ahn, H.K. Prediction Model of Photovoltaic Module Temperature for Power Performance of Floating PVs. *Energies* **2018**, *11*, 447. [CrossRef]
8. Idoko, L.; Anaya-Lara, O.; McDonald, A. Enhancing PV modules efficiency and power output using multi-concept cooling technique. *Energy Rep.* **2018**, *4*, 357–369. [CrossRef]
9. Dubey, S.; Sarvaiya, J.N.; Seshadri, B. Temperature Dependent Photovoltaic (PV) Efficiency and Its Effect on PV Production in the World—A Review. *Energy Procedia* **2013**, *33*, 311–321. [CrossRef]
10. Skoplaki, E.; Palyvos, J.A. On the temperature dependence of photovoltaic module electrical performance: A review of efficiency/power correlations. *Sol. Energy* **2009**, *83*, 614–624. [CrossRef]
11. Popovici, C.G.; Hudisteanu, S.V.; Mateescu, T.D.; Chereches, N.C. Efficiency improvement of photovoltaic panels by using air cooled heat sinks. *Energy Procedia* **2016**, *85*, 425–432. [CrossRef]
12. Berthod, C.; Strandberg, R.; Odden, J.O. Temperature coefficients of compensated silicon solar cells—Influence of ingot position and blend-in-ratio. *Energy Procedia* **2015**, *77*, 15–20. [CrossRef]

13. Hernandez-Perez, J.G.; Carrillo, J.G.; Bassam, A.; Flota-Banuelos, M.; Patino-Lopez, L.D. A new passive PV heatsink design to reduce efficiency losses: A computational and experimental evaluation. *Renew. Energy* **2020**, *147*, 1209–1220. [CrossRef]
14. Photovoltaic (PV) module performance testing and energy rating—Part 1: Irradiance and temperature performance measurements and power rating. In *International Standard*; IEC 61853-1; International Electrotechnical Commission: Geneva, Switzerland, 2011.
15. Gomaa, M.R.; Hammad, W.; Al-Dhaifallah, M.; Rezk, H. Performance enhancement of grid-tied PV system through proposed design cooling techniques: An experimental study and comparative analysis. *Sol. Energy* **2020**, *211*, 1110–1127. [CrossRef]
16. Nizetic, S.; Grubisic-Cabo, F.; Marinic-Kragic, I.; Papadopoulos, A.M. Experimental and numerical investigation of a backside convective cooling mechanism on photovoltaic panels. *Energy* **2016**, *111*, 211–225. [CrossRef]
17. Haidar, Z.A.; Orfi, J.; Kaneesamkandi, Z. Experimental investigation of evaporative cooling for enhancing photovoltaic panels efficiency. *Results Phys.* **2018**, *11*, 690–697. [CrossRef]
18. Herrando, M.; Pantaleo, A.M.; Wang, K.; Markides, C.N. Solar combined cooling, heating and power systems based on hybrid PVT, PV or solar-thermal collectors for building applications. *Renew. Energy* **2019**, *143*, 637–647. [CrossRef]
19. Ibrahim, A.; Fudholi, A.; Sopian, K.; Othman, M.Y.; Ruslan, M.H. Efficiencies and improvement potential of building integrated photovoltaic thermal (BIPVT) system. *Energy Convers. Manag.* **2014**, *77*, 527–534. [CrossRef]
20. Lamnatou, C.; Notton, G.; Chemisana, D.; Cristofari, C. Storage systems for building-integrated photovoltaic (BIPV) and building-integrated photovoltaic/thermal (BIPVT) installations: Environmental profile and other aspects. *Sci. Total Environ.* **2020**, *699*, 134269. [CrossRef]
21. Albatayneh, A.; Jaradat, M.; Al-Omary, M.; Zaquot, M. Evaluation of Coupling PV and Air Conditioning vs. Solar Cooling Systems—Case Study from Jordan. *Appl. Sci.* **2021**, *11*, 511. [CrossRef]
22. Hudișteanu, S.V.; Popovici, C.G. Numerical analysis of the efficiency and energy production of the building integrated photovoltaics for various configurations. In Proceedings of the CLIMA 2019 Congress, *E3S Web of Conf.*, Bucharest, Romania, 26–29 May 2019; Volume 111, p. 03044.
23. Hudișteanu, S.V.; Popovici, C.G. Experimental investigation of the wind direction influence on the cooling of photovoltaic panels integrated in double skin façades. In Proceedings of the CLIMA 2019 Congress, *E3S Web of Conf.*, Bucharest, Romania, 26–29 May 2019; Volume 111, p. 03045.
24. Bahaidarah, H.M.S. Experimental performance evaluation and modeling of jet impingement cooling for thermal management of photovoltaics. *Sol. Energy* **2016**, *135*, 605–617. [CrossRef]
25. Bai, A.; Popp, J.; Balogh, P.; Gabnai, Z.; Palyi, B.; Farkas, I.; Pinter, G.; Zsiboracs, H. Technical and economic effects of cooling of monocrystalline photovoltaic modules under Hungarian conditions. *Renew. Sustain. Energy Rev.* **2016**, *60*, 1086–1099. [CrossRef]
26. Ebrahimi, M.; Rahimi, M.; Rahimi, A. An experimental study on using natural vaporization for cooling of a photovoltaic solar cell. *Int. Commun. Heat Mass Transf.* **2015**, *65*, 22–30. [CrossRef]
27. Eicker, U.; Pietruschka, D.; Schmitt, A.; Haag, M. Comparison of photovoltaic and solar thermal cooling systems for office buildings in different climates. *Sol. Energy* **2015**, *118*, 243–255. [CrossRef]
28. Aelenei, L.; Pereira, R.; Ferreira, A.; Goncalves, H.; Joyce, A. Building Integrated Photovoltaic System with integral thermal storage: A case study. *Energy Procedia* **2014**, *58*, 172–178. [CrossRef]
29. Hammami, M.; Torretti, S.; Grimaccia, F.; Grandi, G. Thermal and Performance Analysis of a Photovoltaic Module with an Integrated Energy Storage System. *Appl. Sci.* **2017**, *7*, 1107. [CrossRef]
30. Bevilacqua, P.; Perrella, S.; Cirone, D.; Bruno, R.; Arcuri, N. Efficiency Improvement of Photovoltaic Modules via Back Surface Cooling. *Energies* **2021**, *14*, 895. [CrossRef]
31. Arifin, Z.; Tjahjana, D.; Hadi, S.; Rachmanto, R.A.; Setyohandoko, G.; Sutanto, B. Numerical and Experimental Investigation of Air Cooling for Photovoltaic Panels Using Aluminum Heat Sinks. *Int. J. Photoenergy* **2020**, *2020*, 1574274. [CrossRef]
32. Hudișteanu, S.V.; Mateescu, T.D.; Chereches, N.C.; Popovici, C.G. Numerical study of air cooling photovoltaic panels using heat sinks. *Rom. J. Civ. Eng.* **2015**, *6*, 11–20.
33. Fatoni, E.K.A.; Taqwa, A.; Kusumanto, R.; Polytechn Sriwijaya, P.S.S.I. Solar Panel Performance Improvement using Heatsink Fan as the Cooling Effect. In Proceedings of the 2nd Forum in Research, Science, and Technology (FIRST), Palembang, Indonesia, 30–31 October 2018.
34. Arifin, Z.; Suyitno, S.; Tjahjana, D.; Juwana, W.E.; Putra, M.R.A.; Prabowo, A.R. The Effect of Heat Sink Properties on Solar Cell Cooling Systems. *Appl. Sci.* **2020**, *10*, 7919. [CrossRef]
35. Fahad, A.-A.; Taher, S.M.; Omar, F.A.-A.; Sajid, A.; Sadaqat, A.; Ijlal, S.A.; Richu, Z.; Tarek, S.K. Innovative technique for achieving uniform temperatures across solar panels using heat pipes and liquid immersion cooling in the harsh climate in the Kingdom of Saudi Arabia. *Alex. Eng. J.* **2021**, *61*, 1413–1424. [CrossRef]
36. Duan, J. A novel heat sink for cooling concentrator photovoltaic system using PCM-porous system. *Appl. Therm. Eng.* **2021**, *186*, 116522. [CrossRef]
37. Bayrak, F.; Oztop, H.F.; Selimefendigil, F. Effects of different fin parameters on temperature and efficiency for cooling of photovoltaic panels under natural convection. *Sol. Energy* **2019**, *188*, 484–494. [CrossRef]
38. Johnston, E.; Szabo, P.S.B.; Bennett, N.S. Cooling silicon photovoltaic cells using finned heat sinks and the effect of inclination angle. *Therm. Sci. Eng. Prog.* **2021**, *23*, 100902. [CrossRef]
39. Mojumder, J.C.; Chong, W.T.; Ong, H.C.; Leong, K.Y.; Abdullah Al, M. An experimental investigation on performance analysis of air type photovoltaic thermal collector system integrated with cooling fins design. *Energy Build.* **2016**, *130*, 272–285. [CrossRef]

40. Amr, A.A.R.; Hassan, A.A.M.; Abdel-Salam, M.; El-Sayed, A.M. Enhancement of photovoltaic system performance via passive cooling: Theory versus experiment. *Renew. Energy* **2019**, *140*, 88–103. [CrossRef]
41. Vittorini, D.; Cipollone, R. Fin-cooled photovoltaic module modeling—Performances mapping and electric efficiency assessment under real operating conditions. *Energy* **2019**, *167*, 159–167. [CrossRef]
42. Pérez Escobar, B.L.; Pérez Hernández, G.; Ocampo Ramírez, A.; Rojas Blanco, L.; Díaz Flores, L.L.; Vidal Asencio, I.; Hernández Perez, J.G.; Ramírez Morales, E. Analysis of Thermomechanical Stresses of a Photovoltaic Panel Using a Passive System of Cooling. *Appl. Sci.* **2021**, *11*, 9806. [CrossRef]
43. Available online: https://ae-solar.com/wp-content/uploads/2018/10/AE_Eclipse-Ultra-Black_HM6-60_310W-320W.pdf (accessed on 15 November 2021).
44. Nizetic, S.; Papadopoulos, A.M.; Giama, E. Comprehensive analysis and general economic-environmental evaluation of cooling techniques for photovoltaic panels, Part I: Passive cooling techniques. *Energy Convers. Manag.* **2017**, *149*, 334–354. [CrossRef]
45. Ansys Fluent Documentation, 2021-R1. Available online: https://www.ansys.com/products/fluids/ansys-fluent (accessed on 15 November 2021).
46. El Fouas, C.; Hajji, B.; Gagliano, A.; Tina, G.M.; Aneli, S. Numerical model and experimental validation of the electrical and thermal performances of photovoltaic/thermal plant. *Energy Convers. Manag.* **2020**, *220*, 112939. [CrossRef]
47. Nguyen, D.P.N.; Neyts, K.; Lauwaert, J. Proposed Models to Improve Predicting the Operating Temperature of Different Photovoltaic Module Technologies under Various Climatic Conditions. *Appl. Sci.* **2021**, *11*, 7064. [CrossRef]
48. Almuwailhi, A.; Zeitoun, O. Investigating the cooling of solar photovoltaic modules under the conditions of Riyadh. *J. King Saud Univ.-Eng. Sci.* **2021**, *186*, 116522. [CrossRef]
49. Mattar, S.J.; Kavian Nezhad, M.R.; Versteege, M.; Lange, C.F.; Fleck, B.A. Validation Process for Rooftop Wind Regime CFD Model in Complex Urban Environment Using an Experimental Measurement Campaign. *Energies* **2021**, *14*, 2497. [CrossRef]
50. Alizadeh, H.; Nazari, M.A.; Ghasempour, R.; Shafii, M.B.; Akbarzadeh, A. Numerical analysis of photovoltaic solar panel cooling by a flat plate closed-loop pulsating heat pipe. *Sol. Energy* **2020**, *206*, 455–463. [CrossRef]

Solar protection influence on dynamic insulation efficiency of double skin façades

Nelu-Cristian Cherecheș[1], *Cătălin George* Popovici[1], *Vasile Valerică* Cîrlan[1], and *Sebastian Valeriu* Hudișteanu[1,*]

[1]"Gheorghe Asachi" Technical University of Iaşi, Faculty of Civil Engineering and Building Services, Romania

Abstract. The objective of the study was to perform a numerical analysis in order to determine the best position for placing sunscreen inside the channel of a double skin façade insulation relative to dynamic insulation efficiency, using ANSYS-Fluent software. The analysis was performed for summer conditions in forced convection for two airspeed regimes inside the channel: 0.2m/s and respectively 0.5m/s. Regime is considered permanent and the only parameter changed is the position of the blinds in the channel. Results are shown by spectra and profiles of temperature and velocity in order to analyse thermodynamic behaviour of a double skin façade. The numerical results emphasize that effectiveness of sunscreen such as blinds, is proportional to the flow velocity inside the channel and inversely proportional to the distance from the outer glazing. Ranked as the most effective sun protection is when it is located at the outer glazing and air velocity at the entrance is 0.5m/s.

1 Introduction

Double skin façade coating (DSF) represents a modern solution for thermal protection of buildings. The façade consists in two layers of glazing, one towards the outside and the other towards the protected area of the building. The space between the two glass panels is often called "channel façade" [1].

The study conducted by Amir Hossein [2] recommends the intelligent façade for the further development of buildings with low energy consumption. Channel thickness varies from 5 centimetres to 2 meters L. Xu et al. [3] analysed channel thicknesses ranged from 0.5 meters to 1 meter. To enhance the effectiveness of the façade in summer, the channel is often vented. Ventilation must ensure reducing overheating in summer, and also reducing energy consumption in winter [4]. Another important component of this type of façade is sunscreen and protection types most commonly used are venetian blinds. In this way the level of natural light inside the building is also controlled. Relevant literature [5-7, 22] reveals studies on thermal behaviour and the flow of air through the double glass façade equipped with solar protection. These studies have focused on analysing the impact of sunscreen on temperature fields, depending on the position of the blinds and the angle of sun protection.

In the studies [8, 9], authors have analysed the behaviour of double skin façade for various configurations. These configurations must necessarily relate to external climatic conditions and those inside the building and a poor operation of the façade could lead to inappropriate results.

Numerical simulations on DSF [10-12] have shown that with the increasing channel thickness, thermal resistance of the façade also increases. This is due to the reduction of convective heat transfer coefficients of the bounding surfaces.

Heating and cooling air inside the channel in comparison with the inner glazed façade is analysed by [13]. Analysis shows heating and cooling loads as well as intermediate surface temperature estimation during three months (January, April, and July) for west-facing ordinary glass façade and high absorption glass. This configuration has lower heat loss in winter, in January, when the channel is closed, while in July this configuration has the smallest façade heat gains. Analysis of the glazing and the ventilation mode given by [13] was performed on 90 combinations of double skin façade glazing. The best results were obtained for triple glazing configuration inside the double skin façade.

The most important element of DSF is glass, and different glass properties are studied in [14]. Climatic conditions for the location of the building are very important in choosing the right type of glass.

Analysis of the cold climate façade was performed by [15] and the number of glass panels resulted in energy performance compared with double and triple glazing, of 22% and 24%. For four and five glass panels' energetic performance was higher, about 40% or 60%, due to external light and natural solar factor provided by the number of panels.

Increased energy consumption for buildings in Hong Kong, has led to the need to implement and study the behaviour of double skin façade. Studies were performed on calculating the value of heat transfer rate for

* Corresponding author: sebastian.hudisteanu@tuiasi.ro

© The Authors, published by EDP Sciences. This is an open access article distributed under the terms of the Creative Commons Attribution License 4.0 (http://creativecommons.org/licenses/by/4.0/).

commercial buildings by [16, 23]. The purpose of this study is to obtain a set of correction factors for the calculation of heat transfer rate for commercial buildings with air conditioning, double skin façade and naturally ventilated. For another study, also in Hong Kong [17] showed that photovoltaic panels placed in ventilated double façade glazing offers the lowest solar heat gain coefficient, while for non-ventilated ones, photovoltaic panels have a better coefficient and cuts heat loss.

Another channel ventilated façade system is presented in [18], which describes a new façade insulation for new buildings and renovated based on sandwich panels with ventilated channels. Calculations show that the configuration examined of the ventilated channel is able to provide a low humidity moisture content and good insulating properties of the walls.

The main objective of this study was to determine the sunscreen optimal position inside the channel façade. This analysis was conducted in relation to dynamic isolation efficiency ε [19] of the system at different flow rates.

2 Model Description

Main characteristics of the model are (Fig. 1):

- dimensions - 2.1m height, 1.5m length and 0.3m channel width;
- façade channel consisting of one exterior simple glass (2) of 6mm thickness and one interior double-glazed type window (3) with 27mm thickness, made of 2 layers of glass of 6mm respectively 5mm thickness and 16mm air interspace;
- venetian type blinds (8) – made of horizontal metallic adjustable blades of 25mm width and 22.5mm interspaces; positioned at 1/4 D behind exterior glazing;
- air flow balancing grilles, with 50% obscuration rate, mounted along the façade channel at both supply and exhaust in/out of the channel (6 and 7).

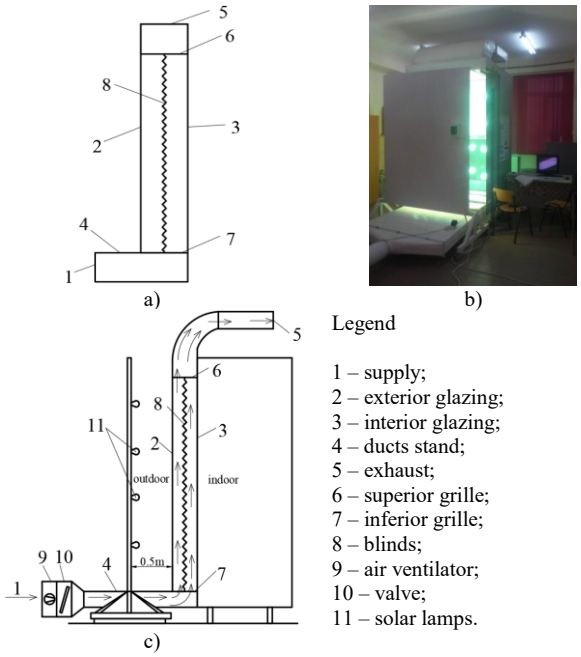


Fig. 1. Main characteristics of the model.

Thermo-physical properties of the façade component are shown in Table 1.

Table 1. Thermo-physical properties.

Component element		ρ	c_p	λ	a	τ	r
exterior glazing		2 500	670	5.3	0.11	0.82	0.07
air		1.225	1 006	0.0242	0	1	0
racks	steel	8 030	502.48	43	0.65	0*	0.35
blind	alum	2 719	871	202.4	0.76	0*	0.24
interior glazing		2 500	670	1.4	0.18	0.69	0.13
*during simulation, solar protection has been considered as semi-transparent surface with refractive coefficient assimilated with the corresponding percentage of free surface resulted for the blades opening angle.							

where:
ρ – Density [kg/m^3]
c_p - Specific heat [J/kg.K]
λ - Thermal conductivity [W/m.K]
a - Absorption index
τ - Refraction index
r - Reflection index

3 Numerical Hypothesis

Air system thermal behaviour simulation was performed considering the following climatic parameters:
- direct solar radiation intensity, normal at the surface of the façade, with a constant value of 285 W/m^2;
- diffuse solar radiation intensity: 82 W/m^2;
- exterior air temperature: 30°C;
- protected surface temperature: 25°C – constant.

Ventilation is achieved by forced convection channel with equivalent flow speed in input section of 0.2m/s respectively 0.5m/s.

Placement distance of the sunscreen related to exterior glass was: 1/4D; 2/4D and 3/4D.

Results were represented as velocity and temperature spectra in the middle section of the channel at H = 0.10m; H = 1.05m; H = 2m (10cm upstream and downstream, respectively input and output section and in the middle of the facade).

Accordingly, there was adopted k-epsilon turbulence model realizable. This model is specific for turbulent air movement because it corresponds with the predominant pressure and recirculation of air currents gradients configurations. Compared with k-epsilon model standard, this model contains alternative formula for the turbulent viscosity and modifies the transport equation for the dissipation rate ε. Studies have shown that this model was validated for configurations where pressure gradients and recirculation are prevalent [20].

The effect of solar radiation was simulated using (DO) model discrete coordinates that solves the radiation transfer equation for a finite number of discrete solid angles. This model is the only pattern that can specify direct and diffuse solar radiation, and is recommended

for tight spaces. DO is also the only pattern that allows calculation of the non-grey radiation using an approximation wavelength band for the radiation spectrum. Diffusion fraction (d_f) can be specified for each surface and can ascertain the amount of radiation reflected and transmitted by diffusion. For semi-transparent materials it is possible to specify an incident input radiation beam.

Solar protection was regarded as semi-transparent surface with incident radiation reduction factor of 0.75 corresponding to a 45° angle to inclination of the slats of the blind.

Numerical analysis was performed using Ansys-Fluent simulation program based on the control volume method using a SIMPLE algorithm.

An irregular structural mesh was chosen with small cells near the wall and solar protections with bigger cells inside airflow (Fig. 2). The calculation is an iterative one, convergence criteria chosen are 10^{-6} for temperature and 10^{-4} both for pressure and speed. An investigation on the input speed of the fluid was performed to study its influence on the heat flow and fluid transfer [21].

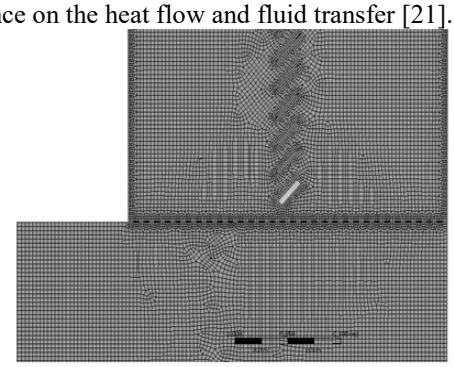


Fig. 2. Mesh of the model.

4 Modelling results

Place Solar protection divides the channel façade into two parallel channels of various thickness and thermo-aeraulic regimes depending on its position.

Results obtained are shown in the temperature spectra (Fig. 3 and Fig. 4) and respectively speed (Fig. 5 and Fig. 6).

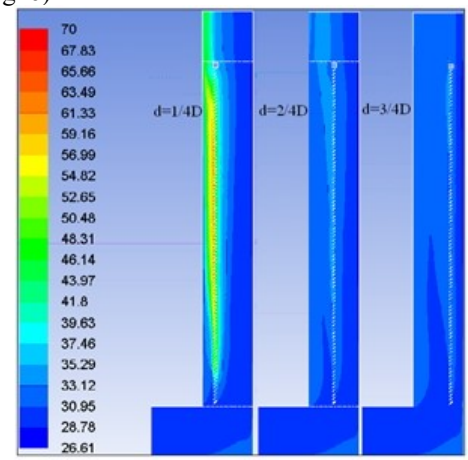


Fig. 3. Spectrum of temperature corresponding to inlet velocity of air of 0.2 m/s.

One can notice in Fig. 2 or Fig. 3 that the maximum temperatures are reached in the solar protection area, with values ranging between 70°C and 65°C, where the protection is placed to the exterior glazing. Blinds prevent heating the space between them and the inner glazing. The blades temperature is dropping when protection is shifted towards interior glazing, reaching 41°C for in the median area and remains approximately constant at around 40°C, when it is shifted towards the interior glazing. External channel air temperature starts growing through the median area of the façade, when placing the blind in 2/4D position, while positioning the blinds towards the interior glazing, outdoor air temperature channel of the façade is high, especially in the exhaust section.

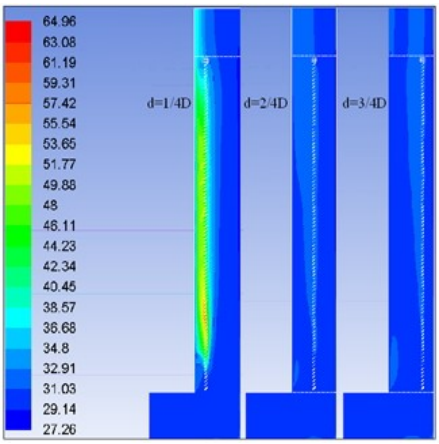


Fig. 4. Spectra of temperature for inlet velocity of 0.5 m/s.

Also, it is noted that once the air flow is increased or the input speed increases from 0.2m/s to 0.5m/s, the temperature of the outside of the façade channel is decreased by about 2°C when sunscreen is located near the middle of the channel or interior glazing. For location of the solar protection near the outside glazing, temperatures can reach values higher to 5°C.

For all three positions of placing the protection velocities are higher in the inner channel, Fig. 4 with values reaching 0.581m/s when the blinds are positioned near the inner glazing.

Maximum speed is reached as soon as the air passes the lower grille. In this way, the air velocity growth in the inner channel causes a lower temperature in this area.

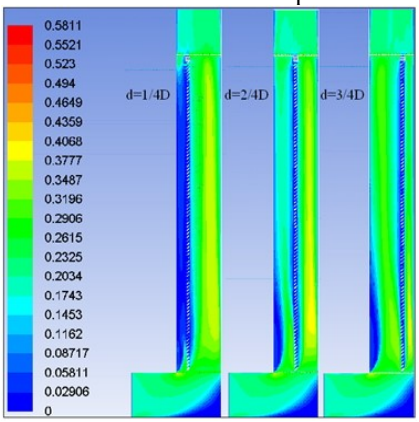


Fig. 5. Spectra of velocities for the three positions of solar protections inside the channels for inlet velocity of 0.2 m/s.

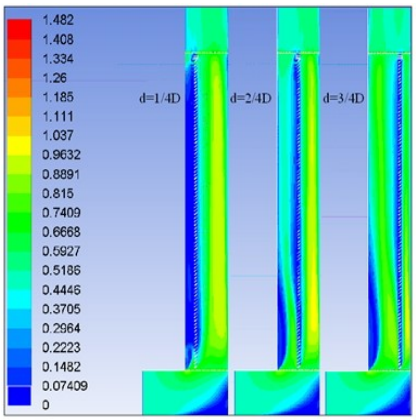


Fig. 6. Spectra of velocities for the three positions of solar protections inside the channels for inlet velocity of 0.5 m/s.

For this purpose, the values for the parameters studied were represented in three stationary regime control sections in the input, median and output of the façade channel.

The parameter values were determined for each regimen examined, on bounding surfaces inside channels with a step of D/12 (2.5cm).

From the analysis of diagrams, it is noticeable the increase in air temperature along the façade, in particular in the outer channel. In cross section, the temperatures are rising from exterior glazing towards solar protection, and it can be seen a reduction in temperature after the protection towards interior glazing.

This phenomenon is caused by the evolution of the airflow speed in the two channels, which are lower in the outer channel of the façade. Temperatures are dropping on sunscreen when blinds are placed towards interior glazing, ranging from 35…37°C to 31…32°C. For all cases studied, interior glazing surface temperature is between 27 to 30°C.

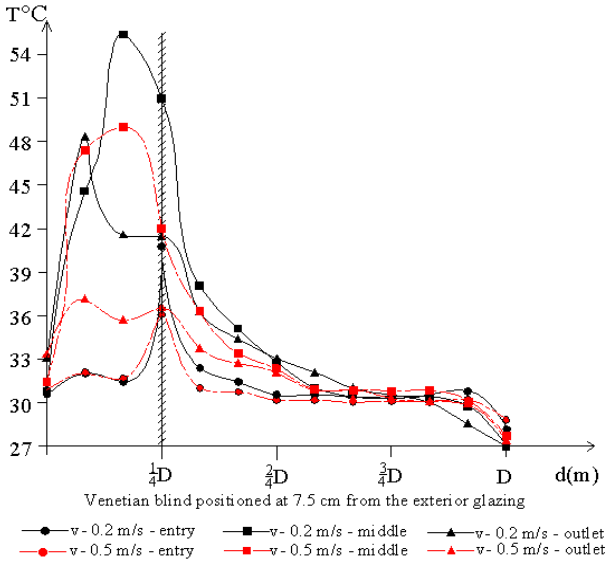


Fig. 7.a. Temperature variation curves for different position of solar protection: 1/4D .

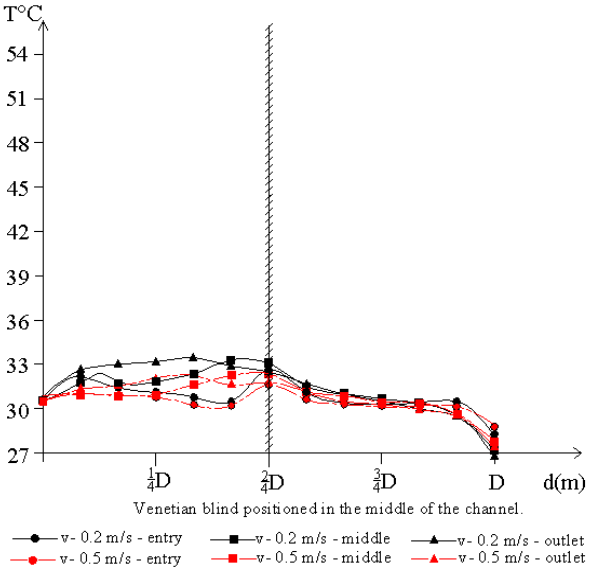


Fig. 7.b. Temperature variation curves for different position of solar protection: 2/4D.

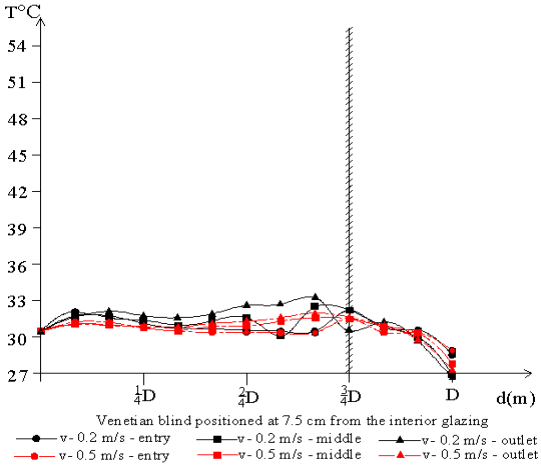


Fig. 7.c. Temperature variation curves for different position of solar protection: 3/4D.

This result is influenced by the fact that part of the incident energy is accumulated in the mass of metal protection, as well as by the reduced solar radiation flow due to the orientation of the blind.

The highest air temperature values are recorded in the middle section and exhaust air channel, for 0.2m/s and for 0.5m/s (Fig. 7a). For a placement of the protection at 7.5cm distance against interior glazing, temperatures become similar in all control sections for both inlet velocities. The exterior glazing temperatures are between 31°C and 34°C, while on the inner one they vary between 27°C and 30°C.

Whether sunscreen is positioned in the middle of the channel (Fig. 7b), the temperature inside inlet and outlet sections have the same values for both the input speed of 0.2m/s and to 0.5m/s. In addition, in Fig. 7b one can observed that the temperature of the exterior glazing is almost identical in all control sections without depending on inlet airflow. Interior glazing temperature varies in the same way as if the protection is placed towards exterior glazing.

When the sun protections are placed towards interior glazing (Fig. 7c), maximum temperature reaches 32.5°C up to 18°C lower than if the protection was placed towards exterior glazing. Protection surface temperature difference, when it is placed in the middle of the channel and to the outer glazing, is of only 0.5°C. Exterior glazing temperature is around 30.5°C for all sections studied, and for both speeds inlet. Interior glazing temperature varies between 26.5°C and 29°C.

Highest speeds are achieved in the middle section of the façade, inside inner channel, for inlet velocity rate of 0.2m/s and for 0.5m/s (Fig. 6 to Fig. 8). Average rates in outer channel of the façade are 10 times less than the rates achieved in the inner channel. Maximum speeds are reached near the inner glazing. For areas where sunscreens are located, speeds do not exceed values above 0.05m/s.

The evolution of phenomena throughout the height and width of the channel is suggestively represented in the temperature variation (Fig. 7) and the speed variation diagrams (Fig. 8).

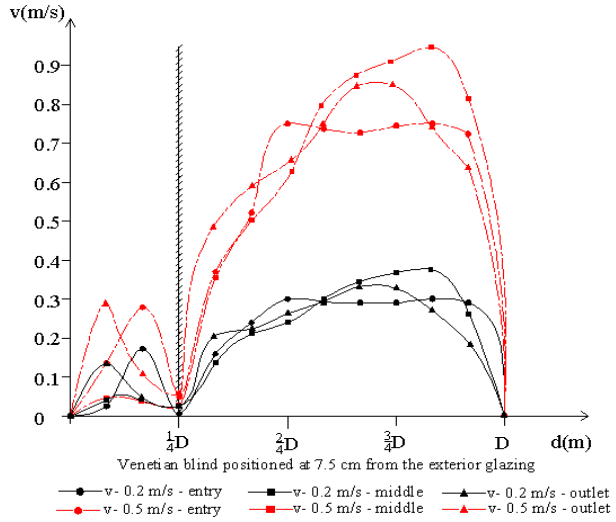


Fig. 8.a. Velocity variation curves for different position of solar protection 1/4D.

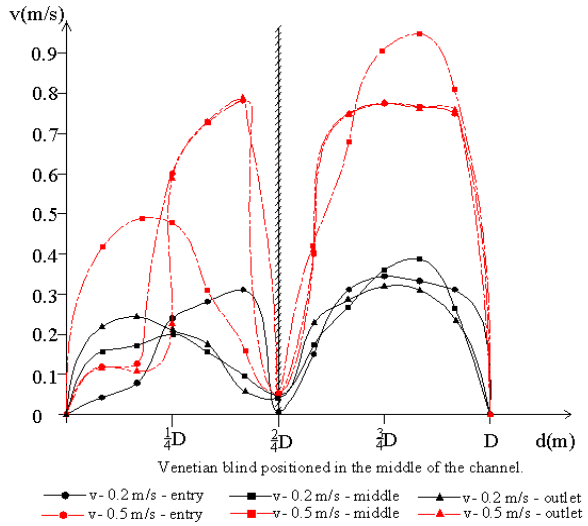


Fig. 8.b. Velocity variation curves for different position of solar protection 2/4D.

Average speed of the façade outer channel is about 0.134m/s, while inside inner channel is almost double, of 0.248m/s when the air is introduced at a speed of 0.2m/s. When the input speed is 0.5m/s, the average velocity is about 0.318m/s to the outer channel and 0.647m/s to the inner one (Fig. 8b). The speed value is recorded in the inner channel of the façade, with the value of 0.95m/s for inlet velocity of 0.5m/s. Therefore, speeds are approximately equal for the two façade channels, both at the inlet air flow rate corresponding to 0.2m/s, as well as for the one corresponding to an air flow rate of 0.5m/s (Fig. 8c). These values do not exceed 0.8m/s.

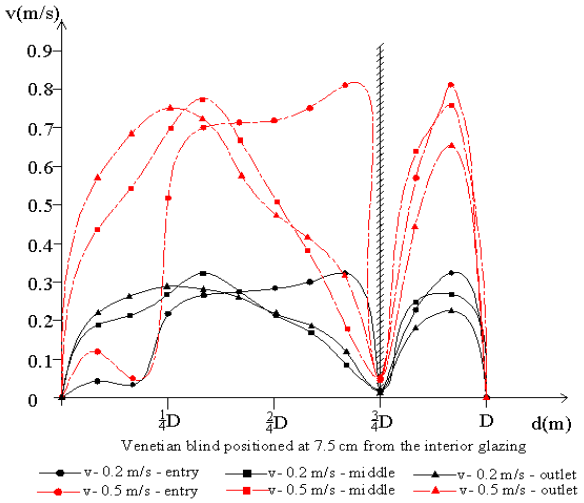


Fig. 8.c. Velocity variation curves for different position of solar protection 3/4D.

In all positions of the protection, speeds between blades do not exceed the value of 0.05m/s.

Sun protection was considered a semi-transparent surface and the refractive index is equated to the corresponding free surface percentage for an angle of 45° blinds opening.

For each position of the blind studied, dimensionless criteria values Re, Nu were calculated, and convective transfer coefficients (α) to the bounding elements surfaces respectively α_c (convective + radiative) inside façade channels (Table 2).

Table 2 presents the convective transfer coefficient values calculated according to the flow regime and the position of venetian blind for the two channels of the façade.

Table 2. Thermo-physical properties.

Config	Position	V_{med} [m/s]	T_{med} [°C]	Re	Nu	α_v [W/m^{2}K]	α_c [W/m^{2}K]
Ext. ch. V=0.2m/s	(1/4)D	0.023	45.7	166.38	1.42	12	0.242
	(2/4)D	0.134	32.1	1846.40	10.35	12	0.927
	(3/4)D	0.194	31.6	3845.60	18.65	12	1.156
Int. ch. V=0.2m/s	(1/4)D	0.251	34.1	4975.49	10.13	8	0.628
	(2/4)D	0.248	31.1	3417.22	17.03	8	1.525
	(3/4)D	0.189	30.9	1367.23	8.24	8	1.400
Ext. ch. V=0.5m/s	(1/4)D	0.029	42.3	209.78	1.73	12	0.294
	(2/4)D	0.318	31.6	4381.76	20.72	12	1.856
	(3/4)D	0.471	31.1	9336.48	38.02	12	2.357

Int. ch. V=0.5m/s	(1/4)D	0.657	33.1	13023.5	49.28	8	3.055
	(2/4)D	0.647	31.2	8915.09	36.65	8	3.283
	(3/4)D	0.518	30.7	3747.23	18.41	8	3.129

Convective transfer index varies between 0.242 and 1.156(W/m^{2}K) for exterior channel and inlet speed of 0.2m/s, and when inlet speed increases to 0.5m/s indexes values double for protection placements at 2/4D and 3/4D. Highest value of the convective exchange coefficient for the inner channel is recorded when protection is located in the middle of the channel, reaching the value of 3.28 (W/m^{2}K), while for other positions, the convective heat exchange coefficient has a close value, ranging between 3.05(W/m^{2}K) and 3.12(W/m^{2}K).

5 Dynamic insulation efficiency

For comparative and quantifies assessment of energetic effect of the blinds over thermal regime inside DFC susceptible to overheat during summer regime, dynamic insulation efficiency has been calculated, for each blade opening angle. Dynamic insulation efficiency is defined as ratio between heat flow of exhausted air and (Q_r) and total heat flow supplied inside the protected area (Q_{inc}).

$$\varepsilon = \frac{Q_r}{Q_{inc}} \tag{1}$$

Due to variable thermal regime, induced in the two compartments of façade by solar protection presence, total flow exhausted, Q_r, has been determined as sum of partial flows.

$$Q_{rc1} = m_{vc1} \times c_p \times \Delta t_{c1} \tag{2}$$

$$Q_{rc2} = m_{vc2} \times c_p \times \Delta t_{c2} \tag{3}$$

where:
m_{vc1} - mass exhausted airflow from the exterior channel;
m_{vc2} - mass air flow exhausted from inside interior channel;
c_p- air specific heat;
Δt_{c1}- difference between air temperatures at supply and exhaust from the exterior channel of the façade;
Δt_{c2}- difference between air temperatures at supply and exhaust from the interior channel of the façade.

Thermal flow received from the external environment supplied in the protected area, by radiation and convection, in double skin façade respectively is determined by the following equation:

$$Q_{inc} = \Pi \tau_i \times A \times I + k_{glo} \times \left(t_{ext} - t_{\text{int}}\right) + Q_{rc1} + Q_{rc2} \tag{4}$$

where:
$\Pi_{\tau i}$ - intermediate surfaces transmittance product;
k_{glo} - global heat transfer coefficient;
t_{int} - inside air temperature, in the protected space;
t_{ext} - outside air temperature;
I - global solar radiation component, normal along façade surface;
A - façade surface.

$$k_{glo} = \frac{1}{\Sigma R_i} = \frac{1}{\frac{1}{\alpha_{ext}} + \frac{1}{\alpha_{\text{int}}} + \Sigma \frac{\delta_i}{\lambda}} \tag{5}$$

where: R_i represent the thermal conductive, convective and radiative transfer trough façade elements.

Table 3 presents consecutive values of solar protection calculated accordingly relation no. (1), accordingly with position of solar protection in channel of double skin façade.

Mass air flow determined inside the façade channels (m_{vc1} and m_{vc2}) was studied according with average velocities for the chosen modelling hypothesis.

Incident solar radiation values over intermediate surfaces had been calculated according to glazing refraction indexes τ_i.

Table 3. Dynamic insulation efficiency.

No. crt.	Config.		$\Pi\tau_i \cdot A \cdot I$ [W]	k_{glo} [W]	m_{vc1} [kg/s]	m_{vc2} [kg/s]	Δt_{c1} [K]	Δt_{c2} [K]
1	v=0.2m/s	(1/4)D	60.47	0.072	0.0031	0.1037	10	1.9
		(2/4)D	90.07	0.076	0.037	0.0683	2	0.9
		(3/4)D	100.36	0.076	0.0802	0.0260	1.6	0.4
2	v=0.5m/s	(1/4)D	60.47	0.076	0.0039	0.271	5.9	1.2
		(2/4)D	90.07	0.077	0.0876	0.178	1.6	0.5
		(3/4)D	100.36	0.077	0.1947	0.0713	1.1	0.3

No. crt.	Config.		Q_{rc1} [W]	Q_{rc2} [W]	Q_r [W]	Q_{inc} [W]	ε [%]
1	v=0.2m/s	(1/4)D	31.90	198.29	**230.19**	**291.38**	**79**
		(2/4)D	74.34	61.91	**136.25**	**227.08**	**60**
		(3/4)D	129.15	10.48	**139.64**	**240.76**	**58**
2	v=0.5m/s	(1/4)D	23.15	327.29	**350.44**	**411.67**	**85**
		(2/4)D	141.13	89.73	**230.86**	**321.76**	**72**
		(3/4)D	215.54	21.55	**237.09**	**338.22**	**70**

Dynamic insulation efficiency varies between 58% and 85%. The optimal solution corresponds to the placement of sun protection at (1/4D), 7.5cm from the exterior glazing and air flow rate corresponding to air inlet velocity of 0.5m/s.

Variation of thermal-energy indexes characteristic for dynamic insulation efficiency ε, relative to placement of sun protection and air flow are shown in the following image (Fig. 9).

Analysing this image, dynamic insulation efficiency in summer decreases when protection is shifted towards the interior of the channel and is significantly influenced by the air flow.

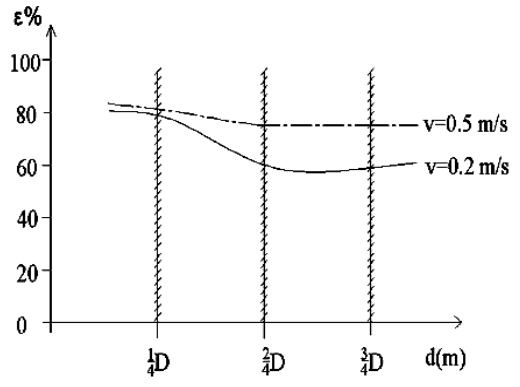


Fig. 9. Variation of dynamic insulation efficiency.

Convective transfer index varies between 0.242 and 1.156 W/m^{2}K for exterior channel and inlet speed of 0.2m/s, and when inlet speed increases to 0.5m/s indexes values double for protection placements at 2/4D and 3/4D. Highest value of the convective exchange coefficient for the inner channel is recorded when protection is located in the middle of the channel, reaching the value of 3.28 (W/m^{2}K), while for other positions, the convective heat exchange coefficient has a close value, ranging between 3.05(W/m^{2}K) and 3.12(W/m^{2}K).

6 Conclusions

This study analysed the influence of sun protection position inside the channel of a double-glazed façade in relation to dynamic insulation efficiency under summer conditions.

Analysing the numerical results, one can emphasize that effective sun protection, blind types, is directly proportional to the air flow speed inside the channel and inversely proportional to the distance against the outer glazing.

Ultimately, the best position of sunscreen with regards to dynamic insulation efficiency is towards exterior glazing, corresponding to an air velocity in inlet section of 0.5m/s.

References

1. Poirazis H, Double Skin Façades for Office Buildings – Literature Review. Lund University Sweeden; 2004

2. AmirHosein G, Umberto B, Ali G, Nastaran M, Intelligent Façades in Low-Energy Buildings. British Journal of Environment & Climate Change 2012:437-464

3. Xu L, Ojima T, Field experiments on natural energy utilization in a residential house with a double skin façade system. Building and Environment 2007;42(5):2014-2023

4. Ye P, Harrison SJ, Oosthuizen PH, Naylor D, Convective Heat Transfer from a Window with Venetian Blind: Detailed Modeling. Refrigerating and Air-Conditioning Engineers (ASHRAE) Transactions 1999;105(2):1031-1037

5. Collins M, Harrison SJ, Oosthuizen PH, Naylor D, Sensitivity Analysis of Heat Transfer from an Irradiated Window and Horizontal Louvered Blind Assembly. ASHRAE Trans 2002;108(1):503-511

6. Manz H, Schaelin A, Simmler H, Airflow patterns and thermal behaviour of mechanically ventilated glass double façades. Building and Environment 2004; 39:1023-1033.

7. Safer N, Modeling of double-skin façades types equipped with sunscreens: multiscale approaches. [PhD thesis]. Centre de Thermique de Lyon (CETHIL): Institut National des Sciences Appliquées de Lyon; 2006.

8. Kuznik F, Catalina T, Gauzere L, Woloszyn M, Roux JJ, Numerical modeling of combined heat transfers in a double skin façade-Full-scale laboratory experiment validation. Thermal engineering 2011;31(14-15):3043-3054

9. Andjelković AS, Cvjetković TB, Djaković DD, Stojanović IH, Development of simple calculation model for energy performance of double skin façades. Thermal Science 2012;16:251-267

10. Pasut W, De Carli M, Evaluation of various CFD modelling strategies in predicting airflow and temperature in a naturally ventilated double skin façade. Thermal Engineering 2012;37:267–274

11. Guohui G, Simulation of buoyancy-induced flow in open cavities for natural ventilation. Energy and Buildings 2006;38:410-420

12. Popa C, Ospir D, Fohanno S, Chereches C, Numerical simulation of dynamical aspects of natural convection flow in a double-skin façade. Energy and Buildings 2012;50:229-233

13. Ignjatović MG, Blagojević BD, Stojanović BV, Stojiljković MM, Influence of glazing types and ventilation principles in double skin façades on delivered heating and cooling energy during heating season in an office building. Thermal Science 2012;16:461-469

14. Perez-Grande I, Meseguer J, Alonso G, Influence of glass properties on the performance of double-glazed façades. Applied Thermal Engineering 2005;25(17-18):3163-3175

15. Thalfeldt M, Pikas E, Kurnitski J, Voll H, Façade design principles for nearly zero energy buildings in a cold climate. Energy and Buildings 2013;67:309-321

16. Chan ALS, Chow TT, Calculation of overall thermal transfer value (OTTV) for commercial buildings constructed with naturally ventilated double skin façade in subtropical Hong Kong. Energy and Buildings 2014;69:14-21

17. Jinqing P, Lin L, Hongxing Y, An experimental study of the thermal performance of a novel photovoltaic double-skin façade in Hong Kong. Solar Energy 2013;97:293-304

18. Nizovtsev MI, Belyi VT, Sterlygov AN, The façade system with ventilated channels, for thermal insulation of newly constructed and renovated buildings. Energy and Buildings 2014;75:60-69

19. Cherecheş M, Cherecheş NC, Hudişteanu S, Specific energy indicators for ventilated façades and glazed. Rev. Constructii 2012;2:24-30

20. Pleşca A, Thermal analysis of a traction system with double conducting points in steady state conditions. Electric Power Systems Research 2013;97:126-132

21. Wakil NE, Chereches NC, Padet J, Numerical study of heat transfer and fluid flow in a power transformer. International Journal of Thermal Sciences 2006;45:615-626

22. CG Popovici, VV Cirlan, TD Mateescu, NC Chereches, SV Hudisteanu, Influence of various angles

of the venetian blind on the efficiency of a double skin façade, Energy Procedia 85, 2016, 416-424

23. C Chereches, M Chereches, L Miron, S Hudisteanu, New criterion proposal for transition from natural to forced convection (prescribed wall flux), Energy Procedia 85, 2016, 109-117

Available online at www.sciencedirect.com

ScienceDirect

Energy Procedia 85 (2016) 416 – 424

Energy Procedia

Sustainable Solutions for Energy and Environment, EENVIRO - YRC 2015, 18-20 November 2015, Bucharest, Romania

Influence of various angles of the venetian blind on the efficiency of a double skin facade

Catalin George Popovici[a], Vasile Valerica Cirlan[a], Theodor Dorin Mateescu[a], Nelu-Cristian Chereches[a]*, Sebastian Valeriu Hudisteanu[a]

[a]*Faculty of Civil Engineering and Building Services, "Gheorghe Asachi" Technical University of Iasi, 13 Dimitrie Mangeron, Iasi, 700050, Romania*

Abstract

The present study analyses the effect of solar protection arrangements on thermo-aeraulic regime inside a double-glazed facade coating (DFC), forced ventilated channel and under imposed working conditions. The facade has been considered being with "full South" guidance, exposed to normal solar radiation, with constant intensity. The "Venetian blinds" protection type has been investigated in optimum assumptions on the basis of previous researches [9], with regard to its positioning at 1/4th of the width of the channel, near exterior glazing and forced ventilation, under constant flow rate of 1260 m^3/h. The opening angle of the blinds, as the sole variable parameter, has been amended in succession between 0° and 90°. Solar protection influence analysis has been carried out by numerical simulation, with the specialized computing program ANSYS-Fluent, laying down, for each opening angle of blinds, variation diagrams of air streams temperatures and velocity along the width and along front panel channels.

© 2016 The Authors. Published by Elsevier Ltd. This is an open access article under the CC BY-NC-ND license (http://creativecommons.org/licenses/by-nc-nd/4.0/).

Peer-review under responsibility of the organizing committee EENVIRO 2015

Keywords: Façade channel; solar protection; blinds angle; radiation; numerical analysis

1. Introduction

Recent technological developments have entailed glass as a highly used material for buildings envelope, due to its multiple and complex functions which transform glazing in an active component regarding from thermal, optical and electrical points of view [1].

* Corresponding author.
E-mail address: cristi_chereches@yahoo.com

1876-6102 © 2016 The Authors. Published by Elsevier Ltd. This is an open access article under the CC BY-NC-ND license (http://creativecommons.org/licenses/by-nc-nd/4.0/).
Peer-review under responsibility of the organizing committee EENVIRO 2015
doi:10.1016/j.egypro.2015.12.222

As far as functional-constructive point of view, double glazed façade arose out of the necessity of protecting a curtain wall by placing in front of it a glass surface. The envelope thus formed influences on the thermo-aeraulic behavior of the hole building – directly or indirectly - based on the connection manner applied between the two glazed surfaces and with inside and outside environments, and also, based on the ventilation solution chosen for the intermediate channel [2].

The two transparent glass elements, placed at a certain distance, form a channel where an air flow circulates [3] and inside which, as applicable, a shading system can be integrated, in order to control the heat quantity acquired from solar radiation [4, 5].

The main function of this system is to improve thermal protection during winter, by passive recovery of the solar energy and exhaust excessive heat accumulated during warm season [6].

The special importance of this system as far as buildings energy efficiency is concerned justifies the technical and scientific interest for thoroughgoing study and acknowledgment of functional outlines and solutions improvements.

In this regard, in the specialized literature are presented results of studies and researches carried out by teams of specialists all over the world that clarifies many of the issues of great interest, such as:

- recommended functional organizational design, geometry and dimensions;
- ventilation methods and functional scenarios;
- energy and comfort efficiency;
- calculation models;
- experimental testing on small scale or natural models and others.

Analyzing behavior of DFC equipped with solar protection is important as it allows identification of various phenomena that influence on system's efficiency [7, 8].

Thermal-aeraulic behavior of the façade depends equally on the geometry of the façade, the characteristics of its components, the ventilation system and the air flow regime inside the façade channels [5].

The main objective of the study was to determine, by numerical modeling, the optimum opening angle of solar protection type venetian blinds blades in relation to dynamic insulation efficiency (ε).

As in a previous study [9], in which the optimum position of the blinds inside the façade channel had been analyzed, resulting that, during summer conditions, maximum efficiency is achieved when blinds are closer to exterior glazing, the present study was developed taking into consideration the above mentioned conclusions.

Numerical analysis has been elaborated for a double glazed façade having the characteristics accordingly with experimental setup, Table 1, inside the laboratory of Building Services Engineering Department, Technical University "Gheorghe Asachi "of Iasi – Fig. 1 [10].

Table 1. Thermo-physical properties of components

Component element	Density ρ [kg/m^3]	Specific heat cp [J/kg·K]	Thermal conductivity λ[W/m·K]	Absorption index, a	Refractive index, τ	Reflection index, r
exterior glazing	2 500	670	5.3	0.11	0.82	0.07
air	1.225	1 006.43	0.0242	0	1	0
racks steel	8 030	502.48	43	0.65	0*	0.35
blinds aluminum	2 719	871	202.4	0.76	0*	0.24
interior glazing	2 500	670	1.4	0.18	0.69	0.13

*during simulation, solar protection has been considered as semi-transparent surface with refractive coefficient assimilated with the corresponding percentage of free surface resulted for the blades angle.

Main characteristics of the model are:

- dimensions- 2.1 m height, 1.5 m length, 30 cm channel width;

- façade channel consisting of one exterior simple glass (2) of 6 mm thickness and one interior double glazed type window (3) with 27 mm thickness, made of 2 layers of glass of 6 mm respectively 5 mm thickness and 16 mm air interspace;
- Venetian type blinds (8) – made of horizontal metallic adjustable blades of 25 mm width and 22,5 mm interspaces;-positioned at 1/4 D behind exterior glazing;
- Air flow balancing grilles, with 50% obscuration rate, mounted along the façade channel at both at supply and exhaust in/out of the channel (6 and 7).

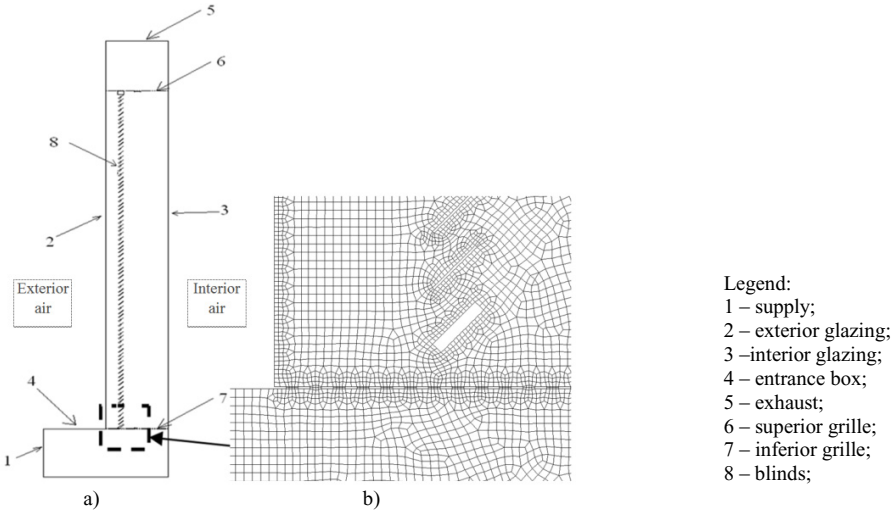


Fig. 1. Description of the geometry (a) and the mesh (b) of the model

2. Modeling hypothesis

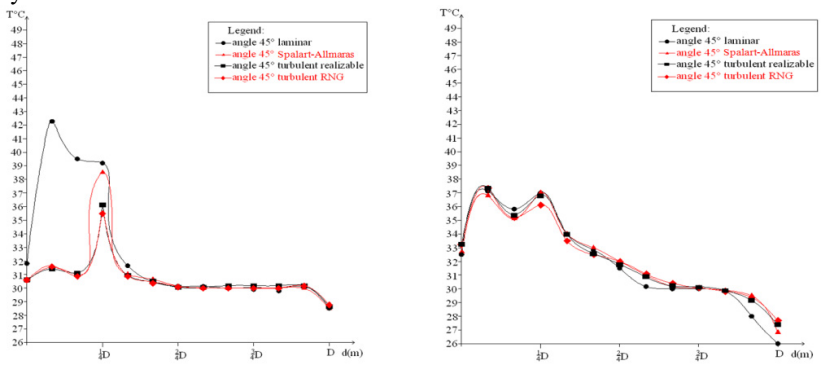
Modeling was carried out under permanent regime, for blades inclination angels of 0°, 30°, 45°, 60°, under the following hypotheses:

- direct solar radiation intensity imposed on exterior glass of the façade : 285 W/m^2;
- diffuse solar radiation intensity: 82 W/m^2;
- outside air temperature, T_e : 30°C (which is the inlet temperature for simulated cases) and convective heat transfer coefficient from the façade with exterior air, α_{ve} : 24 W/m^{2o}C;
- inside temperature, T_i : 25 °C and convective heat transfer coefficient from the façade with interior air, α_{vi} : 8 W/m^{2o}C;
- forced convection, with constant flow rate of 1260 m^3/h, according to the average velocity of 0.5 m/s at the inlet section and turbulence intensity of 4.7 %.

Numerical simulations were conducted with the program ANSYS-Fluent [12] based on control volumes method and using SIMPLE algorithm [13]. For meshing, has been used a non-uniform and rectangular mesh which has maximum face size of 0.0035 m, 96333 elements, 99301 nodes and 195779 faces. The height of the first cell, near the exterior and interior glass is 1.75 mm and the number of the prism layers in the boundary layer is 4.

In order to choose an appropriate model of turbulence were tested and analyzed different turbulence models (k-ε realizable, k-ε RNG and Spalart-Allmaras) and additionally the laminar model, for the opening angle of 45° (Fig. 2). Temperature variations were represented in Fig. 2 and we can observe that is no notable difference between the different turbulence models. Thus, it was chosen the use of k-ε realizable in all cases of study, which is widely used in computational fluid dynamics and validated for classical cases of turbulence flows including the channels with obstacles and layer flows [12].

For radiation, Discrete Ordinates model (DO) which solves the radiative transfer equation for a finite number of discrete solid angles, was adopted to simulate the radiation, being the only model where solar direct and diffuse radiation is mentioned. Calculation is iterative, having convergence limit of 10−6 for temperature and 10−4 for pressure and velocity.



a) supply section, 10 cm above inferior grille (H=0,10m); b) exhaust section, 10 cm beneath superior grille (H=2m)

Fig. 2. Temperature variations for turbulence models simulated

3. Results interpretation

Results are presented as velocity and temperatures spectra (Fig. 3), graphs variations (Fig. 4 and 5) and velocity vectors (Fig. 6), in the vertical median section of the facade, at H=0.10 m; H=1.05 m; H=2.00 m (10 cm upstream and downstream the supply/exhaust section and half façade), with a 2.5 cm step alongside façade width.

Analyzing the results given by the four versions of blades opening, we can underline the following aspects:

General

- Blinds blades opening induce local and transversal circulations between channels, comparatively more intense alongside the supply and exhaust section due to disruptive effect of distribution grilles (Fig. 3) and the spread difference between pressure and temperature;
- For opening angles of 45° and 60° transversal circulations are dominant.

Temperature related

- Temperature values differ along the façade, as they are obviously higher inside exterior channel and decreasing as we focus towards the glazing inside the interior channel;
- Temperature variation inside control sections is relatively uniform inside the interior channel unrelated to opening angles and more pronounced inside the exterior channel (Fig. 4);

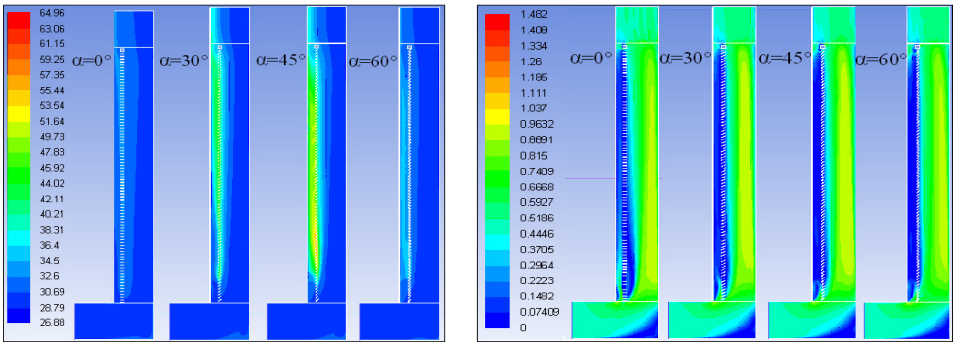
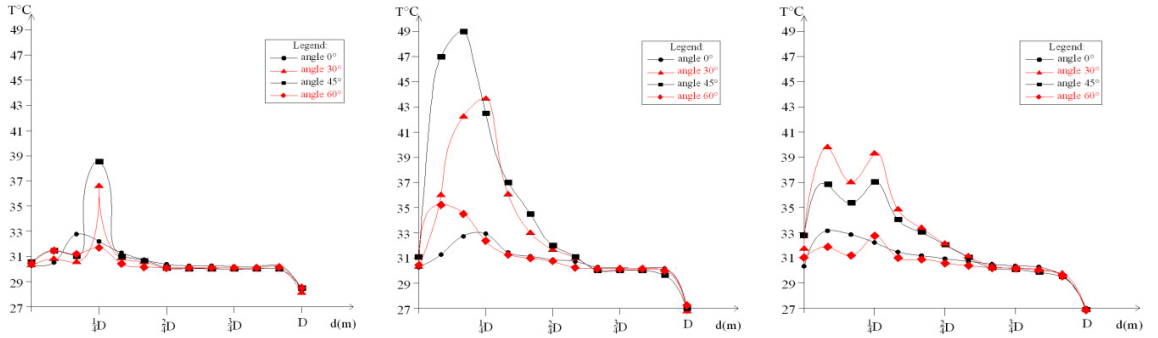


Fig. 3. Temperature (°C) and velocity spectrum (m/s)

- - Solar protection acts like a barrier for the radiative flow accumulating heat and reducing the air heating effect inside the channel and alongside interior glazing for opening angles wider than 30°;
- Maximum temperature along blinds is registered at 45° opening, reaching 65°C, when the minimum value is reached at 0° opening angle;
- Temperature specters are correlated with velocity specters as they are inversely proportionate;
- For all angles, inside glazing temperatures vary between 27 to 29°C, and outside glazing temperatures vary between 30 to 34°C;
- Air temperatures vary between 30 to 31°C in the axis of inside channel and between 31 to 40°C inside exterior channel.

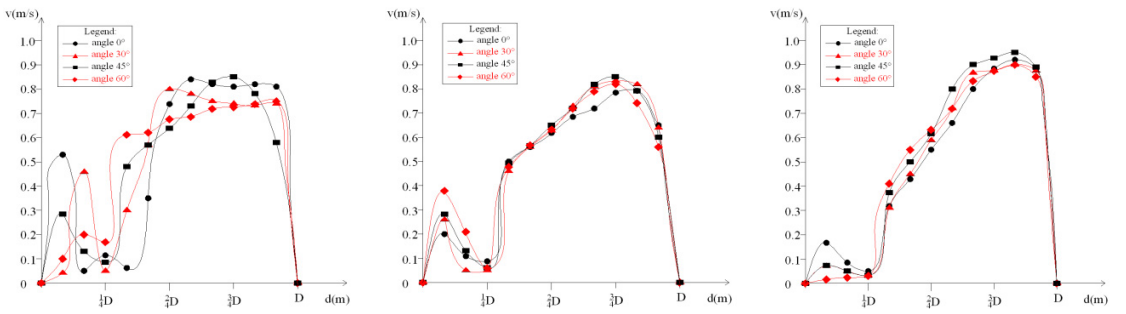


a) supply section, 10 cm above inferior grille (H=0,10m); b) middle section, halfway facade (H=1,05m); c) exhaust section, 10 cm beneath superior grille (H=2m).

Fig. 4. Temperature variation along channel width related with blinds opening angle

Velocity related

- Velocities vary alongside façade with significantly higher values inside the interior channel;
- Medium velocity values are between 0.52 m/s and 0.58 m/s for all sections inside the interior channel and between 0.10 m/s and 0.18 m/s inside exterior channel, (Fig. 5);
- Along control sections maximum values of velocities are registered along channel axis reaching up to 0.5 m/s inside exterior channel, respectively 1.0 m/s inside interior channel and decrease towards glazing and protection section;



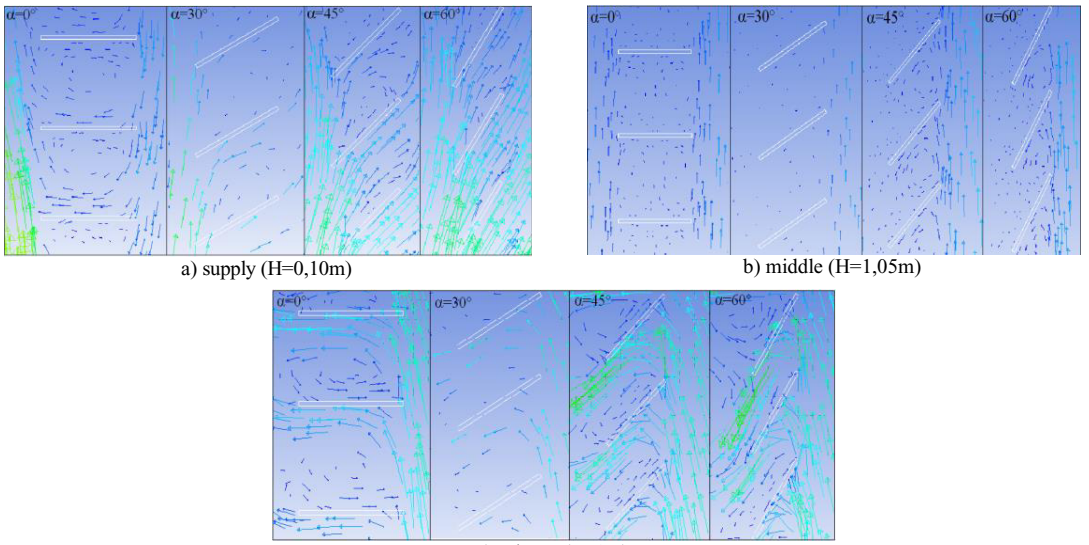
a) supply section, 10 cm above inferior grille (H=0,10m); b) exhaust section, 10 cm beneath superior grille (H=2m) c) middle section, halfway facade (H=1,05m);

Fig. 5. Velocity profiles

Mass transfer related

- Presence of sunscreen facade induces local turbulence and mass transfer between its channels, as shown in Fig. 5;
- Phenomenon intensity and direction of movement is influenced by the opening angle and the gap position control section temperature / pressure between the two channels;

- In the supply area the flow lines indicate transfer from the exterior to the interior channel;
- In the middle area are recorded, especially local circulation phenomena between blades, proportional to the opening angle;
- In the exhaust area the mass transfer is increases from the inner channel to the outer channel.



a) supply (H=0,10m) b) middle (H=1,05m)

c) exhaust (H=2m)

Fig. 6. Velocity spectrum recorded between blades

Table 2. Dimensionless numbers and convective heat transfer coefficients inside façade channel

No.	Façade configuration	Blade angle	V_{med} [m/s]	T_{med} [°C]	Re	Pr	Nu	α_v [W/m^2°C]	α_p [W/m^2 °C]	α_k [W/m^2 °C]
1	Exterior	0	0.182	31.96	1 316.6	0.77	6.43	24	2.31	0.56
	channel	30	0.103	38.72	745.10	0.77	4.08	24	1.45	0.35
		45	0.108	45.71	781.27	0.77	4.24	24	1.66	0.37
		60	0.023	34.21	166.38	0.77	1.23	24	1.93	0.10
2	Interior	0	0.718	30.6	14 232.7	0.77	43.20	8	2.31	1.34
	channel	30	0.740	32.03	14 668.79	0.77	44.26	8	1.45	1.37
		45	0.763	32.22	15 124.72	0.77	45.36	8	1.66	1.40
		60	0.728	30.43	14 430.92	0.77	43.68	8	1.93	1.35

For each blinds study position, dimensionless numbers, Re, Pr, Nu, values had been calculated, as well as convective heat transfer coefficients at surface bounding elements (Table 2) for the two façade channels related on flowing regime and surfaces temperatures, for each opening blades angles, where: αv, αp, αk represents convective heat transfer coefficients respectively from glass surfaces to exterior and interior air (αv), at the surface of the blades (αp) and from glass surfaces to air inside the channels (αk).

Convective transfer coefficient varies between 0.10 and 0.56 (W/m2K) for exterior glazing. The highest value of the convective exchange coefficient is registered at blades opening angles of 45°, reaching 1.40 (W/m2K), as for other angles, convective heat exchange coefficient remains steady around values between 1.37 (W/m2K) and 1.34 (W/m2K).

As far as interior glazing is concerned, coefficient value increases starting to 0° opening angle up to 45°, when it reaches the maximum value, followed by a decrease around de 60° angle.

4. Dynamic insulation efficiency

For comparative and quantifies assessment of energetic effect of the blinds over thermal regime inside DFC susceptible to overheat during summer regime, dynamic insulation efficiency has been calculated, for each blades opening angle. Dynamic insulation efficiency is defined as ratio between heat flow of exhausted air and (Q_r) and total heat flow supplied inside the protected area (Q_{inc}).

$$\varepsilon = \frac{Q_r}{Q_{inc}} \tag{1}$$

Due to variable thermal regime, induced in the two compartments of façade by solar protection presence, total flow exhausted, Q_r, has been determined as sum of partial flows.

$$Q_{rc1} = m_{vc1} \cdot c_p \cdot \Delta T_{c1} \tag{2}$$

$$Q_{rc2} = m_{vc2} \cdot c_p \cdot \Delta T_{c2} \tag{3}$$

where: m_{vc1} –mass exhausted airflow from the exterior channel; m_{vc2} –mass exhausted airflow from inside interior channel; c_p – air specific heat; Δt_{c1} – temperature difference between supply and exhaust air from the exterior channel of the facade; Δt_{c2} – temperature difference between supply and exhaust air from the interior channel of the facade.

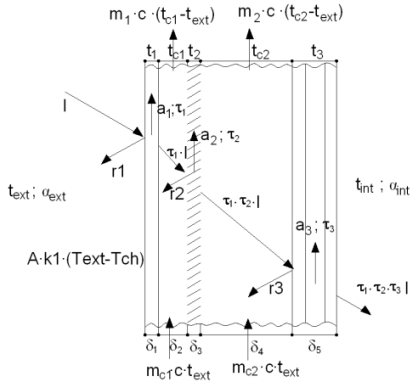
Thermal flow received from the external environment supplied in the protected area, by radiation and convection (Fig. 7), in double skin façade respectively is determined by the following equation:

$$Q_{inc} = \Pi \tau_i \cdot A \cdot I + k_{glo} \cdot \left(T_{ext} - T_{\text{int}}\right) + Q_{rc1} + Q_{rc2} \tag{4}$$

Where: $\Pi\tau_i$ – intermediate surfaces transmittance product; k_{glo} – global heat transfer coefficient; t_{int} – inside air temperature, in the protected space; t_{ext} - outside air temperature; I- global solar radiation component, normal along façade surface; A - façade surface.

$$k_{glo} = \frac{1}{\Sigma R_i} = \frac{1}{\frac{1}{\alpha_{ext}} + \frac{1}{\alpha_{\text{int}}} + \Sigma \frac{\delta_i}{\lambda}} \tag{5}$$

where R_i represent the thermal-conductive-convective and radiative transfer trough façade elements.



$$\varepsilon = \frac{\sum_{i=1}^{2} m_i c \cdot \left(t_{ci} - t_{ext}\right)}{A\left[k_{glob} \cdot \left(t_{ext} - t_{\text{int}}\right) + \prod_{j=1}^{3} \tau_j\right] I + \sum_{i=1}^{2} m_i c \cdot \left(t_{ci} - t_{ext}\right)}$$

Fig. 7. Energy flow schema along the facade

Table 3 presents consecutive values of solar protection calculated, accordingly with blades opening angle, Eq. (1).

Table 3. Dynamic insulation efficiency

No.	Angle of blinds	$\Pi\tau_i \times A \times I$ [W]	k_{glo} [W/m^{2}K]	m_{vc1} [kg/s]	m_{vc2} [kg/s]	Δt_{c1} [K]	Δt_{c2} [K]	Q_{rc1} [W]	Q_{rc2} [W]	Q_r [W]	Q_{inc} [W]	ε [%]
1	0°	632.70	0.077	0.0106	0.2269	2	0.9	21.33	205.52	226.85	859.73	26.4
2	30°	208.77	0.076	0.0057	0.2327	6.9	1.6	39.58	374.71	414.29	623.86	66.4
3	45°	158.12	0.070	0.0039	0.2716	5.9	1.2	23.15	328.01	351.17	509.83	68.9
4	60°	88.56	0.076	0.0023	0.2381	1.7	0.5	3.93	119.81	123.77	189.73	65.2

Dynamic insulation efficiency reaches the maxim value of 68.9% for an opening angle of 45°, and 26.4% for 0°, which can be stated that the blinds offer the best protection for an opening blades angle of 45 degrees. Mass air flow determined inside the façade channels (mvc1 and mvc2) was studied according with average velocities for the chosen modeling hypothesis.

Incident solar radiation values over intermediate surfaces had been calculated according to glazing refraction indexes τi.

Solar protection has been considered as a semi-transparent surface, reflection index being assimilated with free area ratio with regard to blades opening.

$$\tau = \frac{H - n \cdot b \cdot \sin\beta}{H} \tag{6}$$

where: n – number of blind blades; b – blade width; H – total height of solar protection; β – opening blinds blades angles.

5. Conclusions

In this paper, the influence of various angles of the venetian blind was studied in order to determine the efficiency of the double skin façade. The results consist of the optimum opening angle of solar protection.

Solar protection efficiency is directly proportional with air flow velocity inside façade channel and inversely with blades opening angle.

Opening blinds blades angles analysis for the interior surface of DFC reveals that the optimum opening angle is at 45 degrees, when the dynamic insulation efficiency reaches the maxim value of 68.9%.

References

[1]. Perez-Grande I., Meseguer J., Alonso G., Influence of glass properties on the performance of double-glazed façades, Applied Thermal Engineering 2005; 25: 3163-3175

[2]. Chan A. L. S., Chow T. T. , Fong K. F., Lin Z., Investigation on energy performance of double skin façade in Hong Kong Building, Energy and Environmental Technology Research Unit 2009; 41: 1135-1142

[3]. Padet J., Principes des transfer convectifs, Polytehnica, Paris, France; 1997.

[4]. Ye P., Harrison S.J., Oosthuizen P.H., Naylor D., Convective Heat Transfer from a Window with Venetian Blind: Detailed Modeling, Refrigerating and Air- Conditioning Engineers (ASHRAE) Transactions 1999; 105: 1031-1037

[5]. Safer N., Modeling of double-skin facades types equipped with sunscreens: multiscale approaches, (in french language), Institut National des Sciences Appliquées de Lyon, Centre de Thermique de Lyon (CETHIL), France, PhD Dissertation, 2006.

[6]. Arons D., Properties and Applications of Double-Skin Building Facades, Massachusetts Institute of Technology (MIT), USA; 2000

[7]. Hossein G., Mohammad G., Mahdi S., Meisam M., Mohammad M., Analytical solution for energy modeling of double skin facades building, Energy and Buildings 2012; 50: 158-165

[8]. Romila C., Popovici C. G., Chereches N.-C., Reduction of building energy consumption using ventilated façades, Environmental Engineering and Management Journal 2012; 4: 806-811

[9]. Cirlan V. V., Mateescu T., Chereches N. C., Popovici C., Location of this sunscreen in channel of double skin facades in relation to their energy eficiency, (in romanian language), 48th National Conferences of Building Services, Sinaia 2013: 105-113
[10]. Grigoraş C., Mateescu T., Cotorobai V., Chereches N.C., Experimental and numerical study on the influence of radiative flux on the thermodynamic behavior of a double-skin facade, (in romanian language), 47th National Conferences of Building Services, Sinaia 2012: 331-340
[11]. Pasut W., De Carli M., Evaluation of various CFD modelling strategies in predicting airflow and temperature in a naturally ventilated double skin façade, Thermal Engineering 2012; 37 : 267-274
[12]. Fluent Inc. Fluent user's manual, 2013
[13]. Safer N., Woloszyn M., Roux J.J., Three-dimensional simulation with a CFD tool of the airflow phenomena in single floor double-skin façade equipped with a Venetian blind, Solar Energy 2005, 79(2):193-203

Environmental Engineering and Management Journal *April 2014, Vol.13, No. 4, 775-781*
http://omicron.ch.tuiasi.ro/EEMJ/



"Gheorghe Asachi" Technical University of Iasi, Romania



NUMERICAL AND EXPERIMENTAL STUDY OF THE THERMOAERODYNAMIC BEHAVIOR OF A DOUBLE-SKIN GLAZED FAÇADE

Cătălin Grigoraş, Cătălin George Popovici, Theodor Mateescu, Nelu-Cristian Cherecheş*

"Gheorghe Asachi" Technical University of Iasi, Faculty of Civil Engineering and Building Services, Department of Building Services, 700050, Iasi, Romania

Abstract

This paper presents a study of the thermoaerodynamic spectrum inside an asymmetrically heated vertical channel of a double-skin façade. A double-skin façade is an envelope construction that consists of two transparent surfaces separated by an air channel. The numerical modeling was developed using the Ansys-Fluent simulation software under conditions of forced convection, using a three-dimensional geometry and a "k-ε standard" turbulence model. Then, experimental tests were performed on a full-scale stand in laboratory conditions, the results validating the adopted numerical model. The analysis of results for the temperature and the velocity profiles in some horizontal sections of the channel was performed in order to determine the thermoaerodynamic behavior of the double-skin glazed façades. The temperatures of the experimental measurements are compatible with the numerical results, within the limits of deviations between 0 - 6 °C. Further investigation will focus on a numerical and experimental study of natural convection taking into account the impact of solar radiation on the channel of the double façades.

Key words: double - skin façade, experimental analysis, forced convection, numerical study, thermoaerodynamic behavior, turbulent flow

Received: August, 2011; Revised final: June, 2012; Accepted: July, 2012

1. Introduction

In the last few years, the promotion of this particular type of a double glazed façade as an architectural element, important for both office and residential buildings, has become relevant from a functional, as well as from an energetic point of view.

Double-skin façades represent an alternative to the improvement of the thermal performance of the buildings with glass envelope using the natural and organized ventilation and the reduction of the energy consumption during the occupancy period by the exploitation of the solar radiations.

The outdoor climate (temperature, humidity, solar radiation and wind) determines the amount of energy necessary for the heating and cooling of a building. As the envelope of the building acts like a mediator between the inside and outside environment, the architecture and the constructive elements also affect the interior climate, the energy consumption and the payback period of the investment.

Therefore, this constructive solution characterized by the use of a transparent surface before the curtain wall, creates an active and very complex façade from an architectural, technical and functional point of view, which influences the building's thermodynamic behavior. Among the most

* Author to whom all correspondence should be addressed: e-mail: chereches@tuiasi.ro; Phone:+40 721976791

important factors that determine the efficiency of a double-skin façade, we mention the geometry and the ventilation type of the façade channel.

From an energetic point of view, the double-skin façades can reduce the heating requirements up to 50 kWh/m²·an (Mazria, 2006). The air temperature, in winter, can reach up to 60 ºC inside the channel created by the two glazed walls, in accordance, of course, with the specificities of the climate zone. But, the energetic efficiency doesn't only reside in the fact that the energy used for an important part of the year doesn't actually cost anything, but it also reside in the fact that this system provides a thermal compensation by reducing the fossil fuels consumption in power stations, and thus, decreasing the CO_2 emissions.

In the specialized literature, studies regarding air thermal behavior of double–skin façades mainly focus on the following aspects:

- Fedorov (1997) conducted a study in which he develops an induced flow and heat transfer in an asymmetrically heated, vertical parallel-plate channel. This aspect is related to numerous industrial, electronic and power equipment cooling applications. Starting from the experimental results that Miyamoto (1986) obtained, Fedorov develops a numerical approach of this problem. He analyses an asymmetrically heated vertical channel by establishing a condition of constant temperature, or of a constant flow, for the left wall. The right wall is considered to be adiabatic. The simulations were conducted for the air, taking into consideration the thermophysical properties that remained constant and the density that will vary according to the Boussinesque law. The heat transfer through radiation was considered to be negligible. By comparing these results with the experimental ones obtained by Miyamoto, we can see that the "Low Reynolds number k-ε" model can offer satisfactory results regarding the turbulent flow in natural convection from a vertically plane channel. The model predictions were first compared with available experimental data in order to validate the model.
- Numerical and experimental studies that refer to heat transfer and fluids flow in double-skin façades channels were also conducted by Chereches et al. (2009), Popa et al. (2006, 2007), Fohanno (2006). They studied the water flow in an asymmetrically heated channel, determining the temperature and the speed according to the variation of the modified Rayleigh number (upon which depend the thermophysical characteristics of the fluid and of the heat flow), and the dimensions of the channel, thus analyzing the hydrodynamic behavior in natural convection, on the level along the heated channel's wall. Also, Ospir et al. (2006), simulated and analyzed the water flow from the asymmetrically heated channel comparing the thermodynamic behavior of the water for different Rayleigh numbers with the behavior of the air inside the double-skin channel, using the similitude criteria between the two fluids.

In order to determine the thermal-aerodynamic behavior inside the channel that characterizes a double-skin façade, a comparative analysis of the results obtained by numerical and experimental modeling have been made on a full-scale facility in laboratory conditions in forced convection.

2. Description and hypothesis

Both the numerical and the experimental studies have been conducted with the same working hypotheses, on a full-scale facility in the following laboratory conditions:

- Double-skin façade geometry: H = 2.1 m, L = 1.5 m, d = 0.4 m;
- Constant heat flux: q = 408 W/m2, which is generated at the middle of the channel with a height of A=0.6 m (Fig.1) ;
- Air temperature at the entrance (inlet) of the channel is: Ti = 19.4 °C;
- Air velocity at the entrance (inlet) of the channel is: Vi = 0.1 m/s;
- Direct circulation of air inside the channel, ensuring an exterior-exterior ventilation in forced convection;

In order to find out whether in given conditions we register forced convection, it is necessary to apply the Richardson and Reynolds (RiRe) similitude criteria that differentiates between convection types (Padet, 1997):

- *RiRe* = 0 – 400 → natural convection;
- *RiRe* = 400 – 1000 → mixed convection;
- *RiRe* ≥ 1000 → forced convection.

The dimensionless number *RiRe* has been calculated with Eq. (1).

$$Ri\,\mathrm{Re} = \frac{g \cdot \beta \cdot \Delta T \cdot \left(D_h\right)^2}{\upsilon \cdot V_i} = 70755 \quad (1)$$

where the air properties for the temperature of 19.4 °C are: β=3.43x10^{-3} 1/K, v= 15.1x10^{-6} m²/s, ΔT = 8 °C and V_i = 0.1 m/s. The hydraulic diameter D_h is represented in Eq. (2).

$$D_h = 2d \cdot L/(d + L) = 0.63\ m \quad (2)$$

Consequently, the heat transfer inside the channel takes place through forced convection. Also, in order to characterize the air flow regime in forced convection, the Reynolds criteria (R_e) is Eq. (3).

$$R_e = \frac{V_i \cdot D_h}{\upsilon} \quad (3)$$

By replacing terms in Eq. (3) for the given work conditions, it results a turbulent airflow, with R_e = 4172 > 2300.

For a good observation and interpretation of the results obtained with the *Fluent software*, and of the manner in which the double-skin façade channel reacts to certain inside and/or outside factors, we have decided that the heated area in the middle of the channel should be split into sections a, b, c (Fig. 1). Consequently, we can now study the temperature variations and velocity profiles from the channel's main zone of interest.

3. Numerical simulation

The numerical simulation was made using specialized software *Ansys-Fluent*, for the working hypothesis described above, recorded from the experimental measures, according to the airflow in forced convection regime.

Geometry and meshing of the channel were done using the *Gambit* software (Fig. 2) on a tri-dimensional model.

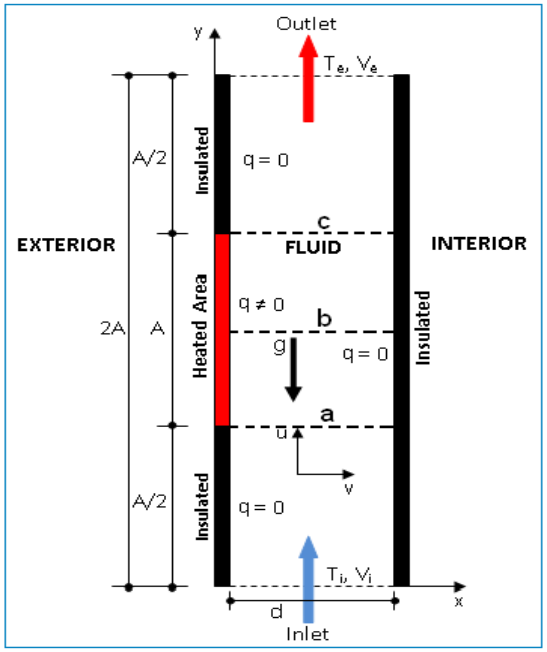


Fig. 1. The geometry of the double-skin façade channel

The transport equations of mass, momentum, energy, turbulent kinetic energy (k) and the dissipation rate (ε) are solved numerically using the finite volume method (e.g. Fluent, 2006, Manca, 2011 and Militaru, 2013). The standard k-ε turbulence model with enhanced wall treatment (e.g. Kader, 1981) is used to close the system of equations. This has the advantage of low time and computing power consumption. The pressure-velocity coupling is solved with the SIMPLE [Semi-Implicit Method for Pressure-Linked Equations] algorithm (Patankar, 1980). This algorithm *deals with*:

- the approximation of the velocity field is obtained by solving the momentum equation;
- the pressure gradient term is calculated using the pressure distribution from the previous iteration or an initial guess;
- the pressure equation is formulated and solved in order to obtain the new pressure distribution.

Thermophysical properties of the fluid are assumed to be constant, except for the density (Boussinesq approximation) in the buoyancy force. Moreover, the density is evaluated in relation to the temperature at the entrance of the channel.

The computational domain was meshed with a structured grid. In order to account for the steep gradients near the walls, a boundary layer type mesh was used in the proximity of these walls. A preliminary study of grid independency from the turbulence model was tested by varying the number of mesh cells in the vertical and transverse directions.

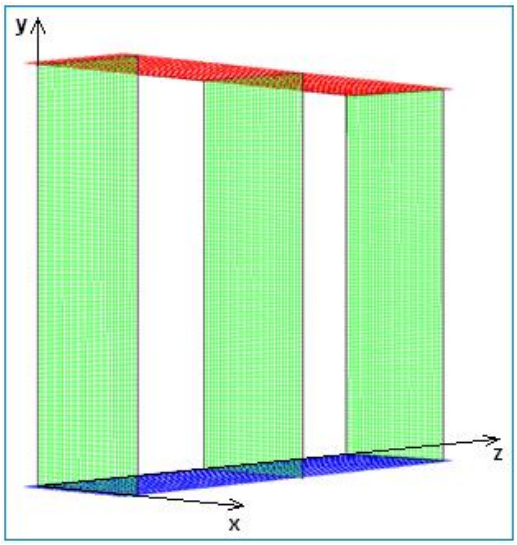


Fig. 2. Meshing of double-skin façade channel and interior sections

A fully implicit numerical scheme is engaged, in which upwind differences are used for the convective terms and central differences for the diffusion terms. Moreover, a structured uniform mesh of 5400 x 2700 x 900 cells has been chosen for the entire 3D system. The calculation is iterative, the chosen convergence criteria are 10^{-6} for the temperature and 10^{-4} for both the pressure and the velocities. The input data in the program is presented in the working hypothesis along with a graphic representation from (Fig. 1).

In Fig. 3 and Fig. 4 we present the temperature and velocity profiles in the median section of the double-skin façade channel.

The temperature variation for different sections is represented in Fig. 3. As we can observe, the temperature is higher near the heated wall in the first three sections and The heat flux that it is given for a certain surface of the glass channel does not have an important influence over the system. becomes homogeneous before exiting the channel.

Given a specific velocity imposed at the entry of the channel, the heat transfer at the glass surface is made preponderant by forced convection.

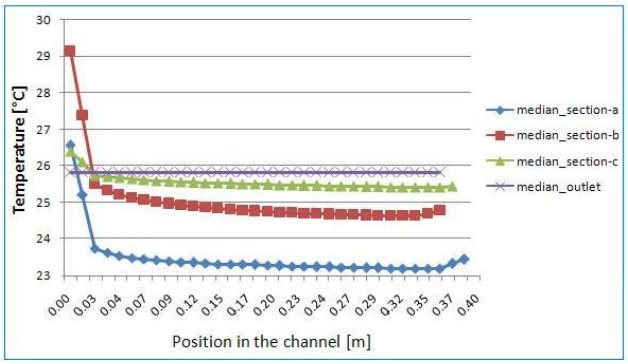


Fig. 3. Temperatures profile in representatives sections in forced convection

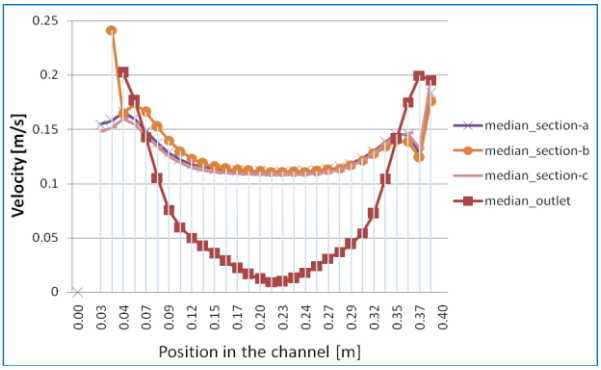
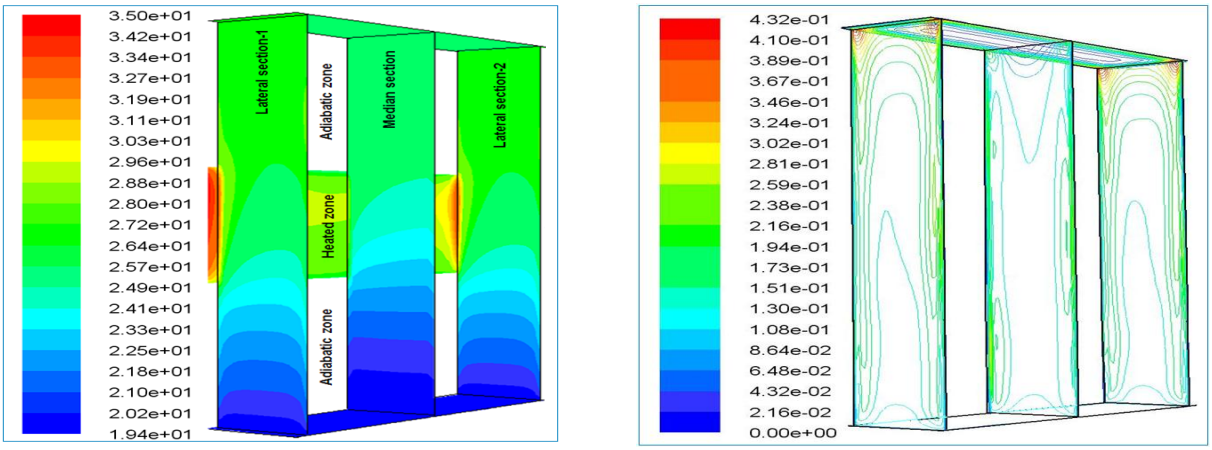


Fig. 4. Velocity profile in representatives sections in forced convection, after 1h



a) b)

Fig. 5. Temperature and velocity ranges in forced convection, in representative sections, a) temperature ranges, °C; b) velocity ranges, m/s;

Thus, Fig. 4 shows a variation of approximately 0.05 m/s of the velocities in all three sections of the channel (a, b, c), except for the exit section, where the velocities decrease due to the re-circulations existing in that zone. In exchange, because the airflow tends first to cover the limit zones of the channel, in the heated and in the adiabatic areas of the channel the measured velocities are 0.24 m/s and 0.2 m/s. The central zone registers smaller velocity values, which contributes to better temperature uniformity at the exit of the channel (Fig. 3). For experimental verification of the thermal-dynamic behavior, values of temperature and velocity were selected and represented in three vertical equal sections, according to the possibility of positioning the thermocouples in the experimental stand (Fig. 5).

Due to the airflow generating conditions in the middle of the channel and to the abrasion resistance at the contact with the closing surfaces, the flow velocity is 0.21 m/s on the surfaces that delimit the channel and approximately 0.13 m/s in the channel's central section. The velocity range indicates the presence of recirculation zones at the channel's superior section (Fig. 5b). In the heating zone, the flow is stabilized, thus justifying the use of the uniformity grill at the entrance in the heated zone and at the exit zone where the airflow is turbulent.

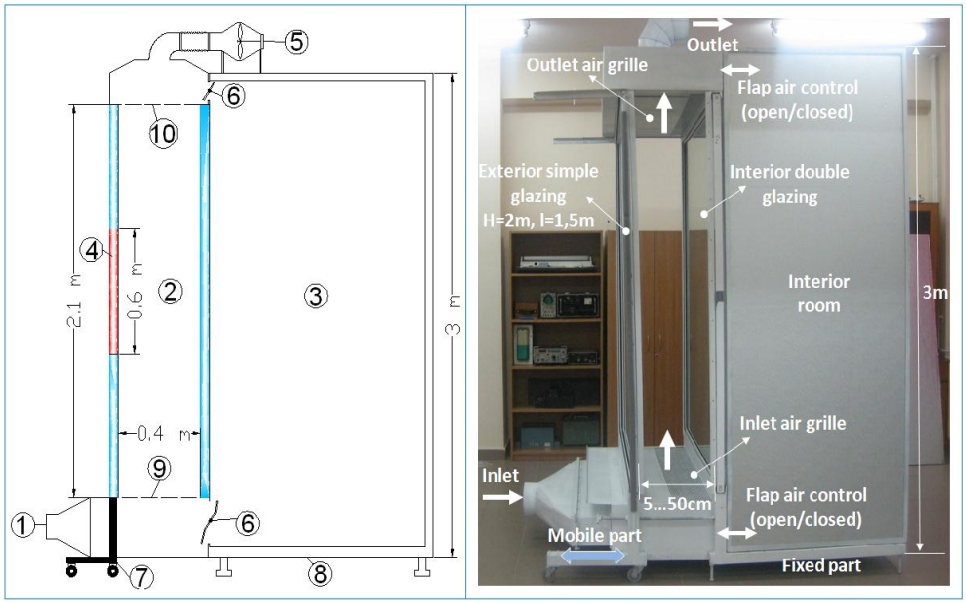
The temperature shows a progressive evolution between the extreme sections (input-output areas) with an evident increase in the radiant plate influence zone (Fig. 3, 5a).

On the horizontal sections, the temperatures maintain an approximate constant level, with a slight influence of the conductive transfer/ heat losses through glass closing elements, the effect being observed by comparing the images of the three vertical sections (Fig. 5a).

4. Experimental simulation

In order to verify and to validate the numerical results obtained using the numerical simulation, we have achieved an experimental stand that helps us observe the thermoaerodynamic behavior inside the channel. We have used the same working hypothesis as those used for the experimental simulations: V_i = 0.1 m/s; T_i = 19.4 °C, and a heat flux at the heating wall: q = 408 W/m^2.

In Fig. 6 we can see the functional scheme for the experimental stand and its components. This experimental study was made only in the double glazing channel without taking into consideration the adjacent chamber.



a) b)

Fig. 6. Experimental stand: a) schema; b) photo image; **1.** air channel inlet; **2.** variable geometry double-skin channel; **3** adjacent chamber; **4.** heating source for inside air; **5.** adjustable speed centrifugal fan; **6.** adjustable flap air control to the ventilation manner chosen; **7.** mobile framework for regulating channel opening from 5 up to 50 cm; **8.** fixed part of the experimental stand; **9.** double-skin façade channel inlet air grille;**10.** double-skin façade channel outlet air grille

The outdoor air enters through the lower part of the channel (1), gets heated from the hot plate (4) before exiting through the upper part, being exhausted by a fan (5) adjusted to ensure a speed of 0.1 m/s at the grid installed at the channel's entrance (9). The hot plate (4) is composed of a heating cable placed in an insulating layer of polystyrene. In addition, the inner glazing that separates the channel (2) from the chamber (3) is insulated on his entire surface with polystyrene. In this case, the flaps (6) directing the air are closed, ensuring a direct exterior-exterior ventilation.

In order to perform the experimental measurements we have used the followings devices:

- The air and glass surfaces temperature was measured with thermocouple model PT1000TGL40/0 for air, respectively model PT1000TG7/0 for glass surfaces, positioned in the three sections (Fig. 7), as follows:

  - the lateral section 1 – thermocouples (T11-T12-T13) for air and thermocouple (T41) for the interior adiabatic glass surface;

  - the lateral section 2 – thermocouples (T31-T32-T33) for air and thermocouple (T43) for the interior adiabatic glass surface;

  - the median section - thermocouples (T21-T22-T23-T24) for air and thermocouple (T42-T44) for the adiabatic glass section.

- The air velocity in median plan was measured as it follows:

  - at the entry of the channel, with a hot wire thermo manometer (measuring domain: 0-3 and 3.1-30 m/s, accuracy ± 3% applied to read value, resolution: 0.01 m/s);

  - at the exit if the channel, with turbine anemometers (measuring domain: 0-3 and 3.1-30 m/s, accuracy ± 3% applied to the read value, resolution: 0.1 m/s).

The double-skin façade was divided into three vertical sections (section 1, section 2, and the median section), so that we can provide measurements in the most representative points of the channel.

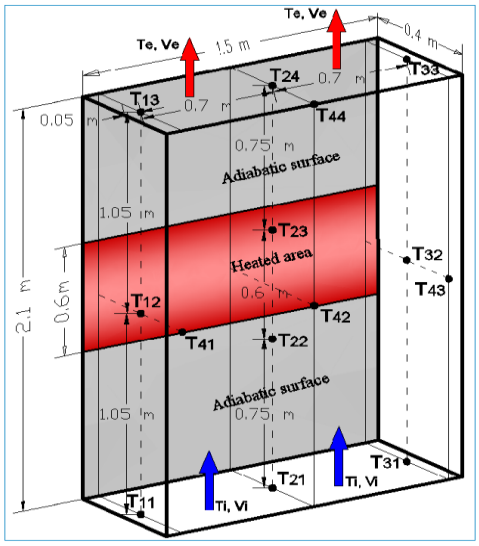


Fig. 7. Thermocouples positioning scheme in the experimental stand channel

The registration of temperatures was made with an acquisition data station (Data Logger MS5), set to memorize temperatures at even time intervals, after the flow regime is established.

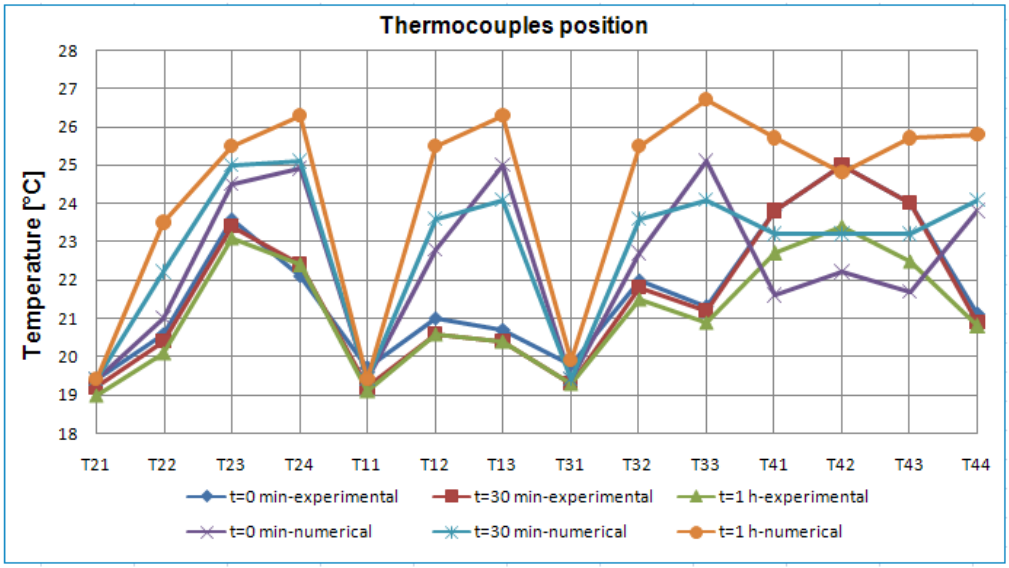


Fig. 8. Experimental and numerical comparative results in forced convection

The characteristic parameters (temperatures and velocities) were registered in forced convection, at time intervals: t = 0 min, t = 30 min, t=60 min.

The permanent regime was obtained one hour after the start of the experiment, when the recorded results suffered a variation smaller than 0.1 °C between temperature values. For the velocity registration, we used an AMI 300 STD apparatus, equipped with a processing software.

5. Comparison

The comparison between numerical and experimental results is showed in Fig. 8. The air temperature decreases from the heated surface trough the adiabatic wall, and the air temperature in the exit section of the channel is approximately 27 °C.

From analysis of the results we can observe that the experimental measured temperatures are compatible with those numerical obtained, with a deviation of 0 °C to 6 °C. These differences are explained by the working conditions: the experimental stand is not positioned in a thermal stabilized room (climate chamber) and the air extraction is made for the superior part of channel.
Since the study was performed under partial thermal flow at the glass channel surface conditions, and under non-stationary regime, the conclusions are only available for the stabilized regime zone and adjacent to incident flow.

6. Conclusions

This study was conducted on a three-dimensional, physical model, in unsteady state in forced convection. We emphasized here the description of the thermaerodynamic behavior from a double-skin façade and the validation of the numerical results with the experimental ones.

The experimental results were numerically validated, thus confirming the model studied in the previously mentioned working hypothesis.

After comparing the experimental and the numerical results, we can observe that the last ones have bigger values varying with about 6 °C. This is owed to the laboratory conditions, which influenced the experimental system, both thought heat losses from leaks and thought the lack of a climatic chamber. In addition, the results show that the airflow inside the channel is present especially near the limiting surfaces, thus modifying the distribution of temperatures.

For a better thermal efficiency of the double-skin façade, it is necessary to use the forced ventilation for the summer season in order to facilitate the quick extraction of hot air from the double-skin façade channel. On the other hand, in order to avoid the supplementary energetic costs for the start of the mechanical ventilation equipments, further studies on the thermal-aerodynamic behavior of these channels will be conducted with the purpose of achieving energetic optimization trough dimensional modifications and configurations, so that the suggested solution should reach, thus, a lower energy consumption.

Practically, by studying the behavior of the air inside a double-skin façade channel, we can determine the energetic consumption of buildings, obtaining this way a thermal balance by taking into consideration the data obtained from numerical simulation and the solar energy according to the climatic zone where the building is located.

This study will be further developed in similar condition by modifying the geometry of the channel, especially the distance between the channel surfaces and to find the optimal configuration that provides thermal comfort inside the buildings with minimum energy consumption.

Nomenclature

A – heated zone height, m;
a,b,c – horizontal sections in the median zone of the double-skin channel, m;
d – distance between interior and exterior surfaces, m;
D_h – hydraulic channel diameter;
g – gravitational acceleration, m/s² ;
H – channel height, m;

L – channel width, m;
q – demanded heat flow for a certain double-skin surface, W/m^2;
Re –Reynolds number, - ;
Ri – Richardson number, - ;
t – time, s;
$T_{i,e}$ – air temperature at the of the channel, respectively at the exit of the channel, ^{o}C;
u, v – velocity axial and transversal components, m/s;
$V_{i,e}$ – entrance, respectively exit for the air velocity, m/s;
x, y, z – Cartesian coordinates, m.

Greek symbols
β – thermal expansion coefficient, 1/K;
ΔT – air temperature differences at channel entrance and exit, ^{o}C;
v – kinematical viscosity of air at a given temperature, m^2/s.

Acknowledgement
The authors acknowledge the support from the Ministry of Education and Research (Romania), CNCSIS – UEFISCU, through PN II-Ideas, Grant No. 603/19.01.2009, CNCSIS Code ID-327.

References

Chereches N.C., Popa C.V., Chereches M., (2009), Numerical study of flow patterns in natural convection in a double-skin façade, *Bulletin of the Polytechnic Institute of Iasi, Construction and Architecture Section*, **LV**, 43-52.

Fedorov A.G., Viskanta R., (1997), Turbulent natural convection heat transfer in an asymmetrically heated, vertical parallel-plate channel, *International Journal of Heat and Mass Transfer*, **40**, 3849-3860.

Fluent, (2006), *Fluent 6.3* Documentation.

Fohanno S., Tribech A., Popa C.V., Polidori G., (2006), *Simulation expérimentale des modes de ventilation dans les parois double-peau*, Actes des XXIV-ème Rencontres de l'AUGC (AUGC06), La Grande Motte, CD Rom.

Kader B., (1981), Temperature and concentration profiles in fully turbulent boundary layers, *International Journal of Heat and Mass Transfer*, **24**, 1541-1544.

Miyamoto M., Katoh Y., Kurima J. Sasaki H., (1986), *Turbulent Free Convection Heat Transfer from Vertical Parallel Plates*, In: *Heat Transfer*, Tien C.I., Carey V.P., Ferrel J.K. (Eds.), **4**, 1593–1598.

Mazria E., (2006), *The Guide of Passive House*, Parentheses Press.

Ospir D., Popa C.V., Defay B., Fohanno S., (2008), Study of a natural convection flow in a vertical channel, *XXVIth University Meetings in Civil Engineering*, AUGC, Nancy, France, 1-8.

Padet J., (1997), *Principles of Convective Transfer*, Polytechnica Press, Reims, France.

Patankar S.V., (1980), *Numerical Heat Transfer and Fluid Flow*, Hemisphere, Washington, DC.

Popa C.V., Fohanno S., Polidori G., (2007), Note on the turbulence transition threshold of a buoyancy-driven flow over an isothermal vertical wall, *WSEAS Transactions on Heat and Mass Transfer*, **2**, 1-5.

Popa C.V., Chereches N.C., Polidori G., Fohanno S., (2006), Experimental simulations of ventilation modes in double-skin envelopes, *Bulletin of the Polytechnic Institute of Iasi, Construction and Architecture Section*, **LII (LVI)**, 125-132.

Manca O., Minea A.A., Nardini S., Tamburrino S. (2011), Numerical investigation on convective heat transfer in high temperature solar receiver, Environmental Engineering and Management Journal, **10** (10), 1467-1475

Militaru C.-M, Todinca T., Filep A.-D., Liné A., Pacala A., (2013), CFD modeling and simulation of a surface water treatment pilot plant, Environmental Engineering and Management Journal,**12** (5), 969-977

Energy and Buildings 50 (2012) 229–233

Contents lists available at SciVerse ScienceDirect

Energy and Buildings

journal homepage: www.elsevier.com/locate/enbuild

Numerical simulation of dynamical aspects of natural convection flow in a double-skin façade

Catalin Popa[a], Dan Ospir[a,b], Stéphane Fohanno[a,*], Cristian Chereches[b]

[a] GRESPI/Thermomécanique, Université de Reims Champagne-Ardenne, Moulin de la Housse, BP 1039, 51687 Reims Cedex 2, France
[b] Faculty of Civil Engineering and Building Equipment Technical University "Gh. Asachi" of Iasi, 45A, bd Dimitrie Mangeron, 700050 Iasi, Romania

ARTICLE INFO

Article history:
Received 9 May 2011
Received in revised form 7 February 2012
Accepted 20 March 2012

Keywords:
Double skin façade
Natural convection
Numerical simulation
Laminar flow

ABSTRACT

A dynamical study of the flow in a double-skin façade was carried out numerically for modified Rayleigh numbers in a range corresponding to the boundary layer-type flow in the laminar regime. The façade is modeled by an asymmetrically heated vertical plane channel. 2D numerical simulations have been carried out with the finite volume approach. Velocity profiles show the asymmetric character of the flow. The presence of a recirculation zone at the channel outlet near the unheated wall has been highlighted. Numerical results are compared with experiments carried out in water. This simulation allows finding the patterns of the recirculation zone observed in the experiments. Numerically predicted recirculation lengths are overestimated by about 6% compared with the experimental results.

© 2012 Elsevier B.V. All rights reserved.

1. Introduction

In the civil engineering sector, controlling the consumption of energy is still a relevant topic. Recent studies [1–4] have shown that the implementation of the concept of double-skin façade in a building with low inertia was essential to improve thermal comfort. This is indicative of an urgent need to deepen knowledge of the dynamic and thermal behaviours of double-skin façades to minimize energy losses. Double-skin facades can be classified into three categories depending on their thickness ($5\,cm < b < 50\,cm$, $50\,cm < b < 200\,cm$, $b > 200\,cm$). Double-skin façades of the first category ($5\,cm < b < 50\,cm$) are commonly used. For example, they can be found in high-rise buildings. In this case, the façade is generally divided horizontally level by level for a better thermal comfort [4].

The constructive element of a double-skin envelope is the vertical plane channel heated asymmetrically. Indeed, the heated vertical plane channel is representative for several problems such as the double-skin façade, the chimney, the solar panel or the Trombe wall. In order to optimize the design of a double-skin envelope, the simulation of the natural convection flow developing in the channel needs to be performed with reliable numerical tools. This requires the development of experimental setups to provide the thermal and dynamic data for validating these numerical tools.

A great number of experimental and numerical studies concerning the vertical plane channel were carried out [5–16]. Among the experimental studies, most of them were limited to thermal measurements for both uniform heat flux (UHF) and uniform wall temperature (UWT) problems. Although uniform wall temperature or uniform heat flux boundary conditions have been chosen for the experiments, these conditions usually cannot be fully satisfied because of experimental constraints. Therefore, results coming from these experiments should be analyzed and used in light of these experimental difficulties. For example, Webb and Hill [6] describe the possible causes of measurement errors and non-uniformity of boundary conditions for their experiments. Although heat loss by conduction through the insulation on the rear side of the heat foil and radiation loss with the environment were taken into account in their study, they point out that two-dimensional conjugate effects are also present, particularly near the leading and trailing edges of the heated foil, and alter the uniformity of the thermal boundary conditions. Kim et al. [17] have also investigated the effect of wall conduction on the wall heat flux distribution. Fewer studies were also interested in the flow behaviour. Two main flow regimes in heated vertical channels were experimentally observed by Elenbaas [5]. Their appearance has been noticed to be Rayleigh number dependent (Ra^* is partly based on the channel width and the aspect ratio between this width and the heated channel length). A fully developed flow regime is observed in the channel for low Rayleigh numbers and a boundary-layer type flow regime along the heated walls occurs for high Rayleigh numbers. In the case of an asymmetrical heating (only one wall heated) and for sufficiently high Rayleigh numbers ($Ra^* > 1000$), the boundary-layer type flow regime is always present on the heated wall, and a reverse flow is also observed close to the unheated wall [6–8].

* Corresponding author. Tel.: +33 326918310; fax: +33 326918152.
E-mail address: stephane.fohanno@univ-reims.fr (S. Fohanno).

0378-7788/$ – see front matter © 2012 Elsevier B.V. All rights reserved.
http://dx.doi.org/10.1016/j.enbuild.2012.03.042

Nomenclature

A	heated length (m)
a	thermal diffusivity (m^2/s)
b	channel wall spacing (m)
C_p	specific heat capacity (J/kg K)
g	acceleration of gravity (m/s^2)
k	thermal conductivity (W/m K)
p	pressure (Pa)
Pr	Prandtl number ($= \nu/a$)
q''	heat flux (W/m^2)
Ra	Rayleigh number ($= (g\beta q'' b^4/k\nu^2)$Pr)
Ra*	modified Rayleigh number ($= Ra/R_f$)
R_f	aspect ratio ($= A/b$)
L	recirculation length (m)
t	time (s)
u, v	axial and transverse velocity components (m/s)
x, y	axial and transverse coordinates (m)

Greek letters

β	volume expansion coefficient (K^{-1})
ρ	density (kg/m^3)
ν	kinematic viscosity (m^2/s)
μ	dynamic viscosity (Pa s)

Index

$\propto$	ambient

In this paper, we report a dynamical study of the flow in a double-skin façade carried out numerically. This numerical work is part of studies initiated by the French research network Ameth (Improved heat transfer) on convective heat transfer in open-channels. The façade is modeled by an asymmetrically heated vertical plane channel. 2D numerical simulations have been carried out with the finite volume approach. The investigations focus specifically on the influence of the aspect ratio (R_f) and the modified Rayleigh number (Ra*) on the structure of the flow. The modified Rayleigh numbers was varied in a range corresponding to the boundary layer-type flow in the laminar regime. Numerical results on the flow dynamics are discussed and compared with experimental observations obtained by flow visualization.

2. Experimental device and visualization technique

Experimental investigations of the dynamics of the natural convection flow have been carried out in a vertical plane channel heated asymmetrically [16]. The channel is located in a vertical tank filled with water. The choice of water as working fluid leads to a negligible effect of heat transfer by radiation. The channel is composed of two vertical parallel plane walls separated by an adjustable distance (b). One wall is composed of a heated central part (height A = 188 mm) and two unheated extensions (height $A/2$) respectively located at the bottom and top open-ends of the channel while the opposite wall remains entirely unheated throughout the duration of the experiments (Fig. 1). The heating of the central half part of the heated wall is provided by a fabric heater which delivers a heat flux density uniformly distributed throughout the heating zone. This thermal system (Fig. 1) consists of a vertical plane thermofoil heater, covered by a 3 mm-thick aluminum plate on the channel side, delivering an adjustable heat flux (q'') to water in the channel. A flow visualization technique based on laser tomography and the use of discrete tracers was used to get the velocity vector field (Fig. 2) and to deduce streamline patterns within the channel [16].

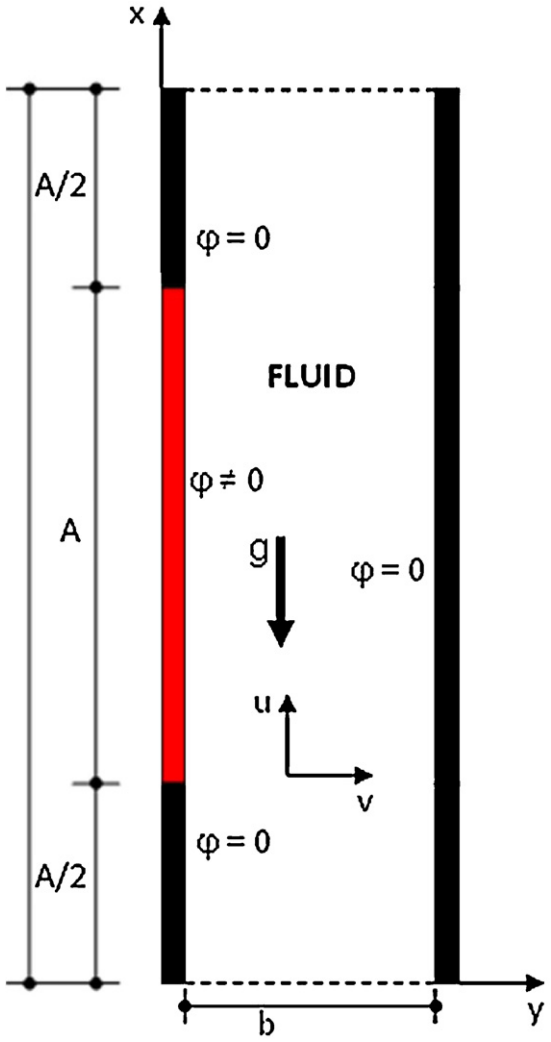


Fig. 1. Sketch of the vertical channel.

2.1. Physical model

The numerical simulations of the channel flow are carried out for a two-dimensional steady laminar flow. The transport equations of mass, momentum and energy (Eqs. (1)–(4)) are solved numerically using the finite volume method [18]. Thermo-physical properties of the fluid are assumed constant except the density (Boussinesq approximation) in the buoyancy force. Moreover, the density is evaluated in relation to the temperature at the channel entrance.

- Continuity equation:

$$\frac{\partial u}{\partial x} + \frac{\partial v}{\partial y} = 0 \tag{1}$$

- Momentum equations:

$$\rho = \left(u\frac{\partial u}{\partial x} + v\frac{\partial u}{\partial y}\right) = -\frac{\partial p}{\partial x} + \mu\left(\frac{\partial^2 u}{\partial x^2} + \frac{\partial^2 u}{\partial y^2}\right) - \rho_\infty g[1 - \beta(T - T_\infty)] \tag{2}$$

$$\rho\left(u\frac{\partial v}{\partial x} + v\frac{\partial v}{\partial y}\right) = -\frac{\partial p}{\partial y} + \mu\left(\frac{\partial^2 v}{\partial x^2} + \frac{\partial^2 v}{\partial y^2}\right) \tag{3}$$

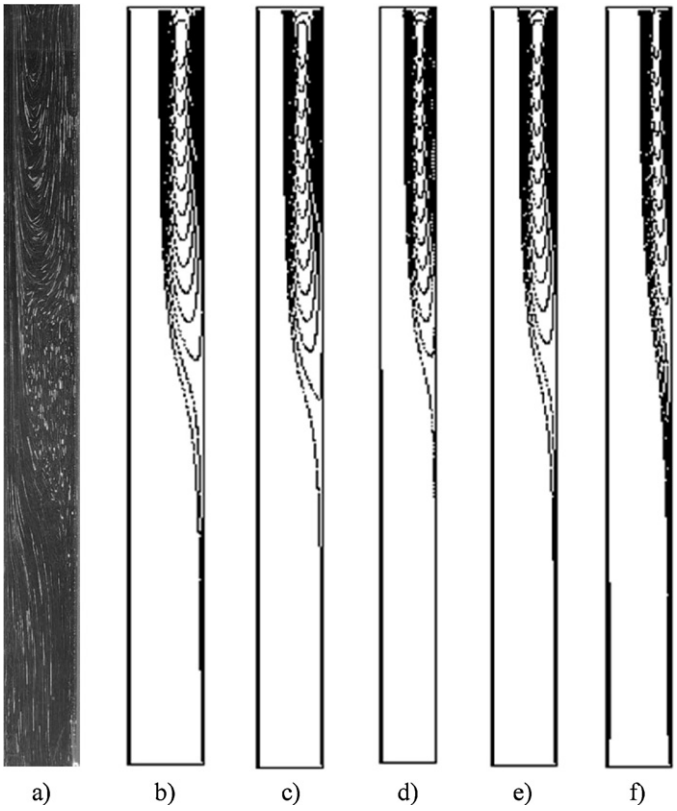


Fig. 2. Experimental recirculation zones: (a) $R_f = 5.2$, $Ra^* \approx 4 \times 10^6$ and numerical (b) $R_f = 5.2$, $Ra^* \approx 4 \times 10^6$, (c) $R_f = 6$, $Ra^* \approx 4 \times 10^6$, (d) $R_f = 6.9$, $Ra^* \approx 4 \times 10^6$, (e) $R_f = 6$, $Ra^* \approx 2 \times 10^6$, (f) $R_f = 6$, $Ra^* \approx 4 \times 10^5$.

- Energy equation:

$$\rho C_p \left(u\frac{\partial T}{\partial x} + v\frac{\partial T}{\partial y} \right) = k \left(\frac{\partial^2 T}{\partial x^2} + \frac{\partial^2 T}{\partial y^2} \right) \quad (4)$$

The results are made dimensionless by means of the thermal diffusivity (a) and the distance between the walls (b). Dimensionless quantities are given below (Eqs. (5)–(8)).

$$X = \frac{x}{b}, \quad Y = \frac{y}{b}, \quad R_f = \frac{A}{b}, \quad U = \frac{ub}{a},$$
$$V = \frac{vb}{a}, \quad T^* = \frac{T - T_i}{\Delta T}, \quad \Delta T = \frac{q''b}{k} \quad (5)$$

$$\text{Prandtl number,} \quad \Pr = \frac{v}{a} \quad (6)$$

$$\text{Rayleigh number,} \quad \text{Ra} = \frac{g\beta q'' b^4}{kv^2}\Pr \quad (7)$$

$$\text{Modified Rayleigh number,} \quad \text{Ra}^* = \frac{\text{Ra}}{R_f} \quad (8)$$

In natural convection flow, the fluid flow rate in the channel depends strongly on the wall heat flux. Therefore, the choice of appropriate boundary conditions becomes critical. Indeed, when the wall is heated, an ascending boundary layer develops along this wall due to the buoyancy force resulting from the local decrease in density of the warmer fluid in the vicinity of the wall. This boundary layer thickens during the progression of the flow along the wall, being supplied by fluid coming from a reverse flow observed near the unheated wall. This reverse flow is itself fed by ambient fluid entering through the top of the channel, near the unheated wall [16]. The pressure boundary conditions chosen to account for these experimental observations are the local Bernoulli relation at the inlet (Eq. (9)) and a zero relative pressure at the outlet (Eq. (10)).

Boundary conditions are as follows:

- at the inlet,

- $X = 0$ and $0 \le Y \le 1$

$$T^* = 0, \quad p(X, Y) = -\frac{1}{2}\rho u(X, Y)^2 \quad (9)$$

- at the outlet

- $X = 2R_f$ and $0 \le Y \le 1$

$$T^* = 0, \quad p(X, Y) = 0 \quad (10)$$

- at the wall

- $y = b$ and $0 \le X \le 2R_f$

$$u(x, Y) = v(x, y) = 0, \quad q'' = 0$$

- $y = 0$ and $0 \le X \le R_f/2$ or $3R_f/2 \le X \le 2R_f$

$$u(X, Y) = v(X, Y) = 0, \quad q'' = 0$$

- $y = 0$ and $R_f/2 \le X \le 3R_f/2$

$$u(X, Y) = v(X, Y) = 0, \quad q'' > 0$$

2.2. Numerical method

The system of governing Eqs. (1)–(4) with appropriate boundary conditions has been successfully solved by using a numerical method mainly based on the volume control approach [18]. This method is based on the spatial integration of the conservation equations over finite control volumes. Numerical simulations have been carried out with the commercial Ansys Fluent® CFD code [19]. The fluid domain is meshed using a structured grid with refined mesh in the vicinity of the walls. The convergence criteria were based on the residuals resulting from the integration of the conservation Eqs. (1)–(4) over finite control-volumes. During the iterative calculation process, these residuals were constantly monitored and carefully scrutinized. For all simulations performed in this study, converged solutions were achieved with residuals as low as 10^{-6} (or less) for all the governing equations.

3. Results

The flow dynamics in the asymmetrically heated vertical channel is investigated numerically. Only the convective aspects related to natural ventilation are studied by carrying out simulation with water as working fluid, thus allowing neglecting radiation effects. First, a comparison of these numerical results is made with corresponding experimental observations. Then, two sets of numerical studies are considered. The simulations were carried out for three modified Rayleigh number $Ra^* = 4 \times 10^6$; 2×10^6 and 4×10^5 and three aspect ratios $R_f = 5.2$, 6 and 6.9. The modified Rayleigh number based on the heat flux density (q'') and the thickness of the channel (b) also takes into account the aspect ratio of the heated part (R_f) through Eq. (8). As concerns the aspect ratios, their values are within the range of those found for horizontally divided double-skin façades of high-rise buildings.

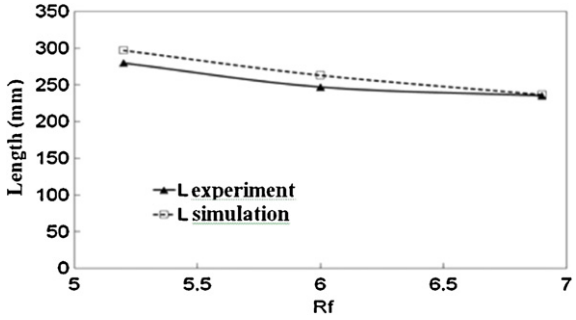


Fig. 3. Comparison of the total recirculation length.

3.1. Comparison with experiments

In Fig. 2, one may observe a boundary layer-type flow which develops near the heated wall due to the fluid alimentation from the bottom of the channel. In the same time, cooler ambient fluid enters the channel from the upper side of the adiabatic wall (reverse flow). This leads to the formation of a recirculation zone which can be observed at the exit of the channel, near the adiabatic wall. The experimental visualization of the flow for $Ra^* = 4 \times 10^6$ and $R_f = 5.2$ is presented over the entire height ($2A$) of the channel in Fig. 2a. The photo is taken when a steady flow regime is reached after about 30 min of heating (Fig. 2a). Regarding the reverse flow, it may be characterized by its eight-shape structure with two recirculation cells. This recirculation zone extends over three quarters of the channel height. For this case, the numerical simulation (Fig. 2b) allows finding the global patterns of the recirculation zone observed in the experiment, especially its penetration in the channel. However, although the total length of the recirculation was well predicted, none of the numerical simulations was able to detect the second recirculation cell observed experimentally.

The same comparison performed for the other aspect ratios ($R_f = 6$ and 6.9) also leads to a good agreement between experimental and numerical results. Numerically predicted total recirculation lengths are only overestimated by 6% compared with the experimental ones (Fig. 3).

3.2. Influence of aspect ratio and Ra*

Then, two sets of numerical studies were conducted. The first set involved the investigation of the influence of the aspect ratio ($R_f = 5.2$, 6 and 6.9) for a fixed Rayleigh number ($Ra^* = 4 \times 10^6$), whereas the second one was conducted to analyze the influence of modified Rayleigh number ($Ra^* = 4 \times 10^6$, 2×10^6 and 4×10^5) on the flow structure for a given aspect ratio ($R_f = 6$).

Fig. 2b–d shows the streamlines patterns numerically predicted for the first set of conditions. A single recirculation zone can always be observed at the exit of the channel whatever the aspect ratio. Its length gradually decreases with increase of the aspect ratio. The increase in the aspect ratio was obtained by reducing the channel width (b) while keeping a constant height (A) of the heated zone. For the second set of conditions, the decrease in Ra*, for a fixed aspect ratio, generates a reduction of the reverse flow height and the modulation of the recirculation length (Fig. 2c–e).

Axial velocity profiles at the entrance ($x = A/2$) and exit ($x = 3A/2$) of the heated zone are presented in dimensionless form as given in Eq. (5). In Fig. 4, axial velocity profiles are presented at the entrance of the heated zone for three aspect ratios. The laminar flow profiles observed in all three cases show a slight asymmetry highlighted by a small acceleration near the heated wall. Axial velocity profiles at the exit of the heated zone are presented in Fig. 5. A strong acceleration of the fluid can be observed near the heated wall whereas a deceleration is observed near the adiabatic wall where the negative velocities indicate the recirculation zone. The recirculation zone is initiated by density difference between the warm (lighter) fluid, near the heated wall, and the cold (denser) ambient fluid, near the adiabatic wall. This is also due to the pressure drop in the moving fluid in the vicinity of the heated wall.

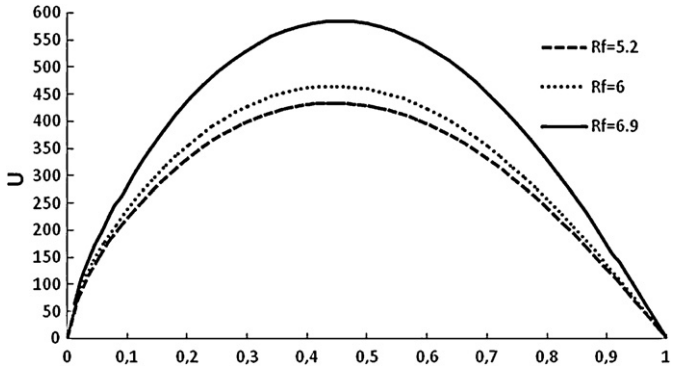


Fig. 4. Axial velocity profiles at the entrance of the heated channel ($x = 0.094$ m) for $Ra^* = 4 \times 10^6$ and different aspects ratio (R_f).

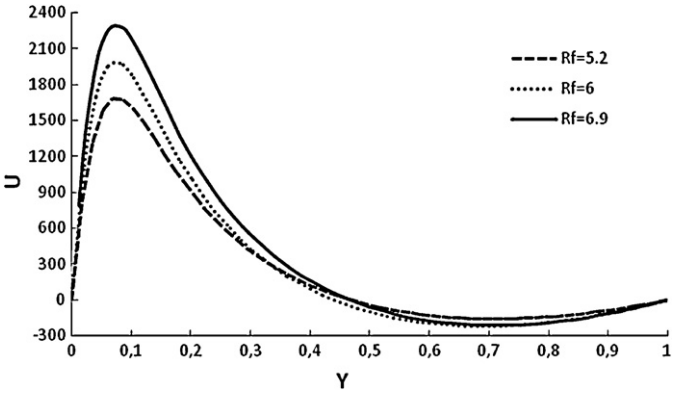


Fig. 5. Axial velocity profiles at the exit of the heated channel ($x = 0.282$ m) for $Ra^* = 4 \times 10^6$ and different aspects ratio (R_f).

It can be seen that maximum values of the axial velocity in all three cases are obtained at a distance $y = 0.1 \times b$ from the heated wall. It can be established that for a higher aspect ratio (R_f) and a smaller channel width (b) respectively, the axial velocity magnitude is higher which will lead to higher fluid flow rate through the channel for the same modified Rayleigh number (Ra*).

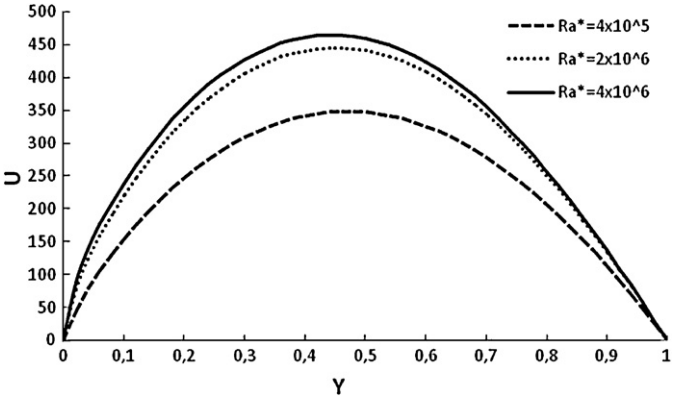


Fig. 6. Axial velocity profiles at the entrance of the heated channel ($x = 0.094$ m) for $R_f = 6$ and different numbers of modified Rayleigh (Ra*).

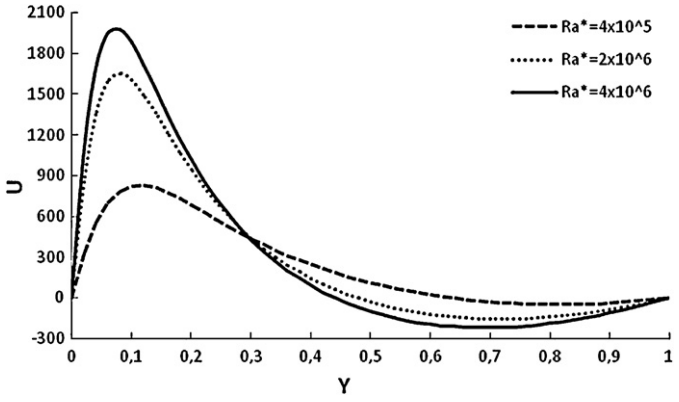


Fig. 7. Axial velocity profiles at the exit of the heated channel ($x = 0.282$ m) for $R_f = 6$ and different numbers of modified Rayleigh (Ra*).

Figs. 6 and 7 present the axial velocity profiles at the entrance and exit respectively of the heated zone for the same aspect ratio ($R_f = 6$) and three Rayleigh numbers ($Ra^* = 4 \times 10^6$, 2×10^6 and 4×10^5). The maximum values for axial velocity at the exit of the heated zone is also obtained for a distance $y = 0.1 \times b$. It can be noted that the axial velocities and the recirculation length increase with the Rayleigh number.

4. Conclusion

A dynamical study of the flow in a double-skin façade was carried out numerically for modified Rayleigh numbers in a range corresponding to the boundary layer flow regime. The façade is modeled by an asymmetrically heated vertical plane channel.

A boundary layer-type flow develops near the heated wall in all cases. The presence of a recirculation zone at the channel outlet near the unheated wall has been highlighted. The channel alimentation is made at the bottom end of the channel across the channel width. This boundary layer-type flow is accompanied by a reverse flow with variable length, fed by the ambient fluid entering through the upper part of the channel near the unheated wall.

In this study, a recirculation zone was always observed at the exit of the channel whatever the aspect ratio or the modified Rayleigh number. Numerically predicted length of the total recirculation zone is overestimated by about 6% compared with the experimental results. Furthermore, the recirculation length gradually decreases with increasing aspect ratio. Moreover, for a fixed aspect ratio, both the axial velocity magnitude and the recirculation length increase with the modified Rayleigh number.

Acknowledgements

The authors acknowledge the partial support from the Ministry of Education, Research and Innovation (Romania), CNCSIS - UEFISCU, through PN II-Ideas, Grant No. 603/19.01.2009, CNCSIS Code ID_327.

The authors are also very grateful to the French research network AMETH (Improved heat exchange).

References

[1] A. Dimoudi, A. Androutsopoulos, S. Lykoudis, Experimental work on a linked, dynamic and ventilated, wall component, Energy and Buildings 36 (2004) 443–453.
[2] H. Manz, A. Schaelin, H. Simmler, Airflow patterns and thermal behavior of mechanically ventilated glass double facades, Building and Environment 39 (2004) 1023–1033.
[3] W. Ding, Y. Hasemi, T. Yamada, Natural ventilation performance of a double-skin façade with a solar chimney, Energy and Buildings 37 (2005) 411–418.
[4] N. Safer, Modélisation des façades de type double-peau équipées de protections solaires: Approches multi-échelles, Ph.D. Thesis, Institut National des Sciences Appliquées, Lyon, 2006 (in French).
[5] W. Elenbaas, Heat dissipation of parallel plates by free convection, Physica 9 (1942) 1–28.
[6] B.W. Webb, D.P. Hill, High Rayleigh number laminar natural convection in an asymmetrical heated vertical channel, ASME Journal of Heat Transfer 111 (1989) 649–656.
[7] T. Yilmast, A. Gilchrist, Temperature and velocity field characteristics of turbulent natural convection in a vertical parallel-plate channel with asymmetric heating, Heat and Mass Transfer 43 (2007) 707–719.
[8] T. Yilmaz, S.M. Fraser, Turbulent natural convection in a vertical parallel-plate channel with asymmetric heating, International Journal of Heat Mass Transfer 50 (2007) 2612–2623.
[9] M. Fossa, C. Ménézo, E. Leonardi, Experimental natural convection on vertical surfaces for building integrated photovoltaic (BIPV) applications, Experimental Thermal and Fluid Science 32 (2008) 980–990.
[10] R.A. Wirtz, R.J. Stutzman, Experiments on free convection between vertical parallel plates with symmetric heating, ASME Journal of Heat Transfer 104 (1982) 501–507.
[11] E.M. Sparrow, G.M. Chrysler, L.F. Azevedo, Observed flow reversals and measured-predicted Nusselt numbers for natural convection in a one-sided heated vertical channel, ASME Journal of Heat Transfer 106 (1984) 325–332.
[12] O. Manca, B. Morrone, V. Naso, A numerical study of natural convection between symmetrically heated vertical parallel plates, in: Proceedings XII Congresso Nazionale sulla Trasmissione, UIT, vol. 1, 1994, pp. 379–390.
[13] C.O. Olsson, Prediction of Nusselt number and flow rate of buoyancy driven flow between vertical parallel plates, ASME Journal of Heat Transfer 126 (2004) 97–104.
[14] R. Ben Mansour, M.A. Habib, H.M. Badr, S. Anwar, Comparison of different turbulence models and flow boundary conditions in predicting turbulent natural convection in a vertical channel with isoflux plates, The Arabian Journal for Science and Engineering 32 (2007) 191–218.
[15] J. Hernandez, B. Zamora, Effects of variable properties and non-uniform heating on natural convection flows in vertical channels, International Journal of Heat Mass Transfer 48 (2005) 793–807.
[16] D. Ospir, C. Popa, C. Chereches, G. Polidori, S. Fohanno, Flow visualization of natural convection in a vertical channel with asymmetric heating, International Communications in Heat and Mass Transfer (2012), http://dx.doi.org/10.1016/j.icheatmasstransfer.2012.02.005.
[17] S.H. Kim, N.K. Anand, W. Aung, Effect of wall conduction on free convection between asymmetrically heated vertical plates: uniform wall heat flux, International Journal of Heat and Mass Transfer 33 (1990) 1013–1023.
[18] S.V. Patankar, Numerical Heat Transfer and Fluid Flow, Hemisphere, Washington, DC, 1980.
[19] ANSYS Fluent, Documentation 2011.

International Communications in Heat and Mass Transfer 39 (2012) 486–493

Contents lists available at SciVerse ScienceDirect

International Communications in Heat and Mass Transfer

journal homepage: www.elsevier.com/locate/ichmt

Flow visualization of natural convection in a vertical channel with asymmetric heating ☆

Dan Ospir [a,b], Catalin Popa [a], Cristian Chereches [b], Guillaume Polidori [a], Stéphane Fohanno [a,*]

[a] GRESPI (EA 4301) / Thermomécanique, Université de Reims Champagne-Ardenne, Moulin de la Housse, BP 1039, 51687 Reims Cedex 2, France
[b] Faculty of Civil Engineering and Building Equipment Technical University "Gh. Asachi" of Iasi, 45A, bd Dimitrie Mangeron, 700050 Iasi, Romania

ARTICLE INFO

Available online 16 February 2012

Keywords:
Natural convection
Vertical channel
Asymmetric heating
Experimental study
Flow visualization

ABSTRACT

A dynamical study of the flow in an asymmetrically heated vertical plane channel has been conducted experimentally. Experiments were carried out in water for three aspect ratios and for a range of modified Rayleigh numbers corresponding to the boundary layer flow regime. The flow dynamics were characterized by means of visualization techniques based on laser tomography using discrete and continuous tracers. Flow visualizations were carried out in the plane of symmetry of the channel along its entire height. The investigations focused more specifically on the influence of the aspect ratio and the modified Rayleigh number on the flow structure both in steady-state regime and during the transitional phase occurring just after the start of the heating. An upward boundary layer flow is found near the heated wall, accompanied by a reverse flow developing on the opposite side from the top open-end of the channel. In steady state, the reverse flow takes the form of an elongated eight-shaped structure with two main recirculation cells. The length of the upper cell of the eight-shape structure decreases with increasing aspect ratio. For a fixed aspect ratio, the increase in modified Rayleigh number results in a decrease in the penetration of the reverse flow. During the transient the flow structure is shown to evolve from a single cell to a final eight-shaped structure.

© 2012 Elsevier Ltd. All rights reserved.

1. Introduction

This study deals with the experimental investigation of the flow dynamics in a vertical plane channel heated asymmetrically. The heated vertical plane channel is representative of several problems such as the chimney, the solar panel or the Trombe wall [1,2]. The simulation of natural convection flow developing in vertical channels needs to be performed with reliable numerical tools. Therefore, the validation step of these numerical simulation tools for the reliable prediction of the thermoconvective behavior requires the development, in parallel, of experimental setups to provide the necessary thermal and dynamic data. Heat transfer and flow dynamics in a vertical channel heated or cooled have been studied for many years. Two main flow regimes in heated vertical channels were experimentally observed by Elenbaas [3]. Their appearance has been noticed to be Rayleigh number dependent. The modified Rayleigh number (Ra^*) is partly based on the channel wall spacing (b) and the aspect ratio ($R_f = \frac{A}{b}$) between the heated channel height (A) and the spacing (b). For a symmetric heating, a fully developed flow regime is observed in the channel for low Rayleigh numbers ($Ra^* < 100$) while a boundary-layer type flow regime along the heated walls occurs for high Rayleigh numbers. In the case of an asymmetrical heating (only one heated wall) and for sufficiently high Rayleigh numbers ($Ra^* > 1000$), the boundary-layer type flow regime is always present along the heated wall, and a reverse flow is also observed close to the unheated wall [4,5].

Furthermore, although many experimental studies on the vertical plane channel have been conducted [3–14], most studies were limited to thermal measurements (flow and wall temperature) both for uniform heat flux (UHF) and for uniform wall temperature (UWT) problems. Fewer studies were interested in the flow dynamics [5,9–14]. However, these dynamic quantities are essential data for validation of numerical simulation tools.

In order to access these data, this paper presents an experimental investigation of the flow dynamics in an asymmetrically heated vertical plane channel by means of flow visualization techniques based on laser tomography using discrete (small solid particles) and continuous (dye) tracers. Experiments were carried out in water for three aspect ratios (R_f) and for a range of modified Rayleigh numbers (Ra^*) corresponding to the boundary layer flow regime. Flow visualizations were performed in the plane of symmetry of the channel along its entire height. The investigations focused more specifically on the influence of the aspect ratio (R_f) and the modified Rayleigh number (Ra^*) on the flow structure both in steady-state regime and during the transitional phase occurring just after the start of the heating.

☆ Communicated by J. Taine and A. Soufiani.

* Corresponding author at: GRESPI/Thermomécanique, Université de Reims Champagne-Ardenne, Moulin de la Housse, BP 1039, 51687 Reims Cedex 2, France.
E-mail address: stephane.fohanno@univ-reims.fr (S. Fohanno).

0735-1933/$ – see front matter © 2012 Elsevier Ltd. All rights reserved.
doi:10.1016/j.icheatmasstransfer.2012.02.005

Nomenclature

Symbols

A	heated length, m
b	channel wall spacing, m
g	acceleration of gravity, m/s²
k	thermal conductivity, W/m.K
Pr	Prandtl number
Gr	Grashof number based on heat flux and channel wall spacing
Ra	Rayleigh number based on heat flux and channel wall spacing
Ra^*	$(=Ra/R_f)$ modified Rayleigh number
R_f	aspect ratio $(=A/b)$
L	recirculation length, m
t	time, s
y	vertical coordinate, m

Greek letters

β	volume expansion coefficient, 1/K
ρ	density, kg/m³
ν	kinematic viscosity, m²/s
φ	heat flux, W/m²

Indices / Exponents

p	particle
w	wall
low	lower
up	upper

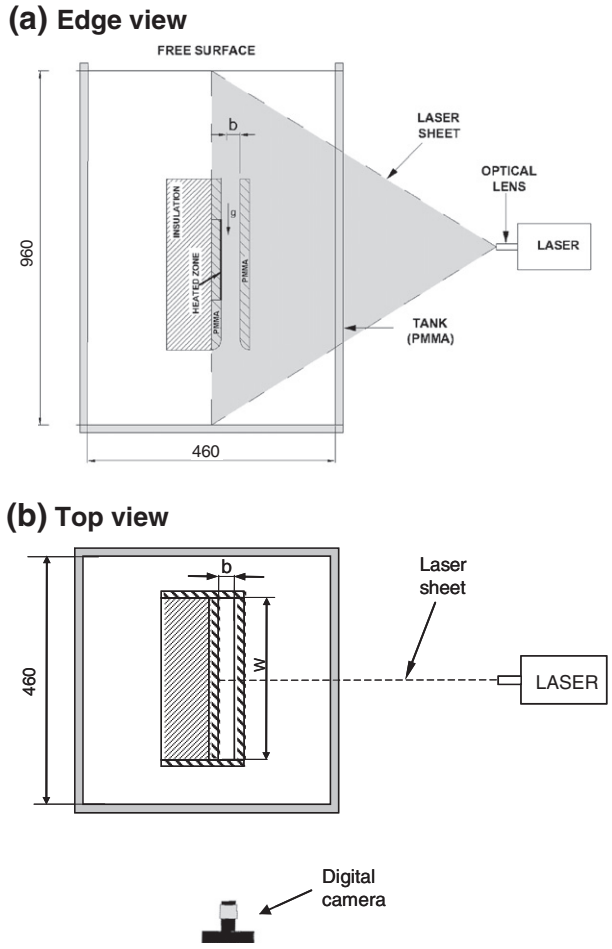


Fig. 1. Schematic edge view and top view of the experimental setup.

2. Experimental setup

2.1. Tank and working fluid

The present work deals with the experimental investigation of the dynamics of the natural convection flow generated inside a vertical plane channel heated asymmetrically. The channel is located in a vertical tank (inner dimensions : $460\times460\times960$ mm³) made up of 20 mm-thick Plexiglas ® plates and filled with water, as shown in Fig. 1. The choice of water as working fluid leads to a negligible effect of heat transfer by radiation.

2.2. Channel geometry

An edge view of the channel is illustrated in Fig. 2. The channel is composed of two vertical parallel plane walls separated by an adjustable distance (b). One wall is composed of a heated central part (height $A=188$ mm) and two unheated extensions (height A/2) respectively located at the bottom and top open-ends of the channel while the opposite wall remains entirely unheated throughout the duration of the experiments. Dimensions of these walls (height: $2A=376$ mm, width: $W=300$ mm) are such that investigations were performed for aspect ratios in the range $5.2<R_f<6.9$ and $8.3<W/b<11$. Two vertical walls were added on side ends to bind the fluid. Therefore, the fluid can only flow through the bottom and top open-ends of the channel. For the sake of brevity, and because the flow is mainly directed upwards, the bottom and top open-ends will respectively be denoted inlet and outlet in the rest of the text. In addition, for a better control of flow conditions at the inlet, a quarter of a circle (radius of curvature $R=36$ mm) was added at the bottom of each wall.

2.3. Composition of walls and heating system

The channel was mainly built in a PMMA transparent material that enables taking photographs. Therefore, the channel walls were built from 10 mm and 20 mm thick PMMA plates. The heating of the central half part of the heated wall is provided by a fabric heater which delivers a heat flux density uniformly distributed throughout the heating zone. As shown in Fig. 2, this thermal system consists of a vertical plane thermofoil heater (20×30 cm²), covered by a 3 mm-thick aluminum plate on the channel side, delivering an adjustable heat flux density (φ_w) to water in the channel. In addition, the backside of the heated wall is heavily insulated (by adding a 140 mm thick layer of extruded polystyrene) in order to minimize heat losses to this side and to prevent the onset of convection phenomena into the environment.

2.4. Wall heat flux distribution

The wall heat flux distribution was checked by means of temperature measurements along the heated plate. For this check, a configuration of natural convection boundary layer flow along a vertical flat plate immersed in a semi-infinite fluid medium was selected. This flow configuration was obtained by simply removing the cold wall of the channel from the experimental setup. Wall surface temperature measurements were carried out along the heated vertical plate. Then, the evolution in the vertical direction of the experimental wall-to-ambient fluid temperature difference was compared with the theoretical

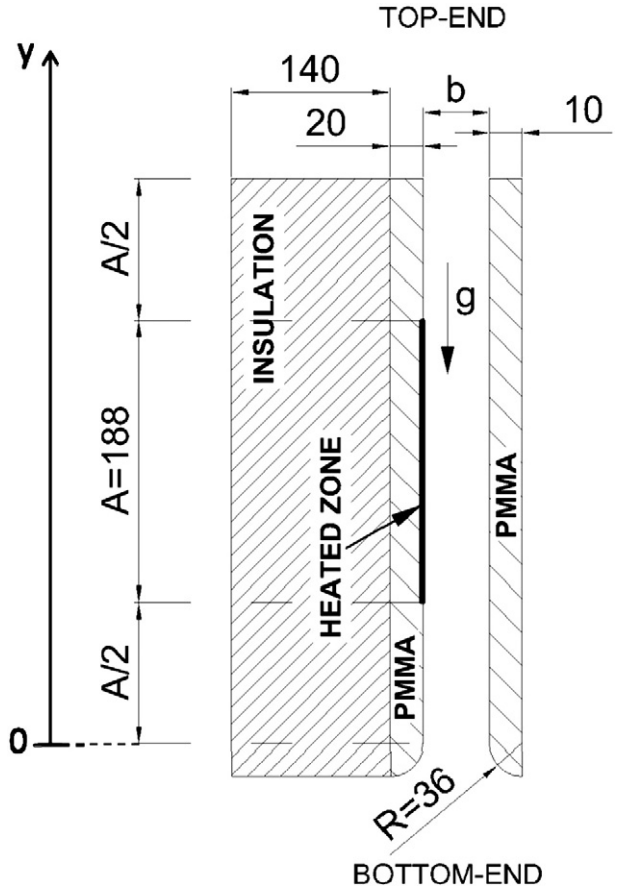


Fig. 2. Edge view of the vertical channel.

one-fifth power law ($T_{wall} - T_{fluid} = Cy^{1/5}$) expected for laminar natural convection along a uniformly heated vertical plane plate [15]. The one-fifth power law was found on the majority of the heated vertical surface, except close to the bottom-end of the heated surface where an increase in the wall-to-ambient fluid temperature difference was observed. These higher temperature differences observed at the bottom-end of the plate may be attributed to two-dimensional effects due to the combination of the high thermal conductivity of the plate and the vertical wall surface temperature gradient due to the boundary layer [16]. Axial heat flux in the heated wall takes place in the downward direction, particularly at the bottom-end of the heated plate where the boundary layer starts its development and the vertical temperature gradients are the most important. The downward axial heat flux leads to a local increase in the wall temperature. This results in an additional heat flux to be transferred from the wall to the fluid in the upstream region of the boundary layer. As shown by Kim et al. [16], the additional heat flux may depend on several parameters such as the thermal conductivity, the thickness of the plate, but also the Grashof number and the thickness of the channel. However, in the present study, the influence of axial conduction is essentially observed over the first 15% of the heated zone. The limited impact of wall conduction on the temperature increase may be explained by the relatively high value of the Grashof number [16], which is about 10^6 for these experiments.

2.5. Flow visualization techniques

The dynamic structure of the flow is characterized by means of flow visualization techniques based on laser tomography and the use of discrete (small solid particles) [17] and continuous (dye) tracers [18]. These two flow visualization techniques are used to provide streamline patterns (discrete tracers) as well as streakline patterns (dye tracers) within the channel. In this study, laser tomography consisted in creating a single plane laser sheet in the mid-plane of the channel as shown in Fig. 1. For both methods, the lighting of the flow was obtained through a 490 mW maximum power Ar-Ion laser source (model 177G Spectra Physics ®) coupled to a sphero-cylindrical optical system to create a laser sheet in the mid-plane of the channel.

The dye flow visualization technique consists in employing one or several fluorescent dye tracers, under laser excitation, in order to provide streaklines in the flow [18]. In the present study, the injection of distinct dye tracers at different locations in the flow allowed to clearly distinguish several types of flow structures in the channel and to observe them simultaneously. Fig. 3 shows an example of application of this technique where fluorescein was used for the boundary layer flow visualization while sulforhodamine was used for the reverse flow visualization.

The main technique used in this study was Particle Tracking Velocimetry. This method consists in the use of discrete solid tracers illuminated by the laser sheet [17]. These tracers are fine (average diameter : $\overline{d_p} \approx 100\mu m$) suspended quasi-spherical Rilsan® particles having a density ($\rho_p = 1060\ kg\ m^{-3}$) close to that of water. Under these conditions, the particle settling velocity remains negligible relative to the flow velocity. One can then consider that the flow dynamics is well approximated by the particle trajectories. In order to get these trajectories, photographs of the illuminated fine solid tracers, as those illustrated in Fig. 4, were taken by a high-resolution digital camera (Pentax® K10D) during a time exposure suitable for the flow dynamics. In the context of the current study, which concerns natural convection flow in water with moderate heating, time-exposures up to 20 s were necessary. The streamline patterns of the water flow were then deduced from the elements of trajectories

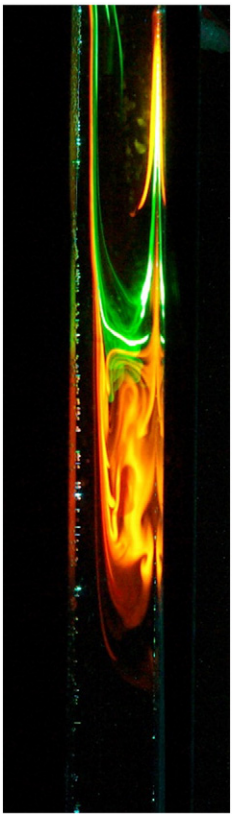


Fig. 3. Dye flow visualization of the eight-shape structure in steady state regime for $Ra^* = 4.5 \times 10^6$ and $R_f = 5.2$.

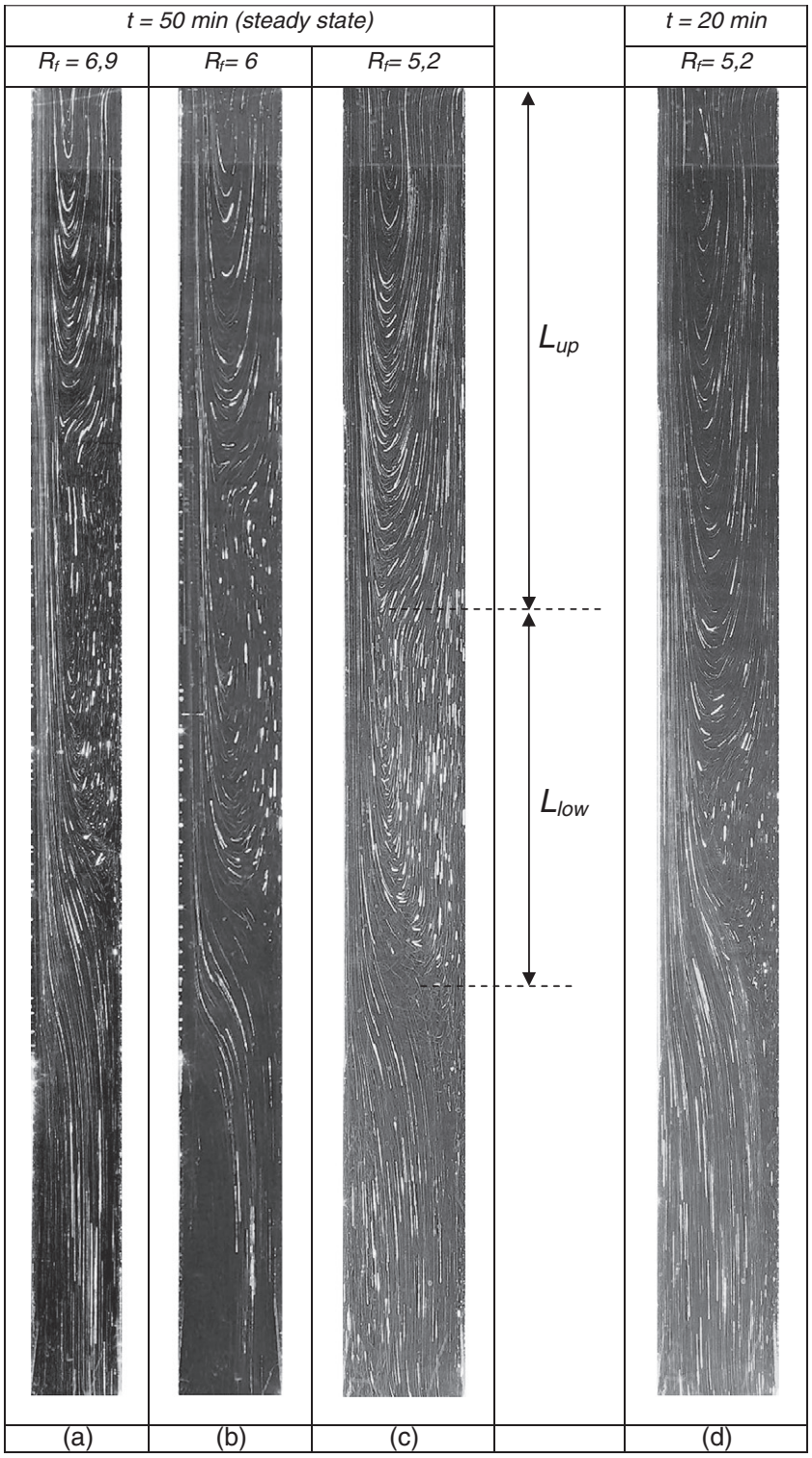


Fig. 4. Flow visualizations showing the influence of the aspect ratio (a, b, c) and of time (c, d) on the flow structure for $Ra^* = 4.5 \times 10^6$.

captured on digital photographs. Given the high resolution of the camera, the uncertainty about the recirculation lengths is primarily due to the uncertainty about the location of the cell ends. There is not necessarily presence of particles (elements of trajectories) to these ends during the reconstruction of the streamlines. This uncertainty is estimated to be 5 mm in size. The flow region under study corresponds to a cross-section of the channel illuminated by a thin laser plane perpendicular to the channel walls. The vertical sides of this illuminated plane cross-section are well localized with a higher brightness at the fluid/vertical wall interfaces. In comparison, optical distortion/lens effects are minimal and may be neglected in the present situation.

3. Results and discussion

3.1. Experimental conditions

Both the influence of the distance between the walls and that of the modified Rayleigh number (Ra^*) on the water flow dynamics

were investigated by means of flow visualization techniques. The modified Rayleigh number based on the heat flux density (φ_w) and the thickness of the channel (b) also takes into account the aspect ratio of the heated part (R_f) through Eqs. (1) and (2):

$$Ra = \frac{g\beta\varphi_w b^4}{k\nu^2} Pr \quad (1)$$

$$Ra^* = \frac{Ra}{R_f} \quad (2)$$

Fluid properties were estimated at the film temperature defined by $T_f = \frac{T_{inlet}+\bar{T}_w}{2}$ where $\bar{T}_w$ is the average wall temperature. The uncertainty in the modified Rayleigh number, $Ra^* = \frac{g\beta\varphi_w b^4}{k\nu^2}\left(\frac{b}{A}\right)$Pr, is primarily due to the uncertainty in the channel wall spacing b. To a lesser extent, the uncertainty in Ra^* is also due to uncertainties in the thermophysical property grouping $\frac{g\beta}{k\nu^2}$Pr and in the heat flux φ_w. The maximum uncertainty in the modified Rayleigh number is estimated at 10%.

Two sets of experiments were carried out. The first series of experiments involved the study of the influence of the aspect ratio $\left(R_f = \frac{A}{b}\right)$ for a fixed modified Rayleigh number (Ra^*). Three aspect ratios ($R_f = 5.2$, 6 and 6.9) were tested and the fixed modified Rayleigh number ($Ra^* = 4.5\times10^6$) was chosen in order to correspond to the boundary layer flow regime. The second series of experiments was conducted to analyze the influence of the modified Rayleigh number (Ra^*) on the flow structure for a given aspect ratio (R_f). This second set of experiments was carried out for a range of modified Rayleigh numbers ($4.3\times10^5 < Ra^* < 4.5\times10^6$) still corresponding to the boundary layer flow regime. For both series, results were obtained in the form of flow visualizations of the natural convection flow dynamics in the mid-plane of the channel, over its entire height (2A). Photographs were taken with a time-exposure suitable for low speed flows and the type of tracers used (1/8 s for dye tracers and 20 s for discrete particles). Regarding flow visualizations with discrete tracers, photographs were taken at a frequency of one image per minute since the start of heating until a steady flow regime is reached. The steady state was determined by comparing the images obtained every minute since the start of the heating. The steady state was considered achieved when the geometrical dimensions of the visualized structures no longer evolved.

In all experiments conducted for this study, the structure of the flow became steady from about 30 min of heating. In fact, the time needed to reach steady state decreases with increasing Ra* and is about 20 to 30 min in this case. Nevertheless, experiments were carried on for 50 min to make sure the steady flow regime was reached.

3.2. Heating and temperature stratification of the ambient fluid

The initial bulk water temperature before heating was set at 16 °C. Then the temperature gradually increases during the experiments due to heating. The average bulk water temperature increase is proportional to the imposed heat flux and the duration of heating. In addition, vertical temperature stratification also occurs from bottom to top of the water tank. Table 1 reports temperature increases observed in ambient water for $Ra^* = 4.5\times10^6$ and $R_f = 5.2$ and corresponding to the maximum heat flux used in these experiments. After an hour of heating, temperature increases range from +0.4 °C below the channel bottom-end to +1.7 °C above the channel top-end, which gives an average temperature stratification of 2.0 °C/m along the channel.

Table 1
Temperature increase of ambient water as a function of altitude for $Ra^* = 4.5\times10^6$ and $R_f = 5.2$ after one hour of heating. Vertical coordinate origin at the channel inlet (see Fig. 2).

Vertical coordinate (y, in m)	−0.132	+0.028	+0.188	+0.348	+0.508
Temperature increase (°C)	+0.4	+0.6	+0.9	+1.4	+1.7

3.3. Cold wall surface temperatures

The temperature field in the PMMA cold plate has been estimated from temperature measurements on the inner surface (channel side) and outer surface (ambient fluid side) of the wall for vertical positions corresponding to the beginning ($y = A/2$) and end ($y = 3A/2$) of the heated zone. These measurements show that the cold wall inner surface temperature remains low and close to that of the fluid entering at the inlet of the channel (T_{inlet}) with differences of about 0.2 °C between these temperatures. As for the temperatures measured on the cold wall outer surface, they remain very close to the temperature of the ambient fluid located at the same altitude. The evolution of the temperature on this outer surface corresponds to the temperature stratification observed in the ambient fluid.

3.4. Influence of the aspect ratio

For this first part of the study, the aspect ratio was changed by varying the distance (b) between the plates. Three aspect ratios have been investigated ($R_f = 5.2$, 6 and 6.9 corresponding to distances $b = 36$ mm, 31.3 mm and 27.3 mm, respectively) and the modified Rayleigh number was kept constant ($Ra^* = 4.5\times10^6$). This value was chosen so as to obtain a boundary-layer type flow regime along the heated wall. As a consequence, the Rayleigh number was kept constant by adjusting the electric power delivered to the fabric heater. Fig. 4 provides flow visualizations carried out in the mid-plane of the channel for $Ra^* = 4.5\times10^6$ showing the typical structures of the flow obtained in steady-state regime (at $t = 50$ min) and during the transient (at $t = 20$ min) before the steady state was reached. In all cases, an upward boundary layer flow is observed near the heated wall. After applying the heat, the dynamics of the convective flow generated in the channel is changing dramatically during a transitional period of about 30 min before reaching a steady state.

In steady state, an ascending boundary-layer flow develops near the heated wall due to a supply of fluid from the bottom of the channel. At the same time, cold fluid enters the channel from its top-end, near the unheated wall and supplies a reverse flow developing near the unheated wall. Indeed, as shown by dye flow visualization in Fig. 3 or discrete flow visualization in Fig. 4 (a, b, c), this gives rise to a vortex structure characterized by two large recirculation cells, connected by a neck and forming an elongated eight-shaped structure. These recirculation cells extend over a distance of up to three-quarters of the channel height. This distance is all the more important than the aspect ratio is small. Furthermore, the adverse pressure gradients at the interface of the upward flow and reverse flow lead to a separation of the upward flow from the unheated wall. This upward flow is then quickly deflected and confined near the heated wall. Regarding the reverse flow, it can be characterized by the lengths of the two main recirculation cells. These lengths are illustrated in Fig. 4 and will be denoted L_{up} (upper recirculation cell length) and L_{low} (lower recirculation cell length), respectively. In Fig. 5, one can observe that the upper recirculation cell stretches out with decreasing aspect ratio. In contrast, the length of the lower recirculation cell remains stable regardless of the aspect ratio.

3.5. Influence of Rayleigh number

The second part of this experimental study has investigated the influence of the change in the modified Rayleigh number. In the same way as in Fig. 4, Fig. 6 shows flow visualizations performed in the mid-plane of the channel with discrete solid particles as tracers. Experiments were carried out for three values of the modified Rayleigh number ($Ra^* = 4.3\times10^5$; 1.7×10^6 and 4.5×10^6) which were obtained by fitting the thermal power delivered by the fabric

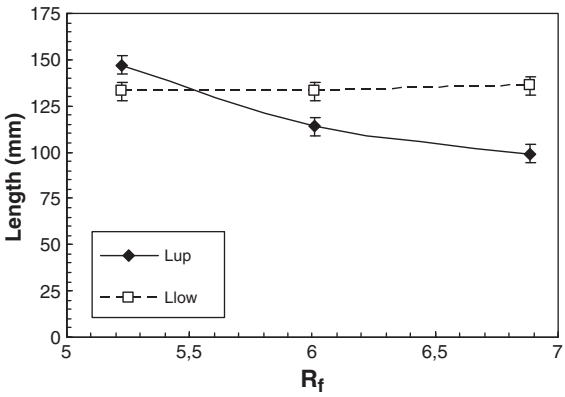


Fig. 5. Recirculation cell lengths as a function of aspect ratio.

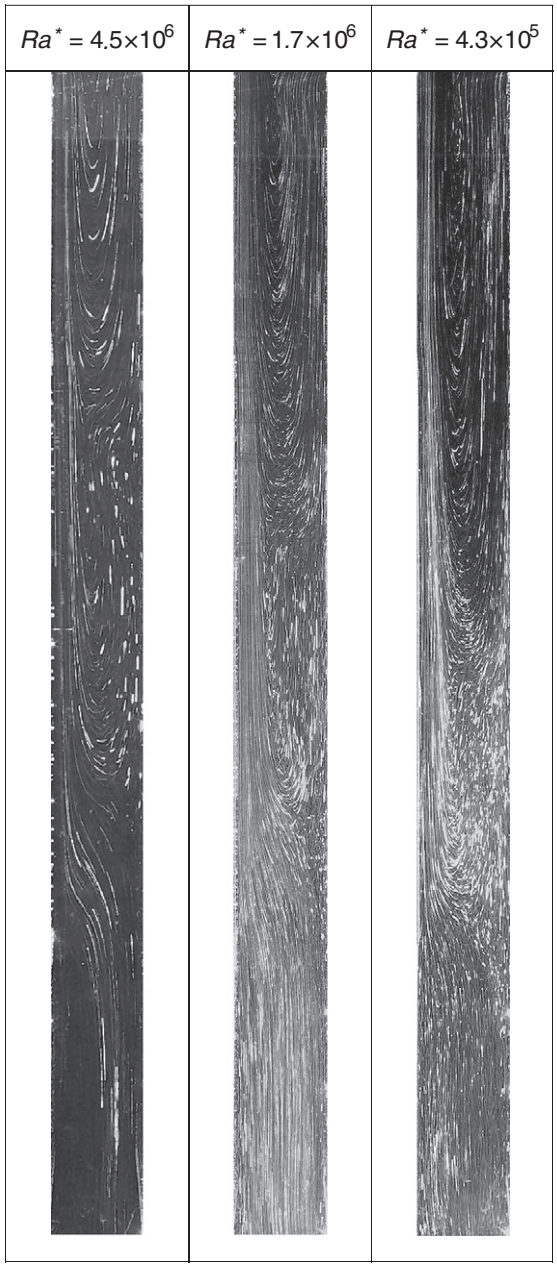


Fig. 6. Influence of Ra^* for a constant aspect ratio ($R_f = 6$).

heater. The aspect ratio was kept constant ($R_f = 6$). Whatever the value of Ra^*, the steady state is still characterized by an ascending boundary-layer flow in the vicinity of the heated plate and a reverse flow on the opposite side with its two large recirculation cells. With a fixed aspect ratio, the increase in Ra^* has resulted in a decrease in the penetration of the reverse flow in the channel and the modulation of the upper and lower recirculation cell lengths. Fig. 7 shows the evolution of the lengths of the vortex zones according to Ra^*. The length of the upper recirculation cell (L_{up}), as well as that of the total recirculation zone (L_{tot}), decrease with increasing Ra^*. This decrease is much more noticeable for the upper recirculation cell. In that case, the reduced extension of the reverse flow can be explained by a higher adverse pressure from the upward flow with increasing Ra^*, delaying the upward flow separation from the unheated wall. In contrast, the lower recirculation cell length (L_{low}) increases with Ra^*. This can also be explained by the growing pressure exerted by the upward flow. This extension occurs mainly at the expense of the upper recirculation.

3.6. Transient flow dynamics

The time-evolution of the flow structure during the transient will now be discussed in this section. As mentioned previously, the steady-state regime was generally observed after about 30 min of heating and was characterized by two main recirculation cells. Fig. 4d shows the flow structure obtained during the transient, at $t = 20$ min, for an aspect ratio and a modified Rayleigh number $Ra^* = 4.5 \times 10^6$. It can be compared with the corresponding steady state flow regime shown in Fig. 4c. Fig. 4d shows a transient dynamic structure where the lower recirculation cell is just emerging. However, the extension of the recirculation in the channel remains substantially the same as at $t = 50$ min, once the steady state regime is reached.

In order to provide a more detailed analysis of the mechanism leading to the steady-state flow structure, streamline patterns showing the flow structure in the channel at three different moments are plotted in Fig. 8. One may note that similar patterns were observed in the range of aspect ratios and modified Rayleigh numbers investigated in this study. Therefore, for the sake of brevity, streamline patterns are only provided for one case, i.e. and $Ra^* = 4.5 \times 10^6$. Thus, two intermediate structures obtained during the transient (at $t = 10$ min and $t = 20$ min

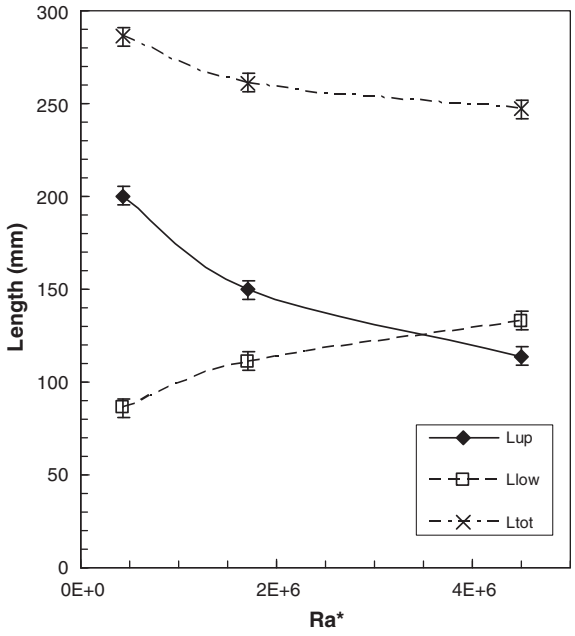


Fig. 7. Recirculation cell lengths as a function of modified Rayleigh number.

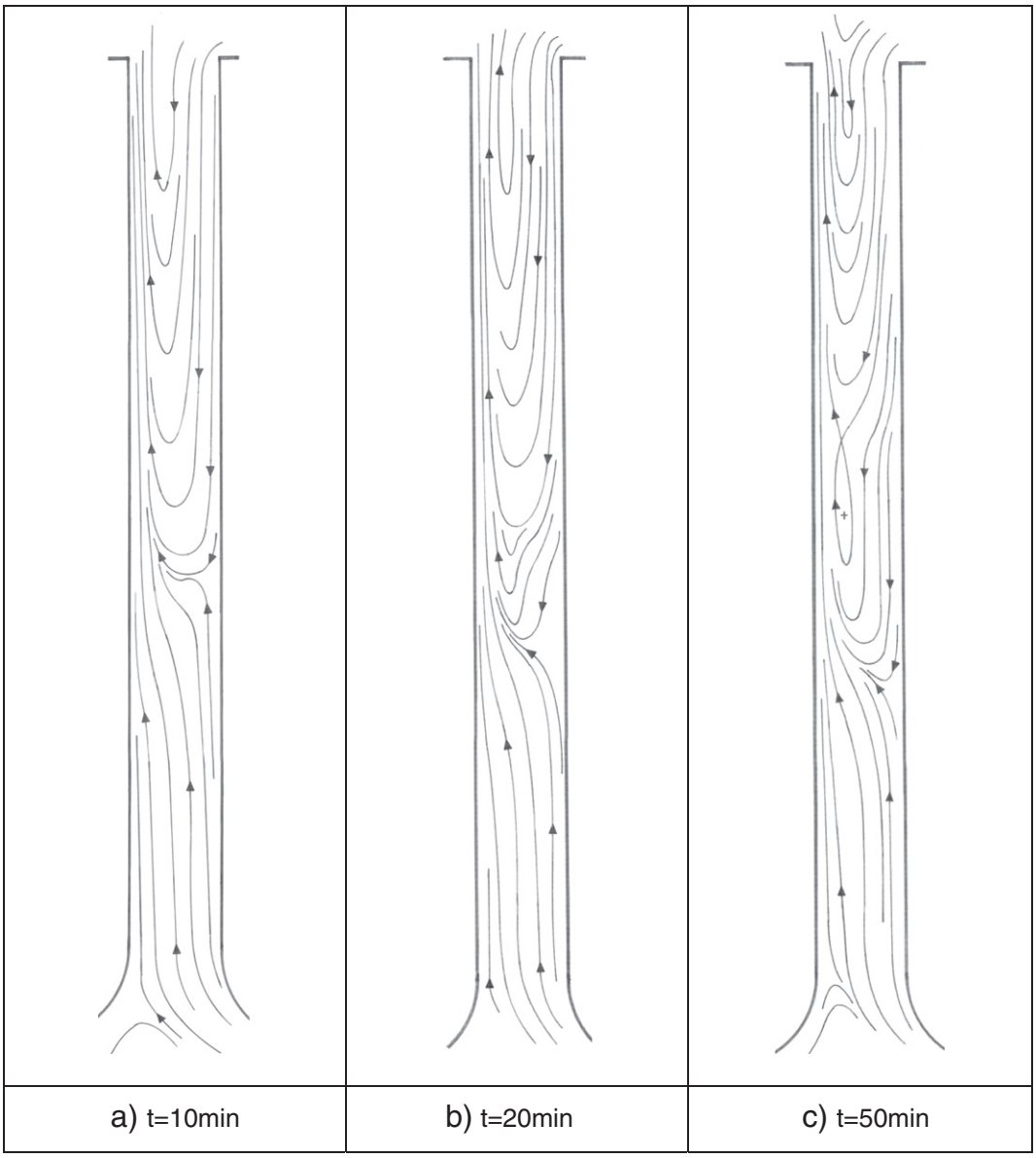


Fig. 8. Streamline patterns during the transient ($t=10$ min and $t=20$ min) and in steady state regime ($t=50$ min) for $Ra^*=4.5\times10^6$ and $R_f=5.2$.

after the start of the heating) as well as one in steady state regime (at $t=50$ min) were chosen. From the beginning of the wall heating, a recirculation cell grows on almost all the width of the channel top-end. This recirculation cell appears only minutes after the start of the heating and is as the recirculation cell that can be observed at the exit of the channel in Fig. 8a. Then, the recirculation extends over most of the channel width. One may also note that the total length of the single recirculation cell observed after 10 min of heating, as illustrated in Fig. 8a, is only slightly shorter than the eight-shaped structure characterizing the steady state regime shown in Fig. 8c. In addition, Fig. 8b shows that, after 20minutes of heating, the single recirculation cell begins to be deformed at the base. This seems to be due to the presence of a strong adverse pressure gradient near the unheated wall exerted by the upward flow. This separation was also highlighted by dye tracers in Fig. 3. In addition, Fig. 8a shows that the eight-shaped structure comes from a large single recirculation cell that developed during the transitional phase corresponding to the first moments of heating. Then, a second cell is progressively forming, as illustrated by Fig. 8b, in order to finally give the eight-shaped structure consisting of two cells observed in Fig. 8c. The bifurcation observed from the streamline patterns in Fig. 8 is due to the presence of a separation point at the cold wall (right wall in Fig. 8) and separation line (not drawn in Fig. 8) occurring in counter-courant flow situations at wall. At the cold wall, the main flow from bottom to top encounters the primary vortex penetrating the open channel from the top. The principal influence on the viscous flow between the main primary vortex and the right cold wall is the induced adverse pressure gradient impressed to the bottom of the primary vortex shown with the distortion of the streamlines (see Fig. 8b; $t=20$ min). Consequently, the compression of the vorticity field near the bottom of the primary vortex leads to "break" this primary vortex to create a secondary co-rotating vortex. The presence of this secondary vortex is essentially similar to that frequently mentioned in descriptions of vortex interactions with walls [19]. The characteristics of the upper cell are similar to that of the initial single cell of the transitional phase, except for its reduced length. As concerns the lower cell, it is located at the bottom of the zone previously occupied by the initial cell and extends a bit further down the channel.

4. Conclusion

A study of the flow dynamics in a vertical water channel asymmetrically heated was carried out experimentally. Flow visualization techniques

using laser tomography with discrete and continuous tracers were employed. Flow visualizations performed in the mid-plane of the channel allowed the observation of the flow dynamics during both the transient and the steady state regimes. Three modified Rayleigh numbers in a range ($4.3\times10^5<Ra^*<4.5\times10^6$) corresponding to the boundary-layer type flow regime as well as three aspect ratios ($R_f=5.2$; 6; 6.9) were investigated. Two sets of experiments were carried out for several values of the modified Rayleigh number (Ra^*) and of the aspect ratio (R_f). Both the influence of the aspect ratio and that of the modified Rayleigh number on the flow structure were investigated.

In all cases, an upward boundary layer flow is found near the heated wall, accompanied by a reverse flow developing on the opposite side from the top-end of the channel. In steady state, the reverse flow takes the form of an elongated eight-shaped structure with two main recirculation cells. For a fixed Ra^*, the total length of the structure is all the more important than the aspect ratio is small. Indeed, the lower recirculation cell length remains constant while the upper cell length decreases when the aspect ratio increases. Furthermore, the increase of Ra^* with a fixed aspect ratio still leads to an eight-shape structure. In the range of Ra^* investigated in this study, and roughly corresponding to an order of magnitude, the increase in Ra^* results in a reduction of the overall size of the recirculation, mainly consisting in a strong reduction of the upper recirculation cell length. Further investigations extending the range of Ra^* could be considered to confirm this trend. Moreover, the investigation of the time-evolution of the flow dynamics during the transient has shown how the flow structure evolved from a single cell to a more complex eight-shaped structure with two main recirculation cells.

Acknowledgments

The authors acknowledge the partial support from the Ministry of Education, Research and Innovation (Romania), CNCSIS-UEFISCU, through PN II-Ideas, Grant No. 603/19.01.2009, CNCSIS Code ID_327.

The authors are also very grateful to the French AMETH network.

References

[1] G. Gan, A parametric study of Trombe walls for passive cooling of buildings, Energy and Buildings 27 (1998) 37–43.
[2] W. Ding, Y. Hasemi, T. Yamada, Natural ventilation performance of a double-skin façade with a solar chimney, Energy and Buildings 37 (2005) 411–418.
[3] W. Elenbaas, Heat dissipation of parallel plates by free convection, Physica 9 (1942) 1–28.
[4] B.W. Webb, D.P. Hill, High Rayleigh number laminar natural convection in an asymmetrical heated vertical channel, ASME Journal of Heat Transfer 111 (1989) 649–656.
[5] E.M. Sparrow, G.M. Chrysler, L.F. Azevedo, Observed flow reversals and measured-predicted Nusselt numbers for natural convection in a one-sided heated vertical channel, ASME Journal of Heat Transfer 106 (1984) 325–332.
[6] A. Bar-Cohen, W.M. Rohsenow, Thermally optimum spacing of vertical, natural convection cooled, parallel plates, ASME Journal of Heat Transfer 106 (1984) 116–123.
[7] R.A. Wirtz, R.J. Stutzman, Experiments on free convection between vertical parallel plates with symmetric heating, ASME Journal of Heat Transfer 104 (1982) 501–507.
[8] W. Aung, L.S. Fletcher, V. Sernas, Developing laminar free convection between vertical flat plates with asymmetric heating, International Journal of Heat and Mass Transfer 15 (1972) 2293–2308.
[9] T. Yilmaz, A. Gilchrist, Temperature and velocity field characteristics of turbulent natural convection in a vertical parallel-plate channel with asymmetric heating, Heat and Mass Transfer 43 (2007) 707–719.
[10] T. Yilmaz, S.M. Fraser, Turbulent natural convection in a vertical parallel-plate channel with asymmetric heating, International Journal of Heat and Mass Transfer 50 (2007) 2612–2623.
[11] M.A. Habib, S.A.M. Said, S.A. Ahmed, A. Asghar, Velocity characteristics of turbulent natural convection in symmetrically and asymmetrically heated vertical channels, Experimental Thermal and Fluid Science 26 (2002) 77–87.
[12] S. Fohanno, N. Dumez, D. Ospir, G. Polidori, C. Popa, Influence du rapport d'aspect sur l'écoulement de convection libre en canal plan, Proceedings of the IXème Colloque Interuniversitaire Franco-Québécois, Lille, France, 2009, pp. 21–26.
[13] K.D. Kihm, J.H. Kim, L.S. Fletcher, Onset of flow reversal and penetration length of natural convective flow between isothermal vertical walls, ASME Journal of Heat Transfer 117 (1995) 776–779.
[14] C.-O. Olsson, Prediction of Nusselt number and flow rate of buoyancy driven flow between vertical parallel plates, ASME Journal of Heat Transfer 126 (2004) 97–104.
[15] G. Polidori, E.-C. Mladin, T. de Lorenzo, Extension de la méthode de Karman–Pohlhausen aux régimes transitoires de convection libre pour Pr > 0,6, Comptes Rendus de l'Académie des Sciences - Série IIb 328 (2000) 763–766.
[16] S.H. Kim, N.K. Anand, W. Aung, Effect of wall conduction on free convection between asymmetrically heated vertical plates: uniform wall heat flux, International Journal of Heat and Mass Transfer 33 (1990) 1013–1023.
[17] S. Fohanno, G. Polidori, Effect of the gap size in the start-up free convective flow around a square prism near a wall, International Journal of Heat and Fluid Flow 26 (2005) 25–33.
[18] S. Fohanno, A. Korichi, G. Polidori, Visualizations of the unsteady interaction of opposite buoyancy induced flows, Heat and Mass Transfer 43 (2007) 997–1002.
[19] T.L. Doligalski, C.R. Smith, J.D.A. Walker, Vortex interactions with walls, Annual Review of Fluid Mechanics 26 (1994) 573–616.